Vol. 25, no. 3, 2025
eISSN 2687-1653
PEER-REVIEWED SCIENTIFIC AND PRACTICAL JOURNAL

Advanced Engineering Research (Rostov-on-Don)

Mechanics

Machine Buiding and Machine Science

Information Technology, Computer Science and Management

www.vestnik-donstu.ru
DOI 10.23947/2687-1653

Advanced Engineering Research (Rostov-on-Don)

Peer-reviewed scientific and practical journal

eISSN 2687–1653

Published since 2000

Periodicity – 4 issues per year

DOI: 10.23947/2687–1653

Founder and Publisher — Don State Technical University (DSTU), Rostov-on-Don, Russian Federation

The journal is aimed at informing the readership about the latest achievements and prospects in the field of mechanics, mechanical engineering, computer science and computer technology. The publication is a forum for cooperation between Russian and foreign scientists, it contributes to the convergence of the Russian and world scientific and information space.

The journal is included in the List of the leading peer-reviewed scientific publications (Higher Attestation Commission under the Ministry of Science and Higher Education of the Russian Federation), where basic scientific results of dissertations for the degrees of Doctor and Candidate of Science in scientific specialties and their respective branches of science should be published.

The journal publishes articles in the following fields of science:

– Theoretical Mechanics, Dynamics of Machines (Engineering Sciences)
– Deformable Solid Mechanics (Engineering, Physical and Mathematical Sciences)
– Mechanics of Liquid, Gas and Plasma (Engineering Sciences)
– Mathematical Simulation, Numerical Methods and Program Systems (Engineering Sciences)
– System Analysis, Information Management and Processing, Statistics (Engineering Sciences)
– Automation and Control of Technological Processes and Productions (Engineering Sciences)
– Software and Mathematical Support of Machines, Complexes and Computer Networks (Engineering Sciences)
– Computer Modeling and Design Automation (Engineering, Physical and Mathematical Sciences)
– Computer Science and Information Processes (Engineering Sciences)
– Machine Science (Engineering Sciences)
– Machine Friction and Wear (Engineering Sciences)
– Technology and Equipment of Mechanical and Physicotechnical Processing (Engineering Sciences)
– Engineering Technology (Engineering Sciences)
– Welding, Allied Processes and Technologies (Engineering Sciences)
– Methods and Devices for Monitoring and Diagnostics of Materials, Products, Substances and the Natural Environment (Engineering Sciences)
– Hydraulic Machines, Vacuum, Compressor Equipment, Hydraulic and Pneumatic Systems (Engineering Sciences)

Registration	Extract from the Register of Registered Mass Media ЭЛ № ФС 77 – 78854 dated August 07, 2020, issued by the Federal Service for Supervision of Communications, Information Technology and Mass Media
Indexing and Archiving	Scopus, RSCI, RISC (core), CyberLeninka, CrossRef, Dimensions, DOAJ, EBSCO, Index Copernicus, Internet Archive, Google Scholar
Website	https://vestnik-donstu.ru
Address of the Editorial Office	1, Gagarin sq., Rostov-on-Don, 344003, Russian Federation
E-mail	vestnik@donstu.ru
Telephone	+7 (863) 2–738–372
Date of Publication No.3,2025	30.09.2025

ДОНСКОЙ ГОСУДАРСТВЕННЫЙ ТЕХНИЧЕСКИЙ УНИВЕРСИТЕТ

Advanced Engineering Research (Rostov-on-Don)

Рецензируемый научно-практический журнал

eISSN 2687–1653

Издается с 2000 года

Периодичность – 4 выпуска в год

DOI: 10.23947/2687–1653

Учредитель и издатель — Федеральное государственное бюджетное образовательное учреждение высшего образования «Донской государственный технический университет» (ДГТУ), г. Ростов-на-Дону

Создан в целях информирования читательской аудитории о новейших достижениях и перспективах в области механики, машиностроения, информатики и вычислительной техники. Издание является форумом для сотрудничества российских и иностранных ученых, способствует сближению российского и мирового научно-информационного пространства.

Журнал включен в перечень рецензируемых научных изданий (К2), в котором должны быть опубликованы основные научные результаты диссертаций на соискание ученой степени кандидата наук, на соискание ученой степени доктора наук (Перечень ВАК) по следующим научным специальностям:

1.1.7 – Теоретическая механика, динамика машин (технические науки)
1.1.8 – Механика деформируемого твердого тела (технические, физико-математические науки)
1.1.9 – Механика жидкости, газа и плазмы (технические науки)
1.2.2 – Математическое моделирование, численные методы и комплексы программ (технические науки)
2.3.1 – Системный анализ, управление и обработка информации, статистика (технические науки)
2.3.3 – Автоматизация и управление технологическими процессами и производствами (технические науки)
2.3.5 – Математическое и программное обеспечение вычислительных систем, комплексов и компьютерных сетей (технические науки)
2.3.7 – Компьютерное моделирование и автоматизация проектирования (технические, физико-математические науки)
2.3.8 – Информатика и информационные процессы (технические науки)
2.5.2 – Машиноведение (технические науки)
2.5.3 – Трение и износ в машинах (технические науки)
2.5.5 – Технология и оборудование механической и физико-технической обработки (технические науки)
2.5.6 – Технология машиностроения (технические науки)
2.5.8 – Сварка, родственные процессы и технологии (технические науки)
2.5.9 – Методы и приборы контроля и диагностики материалов, изделий, веществ и природной среды (технические науки)
2.5.10 – Гидравлические машины, вакуумная, компрессорная техника, гидро- и пневмосистемы (технические науки)

Регистрация	Выписка из реестра зарегистрированных средств массовой информации ЭЛ № ФС 77 – 78854 от 07 августа 2020 г., выдано Федеральной службой по надзору в сфере связи, информационных технологий и массовых коммуникаций
Индексация и архивация	Scopus, RSCI, РИНЦ (ядро), CyberLeninka, CrossRef, Dimensions, DOAJ, EBSCO, Index Copernicus, Internet Archive, Google Scholar
Сайт	https://vestnik-donstu.ru
Адрес редакции	344003, Российская Федерация, г. Ростов-на-Дону, пл. Гагарина, 1
E-mail	vestnik@donstu.ru
Телефон	+7 (863) 2–738–372
Дата выхода №3,2025 в свет	30.09.2025

Contents

Содержание

MECHANICS
МЕХАНИКА

Check for updates

УДК 614

Original Empirical Research

https://doi.org/10.23947/2687-1653-2025-25-3-171-185

EDN: UKVSSN

Finite Element Design and Analysis of Sustainable Mono-Reinforced and Hybrid-Reinforced Fibergeopolymers

Sergey V. Klyuev[1], **Alexander V. Klyuev**[1], **Narman A. Ayubov**[2], **Roman S. Fediuk**[3] ✉, **Elena V. Levkina**[3]

[1] V.G. Shukhov Belgorod State Technological University, Belgorod, Russian Federation

[2] Kh.I. Ibragimov Complex Research Institute of the Russian Academy of Sciences, Grozny, Russian Federation

[3] Far Eastern Federal University, Vladivostok, Russian Federation

✉ roman44@ya.ru

Abstract

Introduction. Environmental improvement involves the recycling of man-made materials for product recovery with high performance characteristics. However, in general, energy-intensive and uneconomical materials have no alternative in construction. Literary information on the problem is insufficient and uncompiled. The presented article is intended to fill this gap. The research objective is to study mono-reinforced and hybrid-reinforced fibergeopolymers. For this purpose, two problems are solved: design of polymers and analysis of beams made from them using the finite element method.

Materials and Methods. The binding base for the production of fibergeopolymers was sintered particles (beads) extracted from basalt wool waste — technogenic fibrous materials (TFM). The fiber was made from metal cord, basalt wool waste and polypropylene. Beams made from hybrid-reinforced fibergeopolymers were studied under bending and shear in the ANSYS 16.1 software environment.

Results. Two types of geopolymers were obtained:

– mono-reinforced (fiber from metal cord, polypropylene fiber, and TFM – fiber from waste from basalt wool production);

– hybrid-fiber-reinforced (metal cord + polypropylene, metal cord + TFM, polypropylene + TFM).

High values of elastic modulus (more than 25 GPa), bending strength (up to 10.19 MPa) and compression strength (up to 46.67 MPa) were defined. The ratio of bending and compression strength for the studied and traditional materials was 1:4 and 1:10, respectively. The simulated and experimental indicators of beam deflections under loads from 5 to 72 kN were compared. It was found that finite element modeling allowed designing structures from the developed materials and predicting their performance characteristics.

Discussion. The cases of the smallest discrepancy between the modeling and experimental data were established. For FGP-1, it was 8% (load — 35 kN), for FGP-2 — 11% (50 kN), for FGP-3 — 7% (38 kN), for FGP-1 (1%) — 3% (30 kN). Among the hybrid-reinforced fibergeopolymers, the best compliance was that of HFGP-3. At a load of 55 kN, the discrepancy was 0.80% (theory — 4.98 mm, experiment — 5.02 mm). For HFGP-1, the best indicator was 1.85% (72 kN, 5.85 mm, 5.96 mm), for HFGP-2 — 9.12% (63 kN, 5.58 mm, 6.14 mm). The applied value of the results was confirmed by their visualization – the similarity and coincidence of the curves on the graphs.

Conclusions. The advantages of the proposed innovative components for the production of building materials are proved. They are environmentally friendly and show sufficient workability. Design of hybrid-reinforced fibergeopolymers makes it possible to obtain high values of bending and compression strength (significantly higher than that of unreinforced concrete). The modulus of elasticity of more than 25 GPa proves good resistance of the material to deformations. The results of the modeling are adequate to the results of the experiments.

Keywords: mono-reinforced fibergeopolymers, hybrid-reinforced fibergeopolymers, processing of technogenic raw materials, technogenic fibrous materials, technical properties of fibers, geopolymer concrete

Acknowledgements. The authors would like to thank the anonymous reviewers for their time and valuable comments.

Funding Information. The research was done with the financial support of the Russian Science Foundation, project No. 25–19–00426 (https://rscf.ru/project/25-19-00426/).

For Citation. Klyuev SV, Klyuev AV, Ayubov NA, Fediuk RS, Levkina EV. Finite Element Design and Analysis of Sustainable Mono-Reinforced and Hybrid-Reinforced Fibergeopolymers. *Advanced Engineering Research* (*Rostov-on-Don*). 2025;25(3):171–185. https://doi.org/10.23947/2687-1653-2025-25-3-171-185

Оригинальное эмпирическое исследование

Проектирование и анализ методом конечных элементов экологически безопасных моноармированных и гибридноармированных фиброгеополимеров

С.В. Клюев[1], А.В. Клюев[1] Н.А. Аюбов[2], Р.С. Федюк[3] ✉, Е.В. Левкина[3]

[1] Белгородский государственный технологический университет им. В.Г. Шухова, г. Белгород, Российская Федерация

[2] Комплексный научно-исследовательский институт им. Х.И. Ибрагимова Российской академии наук, г. Грозный, Российская Федерация

[3] Дальневосточный федеральный университет, г. Владивосток, Российская Федерация

✉ roman44@ya.ru

Аннотация

Введение. Улучшение экологии предполагает переработку техногенных материалов для получения продукции с высокими эксплуатационными характеристиками. Однако в строительстве в целом безальтернативны энергоемкие и неэкономичные материалы. Литературные сведения по проблеме недостаточны и разрознены. Представленная статья призвана восполнить этот пробел. Цель работы — исследование моноармированных и гибридноармированных фиброгеополимеров. Для достижения цели решались две задачи: проектирование полимеров и анализ балок из них методом конечных элементов.

Материалы и методы. Вяжущей основой фиброгеополимеров служили спекшиеся частицы (корольки) из отходов техногенных волокнистых материалов (ТВМ), а именно из базальтовой ваты. Фибру изготавливали из металлокорда, отходов базальтовой ваты и полипропилена. Балки из гибридноармированных фиброгеополимеров изучали при изгибе и сдвиге в программной среде Ansys 16.1.

Результаты исследования. Получены два вида геополимеров:

– моноармированные (фибра из металлокорда, полипропиленовая фибра и ТВМ – фибра из отходов производства базальтовой ваты);

– гибриднофиброармированные (металлокорд + полипропилен, металлокорд + ТВМ, полипропилен + ТВМ).

Выявили высокие значения модуля упругости (более 25 ГПа), прочности при изгибе (до 10,19 МПа) и сжатии (до 46,67 МПа). Отношение прочности при изгибе и сжатии для исследуемых и традиционных материалов — 1:4 и 1:10 соответственно. Сравнили смоделированные и экспериментальные показатели прогибов балок при нагрузках от 5 до 72 кН. Выяснили, что конечноэлементное моделирование позволяет проектировать конструкции из разработанных материалов и прогнозировать их эксплуатационные характеристики.

Обсуждение. Установлены случаи наименьшего расхождения данных моделирования и опытов. Для ФГП-1 это 8 % (нагрузка — 35 кН), для ФГП-2 — 11 % (50 кН), для ФГП-3 — 7 % (38 кН), для ФГП-1 (1 %) — 3 % (30 кН). Среди гибридноармированных фиброгеополимеров наилучшее соответствие — у ГФГП-3. При нагрузке 55 кН расхождение — 0,80 % (теория — 4,98 мм, опыт — 5,02 мм). Для ГФГП-1 лучший показатель — 1,85 % (72 кН, 5,85 мм, 5,96 мм), для ГФГП-2 — 9,12 % (63 кН, 5,58 мм, 6,14 мм). Прикладную ценность результатов подтвердила их визуализация — схожесть и совпадение кривых на графиках.

Заключение. Доказаны преимущества предложенных инновационных компонентов для производства строительных материалов. Они экологичны, демонстрируют достаточную удобоукладываемость. Проектирование гибридноармированных фиброгеополимеров дает возможность получить высокие значения прочности при изгибе и сжатии (существенно выше, чем у неармированных бетонов). Модуль упругости более 25 ГПа доказывает хорошее сопротивление материала деформациям. Итоги моделирования адекватны результатам экспериментов.

Ключевые слова: моноармированные фиброгеополимеры, гибридноармированные фиброгеополимеры, переработка техногенного сырья, техногенные волокнистые материалы, технические свойства фибр, геополимерный бетон

Благодарности. Авторы благодарны анонимным рецензентам за уделенное время и ценные комментарии.

Финансирование. Работа опубликована при финансовой поддержке РНФ, проект № 25–19–00426 (https://rscf.ru/project/25-19-00426/).

Для цитирования. Клюев С.В., Клюев А.В., Аюбов Н.А., Федюк Р.С., Левкина Е.В. Проектирование и анализ методом конечных элементов экологически безопасных моноармированных и гибридноармированных фиброгеополимеров. *Advanced Engineering Research* (*Rostov-on-Don*). 2025;25(3):171–185. https://doi.org/10.23947/2687-1653-2025-25-3-171-185

Introduction. One of the priorities of the strategy of scientific and technical development of the Russian Federation is to counteract man-made, biogenic, sociocultural and other sources of danger to society and the economy [1]. The most important task of environmental safety is the development of processes and techniques [2], resource conservation [3], and complex processing of man-made materials [4], obtaining products with high performance characteristics on their basis [5].

Transdisciplinary approaches provide a new level of development of building composite mixtures. For progress in this area, it is important to move away from the current templates of designing building materials [6]. To reduce the complexity of recipes and the cost of components, it is necessary to use data from various sciences: materials science, physics, chemistry, geology, nanotechnology, etc. In addition, certain operational characteristics can be assigned to the new composite [7].

Improvement of physical, mechanical, operational, protective and environmental properties of modern modified composites is based on:

– optimization of formulations and technologies;

– use of non-traditional types of natural and man-made raw materials [8].

It is known that the economic efficiency of projects is largely determined by the use of high-tech building materials [9]. Modern composites have good prospects in industrial and civil construction [9]. They are often used for unique projects and objects that are operated under various conditions [10].

When producing the materials described above, one of two innovative strategies is usually used:

– recycling for the production of so-called “green” materials [11];

– creation of “smart” concrete for monitoring the condition of building structures [12].

It should be noted that the regulatory framework governing construction design does not contain recommendations on the use of man-made waste as fillers for concrete. Promising approaches are discussed in the literature. As a rule, this concerns the comprehensive processing of used tires, as well as fibrous materials — man-made waste from the production of mineral wool [13]. However, both of these solutions have not been sufficiently studied and tested in practice.

The possibility of using carbon black and TFM waste should also be mentioned. However, even in this case there are no adequate scientific conclusions that would prove the practical feasibility of introducing such composites into construction practice [14].

The objective of the presented work was to study and design unreinforced and hybrid-reinforced fibergeopolymers using the FEM. Within the framework of this study, two problems were solved: design of hybrid-reinforced fibergeopolymers and analysis of beams made from them by the FEM. This was required to reach the stated goal, as well as in general for the creation of sustainable building materials.

Materials and Methods. The binding base for the production of fibergeopolymers was sintered particles (beads) extracted from waste basalt wool — technogenic fibrous materials (TFM). A combination of sodium silicate and sodium hydroxide solution was used as an alkaline activating liquid. Polyfractionated quartz sand with a specific gravity of 2.67 acted as a fine filler. The maximum size of the coarse aggregate used in this study did not exceed 12 mm, which increased the workability of concrete. The fiber from the metal cord of waste tires was heat-treated and cut. The fiber from TFM was obtained through grinding basalt wool. The authors found that sometimes the actual technical properties of the fibers differed from those declared by the manufacturers, and these actual parameters are given in Table 1.

Table 1

Properties of Different Types of Fiber

Properties	Metal cord	Polypropylene	TFM
Diameter, mm	0.75	0.002	0.013
Length, mm	60–75	12.0	40–70
Length to diameter ratio	80–100	6,000	3,077–5,385
Tensile strength, MPa	2,500	3.50	2,000
Modulus of elasticity, MPa	210	3.45	75,000
Specific gravity	8	0.90	2.6

The behavior of 1,000×200×100 mm beams made from hybrid-reinforced fiber-geopolymers was studied. They were analyzed by the FEM in bending and shear. The deflection of geopolymer concrete beams was calculated to prevent unacceptable deformations and provide normal operation of structures. The FEM is suitable for computer processing, it can be used to solve problems in solid mechanics, fluid mechanics, heat transfer and vibrations.

Research Results. Compositions of sustainable fibergeopolymer mixtures have been developed, which show satisfactory workability characteristics (Table 2). Workability provides high-quality, safe transportation of the geopolymer mixture to the place of installation.

Table 2

Developed Compositions and Cone Slump Measurement Results

Composition	Fiber content, % by volume	Slump, mm	Workability
Cement concrete	–	112.1	High
Unreinforced geopolymer (GP)	–	103.5	High
Fibergeopolymer (FGP-1), metal cord	0.5	80.3	Average
FGP-2, polypropylene	0.5	78.4	Average
FGP-3, TFM	0.5	76.5	Average
Hybrid fibergeopolymer (HFGP-1), metal cord + polypropylene	0.25 + 0.25	65.4	Average
HFGP-2, metal cord + TFM	0.25 + 0.25	70.2	Average
HFGP-3, TFM + polypropylene	0.25 + 0.50	68.7	Average

The composites were cured for 28 days under normal, unintentionally specified conditions. Their final mechanical properties were summarized in Table 3. High values of compressive strength (up to 46.67 MPa) and bending strength (up to 10.19 MPa) were shown. An extremely important difference in the ratio of bending and compressive strength for the studied and traditional materials was established — 1:4 and 1:10, respectively. High modulus of elasticity (more than 25 GPa) is especially important for designers and engineers, since it determines the ability of the material to resist deformation, i.e., the strength and stability of building structures. In Table 3, the compositions with the best characteristics are highlighted in color.

Table 3

Mechanical Properties of Composite Materials after Curing for 28 Days

Composition	Strength, MPa		Modulus of elasticity, GPa
	compressive	bending	
Cement concrete	40.89	4.60	19.24
Unreinforced geopolymer (GP)	41.33	4.40	19.32
Fibergeopolymer (FGP-1)	46.67	8.79	25.01
FGP-2	45.78	8.60	24.57
FGP-3	34.67	8.00	20.02
Hybrid fibergeopolymer (HFGP-1)	46.67	8.39	25.03
HFGP-2	44.44	10.19	23.49
HFGP-3	40.44	9.50	20.11

The statics problems were solved by the FEM. The sequence of analysis in the Ansys software environment is described below.

1. Setting the algorithm.
2. Specifying the geometry.
3. Specifying and determining the material properties (modulus of elasticity and Poisson's ratio).

For the modeling, a geopolymer beam with three degrees of freedom at each node was used. It moved and was elastically deformed in x, y, z directions.

Modulus of elasticity of concrete:

$$E_c = 5000\sqrt{R_{\text{сж.}}}, \tag{1}$$

where E_c — short-term static modulus of elasticity, MPa; $R_{сж.}$ — compressive strength, MPa.

Poisson's ratio is usually less than 0.5. In [15], the values from 0.18 to 0.24 are given, while in [16], the figures are from 0.23 to 0.32.

Meshing is based on the geometry of the structure. Visualization of the bending analysis in Ansys is shown in Figures 1–11.

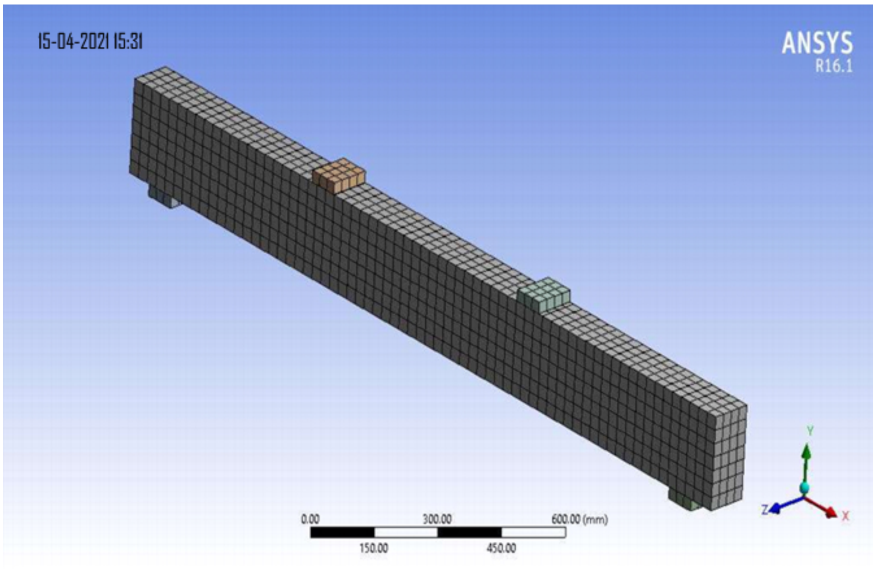

Fig. 1. Beam discretization

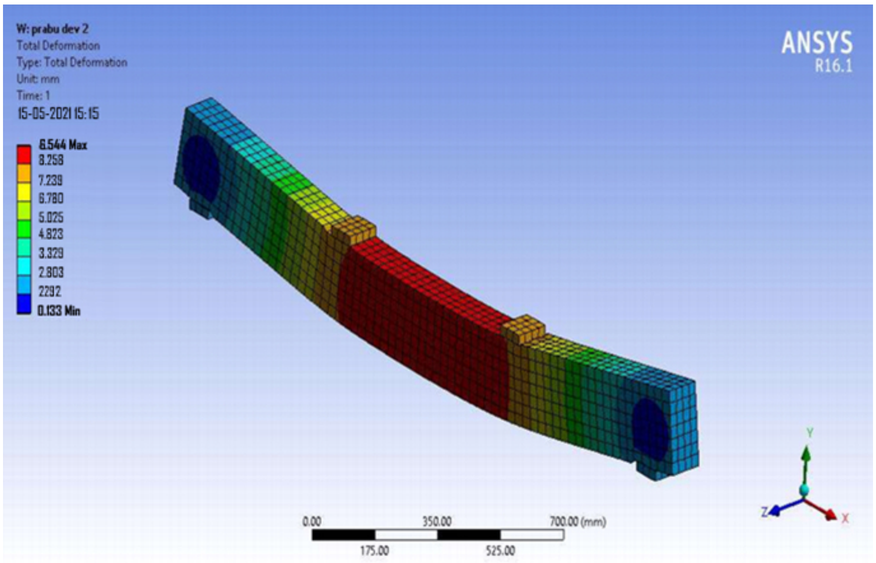

Fig. 2. Deformation of beam FGP-1

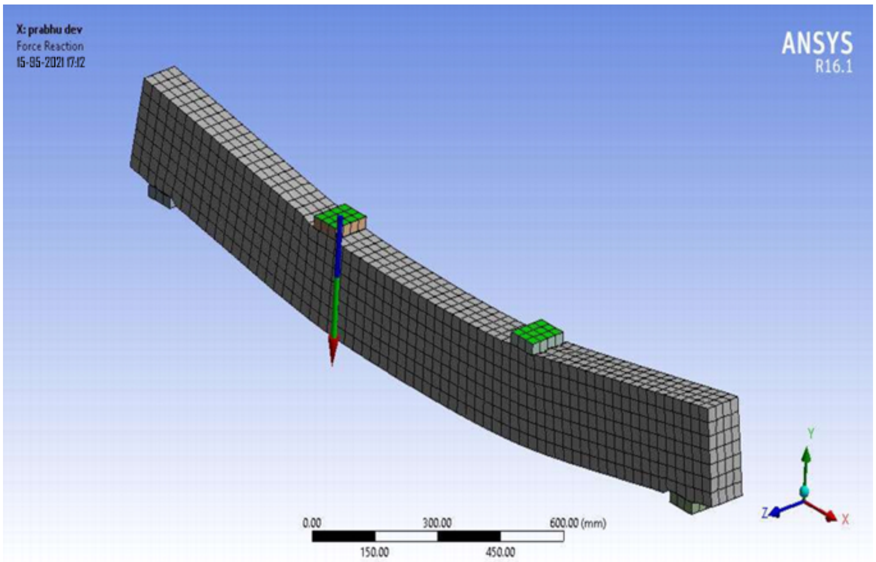

Fig. 3. Deflection of beam FGP-1

Mechanics

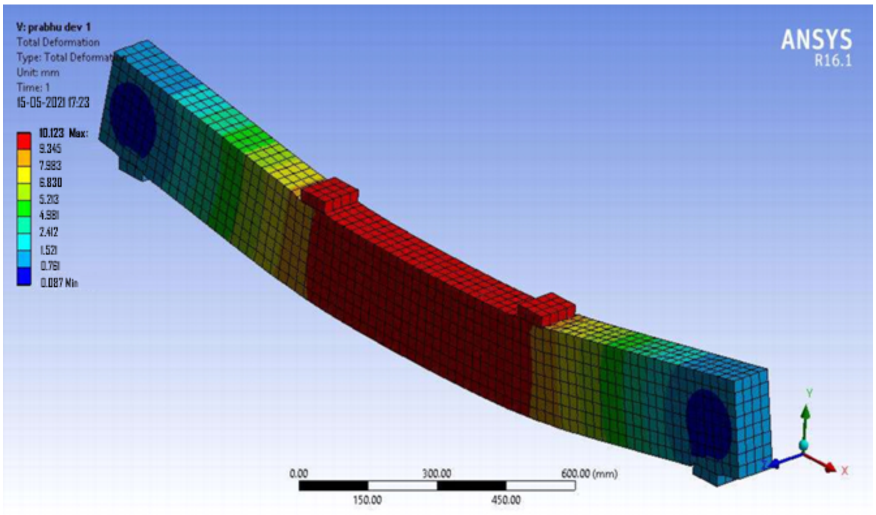

Fig. 4. Deformation of GP beam

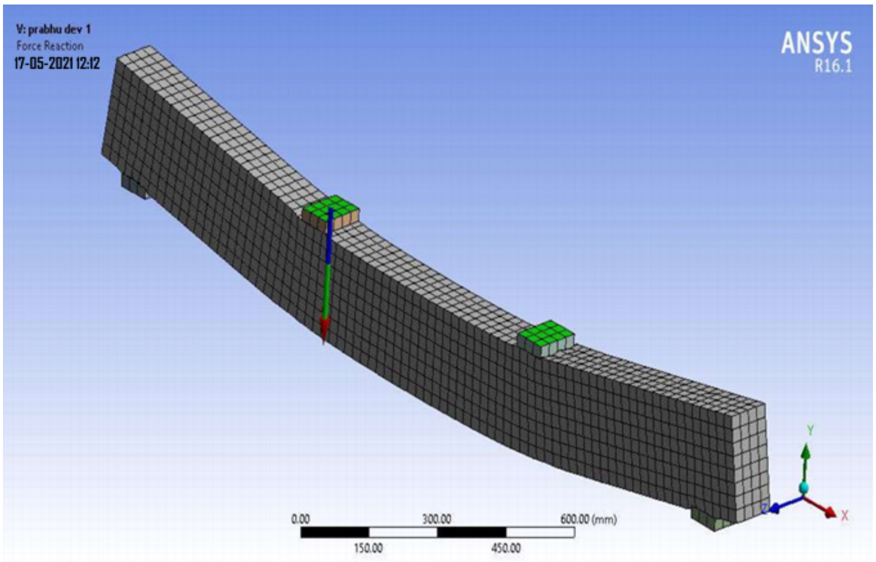

Fig. 5. Deflection of GP beam

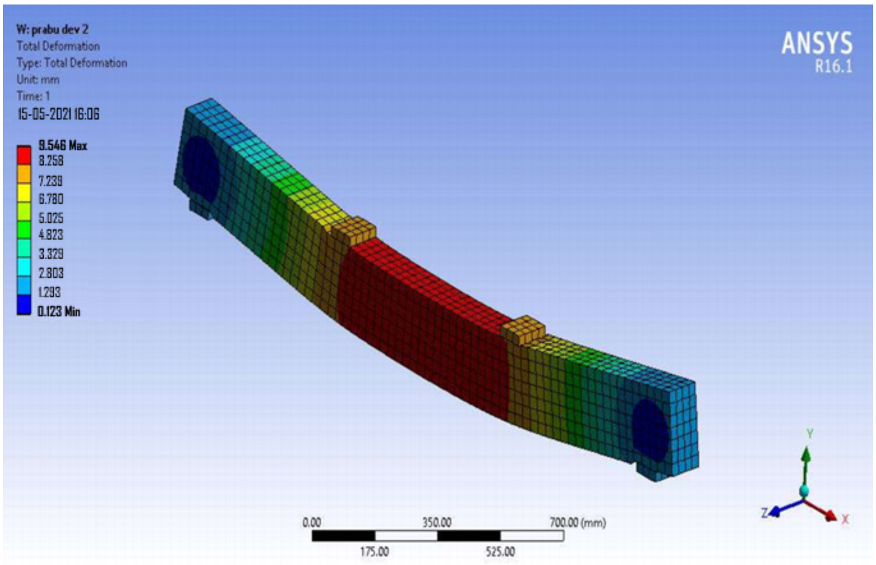

Fig. 6. Deformation of beam HFGP-1

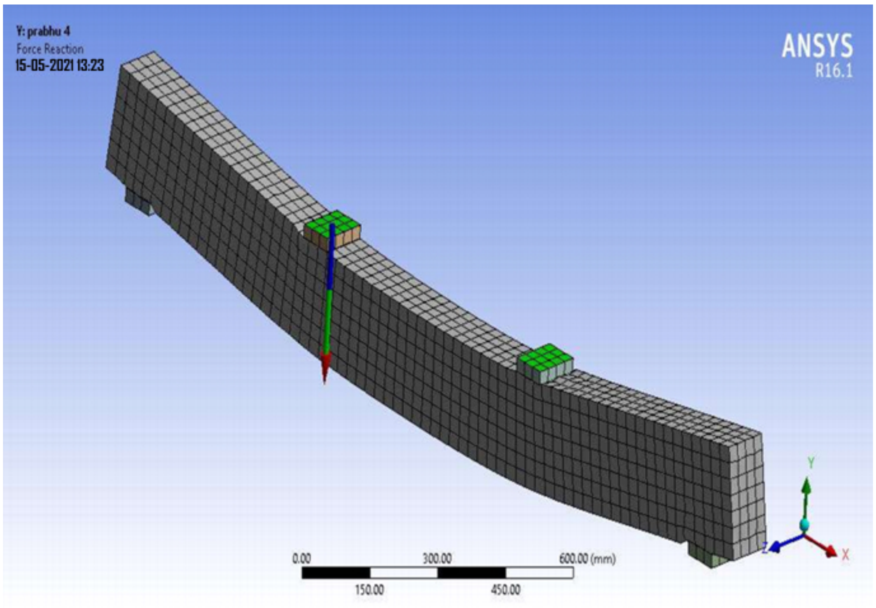

Fig. 7. Deflection of beam HFGP-1

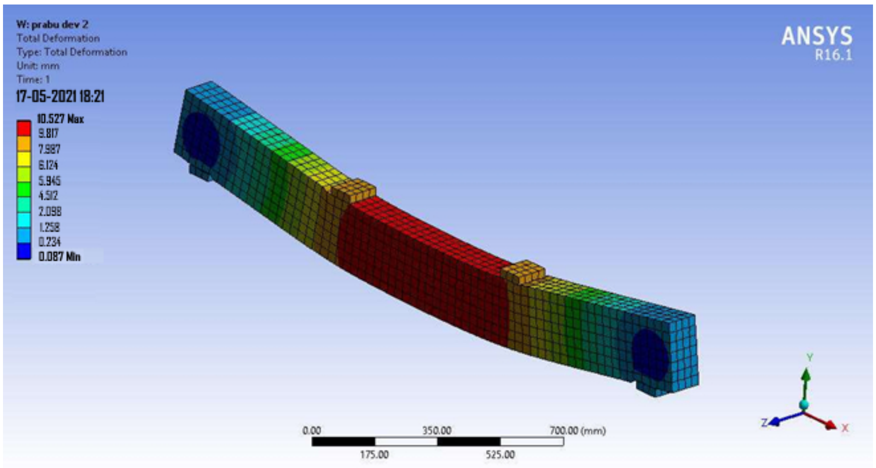

Fig. 8. Deformation of beam HFGP-2

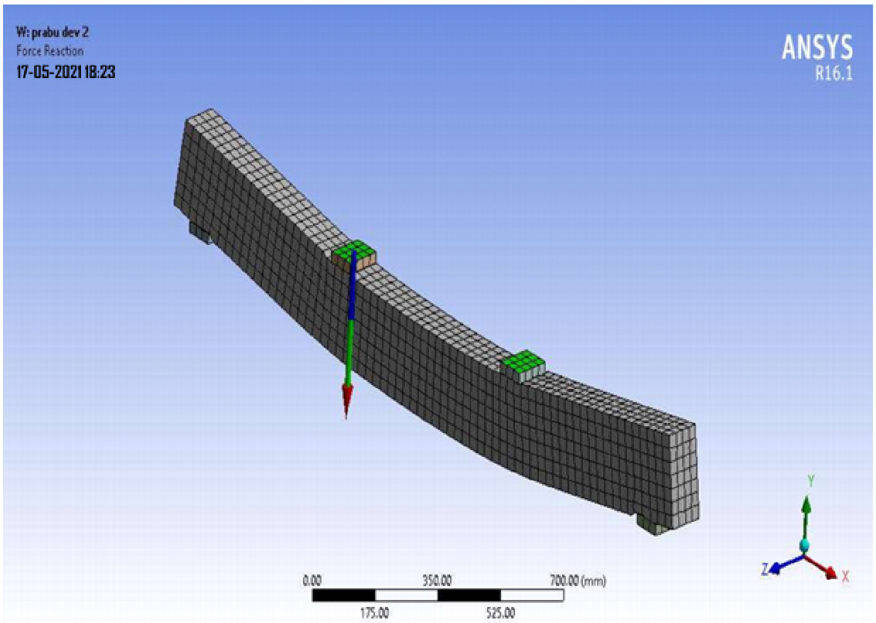

Fig. 9. Deflection of beam HFGP-2

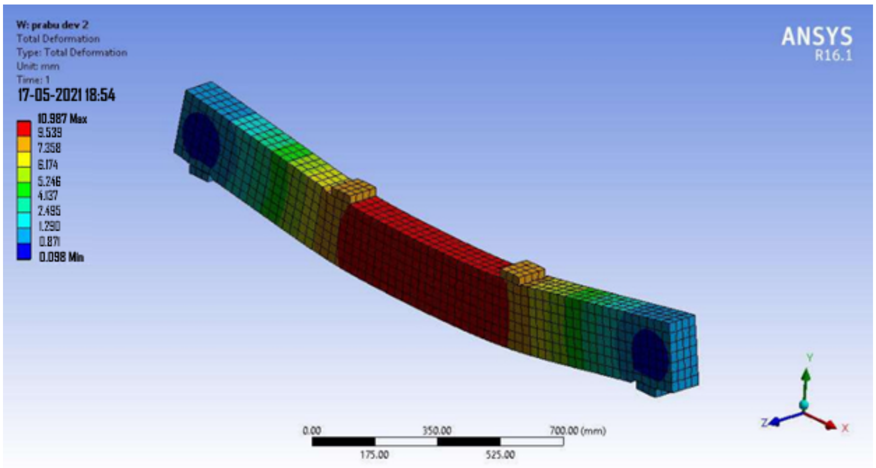

Fig. 10. Deformation of beam HFGP-3

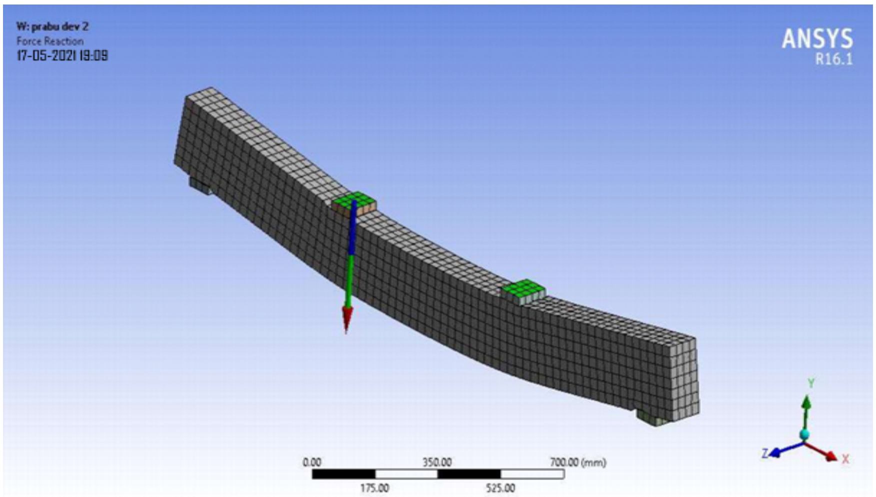

Fig. 11. Deflection of beam HFGP-3

Comparison of the experimental and theoretical results of deflection is given in Tables 4, 5 and Figures 12–17. Geopolymer concrete is an elastic-plastic material, therefore the stress-strain graph is nonlinear.

Table 4

Comparison of Experimental and Theoretical Results of Deflection

Load, kN	Cement concrete			GP			FGP-1			FGP-2			FGP-3			FGP-1(1 %)		
	Deflection, mm		Difference, %	Deflection, mm		Difference, %	Deflection, mm		Difference, %	Deflection, mm		Difference, %	Deflection, mm		Difference, %	Deflection, mm		Difference, %
	exper.	calc.		exper.	calc.		exper.	calc.		exper.	calc.		exper.	calc.		exper.	calc.	
0	0	0	0	0	0	0	0	0	0	0	0	0	0	0	0	0	0	0
5	0.85	0.65	24	0.74	0.58	22	0.48	0.35	27	0.55	0.43	22	0.70	0.42	40	0.64	0.47	27
10	1.72	1.45	16	1.52	1.58	4	1.28	1.14	11	1.28	0.98	23	1.56	0.95	39	1.44	1.05	27
15	2.45	2.35	4	2.35	2.14	9	1.96	1.56	20	1.84	1.14	38	2.18	1.47	33	2.02	1.87	7
20	2.54	3.05	20	2.96	3.05	3	2.38	2.02	15	2.64	1.45	45	2.89	2.04	29	2.74	2.43	12
25	4.35	3.96	9	3.70	3.65	1	2.96	2.48	16	3.04	2.02	34	3.34	2.90	13	3.64	3.05	16
30	5.04	4.57	9	4.20	4.14	1	3.43	3.05	11	3.78	2.75	27	4.10	3.47	15	3.98	3.85	3
35	6.25	5.43	13	4.75	4.56	4	4.14	3.81	8	4.21	3.24	23	4.98	4.25	15	4.64	4.00	14
38	7.12	6.85	4	5.20	5.10	2	4.97	4.26	14	5.02	3.75	25	5.47	5.07	7	5.08	4.56	10
44	–	–	–	5.35	5.15	4	5.14	4.58	11	5.28	4.33	18	6.76	5.48	19	5.38	4.95	8
50	–	–	–	6.75	5.45	19	5.48	4.97	9	5.58	4.98	11	–	–	–	6.57	5.50	16
52	–	–	–	–	–	–	6.03	5.05	16	6.42	5.52	14	–	–	–	–	–	–
63	–	–	–	–	–	–	6.12	5.55	9	–	–	–	–	–	–	–	–	–

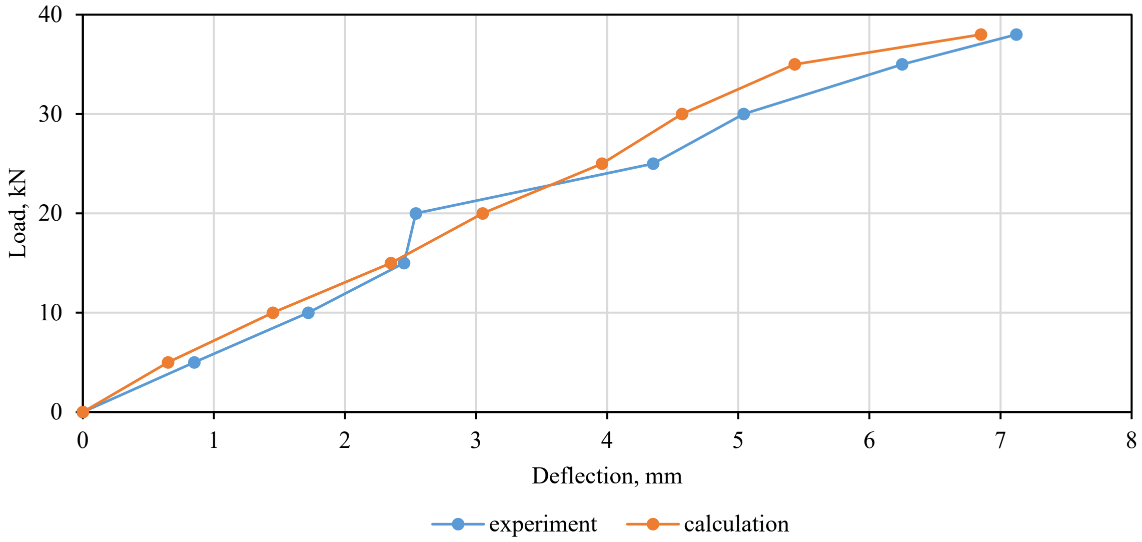

Fig. 12. Deflection of a cement concrete beam

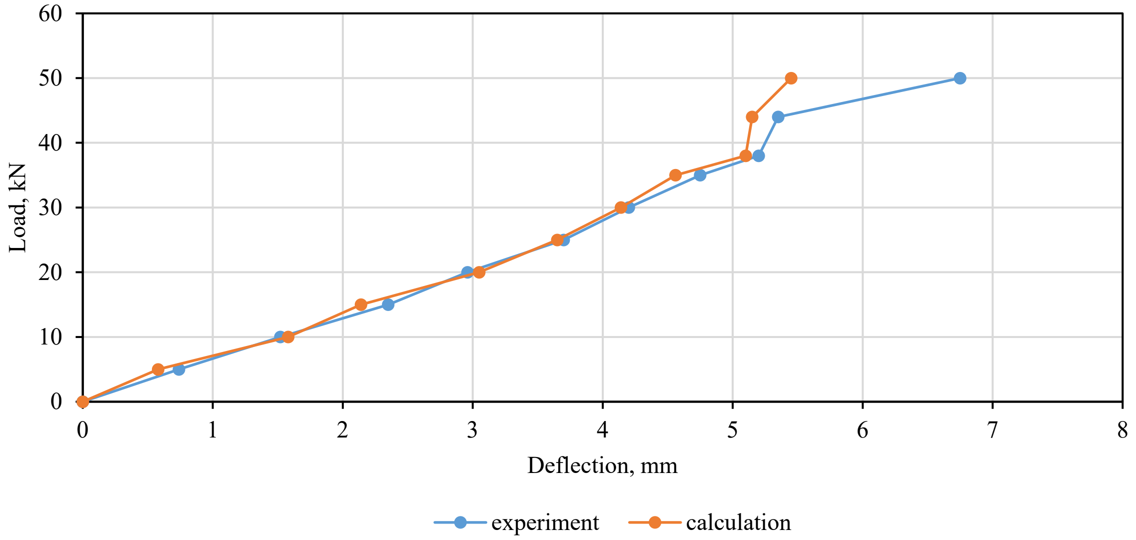

Fig. 13. Deflection of GP beam

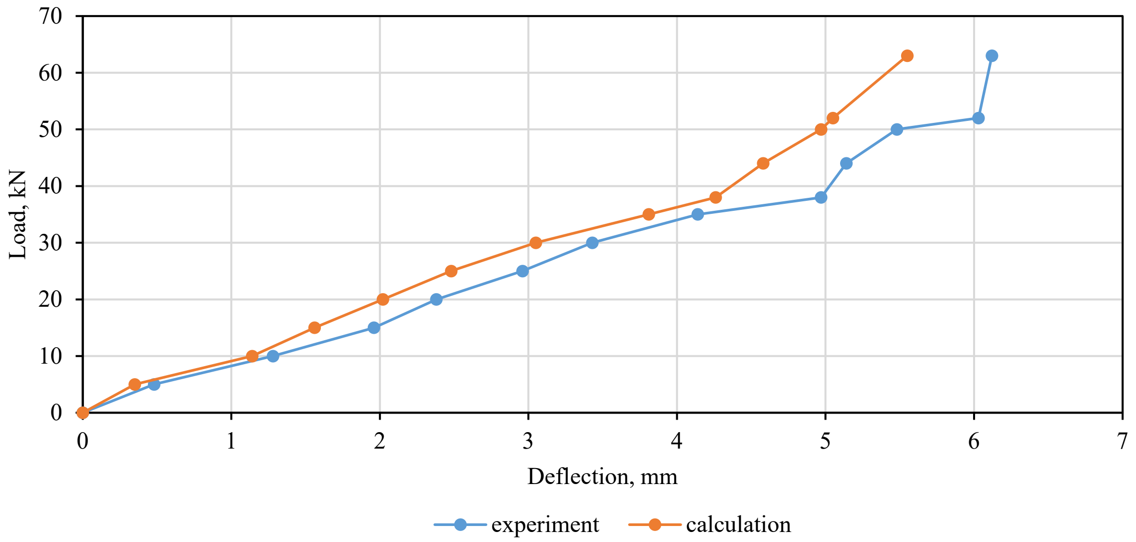

Fig. 14. Deflection of beam FGP-1

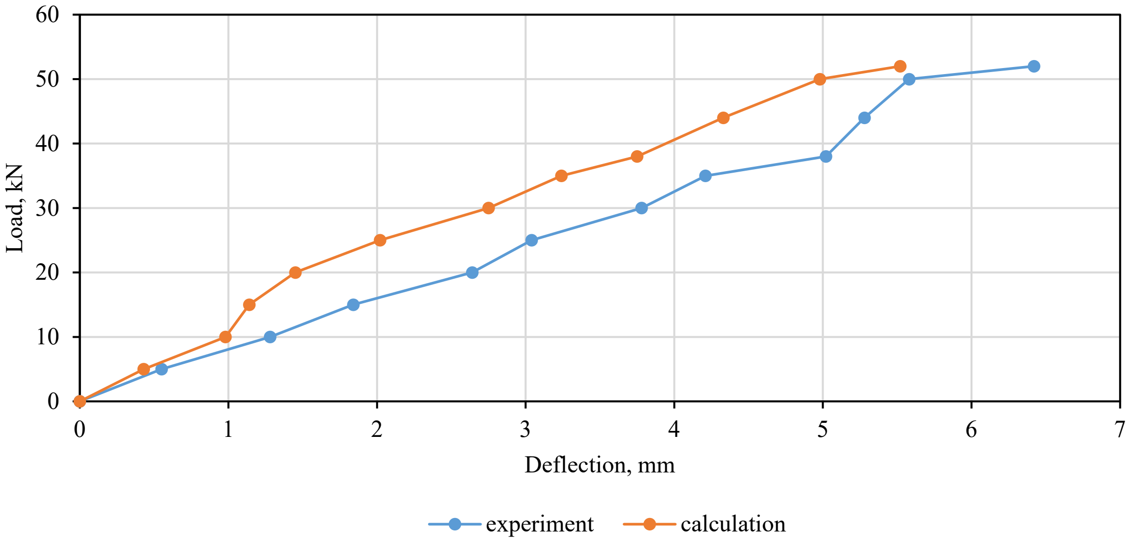

Fig. 15. Deflection of beam FGP-2

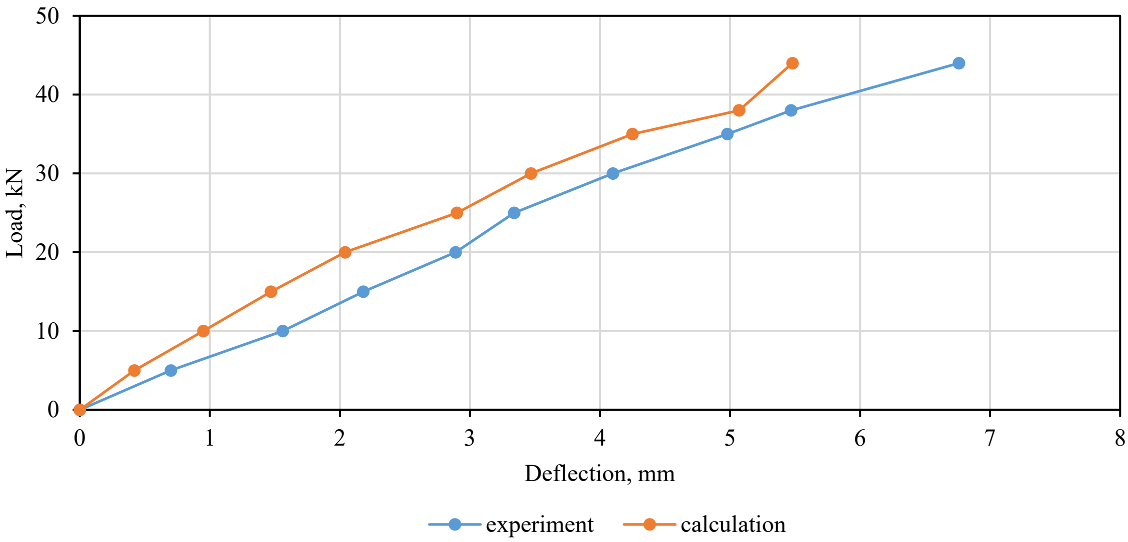

Fig. 16. Deflection of beam FGP-3

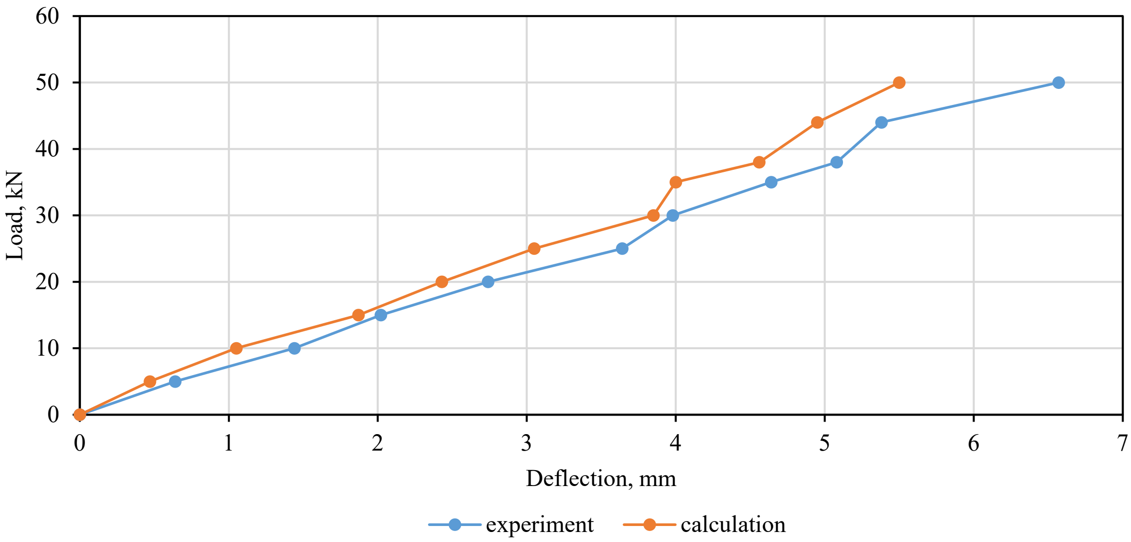

Fig. 17. Deflection of beam FGP-1 with 1% of metal cord fiber

Table 5

Comparison of Experimental and Theoretical Deflection Results for Hybrid-Reinforced Fibergeopolymers

Load, kN	Deflection, mm					
	HFGP-1		HFGP-2		HFGP-3	
	exper.	calc.	exper.	calc.	exper.	calc.
0	0	0	0	0	0	0
5	0.26	0.14	0.32	0.18	0.30	0.17
10	0.55	0.37	0.67	0.42	0.58	0.37
15	0.97	0.64	1.18	0.71	1.05	0.82
20	1.28	0.99	1.64	1.07	1.54	1.02
25	1.86	1.14	2.03	1.84	2.07	1.71
30	2.04	1.86	2.85	2.04	2.48	2.10
35	2.74	2.41	3.12	2.26	3.99	2.89
40	3.04	2.74	3.98	3.24	4.29	3.12
45	3.65	3.24	4.26	3.75	4.54	3.92
50	3.98	3.74	5.24	4.36	4.96	4.26
55	4.18	4.08	6.05	5.05	5.02	4.98
63	4.86	4.66	6.14	5.58	5.64	5.21
64	5.26	4.89	–	–	6.03	5.74
70	5.77	5.14	–	–	–	–
72	5.96	5.85	–	–	–	–

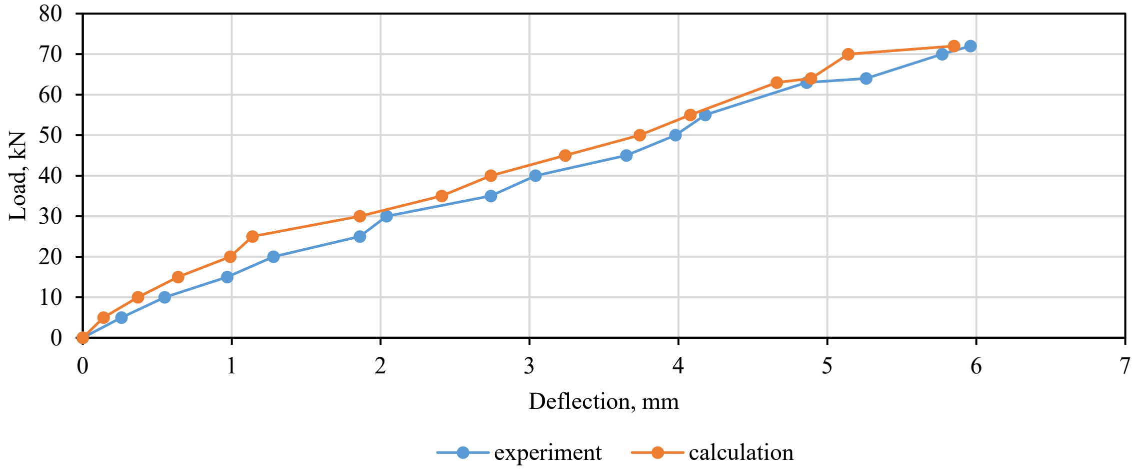

Fig. 18. Deflection of beam HFGP-1

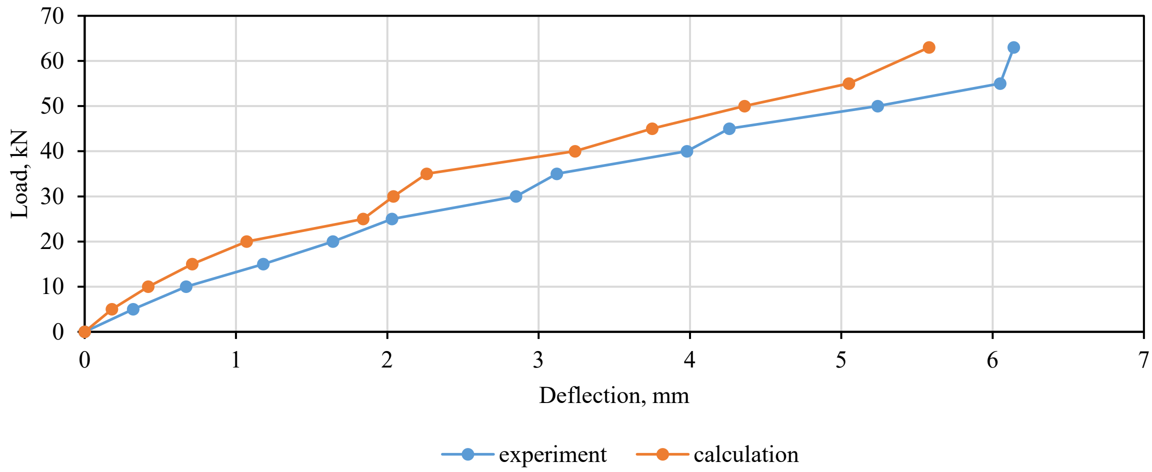

Fig. 19. Deflection of beam HFGP-2

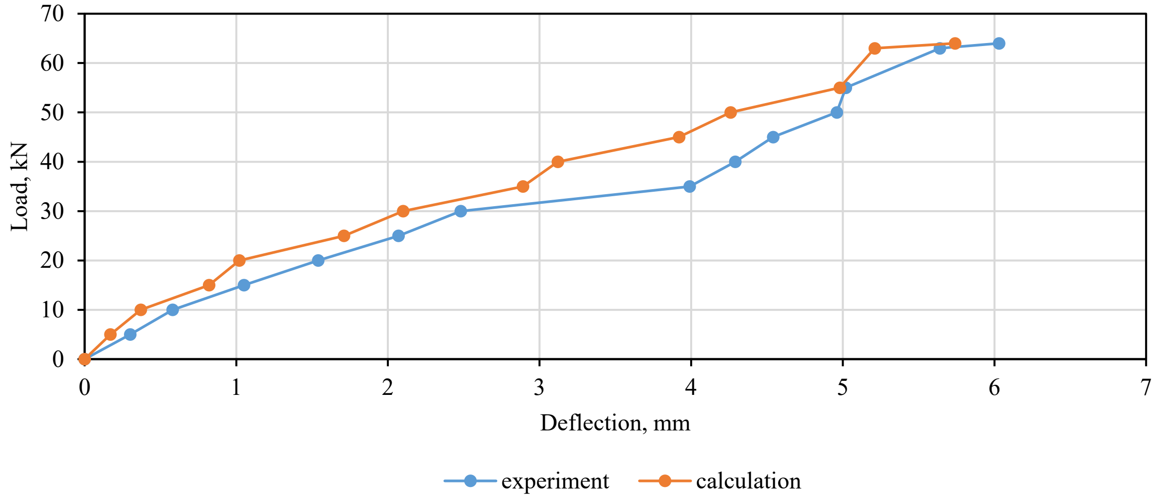

Fig. 20. Deflection of beam HFGP-3

Thus, the finite element modeling of beams made from mono-reinforced and hybrid-reinforced fibergeopolymers has shown good convergence of experimental and theoretical results, which allows for the efficient design of structures from the developed materials and the prediction of their operational characteristics.

Discussion. The most noticeable discrepancy between the results of experiments and calculations (45%) was found for FGP-2 at a load of 20 kN. At 15 kN, the difference was 38%. However, in this and the following cases, it is important to emphasize the low absolute values. At 20 kN, a deflection of 1.45 mm was theoretically assumed, but the experiment showed 2.64 mm. The corresponding data at 15 kN were 1.14 and 1.84. At other loads, the difference was significantly smaller. For FGP-3, the maximum discrepancy was recorded at minimum loads: 40% at 5 kN and 39% at 10 kN. If we are talking about absolute figures, then in the first case, the calculation is 0.42 mm, the experiment is 0.70 mm. In the second case, 0.95 mm and 1.56 mm, respectively. For FGP-1 and FGP–1 (1%), the maximum discrepancy did not exceed 27%, and at low loads. At loads of 5 kN, the theoretically obtained deflection indicator for FGP-1 is 0.35 mm, established empirically — 0.48 mm. The difference is 27%. At a load of 5 kN for FGP-1 (1%), the calculation shows a deflection of 0.47 mm, the experiment — 0.64 mm. The corresponding data for 10 kN are 1.05 and 1.44. The difference in both cases is 27%. For other loads, it is significantly less.

Let us also note the cases of the best convergence of the calculation and experimental data. For FGP-1, this is 8% (load — 35 kN), for FGP-2 — 11% (50 kN), for FGP-3 — 7% (38 kN), for FGP-1 (1%) — 3% (30 kN).

The results of the study of hybrid-reinforced fibergeopolymers allow us to state that the most significant discrepancy between theory and experiments is recorded at minimum loads (in this case, 5 kN). Thus, for HFGP-1, it is 46.2% (calculation shows a deflection of 0.14 mm, experiment — 0.26 mm). The corresponding difference for HFGP-2 is 43.8% (0.18 mm and 0.32 mm), for HFGP-3 — 43.3% (0.17 and 0.30). At other loads, the discrepancies are smaller.

The best agreement between calculations and experimental results for HFGP-1 is 1.85%. This figure is recorded at a load of 72 kN (theory — 5.85 mm, experiment — 5.96 mm). The smallest discrepancy, obtained when modeling the deflection for HFGP-2, is 9.12% (63 kN, 5.58 mm and 6.14 mm, respectively). For HFGP-3 — 0.80% (55 kN, 4.98 mm and 5.02 mm). As noted above, extremely minor discrepancies in absolute figures should be taken into account. Both individual and generalized data are of interest for design and engineering practice. This is confirmed by the visualization of the results of the work — the curves in Figures 12-20 are similar or coincide in numerous cases.

Conclusion. Innovative components for the production of sustainable building materials have been obtained [17]. Ecological compatibility is due to the fact that an alternative to cement is used [18], and this provides a significant reduction in greenhouse gas emissions. The design of hybrid-reinforced fibergeopolymers makes it possible to obtain high strength values — both in compression (from 46 MPa) and in bending (from 10 MPa). When using hybrid fiber, it is possible to reach bending and compression strength at the level of 1:4, and this is several times higher than for unreinforced Portland cement concrete [19]. The modulus of elasticity of more than 25 GPa shows good resistance of the material to deformations, which has a positive effect on the strength and stability of building structures [20]. The finite element analysis of hybrid-reinforced fibergeopolymer beams confirmed the experimental results obtained [21].

The three main research results are described below.

1. Two types of geopolymers were obtained:

– mono-reinforced (fiber from metal cord, polypropylene fiber, and fiber from waste from basalt wool production — TFM);

– hybrid fiber-reinforced (metal cord+polypropylene, metal cord+TFM, polypropylene+TFM).

2. Fiber-reinforced geopolymer concrete mixtures have standard workability characteristics that allow them to be efficiently transported to the place of use and placed in formwork.

3. Finite component modeling of beams made from mono-reinforced and hybrid-reinforced fibergeopolymers show good agreement between experimental and theoretical results, which allows for efficient design of structures made from the developed materials and prediction of their performance characteristics [22].

References

1. Laihao Yu, Yingyi Zhang, Zhenghao Zhang, Jialong Yang. Conversion of Recycled Sludge Waste into High Value-Added Ceramics as Engineering Construction Materials: Fabrication, Characterization and Performance Evaluation. *Chemical Engineering Journal*. 2023;475:146509. https://doi.org/10.1016/j.cej.2023.146509

2. Klyuev AV, Kashapov NF, Klyuev SV, Zolotareva SV, Shchekina NA, Shorstova ES, et al. Experimental Studies of the Processes of Structure Formation of Composite Mixtures with Technogenic Mechanoactivated Silica Component. *Construction Materials and Products.* 2023:6(2):5–18. https://doi.org/10.58224/2618-7183-2023-6-2-5-18

3. Fediuk R, Amran M, Klyuev S, Klyuev A. Increasing the Performance of a Fiber-Reinforced Concrete for Protective Facilities. *Fibers*. 2021;9(11):64. https://doi.org/10.3390/fib9110064

4. Bespolitov DV, Konovalova NA, Pankov PP, Shavanov ND. Overburden Recycling in Manufacture of Composite Materials for Road Construction at Mines. *Journal of Mining Science*. 2023;59(1):167–175. https://doi.org/10.1134/S1062739123010180

5. Klyuev S, Klyuev A, Fediuk R, Ageeva M, Fomina E, Amran M, et al. Fresh and Mechanical Properties of Low-Cement Mortars for 3D Printing. *Construction and Building Materials*. 2022;338:127644. https://doi.org/10.1016/j.conbuildmat.2022.127644

6. Volokitina I, Kolesnikov A, Fediuk R, Klyuev S, Sabitov L, Volokitin A, et al. Study of the Properties of Antifriction Rings under Severe Plastic Deformation. *Materials.* 2022;15(7):2584. https://doi.org/10.3390/ma15072584

7. Gilbert Sebastiano Gondokusumo, Akshay Venkateshwaran, Kiang Hwee Tan, GY Richard Liew. Shear Strength and Ductility of Novel Steel Fibre-Reinforced Concrete Dowel Connections for Composite Beams. *Construction and Building Materials*. 2024;447:138159. https://doi.org/10.1016/j.conbuildmat.2024.138159

8. Wenjie Ge, Feng Zhang, Yi Wang, Ashraf Ashour, Laiyong Luo, Linfeng Qiu, et al. Machine Learning Predictions for Bending Capacity of ECC-Concrete Composite Beams Hybrid Reinforced with Steel and FRP Bars. *Case Studies in Construction Materials*. 2024;21:e03670. https://doi.org/10.1016/j.cscm.2024.e03670

9. Klyuev AV, Kashapov NF, Klyuev SV, Lesovik RV, Ageeva MS, Fomina EV, et al. Development of Alkali-Activated Binders Based on Technogenic Fibrous Materials. *Construction Materials and Products*. 2023:6(1):60–73. https://doi.org/10.58224/2618-7183-2023-6-1-60-73

10. Qi Chen, Xiaoyong Luo, Wangcheng Luo, Zheng Yang, Dan Yang, Xutong Zheng, et al. Seismic Performance of Innovative Precast Concrete Composite Walls with Embedded XPS Insulation Layer. *Engineering Structures*. 2024;316:118605. https://doi.org/10.1016/j.engstruct.2024.118605

11. Novoselov OG, Sabitov LS, Sibgatullin KE, Sibgatullin ES, Klyuev AS, Klyuev SV, et al. Method for Calculating the Strength of Massive Structural Elements in the General Case of Their Stress-Strain State (Kinematic Method). *Construction Materials and Products.* 2023;6(3):5–17. https://doi.org/10.58224/2618-7183-2023-6-3-5-17

12. Novoselov OG, Sabitov LS, Sibgatullin KE, Sibgatullin ES, Klyuev AS, Klyuev SV, et al. Method for Calculating the Strength of Massive Structural Elements in the General Case of Their Stress-Strain State (Parametric Equations of the Strength Surface). *Construction Materials and Products.* 2023;6(2):104–120. https://doi.org/10.58224/2618-7183-2023-6-2-104-120

13. Edlaine Feital Barbosa Motta, Aldo Ribeiro de Carvalho, Júlia Gargiulo Duarte Barra, Indhira Oliveira Maciel, Thaís Mayra de Oliveira. Thermomechanical Behavior of Concretes with Addition of Non-Functionalized and Functionalized Carbon Nanotubes. *Journal of Building Engineering*. 2024;96:110642. https://doi.org/10.1016/j.jobe.2024.110642

14. Yuqiang Lin, Wenyong Zheng, Shuhua Liu, Min Yuan, Xi Qin. Multi-Ion Erosion Test and Molecular Dynamics Simulation of Carbon Nanotube Concrete under Stray Current and Salt Brine Environment. *Developments in the Built Environment*. 2024;17:100335. https://doi.org/10.1016/j.dibe.2024.100335

15. Ige Samuel Ayeni, Nor Hasanah Abdul Shukor Lim, Mostafa Samad. Engineering Properties of Natural Fibre-Reinforced One-Part Geopolymer Concrete. *Construction and Building Materials*. 2024;456:139161. https://doi.org/10.1016/j.conbuildmat.2024.139161

16. Sarici T, Ozcan M. Using Geopolymer Coated and Uncoated Geotextile as a Hybrid Method to Improve Uplift Capacity of Screw Piles in Cohesionless Soil. *Alexandria Engineering Journal*. 2024;105:666–681. https://doi.org/10.1016/j.aej.2024.08.042

17. Kachurin NM, Stas GV, Prokhorov DO, Gavrina OA. Selection of Technologies and Directions for Reducing the Technogenic Impact of Mineral Formations on the Environment. *Sustainable Development of Mountain Territories*. 2024;16(1):283–291. https://doi.org/10.21177/1998-4502-2024-16-1-283-291

18. Zaalishvili VB, Kambolov DA, Melkov DA, Fidarova MI. Statistical Characteristics Calculation of Seismic Intensity Increments for the Purpose of Seismic Microzoning in Mountain Territories. *Sustainable Development of Mountain Territories*. 2024;16(1):345–357. https://doi.org/10.21177/1998-4502-2024-16-1-345-357

19. Kachurin NM, Prokhorov DO, Stas GV, Gavrina OA. Justification of Technology for Anthropogenic Deposits Development. *Sustainable Development of Mountain Territories*. 2024;16(3):833–841. https://doi.org/10.21177/1998-4502-2024-16-3-833-841

20. Tyulyaeva Yu, Khayrutdinov A, Galachieva I, Totrukova I. Creation of a High-Strength Backfill Composite Based on Sulfide-Bearing Technogenic Waste from Mining Production. *Sustainable Development of Mountain Territories*. 2024;16(3):1384–1396. https://doi.org/10.21177/1998-4502-2024-16-3-1384-1396

21. Yazyev SB, Chepurnenko AS. Buckling of Rectangular Plates under Nonlinear Creep. *Advanced Engineering Research* (*Rostov-on-Don*). 2023;23(3):257–268. https://doi.org/10.23947/2687-1653-2023-23-3-257-268

22. Kondratieva TN, Chepurnenko AS. Prediction of Rheological Parameters of Polymers by Machine Learning Methods. *Advanced Engineering Research* (*Rostov-on-Don*). 2024;24(1):36–47. https://doi.org/10.23947/2687-1653-2024-24-1-36-47

About the Authors:

Sergey V. Klyuev, Dr.Sci. (Engineering), Professor, Leading Researcher of the Scientific Research Laboratory of Resource and Energy-Saving Technologies, Equipment and Complexes, V.G. Shukhov Belgorod State Technological University (46, Kostyukov Str., Belgorod, 308012, Russian Federation), SPIN-code, ORCID, ScopusID, ResearchGate, klyuyev@yandex.ru

Alexander V. Klyuev, Cand.Sci. (Engineering), Associate Professor, Senior Researcher of the Scientific Research Laboratory of Resource and Energy-Saving Technologies, Equipment and Complexes, V.G. Shukhov Belgorod State Technological University (46, Kostyukov Str., Belgorod, 308012, Russian Federation), SPIN-code, ORCID, ScopusID, klyuyevav@yandex.ru

Narman A. Ayubov, Cand.Sci. (Economics), Senior Researcher of the Kh.I. Ibragimov Complex Research Institute, Russian Academy of Sciences (21a, Staropromyslovskoe shosse, Grozny, 364906, Russian Federation), SPIN-code, ORCID, yrekly@mail.ru

Roman S. Fediuk, Dr.Sci. (Engineering), Professor of the Military Training Center, Far Eastern Federal University (10, Ajax Bay, Russky Island, Vladivostok, 690922, Russian Federation), SPIN-code, ORCID, ScopusID, ResearchGate, ResearcherID, roman44@yandex.ru

Elena V. Levkina, Cand.Sci. (Economics), Associated Professor, Head of the Department for Work with Dissertation Councils, Far Eastern Federal University (10, Ajax Bay, Russky Island, Vladivostok, 690922, Russian Federation), SPIN-code, ORCID, levkina.ev@dvfu.ru

Claimed Contributorship:

SV Klyuev: conceptualization, writing – original draft preparation.
AV Klyuev: data curation, writing – original draft preparation.
NA Ayubov: formal analysis, writing – original draft preparation.
RS Fediuk: investigation, writing – original draft preparation.
EV Levkina: methodology, writing – original draft preparation.

Conflict of Interest Statement: **the authors declare no conflict of interest.**

All authors have read and approved the final version of manuscript.

Об авторах:

Сергей Васильевич Клюев, доктор технических наук, профессор, ведущий научный сотрудник Научно-исследовательской лаборатории ресурсо-энергосберегающих технологий, оборудования и комплексов Белгородского государственного технологического университета им. В.Г. Шухова (308012, Российская Федерация, г. Белгород, ул. Костюкова, 46), SPIN-код, ORCID, ScopusID, ResearchGate, klyuyev@yandex.ru

Александр Васильевич Клюев, кандидат технических наук, доцент, старший научный сотрудник Научно-исследовательской лаборатории ресурсо-энергосберегающих технологий, оборудования и комплексов Белгородского государственного технологического университета им. В.Г. Шухова (308012, Российская Федерация, г. Белгород, ул. Костюкова, 46), SPIN-код, ORCID, ScopusID, klyuyevav@yandex.ru

Нарман Аюбович Аюбов, кандидат экономических наук, старший научный сотрудник Комплексного научно-исследовательского института им. Х.И. Ибрагимова Российской академии наук (364906, Российская Федерация, г. Грозный, Старопромысловское шоссе, 21 а), SPIN-код, ORCID, yrekly@mail.ru

Роман Сергеевич Федюк, доктор технических наук, профессор военного учебного центра при Дальневосточном федеральном университете (690922, Российская Федерация, г. Владивосток, о. Русский, п. Аякс, 10), SPIN-код, ORCID, ResearchGate, ScopusID, ResearcherID, roman44@yandex.ru

Елена Владимировна Левкина, кандидат экономических наук, доцент, начальник отдела по работе с диссертационными советами Дальневосточного федерального университета (690922, Российская Федерация, г. Владивосток, о. Русский, п. Аякс, 10), SPIN-код, ORCID, ScopusID, levkina.ev@dvfu.ru

Заявленный вклад авторов:
С.В. Клюев: разработка концепции, написание черновика рукописи.
А.В. Клюев: курирование данных, написание черновика рукописи.
Н.А. Аюбов: формальный анализ, написание черновика рукописи.
Р.С. Федюк: проведение исследования, написание черновика рукописи.
Е.В. Левкина: разработка методологии, написание черновика рукописи.

Конфликт интересов: **авторы заявляют об отсутствии конфликта интересов.**

Все авторы прочитали и одобрили окончательный вариант рукописи.

Received / Поступила в редакцию 20.06.2025
Reviewed / Поступила после рецензирования 15.07.2025
Accepted / Принята к публикации 28.07.2025

MECHANICS
МЕХАНИКА

UDC 531.132.1
Original Empirical Research
https://doi.org/10.23947/2687-1653-2025-25-3-186-196

Optimal Control Method for a Lower Limb Exoskeleton with Elastic Elements

EDN: HCPJJV

Delshan Deeb ✉, **Igor V. Merkuryev**
National Research University "MPEI", Moscow, Russian Federation
✉ delshan2deeb@gmail.com

Abstract

Introduction. Modern development of exoskeletons opens new horizons for rehabilitation and improving the quality of life of people with limited mobility. The relevance of the study on methods of optimal control of exoskeletons is due to the growing demand in medicine and industry. However, there are numerous challenges related to the efficient control of exoskeletons, especially in the context of the integration of elastic elements. Topics related to optimal control and tuning of system parameters to reach maximum efficiency and user comfort remain insufficiently studied. The objective of this study is to develop a method of optimal control of a lower limb exoskeleton (LLE) with elastic elements while optimizing energy costs and accounting for external disturbances.

Materials and Methods. The LLE is represented by a simplified model of an inverted pendulum with elastic elements in the feet. The dynamic model of the LLE was developed using Lagrange equations. The optimal control method was based on the synthesis of a linear quadratic regulator designed to minimize energy costs. To account for the influence of external disturbances, a Kalman filter was integrated into the control loop. The parameters of the mathematical model of the LLE were obtained from published data. System simulation was performed in the Wolfram Mathematica environment.

Results. A method of optimal control of the LLE with elastic elements has been developed. This method optimizes energy costs while maintaining vertical equilibrium. The system was modeled using optimal terminal control, followed by optimal feedback control. During feedback control, key parameters affecting system stability were identified: spring stiffness and damping coefficients. Integration of the Kalman filter enabled compensation for external disturbances.

Discussion. The use of terminal control within the developed method reduced energy costs by 98% within a specified stabilization timeframe. Optimal values of spring stiffness and damping coefficients for obtaining the best system response were identified. The use of the optimal control method of the LLE in combination with the Kalman filter confirmed the effective compensation of external disturbances and noise, which provided the convergence of transient processes with minimal energy consumption.

Conclusion. The proposed method for achieving optimal control while minimizing energy costs is a promising solution in the field of control signal calculation required to ensure stability and determine the optimal energy cost function. This is especially true for medical rehabilitation tasks. These results may be useful for further research and development in the field of robotics and wearable devices.

Keywords: exoskeleton, mathematical model, elastic elements, artificial foot, optimal control, Kalman filter

Acknowledgements. The authors would like to thank the staff of the Department of Robotics, Mechatronics, Dynamics, and Strength of Machines, National Research University "MPEI", for their support in preparing this article. We also thank the reviewers for their constructive comments and recommendations, which significantly improved the quality of the work.

For Citation. Delshan D, Merkuryev IV. Optimal Control Method for a Lower Limb Exoskeleton with Elastic Elements. *Advanced Engineering Research (Rostov-on-Don).* 2025;25(3):186–196. https://doi.org/10.23947/2687-1653-2025-25-3-186-196

Оригинальное эмпирическое исследование

Метод оптимального управления экзоскелетом нижних конечностей с упругими элементами

Д. Диб ✉, И.В. Меркурьев

Национальный исследовательский университет «МЭИ», г. Москва, Российская Федерация

✉ delshan2deeb@gmail.com

Аннотация

Введение. Современное развитие экзоскелетов открывает новые горизонты для реабилитации и повышения качества жизни людей с ограниченной подвижностью. Актуальность исследования методов оптимального управления экзоскелетами обусловлена растущим спросом в медицине и промышленности. Однако существует множество проблем, связанных с эффективностью управления экзоскелетами, особенно в контексте интеграции упругих элементов. Темы, связанные с оптимальным управлением и настройкой параметров систем для достижения максимальной эффективности и комфорта пользователя, остаются недостаточно изученными. Целью данного исследования является разработка метода оптимального управления экзоскелетом нижних конечностей (ЭНК) с упругими элементами при оптимизации энергозатрат и учете внешних возмущений.

Материалы и методы. ЭНК представлен упрощенной моделью перевернутого маятника с упругими элементами в стопах. Динамическая модель ЭНК разработана с использованием уравнений Лагранжа. Метод оптимального управления основан на синтезе линейно-квадратичного регулятора, ориентированного на минимизацию энергозатрат. Для учета влияния внешних возмущений в контур управления интегрирован фильтр Калмана. Параметры математической модели ЭНК были получены из литературных данных. Моделирование проведено в среде Wolfram Mathematica.

Результаты исследования. Разработан метод оптимального управления ЭНК с упругими элементами, который обеспечивает оптимизацию энергозатрат при достижении вертикального метода равновесия. Проведено моделирование системы с использованием оптимального терминального управления, а затем оптимального управления с обратной связью. При управлении с обратной связью были определены ключевые параметры, оказывающие влияние на устойчивость системы: коэффициенты жесткости пружины и демпфирования. Интеграция фильтра Калмана в систему позволила учитывать влияние внешних возмущений.

Обсуждение. Применение терминального управления в рамках разработанного метода оптимального управления позволило снизить энергозатраты на 98 % за определенное время стабилизации. Найдены оптимальные значения жёсткости пружин и коэффициентов демпфирования для достижения наилучшего отклика системы. Использование метода оптимального управления ЭНК в сочетании с фильтром Калмана подтвердило эффективную компенсацию внешних возмущений и шумов, что обеспечило сходимость переходных процессов при минимальных энергозатратах.

Заключение. Предложенный метод достижения оптимального управления при минимизации энергозатрат является перспективным решением в области расчёта управляющих сигналов, необходимых для обеспечения устойчивости и определения оптимальной функции энергозатрат. Это особенно актуально для задач медицинской реабилитации. Данные результаты могут быть полезны для дальнейших исследований и разработок в области робототехники и носимых устройств.

Ключевые слова: экзоскелет, математическая модель, упругие элементы, искусственная стопа, оптимальное управление, фильтр Калмана

Благодарности. Авторы выражают благодарность сотрудникам кафедры «Робототехника, мехатроника, динамика и прочность машин» НИУ «МЭИ» за поддержку в подготовке данной статьи. Авторы также признательны рецензентам за их конструктивные замечания и рекомендации, которые позволили существенно улучшить представленную работу.

Для цитирования. Диб Д., Меркурьев И.В. Метод оптимального управления экзоскелетом нижних конечностей с упругими элементами. *Advanced Engineering Research (Rostov-on-Don).* 2025;25(3):186–196. https://doi.org/10.23947/2687-1653-2025-25-3-186-196

Introduction. Lower limb exoskeletons (LLE) are of increasing interest due to the need to address global health issues, such as aging population and increase in neuromuscular injuries [1]. These devices are designed to provide effective solutions to support and improve human motor functions, such as walking assistance [2], rehabilitation and compensation for loss of balance [3], thereby increasing independence and quality of life.

LLE are often designed without elastic elements due to the increased complexity of the stabilization during movement and the influence of additional factors that arise when using elastic elements [4]. On the other hand, these exoskeletons may require elastic elements that improve the ability of the structure to adapt to uneven surfaces. Elastic elements can be installed in the ankle area [5] or used to completely replace it [6].

LLE control is a complex task. Various approaches to its solution have been proposed previously. The development of an effective control method depends on numerous factors, maintaining the constant relevance of research in this area. There are different methods for LLE control: adaptive control method [1, 7], robust (stable) methods [8, 9], and optimal control method [10, 11]. Despite the efficiency of the first two methods, the third is the most successful. The optimal control method takes into account not only the increase in the stability and efficiency of LLE control under dynamic and unpredictable conditions, but also allows for reducing energy costs and the consumption of resources of the control system [10, 11]. However, the integration of elastic elements into the LLE feet causes complications in their control. In addition, taking into account external disturbances when controlling the LLE is accompanied by new problems in providing the dynamic stability of the LLE control system.

Based on the above, it can be argued that there is a need to develop a method for optimal control of LLE with elastic elements. Therefore, the objective of this study was to develop a method for optimal control of the lower limb exoskeleton and elastic elements while optimizing energy costs and taking into account external disturbances. This method allows minimizing the quadratic function of energy costs in the presence of elastic elements and external disturbances.

One of the factors that further complicates the solution to the issue of dynamic stability of LLE is the presence of white noise, which is an interference to the control signal [12], which is investigated in this work.

To achieve the stated goal, the following tasks were set:

– development of a mathematical model of an inverted pendulum with elastic elements in the feet;

– development of a method for optimal control of LLE with elastic elements;

– accounting for the impact of external disturbances (Gaussian white noise);

– conducting numerical modeling in the Wolfram Mathematica environment for two types of controls: terminal control and feedback control;

– analysis of the obtained results of the transient processes study on the key parameters of the dynamics of LLE with elastic elements.

Materials. To develop a mathematical model of the LLE with elastic elements in the feet, its kinematic scheme is considered. The foot is represented by elastic elements and is connected to the model by the type of an inverted pendulum (Fig. 1). The model includes inertial properties, kinematic limitations of the joints, and external forces acting on the system**.**

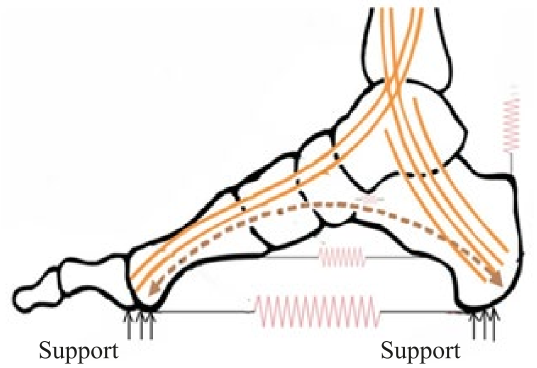

a)

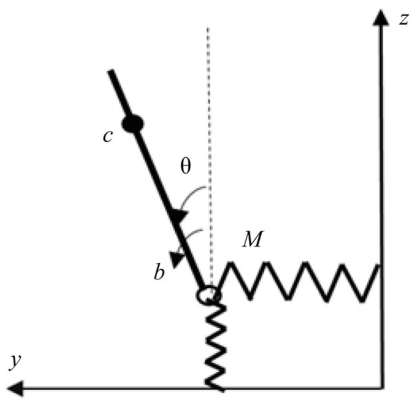

b)

Fig. 1. Kinematic scheme of LLE: *a* — biomechanical model of physiological "foot spring"[1];
b — simplified dynamic model of exoskeleton:
c — center of mass; θ — angle of ankle joint; *M* — control moment

[1] Subbotin F. Biomechanics of the Foot. Part 1. Fidel Subbotin School; 2024. (In Russ.) URL: https://fs-school.ru/blog/988624 (accessed: 10.05.2025).

The characteristics of the elastic elements and the parameters of the model are as follows: k_y, k_z — stiffness coefficients of the horizontal and vertical springs, respectively. Their values — $k_y \in [500, 1500]$ N/m [13], $k_z \in [7000, 20000]$ N/m [14]. c_y, c_z — horizontal and vertical damping coefficients, respectively, $c_y \in [30, 200$ N·s/m], $c_z \in [500–2000$ N·s/m] [15]. $J_c = \frac{1}{3} m\, h^2$ — moment of exoskeleton inertia relative to the center of mass, kg·m^2; $m = 70$ — mass of exoskeleton with patient, kg; $h = 1$ — length of exoskeleton to the center of mass, m; $\mu_y = 0.7$ and $\mu_z = 0$ — friction coefficients; $N_y = 0$ and $N_z = m\, g$ — normal forces, N; $g = 9.8$ — acceleration of gravity, m/s².

Methods. The dynamics of the LLE is described by the Lagrange equations of the second kind in general form[2]:

$$\frac{d}{dt}\left(\frac{\partial L}{\partial \dot{q}_i}\right) - \frac{\partial L}{\partial q_i} = Q_i, \quad (i = 1, \ldots, 3), \tag{1}$$

where $L = T - V$ — Lagrange function; T — kinetic energy of the system; V — potential energy of the system; Q — generalized forces; $q = (\theta, y_b, z_b)^T$ — vector of generalized coordinates; θ — rotary angle of exoskeleton link, measured from horizontal surface (parallel to reference plane) in counterclockwise direction; y_b, z_b — horizontal and vertical displacement of the base.

The coordinates of the center of mass of the pendulum are determined by the following equations:

$$\begin{aligned} y_c &= y_b + h \sin\theta; \\ z_c &= z_b + h \cos\theta. \end{aligned} \tag{2}$$

The kinetic energy of a pendulum is given by the formula:

$$T = \frac{1}{2} m v_c^2 + \frac{1}{2} J_c \dot{\theta}_2, \tag{3}$$

where v — speed of the center of mass, it is equal to $\dot{y}_c^2 + \dot{z}_c^2 = \left(\dot{y}_b + h \cos\theta\, \dot{\theta}\right)^2 + \left(\dot{z}_b + h \sin\theta\, \dot{\theta}\right)^2$.

The potential energy of the systems is described by the following equation:

$$V = mgz_c + \frac{1}{2} k_z z_b^2 + \frac{1}{2} k_y y_b^2. \tag{4}$$

The generalized damping forces applied through the Rayleigh dissipation function to simulate linear damping are written as [15]:

$$Q_i^{демп} = -\frac{\partial D}{\dot{q}_i}; \quad D = \frac{1}{2} c_y \dot{y}_b^2 + \frac{1}{2} c_z \dot{z}_b^2. \tag{5}$$

The Coulomb friction model is given by the following equations [15]:

$$\begin{aligned} Q_y^{mp} &= -\mu_y N_y \tanh\left(\alpha \dot{y}_b\right); \\ Q_z^{mp} &= -\mu_z N_z \tanh\left(\alpha \dot{z}_b\right), \end{aligned} \tag{6}$$

where $\alpha >> 1$ — regularization parameter (for approximating the discontinuous function $sign(v)$), in this paper, $\alpha = 100$ is selected.

After intermediate calculations, equations (2–6) take the form:

$$\begin{aligned} &\left(mh^2 + J_c\right)\ddot{\theta} + mh \cos(\theta)\, \ddot{y}_b - mh \sin(\theta)\, \ddot{z}_b - mgh \sin(\theta) = M; \\ &m\ddot{y}_b + mh \cos(\theta)\ddot{\theta} - mh \sin(\theta)\dot{\theta}^2 + k_y y_b = -c_y \dot{y}_b - \mu_y N_y \tanh\left(\alpha \dot{y}_b\right) + F_y^{ext}; \\ &m\ddot{z}_b - mh \sin(\theta)\ddot{\theta} - mh \cos(\theta)\dot{\theta}^2 + k_z z_b = -c_z \dot{z}_b - \mu_z N_z \tanh\left(\alpha \dot{z}_b\right) - mg + F_z^{ext}, \end{aligned} \tag{7}$$

where M, F_y^{ext}, F_z^{ext} — external generalized forces.

In the vicinity of vertical equilibrium ($\theta \approx 0$), assumptions are valid: $\sin\theta \approx \theta$, $\cos\theta = 1$, $z_b \approx -mg/k_z$. Equations (7) are linearized taking into account smallness (θ^2, $\dot{\theta}^2$) ≈ 0 and $\tanh(\alpha \dot{y}_b) \approx \alpha \dot{y}_b$ at low speeds:

$$\begin{aligned} &\left(mh^2 + J_c\right)\ddot{\theta} + mh\ddot{y}_b - mgh\theta = M; \\ &m\ddot{y}_b + mh\ddot{\theta} + k_y y_b = -c_y \dot{y}_b - \mu_y N_y \alpha \dot{y}_b + F_y^{ext}; \\ &m\ddot{z}_b + k_z z_b = -c_z \dot{z}_b - \mu_z N_z \alpha \dot{z}_b + F_z^{ext}. \end{aligned} \tag{8}$$

Under the assumptions of small angles, the vertical displacement of z becomes dynamically independent of horizontal y and angular θ states. Its behavior is reduced to a harmonic oscillator, which can be analyzed separately [12].

[2] Lynch KM, Park FC. Modern Robotics: Mechanics, Planning, and Control: Video Supplements and Software. Cambridge University Press; 2017. URL: http://hades.mech.northwestern.edu/index.php/Modern_Robotics (accessed: 10.05.2025).

For control synthesis, we present the system in the canonical form of the state space, taking into account external disturbances and measurement noise. Given the state vector $[x_1, x_2, x_3, x_4]^T=[\theta, \dot{\theta}, y, \dot{y}]^T$, we write the system in the Cauchy form:

$$\begin{aligned} \dot{x}(t) &= Ax(t) + Bu(t) + Dw(t); \\ y(t) &= Cx(t) + v(t), \end{aligned} \tag{9}$$

where A — state matrix; B — control matrix; $u(t)$ — vector of control signals; D — matrix of disturbances; $w(t)$ — vector of external disturbances; C — matrix of measurements; $v(t)$ — vector of external disturbances.

The main task of the regulator is to transfer the dynamic system from the initial state $x(t_0)$ to the specified final state $x(t_1)$ in a certain time t_1.

Controllability Gramian W characterizes the ability of the system to reach arbitrary states in a finite time T and is determined by the formula [12]:

$$W(t_1, t_0) = \int_{t_0}^{t_1} \Phi(t_0, t) B(t) B^T(t) \Phi^T(t_0, t) dt, \tag{10}$$

where $\Phi(t_0, t) = e^{A(t0-t)}$ — matrix exponent.

The system is fully controllable on $[t_0, t_1]$ if and only if $W(t_1, t_0)$ is invertible. If the Gramian is invertible, any state $x_T \in \mathbb{R}^n$ can be reached using the appropriate control $u(t)$ [12].

The control that minimizes the quadratic function of energy consumption and transfers the system from state $x(t_0)$ to state $x(t_1)$, has the form [12]:

$$u(t) = -B^T(t) \Phi^T(t_1, t) W^{-1}(t_1, t_0) \left[x(t_0) - \Phi(t_0, t_1) x(t_1) \right]. \tag{11}$$

After intermediate calculations, the quadratic function of energy consumption can be calculated using expression (12):

$$J\,min = \left[x(t_0) - \Phi(t_0, t_1) x(t_1) \right]^T W^{-1}(t_1, t_0) \left[x(t_0) - \Phi(t_0, t_1) x(t_1) \right]. \tag{12}$$

The control given by equation (11) is programmatic (open-loop) and time-dependent. To provide asymptotic stabilization of the system at the origin of coordinates under arbitrary initial conditions, it is required to synthesize the closed-loop control law based on real-time feedback. The control task is formulated in the form of minimizing the quadratic function of energy consumption [12]:

$$J = \int_0^{\infty} \left[x^T(t) Q x(t) + x^T(t) R x(t) \right] dt. \tag{13}$$

where R — positive definite matrix; Q — positive semi-definite matrix.

Optimal control that minimizes energy costs can be implemented as a negative feedback with variable parameters:

$$u(t) = -k(t) x(t), \tag{14}$$

where $k(t) = R^{-1}B^TP(t)$; $k(t)$ — feedback coefficient matrix; $P(t)$ — solution to the Riccati equation.

To find $P(t)$ as $t \to \infty$, it is required to solve the algebraic Riccati equation, which is given as follows:

$$-A^T P - PA + PBR^{-1}B^T P - Q = 0, \tag{15}$$

The system with control signal $u(t)$ is described by the equation:

$$\dot{x}(t) = Ax(t) - BKx(t) = \left[A - BK \right] x(t). \tag{16}$$

In practice, measuring all states is impossible due to the limited number of sensors, noise and measurement errors [12]. To estimate the state vector from the inputs and outputs, an optimal Kalman filter is used.

The system with control signal $u(t)$ and Kalman filter for determining the state vector has the following form [12]:

$$\frac{d}{dt}\hat{x}(t) = A\hat{x}(t) + Bu(t) + L\left[y(t) - C\hat{x}(t) \right], \tag{17}$$

where $\hat{x}$ — estimated state; $C\hat{x}$ — observer output; L — Kalman gain matrix.

In the presence of external disturbances $w(t)$ and measurement noise $v(t)$ with zero mathematical expectations $M[v(t)] = 0$, $M[w(t)] = 0$ and covariance matrices s_w and s_v, respectively, gain matrix L is determined from the solution to the algebraic Riccati equation (18), and, accordingly, stationary Kalman filter is found:

$$\begin{gathered} AP_x + P_x A^T - P_x C^T s_v^{-1} C P_x + D s_w D^t = 0; \\ L = P_x C^T s_v^{-1}. \end{gathered} \tag{18}$$

Control of a linear non-stationary system with external disturbances at the input and output is implemented using linear feedback on the state estimate:

$$u(t) = -k(t)\hat{x}(t). \tag{19}$$

The type of closed-loop system with feedback for estimating the state vector is determined by the formula:

$$\frac{d}{dt}\begin{pmatrix} x \\ \hat{x} \end{pmatrix}_{2n\times 1} = \begin{pmatrix} A-BK & BK \\ 0 & A-LC \end{pmatrix}_{2n\times 2n} \begin{pmatrix} x \\ \hat{x} \end{pmatrix}_{2n\times 1} + \begin{pmatrix} D & w \\ L & y \end{pmatrix}. \tag{20}$$

After developing the optimal control method for LLE with elastic elements and taking into account the impact of external disturbances, it remains to perform numerical modeling and analysis of the obtained results of the study on transient processes for the angle of deviation and displacement. For this purpose, at the first stage, the optimal control method is focused on restoring equilibrium for a certain stabilization time without taking into account the intermediate trajectory of motion. At the second stage, the optimal feedback control method is used to find the optimal intermediate trajectory of motion both with and without the Kalman filter.

Research Results. The paper investigates the transient processes of the control moment, force, displacement and angle during the transition of the LLE with elastic elements from an unstable position to a vertical equilibrium position. The results of numerical modeling are shown in Figures 2–6 for three initial conditions: Y_1 = [1/10, 0, 0 ,0], Y_2 = [1/10, 0, 1/10 ,0], Y_3 = [1/10 0 1/10 0 0 1/10 0 1/20 0].

The results of terminal control are calculated for a stabilization time of 0.6 s. Figure 2 shows the curves of the control moments of the open-loop system under the initial conditions Y_1 and the target position in the vertical equilibrium state. The blue curve corresponds to control moment M, the orange one — to control force F_y.

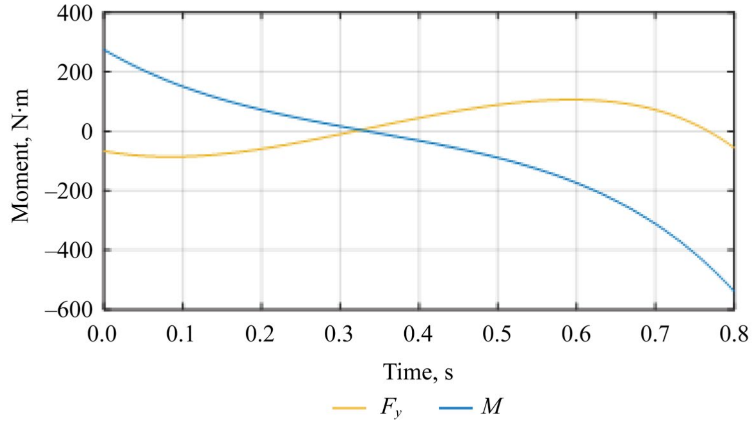

Fig. 2. Open-loop control signal curves

The values of the quadratic function of energy consumption for terminal control for different values of stabilization time are calculated using equation (12) and are presented in Table 1. A decrease in the value of the function of energy consumption with an increase in stabilization time can be noticed.

Table 1

Values of Quadratic Energy Consumption Function

Stabilization time, s	0.1	0.2	0.3	0.4
Value of quadratic function of energy consumption (J)	1,648.8	212.1	66.1	29.9

Figure 3 shows the curves of transient processes of the key parameters of the dynamic LLE system (θ, y_b) under the initial conditions Y_1. The blue curve represents the transient process of the deviation angle θ, and the orange curve — change in the coordinate along the ordinate axis y_b during the specified stabilization time of 0.6 s under terminal control.

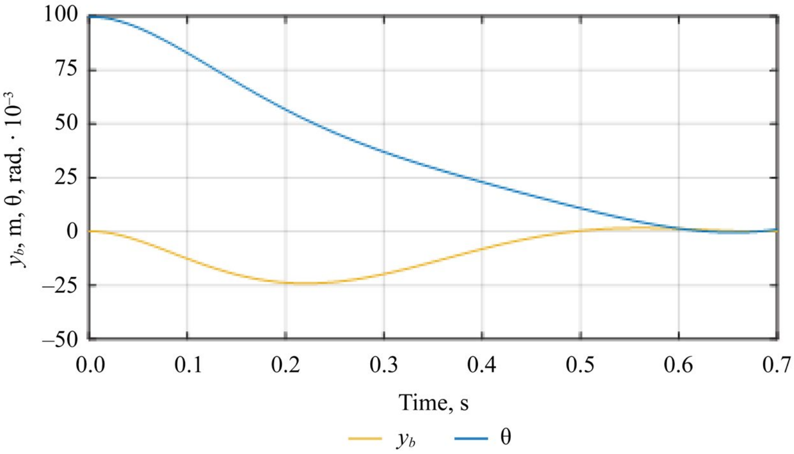

Fig. 3. Transient response curves

The simulation results in Figures 4–6 are obtained using the feedback control type, which allows searching for the optimal intermediate trajectory of motion. To study the impact of the elastic elements' stiffness (changes in spring stiffness coefficient k_y) on the stability of the dynamic LLE system while minimizing energy costs, transient processes of the key parameters of the dynamic LLE system (Fig. 4) were considered under the initial conditions Y_2 and the following parameters of the feedback system: $c_y = 100$, $k_z = 20{,}000$, $Q = eye(4) \cdot 10^3$, $R = eye(2)$.

The orange line represents y_b dependence, and the green line — θ. The following values of the stiffness coefficient are selected: k_y = [700, 1000, 1500] N/m. The transient processes are shown in Figure 4 *a, b, c*, respectively.

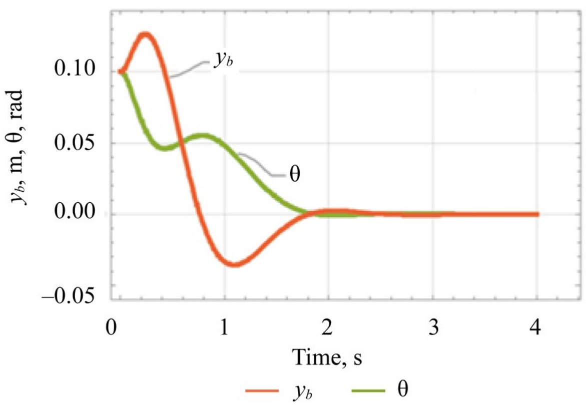

a)

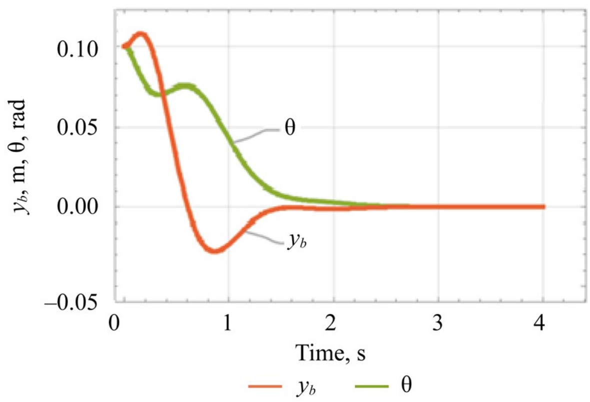

b)

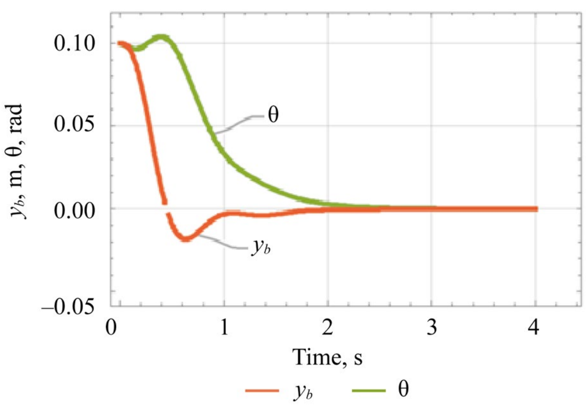

c)

Fig. 4. Transients when changing the spring stiffness coefficient:
a — at $k_y = 700$ and $c_y = 100$; *b* — at $k_y = 1000$ and $c_y = 100$;
c — at $k_y = 1500$ and $c_y = 100$

To study the effect of damping of elastic elements (changes in damping coefficient c_y) on the stability of the dynamic LLE system while minimizing energy costs, transient processes of the key parameters of the dynamic LLE system(θ, y_b) (Fig. 5) are considered under the initial conditions Y_2 and k_y =1000 with feedback. The orange line represents the y_b dependence, and the green line — θ. The damping coefficient values are c_y = [0, 50, 100] N·s/m, and the transient processes are shown in Figure 5 *a, b* and *c*, respectively.

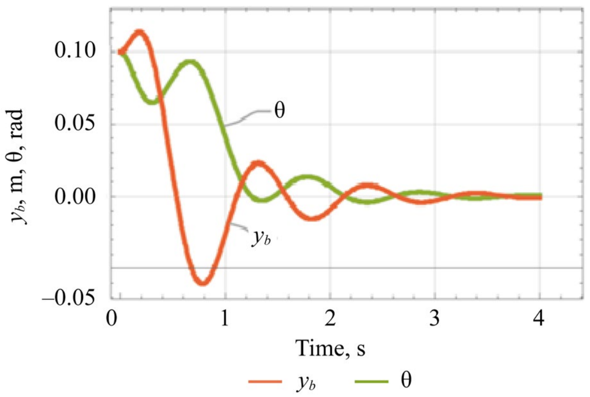

a)

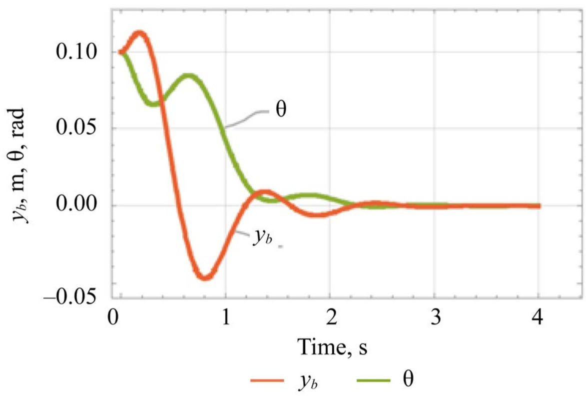

b)

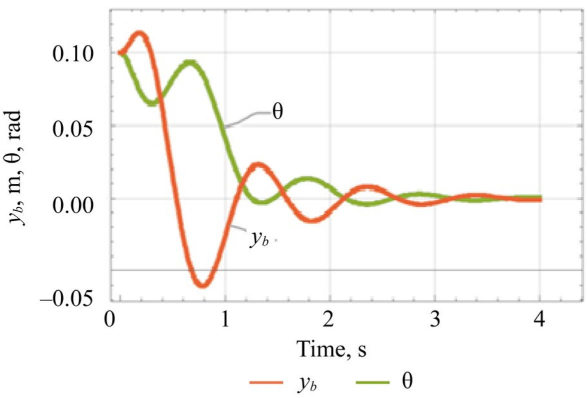

c)

Fig. 5. Transients of damping coefficient variation:
a — at c_y = 0 and k_y =1000; *b* — at c_y = 0 and k_y =1000;
c — at c_y = 100 and k_y =1,000

This research also takes into account the effect of noise through adding Kalman filter. Figure 6 shows the transient response curves under the initial conditions Y_3 = [1/10 0 1/10 0 0 1/10 0 1/20 0] and the covariance matrices s_w = *eye*(1) and s_v = 0.1 *eye*(2). The orange line illustrates the transient response y_b, and the green line — transient response θ.

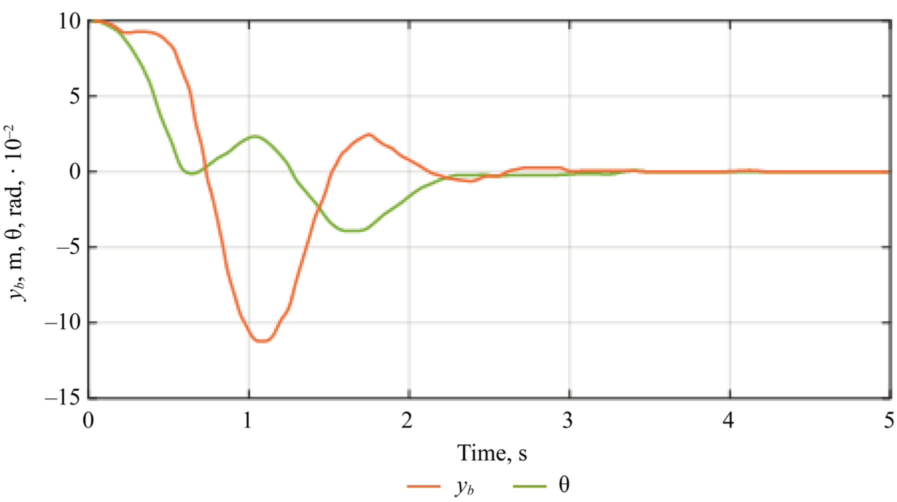

Fig. 6. Transient response curves using Kalman filter

Discussion. To achieve the research objective, the previous section presented the simulation results obtained using the proposed optimal control method to minimize energy costs during the transition of the studied LLE from an unstable position to a vertical equilibrium position.

Table 1 shows that as the time required to reach the target stable state increases, energy costs decrease proportionally. This dependence is consistent with the dynamics of control signals: as the permissible stabilization time increases, the amplitudes of the control moments M and F_y decrease, which, according to formulas (12)–(14), reduces the energy costs. It can be concluded that an increase in the stabilization time (within 0.1–0.4 seconds) reduces energy costs by 98%.

The curves in Figure 3 demonstrate a transient process lasting 0.6 s before reaching the vertical equilibrium position, which is consistent with the principles of terminal control (reaching the target stable state within a certain stabilization time).

The curves in Figure 4 illustrate the effect of changing the stiffness coefficient on the transient processes of the key parameters of the LLE dynamic system (θ, y_b). Changing the coordinate along the ordinate axis y_b at a low value of the stiffness coefficient is characterized by significant overshoot and slow stabilization, and an increase in the stiffness coefficient eliminates overshoot and accelerates the stabilization of the system. On the contrary, changes in angle θ demonstrate an inverse relationship: at a low value of the stiffness coefficient, a smooth transient process without overshoot and a short stabilization time of the system are observed, while an increase in the stiffness coefficient to 1500 causes overshoot in the angle, despite accelerated stabilization. This contradiction emphasizes the competing dynamics between y_b and θ. At the stiffness coefficient k_y =1000 (Fig. 4 *b*), an optimal compromise is reached: minimization of overshoot in the coordinate y_b, maintaining the stability of angle θ and fast convergence. This mode provides balanced operation of the system.

The reliability of the results obtained is validated by the stability of the closed system, which is confirmed by the negative real parts of its poles for all the studied values of the stiffness coefficient given in Table 2.

Table 2

Poles of a Closed System

Process option	K_y	Poles of closed system
1	700	–2.2445 + 3.8530i –2.2445 – 3.8530i –4.5071 – 3.2807i
2	1000	–2.6133 + 5.4608i –2.6133 – 5.4608i –3.6385 – 3.1496i
3	1500	–2.7679 + 7.5731i –2.7679 – 7.5731i –3.2042 – 3.0242i

The curves in Figure 5 show the effect of the damping coefficient. At a low value of the damping coefficient, significant vibration of the system is observed before reaching the steady state, accompanied by overshoot. Increasing c_y reduces the amplitude of vibrations and eliminates overshoot, but results in a growth of energy costs. To provide a balance between stability and the value of the quadratic function of energy costs, the value of coefficient c_y = 100 is selected, which guarantees the stability of the LLE control system with elastic elements.

From the image in Figure 6, it follows that the Kalman filter provides the convergence of transient processes to zero values within three seconds when exposed to white noise, confirming its robust stabilizing properties.

The results obtained show the following picture. Firstly, the use of open control as a basic stage allows minimizing energy costs at the stage of bringing the system from an unstable state to the target vertical equilibrium at a given stabilization time. Secondly, the transition to closed loop control based on the state feedback provides asymptotic stability and stability of transient modes through solving the Riccati equation and implementing an effective Kalman filter. Thirdly, numerical modeling revealed an important effect of the parameters of elastic elements on the dynamics of the system: increasing the spring stiffness reduces overshoot in angle θ and accelerates stabilization, but it can cause difficulties on the way to a stable trajectory; increasing damping reduces vibrations and reduces overshoot, but increases energy costs. A balance between stability and energy costs is found, which is reached at specific values k_y and c_y (in the examples: k_y = 1000 N/m, c_y = 100 N·s/m).

Based on the previous discussion and analysis of the results obtained in the paper, it can be said that the developed method of optimal control of the LLE with elastic elements has managed to provide the stability of the control system of this exoskeleton for a certain stabilization time and with minimal energy consumption.

Conclusion. A technique for optimal control of a lower limb exoskeleton (LLE) with elastic elements in the feet, taking into account external disturbances and measurement noise, has been formulated and implemented. The main approach is based on representing the LLE dynamics as a system of Lagrange equations, translating it into a canonical form of the state space, and synthesizing the control law through optimization of quadratic functions of energy consumption and system stability. A Kalman filter was used to assess the state, which allowed for correct operation under conditions of a limited number of sensors and the presence of external disturbances.

The practical significance of the results consists in the development of a technique that allows adaptively selecting the parameters of elastic elements and the control mode depending on the conditions of the task and objectives (minimization of energy costs, acceleration of stabilization, minimization of overshoot). In terms of potential applications, this can help improve the efficiency of rehabilitation technologies, reduce energy consumption in prosthetic and orthotic systems, and improve the stability of movements on uneven surfaces. The prospects for the research include experimental verification of the technique and its adaptation to variable loads and complex surfaces, which is a challenge for medical rehabilitation and robotics.

References

1. Yatsun SF, Loktionova OG, Khalil Hamed Mohammed Hamood Al Manji, Yatsun AS, Karlov AE. Simulation of Controlled Motion of a Person When Walking in an Exoskeleton. *Proceedings of Southwest State University.* 2019;23(6):133–147. https://doi.org/10.21869/2223-1560-2019-23-6-133-147

2. Habib Mohamad, Sadjaad Ozgoli. Online Gait Generator for Lower Limb Exoskeleton Robots: Suitable for Level Ground, Slopes, Stairs, and Obstacle Avoidance. *Robotics and Autonomous Systems.* 2023;160:104319. https://doi.org/10.1016/j.robot.2022.104319

3. Bottin-Noonan J, Sreenivasa M. Model-Based Evaluation of Human and Lower-Limb Exoskeleton Interaction during Sit to Stand Motion. In: *Proc. IEEE International Conference on Robotics and Automation (ICRA).* New York City: IEEE; 2021. P. 2063–2069. https://doi.org/10.1109/ICRA48506.2021.9561727

4. Shchurova EN, Prudnikova OG, Kachesova AA, Saifutdinov MS, Tertyshnaya MS. Improvement of Functional State of Patients after Spinal Cord Injury During Epidural Electrical Stimulation: Prospective Study. *Bulletin of Rehabilitation Medicine*. 2023;22(6):28–41. https://doi.org/10.38025/2078-1962-2023-22-6-28-41

5. Nuckols RW, Sawicki GS. Impact of Elastic Ankle Exoskeleton Stiffness on Neuromechanics and Energetics of Human Walking across Multiple Speeds. *Journal of NeuroEngineering and Rehabilitation.* 2020;17(1):75. https://doi.org/10.1186/s12984-020-00703-4

6. Orekhov G, Lerner ZF. Design and Electromechanical Performance Evaluation of a Powered Parallel-Elastic Ankle Exoskeleton. *IEEE Robotics and Automation Letters.* 2022;7(3):8092–8099. https://doi.org/10.1109/LRA.2022.3185372

7. Hamed Jabbari Asl, Tatsuo Narikiyo, Michihiro Kawanishi. Neural Network-Based Bounded Control of Robotic Exoskeletons without Velocity Measurements. *Control Engineering Practice.* 2018;80:94–104. https://doi.org/10.1016/j.conengprac.2018.08.005

8. Jinghui Cao, Sheng Quan Xie, Raj Das. MIMO Sliding Mode Controller for Gait Exoskeleton Driven by Pneumatic Muscles. *IEEE Transactions on Control Systems Technology.* 2017;26(1):274–281. https://doi.org/10.1109/TCST.2017.2654424

9. Madani T, Daachi B, Djouani K. Non-Singular Terminal Sliding Mode Controller: Application to an Actuated Exoskeleton. *Mechatronics.* 2016;33:136–145. https://doi.org/10.1016/j.mechatronics.2015.10.012

10. Rigatos G, Abbaszadeh M, Pomares J, Wira P. A Nonlinear Optimal Control Approach for a Lower-Limb Robotic Exoskeleton. *International Journal of Humanoid Robotics.* 2020;17(5):2050018. https://doi.org/10.1142/S0219843620500188

11. Jun Chen, Yuan Fan, Mingwei Sheng, Mingjian Zhu. Optimized Control for Exoskeleton for Lower Limb Rehabilitation with Uncertainty. In: *Proc. Chinese Control and Decision Conference (CCDC).* New York City: IEEE; 2019. P. 5121–5125. https://doi.org/10.1109/CCDC.2019.8833418

12. Rigatos G, Busawon K**.** *Robotic Manipulators and Vehicles: Control, Estimation and Filtering.* Cham: Springer; 2018. 734 p. https://doi.org/10.1007/978-3-319-77851-8

13. Madhusudhan Venkadesan, Ali Yawar, Carolyn M Eng, Marcelo A Dias, Dhiraj K Singh, Steven M Tommasini, et al. Stiffness of the Human Foot and Evolution of the Transverse Arch. *Nature.* 2020;579:97–100. https://doi.org/10.1038/s41586-020-2053-y

14. Juanjuan Zhang, Collins SH. The Passive Series Stiffness that Optimizes Torque Tracking for a Lower-Limb Exoskeleton in Human Walking. *Frontiers in Neurorobotics.* 2017;11:68. https://doi.org/10.3389/fnbot.2017.00068

15. Tsapenko V, Tereshchenko M, Tymchik G, Matvienko S, Shevchenko V. Analysis of Dynamic Load on Human Foot. In: *Proc. IEEE 40th International Conference on Electronics and Nanotechnology (ELNANO).* New York City: IEEE; 2020. P. 400–404. https://doi.org/10.1109/ELNANO50318.2020.9088788

About the Authors:

Delshan Deeb, Postgraduate student, Teaching Assistant of the Department of Robotics, Mechatronics, Dynamics and Strength of Machines, National Research University "MPEI" (14, Krasnokazarmennaya Str., Moscow, 111250, Russian Federation), SPIN-code, ORCID, ScopusID, delshan2deeb@gmail.com

Igor V. Merkuryev, Dr.Sci. (Eng.), Associate Professor, Head of the Department of Robotics, Mechatronics, Dynamics and Strength of Machines, National Research University "MPEI" (14, Krasnokazarmennaya Str., Moscow, 111250, Russian Federation), SPIN-code, ORCID, ScopusID, MerkuryevIV@mpei.ru

Claimed Contributorship:

D Deeb: formal analysis, writing – original draft preparation.

IV Merkuryev: supervision, conceptualization, project administration.

Conflict of Interest Statement: **the authors declare no conflict of interest.**

All authors have read and approved the final manuscript.

Об авторах:

Диб Делшан, аспирант, ассистент кафедры «Робототехника, мехатроника, динамика и прочность машин» Национального исследовательского университета «МЭИ» (111250, Российская Федерация, г. Москва, ул. Красноказарменная, 14), SPIN-код, ORCID, ScopusID, delshan2deeb@gmail.com

Игорь Владимирович Меркурьев, доктор технических наук, доцент, заведующий кафедрой «Робототехника, мехатроника, динамика и прочность машин» Национального исследовательского университета «МЭИ» (111250, Российская Федерация, г. Москва, ул. Красноказарменная, 14), SPIN-код, ORCID, ScopusID, MerkuryevIV@mpei.ru

Заявленный вклад авторов:

Д. Диб: формальный анализ, написание черновика рукописи.

И.В. Меркурьев: научное руководство, разработка концепции, административное руководство исследовательским проектом.

Конфликт интересов: **авторы заявляют об отсутствии конфликта интересов.**

Все авторы прочитали и одобрили окончательный вариант рукописи.

Received / Поступила в редакцию 22.06.2025

Reviewed / Поступила после рецензирования 10.08.2025

Accepted / Принята к публикации 25.08.2025

MACHINE BUILDING AND MACHINE SCIENCE
МАШИНОСТРОЕНИЕ И МАШИНОВЕДЕНИЕ

UDC 62-522.7
https://doi.org/10.23947/2687-1653-2025-25-3-197-207

Original Empirical Research

EDN: DFVDDQ

Experimental Study on Positioning Accuracy of an Automated Long-Stroke Rodless Pneumatic Actuator

Daniil A. Korotych
Don State Technical University, Rostov-on-Don, Russian Federation
✉ daniilberuk@gmail.com

Abstract

Introduction. In modern industrial processes, pneumatic actuators with long-stroke movements play an important role. However, their use is limited by low accuracy resulting from the difficulties of controlling air flows. These limitations are caused by the compressibility of air and thermodynamic processes, which makes it urgent to improve the accuracy of such systems. The conducted analysis of scientific literature shows that modern research is mainly focused on the use of systems with standard cylinders with a working stroke limited to three meters. At the same time, the issues of development and research of long-stroke systems of rodless pneumatic drives, capable of having a stroke length of up to six meters, remain insufficiently studied. The introduction of advanced control systems in this type of drives involves significant investments in a high-tech electronic base and additional structural elements. In this regard, the development of fundamentally new technical solutions that allow for the efficient operation of mechanisms with a working stroke of more than three meters while maintaining the required technical parameters and economic efficiency, is of particular relevance. In the framework of previous studies, the author proposed a design of a pneumatic drive for long-stroke movements, equipped with a unique control system based on a jet sensor and an external brake mechanism. Its mathematical modeling and theoretical analysis were also performed, which made it possible to identify key factors affecting the accuracy of positioning. To validate the mathematical model and the hypotheses put forward, the objective of this research is to experimentally verify the results of mathematical modeling of a positional long-stroke rodless pneumatic actuator, as well as to confirm the degree of influence of key factors on positioning accuracy.

Materials and Methods. The work involved a stand that was a technical model of a pneumatic drive with an original control system, including a jet sensor and an external brake device. To verify the operability and accuracy of the jet sensor readings, the spillage method was applied using the Camozzi MF4008-10-R-BV-A flow sensor after the element under study, and Camozzi SWCN-P10-P3-2 pressure sensors placed before and after the considered element. The tests conducted on the developed jet sensor showed high reliability and stability of operation in various operating modes. The experimental study of a long-stroke rodless pneumatic actuator included evaluation of the actuator's technical capabilities, analysis of positional cycles, study on the effect of external factors, and comparison of the results of computational and full-scale experiments. The results of computational and full-scale experiments were processed using the Mathcad and MATLAB software packages. The dependences of positioning accuracy on mass and stroke length were constructed.

Results. The reliability of the model was established at the level of the maximum discrepancy between the experimental data and the results of mathematical modeling, which amounted to 18%. That confirmed the adequacy of the developed model for engineering calculations. The effect of the load mass on the accuracy of positioning was experimentally established. With an increase in mass from 10 to 30 kg, the accuracy decreased by 1.47 times, and with a mass of 60 kg, the accuracy deteriorated by another 1.37 times relative to the base mass of 10 kg. In addition, the effect of stop coordinates was studied: the dependence of positioning accuracy on the position of the actuator was established. When moving from 0.1 m to 0.22 m, the accuracy deteriorated by 3.2 times, but with further movement to 0.35 m, it improved by 2.2 times.

Discussion. The conducted experimental studies allowed achieving good results in the development of long-stroke pneumatic drives. Successful verification of the mathematical model confirmed the correctness of both the model itself and the theoretical studies conducted in the author's previous works. The positioning accuracy of the drive of 77 microns at a distance of over three meters was reached. This indicator significantly exceeds the results presented in the studies of other authors, which shows the high potential of the developed design. The economic efficiency of the proposed solution is due to the absence of an electronic component base in the control system. This not only reduces initial production costs, but also significantly simplifies maintenance of the drive under operation. The comparative analysis with existing developments confirms the superiority of the proposed system in terms of cost criteria.

Conclusions. The conducted studies confirmed the efficiency of the developed solutions for a long-stroke rodless pneumatic actuator. Practical significance of the study is determined by the possibility of using the obtained results in creating high-precision long-stroke mechanisms in various industries. The developed design can be used in automated production lines, robotic complexes, and other areas where precise positioning over significant distances is required. Promising areas for further research are the optimization of the control system parameters to reach even higher positioning accuracy, and the development of calculation methods for positional long-stroke pneumatic drives.

Keywords: jet control system for a rodless pneumatic actuator, rodless long-stroke pneumatic actuator, positioning of a pneumatic actuator, pneumatic sensor for a rodless pneumatic actuator

Acknowledgments. The author would like to thank the editors and reviewers for their attentive attitude to the article and the comments indicated, which made it possible to improve its quality.

For Citation. Korotych D.A. Experimental Study on Positioning Accuracy of an Automated Long-Stroke Rodless Pneumatic Actuator. *Advanced Engineering Research (Rostov-on-Don).* 2025;25(3):197–207. https://doi.org/10.23947/2687-1653-2025-25-3-197-207

Оригинальное эмпирическое исследование

Экспериментальное исследование точности позиционирования автоматизированного длинноходового бесштокового пневмопривода

Д.А. Коротыч

Донской государственный технический университет, г. Ростов-на-Дону, Российская Федерация

✉ daniilberuk@gmail.com

Аннотация

Введение. В современных промышленных процессах пневматические приводы с длинноходовыми перемещениями играют важную роль. Однако их использование ограничено низкой точностью, вызванной сложностями управления воздушными потоками. Эти ограничения обусловлены сжимаемостью воздуха и термодинамическими процессами, что делает актуальной задачу повышения точности таких систем. Проведённый анализ научной литературы показывает, что современные исследования в основном сосредоточены на применении систем со стандартными цилиндрами, рабочий ход которых ограничен тремя метрами. В то же время вопросы разработки и исследования длинноходовых систем бесштоковых пневмоприводов, способных иметь длину хода до шести метров, остаются недостаточно изученными. Внедрение усовершенствованных систем управления в такие приводы связано со значительными инвестициями в высокотехнологичную электронную базу и дополнительные конструктивные элементы. В связи с этим особую актуальность приобретает разработка принципиально новых технических решений, позволяющих эффективно эксплуатировать механизмы с рабочим ходом более трёх метров при сохранении необходимых технических параметров и экономической эффективности. В рамках предыдущих исследований автором была предложена конструкция пневмопривода длинноходовых перемещений, оснащённая уникальной системой управления на базе струйного датчика и внешнего тормозного механизма; также было выполнено его математическое моделирование и теоретический анализ, что позволило выделить ключевые факторы, влияющие на точность позиционирования. Для подтверждения адекватности математической модели и выдвинутых гипотез целью настоящей работы является экспериментальная верификация результатов математического моделирования позиционного длинноходового бесштокового пневмопривода, а также подтверждение степени влияния ключевых факторов на точность позиционирования.

Материалы и методы. В работе был использован стенд, представляющий собой техническую модель пневмопривода с оригинальной системой управления, включающей струйный датчик и внешнее тормозное устройство. Для верификации работоспособности и точности показаний струйного датчика был применён метод проливки с использованием датчика расхода Camozzi MF4008-10-R-BV-A, установленного после исследуемого элемента, а также датчиков давления Camozzi SWCN-P10-P3-2, размещённых перед и после исследуемого элемента. Проведённые испытания разработанного струйного датчика продемонстрировали высокую надёжность и стабильность работы в различных эксплуатационных режимах. Экспериментальное исследование длинноходового бесштокового пневмопривода включало в себя: оценку технических возможностей привода, анализ позиционных циклов,

изучение влияния внешних факторов и сравнение результатов вычислительных и натурных экспериментов. С помощью пакета прикладных программ Mathcad и Matlab обрабатывались результаты вычислительного и натурного экспериментов, а также были построены зависимости точности позиционирования от массы и длины хода.
Результаты исследования. Достоверность модели была установлена на уровне максимального расхождения между экспериментальными данными и итогами математического моделирования, составившего 18 %, что подтверждает адекватность разработанной модели для инженерных расчетов. Экспериментально установлено влияние массы груза на точность позиционирования. При увеличении массы с 10 до 30 кг точность снижается в 1,47 раза, а при массе в 60 кг точность ухудшается еще на 1,37 раза относительно базовой массы в 10 кг. Кроме того, исследовано воздействие координат остановки: установлена зависимость точности позиционирования от положения исполнительного элемента. При перемещении от 0,1 м до 0,22 м точность ухудшается в 3,2 раза, однако при дальнейшем перемещении до 0,35 м она улучшается в 2,2 раза.
Обсуждение. Проведенные экспериментальные исследования позволили добиться хороших результатов в области разработки длинноходовых пневмоприводов. Успешная верификация математической модели подтверждает корректность как самой модели, так и теоретических исследований, проведенных в предыдущих работах автора. Достигнута точность позиционирования привода 77 мкм на дистанции свыше трех метров. Этот показатель существенно превосходит результаты, представленные в исследованиях других авторов, что свидетельствует о высоком потенциале разработанной конструкции. Экономическая эффективность предложенного решения обусловлена отсутствием электронной компонентной базы в системе управления. Это не только снижает первоначальные затраты на производство, но и существенно упрощает техническое обслуживание привода в процессе эксплуатации. Сравнительный анализ с существующими разработками подтверждает превосходство предложенной системы по критерию затрат.
Заключение. Проведенные исследования подтвердили эффективность разработанных решений для длинноходового бесштокового пневмопривода. Практическая значимость исследования определяется возможностью применения полученных результатов при создании высокоточных длинноходовых механизмов в различных отраслях промышленности. Разработанная конструкция может быть использована в автоматизированных производственных линиях, робототехнических комплексах и других областях, где требуется точное позиционирование на значительных расстояниях. Перспективными направлениями дальнейших исследований являются оптимизация параметров управляющей системы для достижения еще более высокой точности позиционирования и разработка методик расчета позиционных длинноходовых пневмоприводов.

Ключевые слова: струйная система управления бесштоковым пневмоприводом, бесштоковый длинноходовой пневмопривод, позиционирование пневмопривода, пневматический датчик бесштокового пневмопривода

Благодарности. Автор выражает благодарность редакции и рецензентам за внимательное отношение к статье и указанные замечания, которые позволили повысить ее качество.

Для цитирования. Коротыч Д.А. Экспериментальное исследование точности позиционирования автоматизированного длинноходового бесштокового пневмопривода. *Advanced Engineering Research (Rostov-on-Don).* 2025;25(3):197–207. https://doi.org/10.23947/2687-1653-2025-25-3-197-207

Introduction. The efficiency of the drives used in modern processing equipment is determined by the speed of movement of the actuating element along the coordinate axes, and the accuracy of positioning the actuators of the drive in real time during the implementation of the required work cycles [1]. These cycles, as a rule, consist of a rapid approach of the actuator, its deceleration to the positioning speed, precise stopping, and rapid withdrawal [2].

Pneumatic drives are characterized by high speed of movement and protection against fire. They also have explosion safety, environmental friendliness, reliability and flexibility in confined spaces [3]. They are effectively used in mechanical engineering, as well as in the food, chemical and woodworking industries, where the combination of speed and positioning accuracy of the power elements of the drive is important [4].

Modern transport and production machines are equipped with various actuators based on pneumatic drives [5]. Such systems are constantly subject to ever higher demands on the speed, accuracy and reliability of their operation [6]. In this context, pneumatic automation offers universal approaches to the control of similar systems.

Most modern industrial drive equipment operates on the basis of automatic pneumatic drives with long-stroke movements of the actuators [7]. These industrial positioning drives guarantee positioning accuracy of about 1% (in some special designs, it can reach up to 0.4%) of the maximum stroke length. This has a negative impact on the accuracy of pneumatic long-stroke drives [8]. Air compressibility and complex thermodynamic processes occurring in air flows have a significant impact on the control of air flows in the drive lines and cavities of the pneumatic cylinder, which limits the positioning accuracy of the drive [9].

Research by D.V. Shilin [10] demonstrated that the implementation of a hybrid control system significantly increased the accuracy of positioning the carriage of a rodless pneumatic cylinder. Experiments made it possible to reduce the error to 0.2% of the stroke length, which was a good result. In [11], the authors proposed a new controller circuit based on fuzzy logic, used to monitor the actuator trajectory following of a robot manipulator with two degrees of freedom.

A promising direction is the development of flexible rodless pneumatic cylinders for long-stroke McKibben-type actuators [12]. Pneumatic cylinders with a self-holding function were tested, providing precise positioning even without applying pressure. Dao The Anh [13] developed and investigated an automated positioning pneumatic actuator with increased accuracy and operating speed, identifying the dependence of the actuator characteristics on the mass of the objects being moved, the deceleration coefficient, relative displacement, and braking force.

Paper [14] presents an adaptive second-order sliding mode tracking control scheme for robotic manipulators. A new control law is proposed that allows for the transition of the robotic manipulator trajectories from all initial conditions to the switching surface of the proportional-integral derivative in a finite time with subsequent retention on this surface.

There is a jet positioning numerical control system [15] based on a cylinder with a piston and a rod connected to a measuring scale. The system uses a "nozzle-receiving channel" sensor to generate a control signal. The device operates on a pneumatic sensor that measures the gap between the sensor and the inclined measuring bar, whose angle is adjusted by a screw. The sensor output is connected to the control input of a threshold device that generates a signal to stop the piston, whose position is adjusted by a throttle [15].

The key drawback of the modern technical solutions under consideration is that they are designed exclusively for the use of standard cylinders [16] with a working stroke not exceeding three meters. When attempting to implement mechanisms with an increased stroke of over three meters, developers encounter a set of serious technical obstacles [17]. The main problem is that to provide the functioning of such systems, it is required to modernize the control system, which causes a significant increase in the costs of manufacturing the end product. The increase in cost occurs in two main areas: the first is associated with the introduction of more complex control electronics, the second is due to the need for additional elements for reliable operation at increased distances [18]. Under such conditions, it is critically important to create an innovative approach capable of effectively solving problems associated with long strokes (more than three meters). At the same time, the new solution must not only provide the required technical characteristics, but also remain economically justified for potential users, while maintaining a high level of operational qualities [19].

This research objective was to experimentally verify the results of mathematical modeling of a positioning long-stroke rodless pneumatic actuator, as well as to confirm the degree of influence of key factors on positioning accuracy.

Materials and Methods. Experimental studies were aimed at validating the results obtained through the mathematical modeling of pneumatic drive systems, which was carried out earlier in paper [8].

During preliminary calculations, the element base of the stand was selected, and its assembly drawing was made, which is presented in Figure 1.

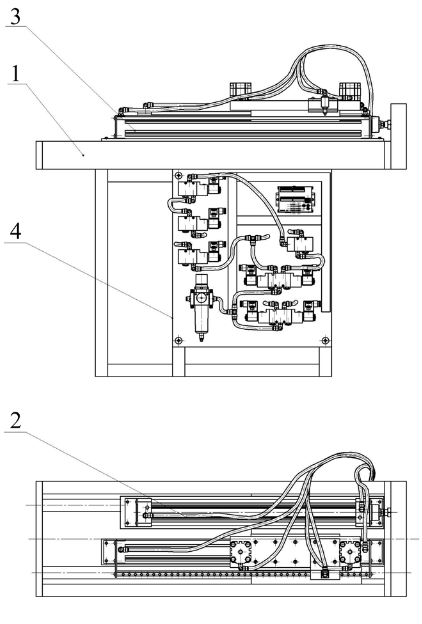

Fig. 1. Assembly drawing of the model stand: 1 — stand frame; 2 — loading pneumatic cylinder; 3 — automated long-stroke rodless pneumatic actuator in assembly; 4 — control panel

The stand, as a technical model of a pneumatic drive for experimental research, assembled on the basis of design documentation, is shown in Figure 2. To study the pneumatic and kinematic characteristics of the drive, an original control system was developed and applied, including a jet sensor and an external brake device [20].

In the course of the development of the experimental setup, a Camozzi 52G2P40A0400 rodless pneumatic cylinder with a working stroke of 400 mm and a piston diameter of 40 mm was mounted on the testing stand. The proposed original control system, developed as part of previous studies, was fixed on the movable carriage of this device [20].

This system included a jet sensor of an original design, consisting of two nozzle elements and a special rack with holes, as well as an external brake device, represented by two Camozzi 31F4A040A005 pneumatic cylinders with friction linings on the rods [8]. Friction linings of Argolon-TX material were selected due to their friction coefficient of 0.4 and linear wear, which is up to 5.5 µm/brake [13].

Additionally, a standard Camozzi 40M2L050A0400 pneumatic cylinder with a stroke length of 400 mm and a piston diameter of 50 mm was installed on the stand, which made it possible to simulate external loads on the drive. To verify the operability and accuracy of the jet sensor readings, a spillage method was used using a Camozzi MF4008-10-R-BV-A flow sensor located after the element under study, and two Camozzi SWCN-P10-P3-2 pressure sensors placed before and after this element. The tests of the jet sensor showed high reliability and stability of operation in various operating modes.

For the water drawing, a Camozzi MF4008-10-R-BV-A flow sensor was used, which had the following technical characteristics: analog output 0.5–4.5 V; measured value — volumetric flow rate; initial value of the flow measurement range — 0 l/min; final value of the flow measurement range — 10 l/min; accuracy (1.5+0.2·FS/MV) %; operating pressure — 0–5 bar. Camozzi SWCN-P10-P3-2 pressure sensors were also used for the tests, which had the following technical characteristics: maximum measurement pressure — 10 bar; minimum measurement pressure — 1 bar; measurement pressure drop — 0.01 bar; maximum error — no more than 2.01%; scaling factor — 1.543. Additionally, Camozzi M043R-12 pressure gauges were used to provide measurement accuracy and pressure control in various drive units. The experimental stand was equipped with a modern electronic control unit, which included a Giga Device GD32F103VET6 microcontroller. It was responsible for collecting and processing data from all sensors of the pneumatic system, as well as for controlling the pneumatic distributors. To improve the accuracy of the actuator positioning, an encoder of the New Hong OVW6-10-2HC model was used, which had the following technical parameters [21]: power supply — DC 5–12 V, 12–24 V; response frequency — 0–100 kHz; consumption current — 80 mA. All data from the pressure sensors and the encoder were recorded in the system using the Modbus protocol [22]. Information from all measuring devices was collected by a personal computer synchronized with the microcontroller via the W5500 interface.

The DD1 controller interacted with the system, generating control signals for electromagnetic relays via a Unisonic Technologies ULN2003 transistor unit. This provided precise and reliable control of the pneumatic distributor solenoids, as well as maintaining the specified operating parameters of the drive in various operating modes [23].

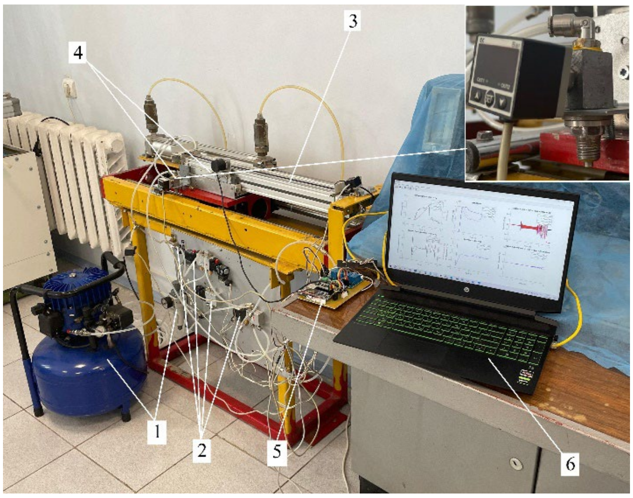

Fig. 2. Research complex: 1 — power subsystem; 2 — drive control devices;
3 — main pneumatic cylinder for long-stroke movements with a loader;
4 — control system in the form of a jet sensor and an external brake device;
5 — electrical subsystem; 6 — personal computer

Figure 3 shows the research complex appearance. The principle of its operation is described in [8, 20], etc. The control system of this complex consists of a contactless jet sensor and an external brake device.

The contactless jet sensor transmits information about the current position of the actuator of the pneumatic cylinder, switches the drive controls for its deceleration and precise stopping.

The external braking device performs the work of fixing the actuator of the pneumatic drive when it is out of operation and precisely stops at a given coordinate. Then the actuator switches to the positioning speed.

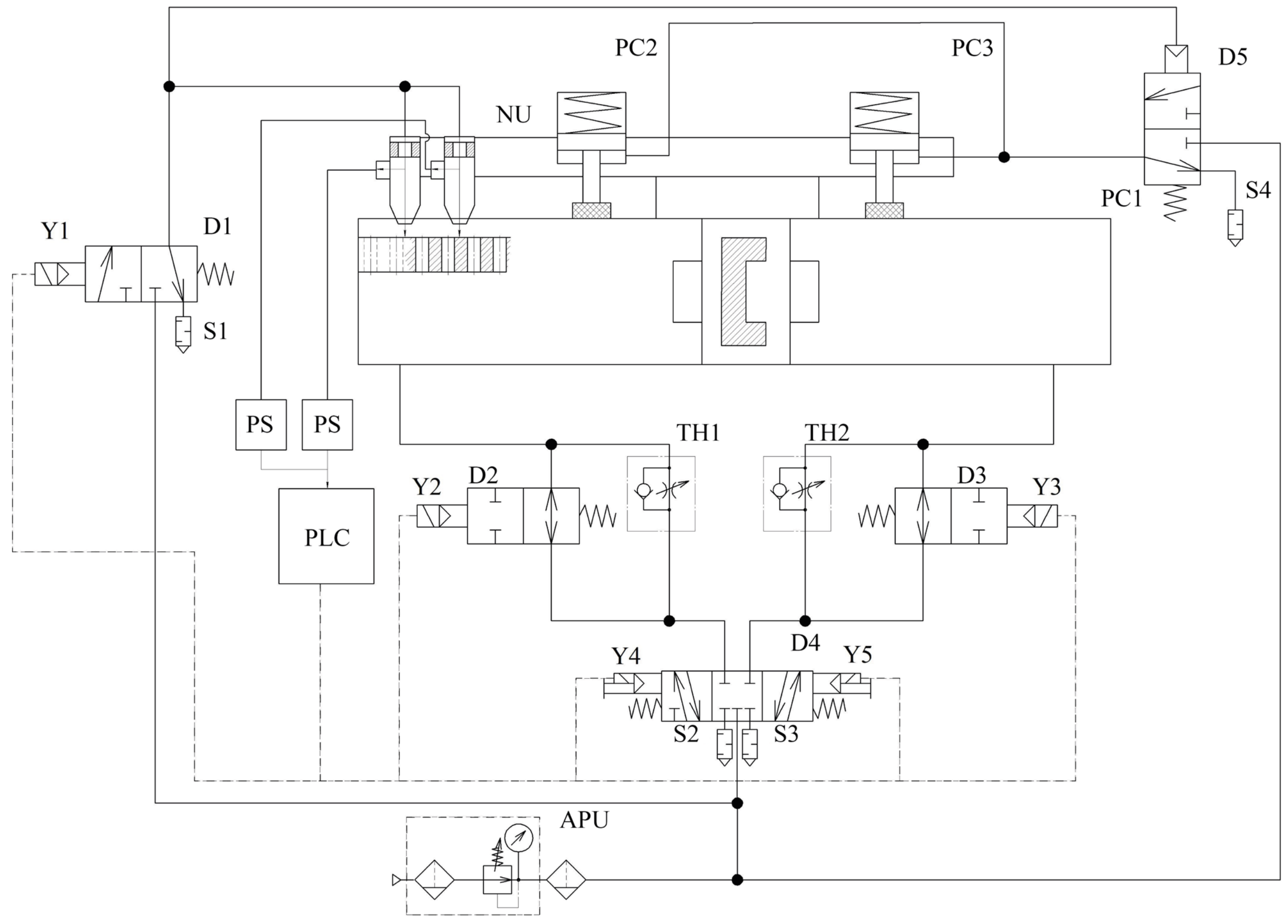

Fig. 3. Pneumatic scheme of the research complex: PC1 — long-stroke pneumatic cylinder; PC2 and PC3 — external brake system pneumatic cylinders; NU — nozzle unit; D1 — sensor feed control distributor; D2; D3 — deceleration distributors; D4 — control distributor; D5 — external brake device control distributor; S1–S4 — pneumatic silencers; PS — pressure sensor; PLC — programmable logic controller; TH1 and TH2 — PC1 travel speed control throttles; APU — air preparation unit [4, 6]

Experimental studies were conducted under the following conditions:

– maximum travel speed $V_{\text{макс}}$ = 0.26 m/s;

– pressure in the drive pneumatic system $p_{\text{м}}$ = 6 bar;

– maximum stroke length of a rodless pneumatic cylinder L = 400 mm;

– mass of the moved load $M_{\text{пр1}}$ = 10, 30, 60 kg;

– positioning stop coordinate (working stroke length) $L_{\text{пз}}$ = 150, 250, 350 mm;

– positioning speed $V_{\text{пз}}$ = 0.025–0.04 m/s.

During the field experiment, the following were investigated:

– trajectories of the long-stroke pneumatic actuator: acceleration and movement with a steady maximum speed; deceleration of the speed of movement to the positioning speed; movement at the positioning speed and stopping at a given coordinate;

– speed of the long-stroke pneumatic actuator and its components, which includes: acceleration time of the actuator; duration of the positioning stage and determination of the accuracy of reaching the specified final position;

– impact of the external load and the length of movement on the speed and accuracy of positioning.

Research Results. The graphs of the movement of the drive power elements, their speed, as well as the dependence of the air pressure in the drive pneumatic system, in comparison to the graphs of the same drive parameters obtained during the simulation, are presented in Figures 4–6.

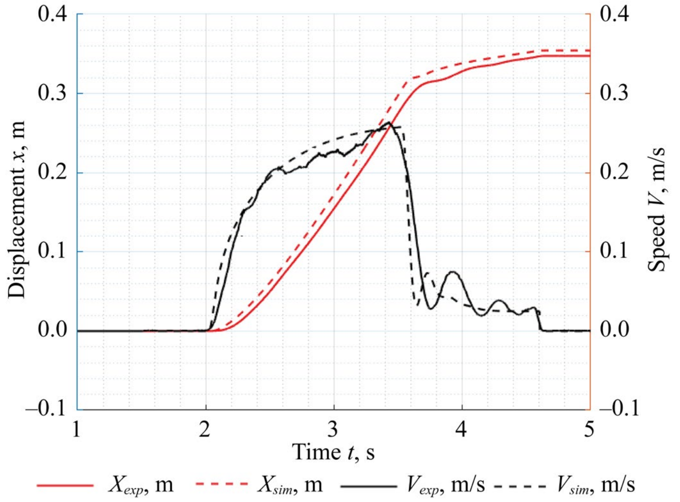

Fig. 4. Graphs of change in time of speed and coordinates of displacement of the actuator of the studied pneumatic drive from time: X_{exp}, V_{exp} — displacement and speed obtained experimentally, respectively; X_{sim}, V_{sim} — displacement and speed obtained during the conducted mathematical modeling, respectively

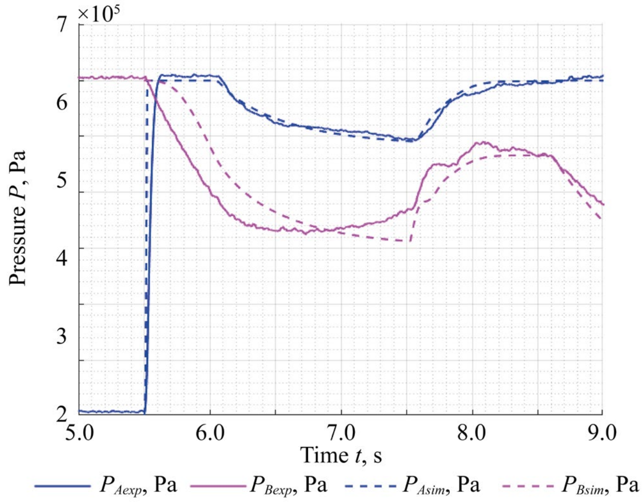

Fig. 5. Graph of change in air pressure in the pressure and drain cavities of the studied pneumatic drive over time: P_{Aexp}, P_{Bexp} — working gas pressure in the pressure and drain cavities, obtained experimentally, respectively; P_{Asim}, P_{Bsim} — gas pressure in the pressure and drain cavities, obtained during mathematical modeling, respectively

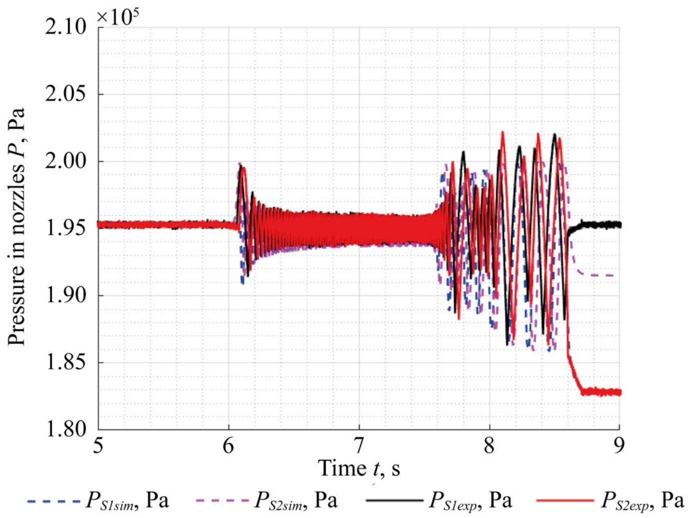

Fig. 6. Graph of the change in gas pressure in the nozzle units of a contactless jet sensor over time: P_{S1exp}, P_{S2exp} — gas pressure in nozzle unit 1 and 2, obtained experimentally, respectively; P_{S1sim}, P_{S2sim} — pressure in nozzle unit 1 and 2, obtained during mathematical modeling, respectively

The maximum discrepancy between the experimental data and the mathematical modeling data (Fig. 4–6) does not exceed 18%, which confirms the reliability of the research results [24].

The discrepancy between the research results was determined for all the data obtained (Fig. 4–6) using the following formula [25]:

$$a = \frac{a_{т} - a_{э}}{a_{э}} \cdot 100\,\%, \tag{1}$$

where $a_э$ — data obtained during the experimental study (displacement, speed, pressure), $a_т$ — data obtained as a result of the theoretical study [26].

In Figures 7 and 8, the captions "L_{exp}" and "L_{mod}" denote oscillograms obtained as a result of full-scale and computational experiments, respectively.

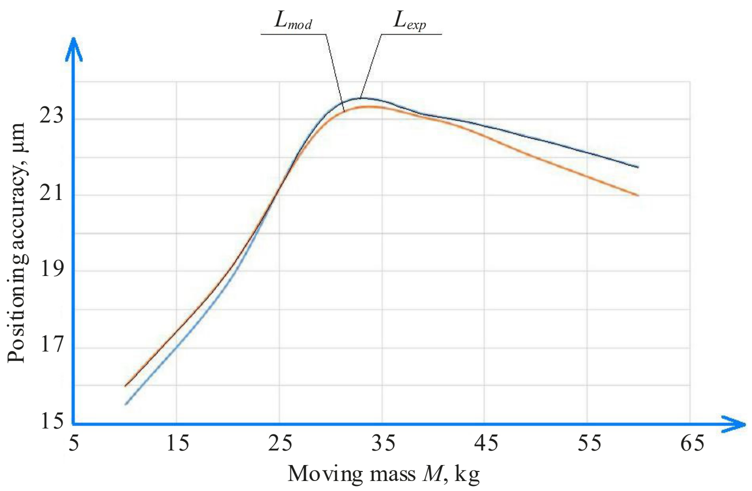

Fig. 7. Effect of mass M of the moving structure on the value of the positioning accuracy of the pneumatic drive: L_{exp} — result obtained during a full-scale experiment, L_{mod} — result obtained during mathematical modeling

Figure 7 shows the result of the study on the effect of mass M of the moving structure on the value of the positioning accuracy of the pneumatic cylinder.

The studies have shown that the positioning accuracy of the drive depends on the mass of the moving object. With an increase in mass from 10 to 30 kg, the positioning accuracy decreased by 1.47 times, and with an increase in mass to 60 kg, the accuracy worsened compared to a mass of 10 kg by 1.37 times.

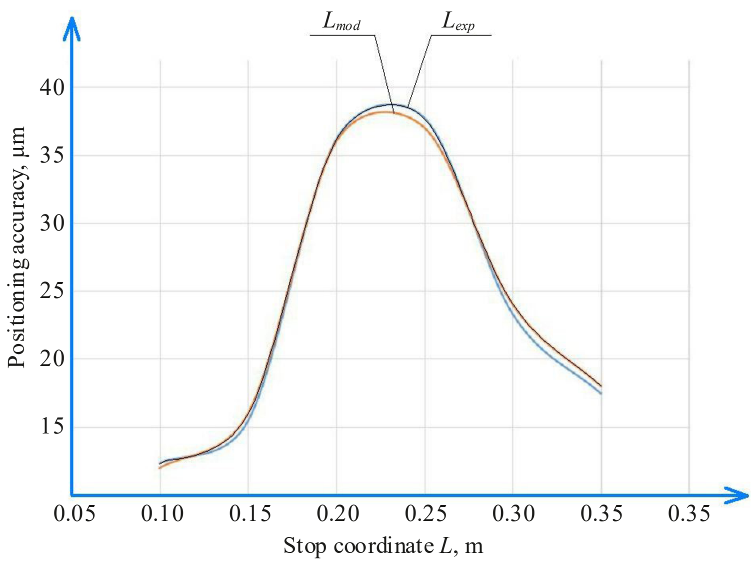

Fig. 8. Effect of working stroke length of the drive on value of its positioning accuracy: L_{exp} — result obtained during a full-scale experiment, L_{mod} — result obtained during mathematical modeling

Figure 8 shows the result of the study on the effect of the stop coordinate of the drive actuator on the accuracy of its positioning at the same maximum speed of movement. It was found that the accuracy of the drive positioning depends on the length of its working stroke to a complete stop (stop coordinates): when changing the stop coordinate from 0.1 m to 0.22 m, the positioning accuracy worsened by 3.2 times, and when changing the stop coordinate from 0.22 m to 0.35 m, the positioning accuracy increased by 2.2 times. This is due to the fact that during the operation of the drive, back pressure is created in the air cavity of the pneumatic cylinder when the piston approaches its extreme walls (and the closer to the wall, the greater the pressure) [27]. Back pressure also increases additionally during throttling due to the narrowing of the flow section of the channels of the holes intended for pumping and bleeding gas [28]. The narrowing of the flow sections of the channels causes the deceleration of gas flows [29]. This is observed when the actuator of the drive is moved at the positioning speed [30].

Discussion. The conducted experimental studies allowed obtaining good results in the development of long-stroke pneumatic drives. Successful verification of the mathematical model confirmed the correctness of the theoretical studies carried out in previous works [8, 19].

The obtained positioning accuracy of the drive is 77 μm at a distance of over three meters. This figure significantly exceeds similar results presented in [13, 15], which demonstrates high potential of the developed design, since the economic efficiency of the proposed solution is due to the absence of an electronic component base in the control system [31]. This not only reduces initial production costs, but also significantly simplifies maintenance of the drive during operation [32]. Comparative analysis with existing developments [2, 13] confirms the superiority of the developed system in terms of cost criteria.

Conclusion. The main research results are as follows:

– experimental verification of the results of mathematical modeling of a positioning long-stroke rodless pneumatic actuator was carried out; the maximum error of the research was 18%, which confirmed the adequacy of the mathematical model and its possibility of application for engineering calculations;

– key factors that determine the accuracy of drive positioning were identified: with an increase in the moved mass from 10 to 60 kg, the positioning accuracy decreased by 40%. A significant influence of the position of the pneumatic cylinder piston in the extreme positions on the positioning accuracy was also established, which caused a deterioration in accuracy up to four times in the central positions due to the occurrence of back pressure in the drain cavity when the positioning speed was reached.

The conducted studies confirmed the efficiency of the developed solutions for long-stroke rodless pneumatic actuators.

The practical significance of the study is validated by the possibility of using the obtained results in the creation of high-precision long-stroke mechanisms in various industries [33]. The developed design can be used in automated production lines, robotic complexes, and other areas where precise positioning over significant distances is required.

Promising areas for further research include optimizing the parameters of the control system to obtain even higher positioning accuracy, as well as developing calculation methods for positioning long-stroke pneumatic drives.

References

1. Hongwei Zhu, Zhiwen Wang, Hu Wang, Zecheng Zhao, Wei Xiong. Leakage Fault Diagnosis of Two Parallel Cylinders in Pneumatic System with a Minimal Number of Sensors. *Electronics*. 2023;12(15):3261. https://doi.org/10.3390/electronics12153261

2. Rakulenko SV. *Hydraulic Drive of Dependent Tool Advance (Using a Mobile Drilling Machine)*. Cand.Sci. (Engineering) diss. Rostov-on-Don: DSTU; 2019. 165 p. (In Russ.)

3. Mosadegh B, Polygerinos P, Keplinger C, Wennstedt S, Shepherd RF, Gupta U, et al. Pneumatic Networks for Soft Robotics that Actuate Rapidly. *Advanced Functional Materials*. 2014;24(15):2163–2170. https://doi.org/10.1002/adfm.201303288

4. Thanh Nguyen Truong, Anh Tuan Vo, Hee-Jun Kang. A Backstepping Global Fast Terminal Sliding Mode Control for Trajectory Tracking Control of Industrial Robotic Manipulators. *IEEE Access*. 2021;9:31921-31931. https://doi.org/10.1109/ACCESS.2021.3060115

5. Yilmaz BM, Tatlicioglu E, Savran A, Alci M. Self-Adjusting Fuzzy Logic Based Control of Robot Manipulators in Task Space. *IEEE Transactions on Industrial Electronics*. 2021;69:1620–1629. https://doi.org/10.1109/TIE.2021.3063970

6. Jihong Wang, Tim Gordon. Energy Optimal Control of Servo-Pneumatic Cylinders through Nonlinear Static Feedback Linearization. *Journal of Dynamic Systems, Measurement, and Control.* 2012;134(5):051005. https://doi.org/10.1115/1.4006084

7. Fracczak L, Nowak M, Koter K. Flexible Push Pneumatic Actuator with High Elongation. *Sensors and Actuators A: Physical*. 2021;321:112578. https://doi.org/10.1016/j.sna.2021.112578

8. Korotych DA, Sidorenko VS, Prikhodko SP. Investigation of Dynamic Characteristics of an Automated Position Long-Stroke Pneumatic Actuator of Fabrication System. *Advanced Engineering Research (Rostov-on-Don)*. 2023;23(3):283–295. https://doi.org/10.23947/2687-1653-2023-23-3-283-295

9. Kurmyshev E, Jiménez M, Castaneda C. Experimental Study of Double-Acting Cylinder. *Experimental Techniques*. 2020;44(2):355–367. https://doi.org/10.1007/s40799-020-00359-8

10. Shilin DV. *Increasing the Accuracy of Positioning the Carriage of a Rodless Pneumatic Unit.* Cand.Sci. (Engineering) diss. Moscow: National Research University MPEI; 2016. 257 p. (In Russ.)

11. Urrea C, Kern J, Alvarado J. Design and Evaluation of a New Fuzzy Control Algorithm Applied to a Manipulator Robot. *Applied Sciences*. 2020;10(21):7482. https://doi.org/10.3390/app10217482

12. Behrouz Najjari, Masoud Barakati S, Ali Mohammadi, Mohammad Javad Fotuhi, Saeid Farahat, Mohammad Bostanian. Modelling and Controller Design of Electro-Pneumatic Actuator Based on PWM. *International Journal of Robotics and Automation (IJRA)*. 2012;1(3):125–136.

13. Dao The Anh. *High-Speed and High-Precision Positional Pneumatic Drive*. Cand.Sci. (Engineering) diss. Rostov-on-Don: DSTU; 2015. 206 p. (In Russ.)

14. Mobayen S, Mofid O, Din SU, Bartoszewicz A. Finite-Time Tracking Controller Design of Perturbed Robotic Manipulator Based on Adaptive Second Order Sliding Mode Control Method. *IEEE Access.* 2021;9:71159–71169. https://doi.org/10.1109/ACCESS.2021.3078760

15. Chaplygin EhI, D'jachkov EA, Gorjunov VA, Burkov JuG. *Jet Device for Positioning of Reciprocal Motion Drive.* RF Patent No. RU 2352973 C1. 2009. 6 p. URL: https://patents.s3.yandex.net/RU2352973C1_20090420.pdf (accessed: 20.06.2025).

16. Bae Hyo-Jeong, Jin Maolin, Suh Jinho, Lee Jun Young, Chang Pyung-Hun, Ahn Doo-sung. Control of Robot Manipulators Using Time-Delay Estimation and Fuzzy Logic Systems. *Journal of Electrical Engineering and Technology*. 2017;12(3):1271–1279. http://doi.org/10.5370/JEET.2017.12.3.1271

17. Obukhova EN, Popov AN. Synergetic Synthesis of Nonlinear Adaptive Control for Pneumatic Drives. In: *Proc. IV International Conference on Control in Technical Systems (CTS)*. New York City: IEEE; 2021. P. 45–48. https://doi.org/10.1109/CTS53513.2021.9562786

18. Shenglin Mu, Seigo Goto, Satoru Shibata, Tomonori Yamamoto. Intelligent Position Control for Pneumatic Servo System Based on Predictive Fuzzy Control. *Computers and Electrical Engineering.* 2019;75:112–122. https://doi.org/10.1016/j.compeleceng.2019.02.016

19. Novoselov OG, Sabitov LS, Sibgatullin KE, Sibgatullin ES, Klyuev AV, Klyuev SV, et al. Method for Calculating the Strength of Massive Structural Elements in the General Case of Their Stress-Strain State (Parametric Equations of the Strength Surface). *Construction Materials and Products*. 2023;6(2):104–120. https://doi.org/10.58224/2618-7183-2023-6-2-104-120

20. Korotych DA, Sidorenko VS, Prikhodko SP. *Jet Positional Pneumatic Drive System for Long-Stroke Positioning Coordinate Movements*. RF Patent No. RU 2802568 C1. 2023. 10 p. URL: https://patentimages.storage.googleapis.com/f5/07/6c/7d26ddebc8dd07/RU2802568C1.pdf (accessed: 20.06.2025).

21. Božek P, Nikitin Yu. The Development of an Optimally-Tuned PID Control for the Actuator of a Transport Robot. *Actuators*. 2021;10(8):195. https://doi.org/10.3390/act10080195

22. Hailin Sun, Longlong Gao, Zhixin Zhao, Baoren Li. Finite-Time Active Disturbance Rejection Control for High-Pressure Pneumatic Servo System Subject to Matched and Mismatched Disturbances. In: *Proc. 9th International Conference on Fluid Power and Mechatronics (FPM)*. New York City: IEEE; 2023. P. 1–7. https://doi.org/10.1109/FPM57590.2023.10565461

23. Weiping Hu, Rahim Mutlu, Weihua Li, Gursel Alici. A Structural Optimisation Method for a Soft Pneumatic Actuator. *Robotics*. 2018;7(2):24. https://doi.org/10.3390/robotics7020024

24. Gallyamov ShR, Starikov KV, Celischev VA. Experimental Study on the Characteristics of the FESTO Pneumatic Drive with a Proportional Flow Distributor. *Vestnik UGATU*. 2011;15(1):26–33. (In Russ.). URL: http://journal.ugatu.su/index.php/Vestnik/article/view/900 (accessed: 20.06.2025).

25. Novoselov OG, Sabitov LS, Sibgatullin KE, Sibgatullin ES, Klyuev AS, Klyuev SV, et al. Method for Calculating the Strength of Massive Structural Elements in the General Case of Their Stress-Strain State (Kinematic Method). *Construction Materials and Products*. 2023;6(3):5–17. https://doi.org/10.58224/2618-7183-2023-6-3-5-17

26. Vardhan Alok, Dasgupta Kaustubh, Mishra Santosh. Dynamic Analysis of a Closed-Circuit Hydraulic Drive System Used in the Rotary Head of Blasthole Drilling Machine Using MATLAB–Simulink Environment. *Proceedings of the Institution of Mechanical Engineers, Part I: Journal of Systems and Control Engineering*. 2018;233(6):702–719. https://doi.org/10.1177/0959651818808870

27. Abela K, Refalo P. Analysis of Pneumatic Parameters to Identify Leakages and Faults on the Demand Side of a Compressed Air System. *Cleaner Engineering and Technology.* 2022;6:100355. https://doi.org/10.1016/j.clet.2021.100355

28. The Anh Dao, Sidorenko VS, Dymochkin DD. Study on Positioning Accuracy of Automated Pneumatic Drive with an Outer Brake. *Vestnik of Don State Technical University*. 2015;15(4):46–53. https://doi.org/10.12737/16077

29. Grishchenko VI, Kilina MS, Dolgov GA. Mathematical Model of Hydraulic Shock Absorber with Feedback. In: Radionov AA, Gasiyarov VR (eds). *Proc. 6th International Conference on Industrial Engineering. Lecture Notes in Mechanical Engineering*. Cham: Springer; 2021. P.1262–1270. https://doi.org/10.1007/978-3-030-54817-9_147

30. Lemeshko M, Molev M, Golovin I. Hydraulic Technological Machines with Adaptive Drive Structure. *MATEC Web of Conferences*. 2018;224:02087. https://doi.org/10.1051/matecconf/201822402087

31. Ling Zhao, Shaomeng Gu, Jinhui Zhang, Sihang Li. Finite-Time Trajectory Tracking Control for Rodless Pneumatic Cylinder Systems with Disturbances. *IEEE Transactions on Industrial Electronics*. 2022;69(4):137–4147. https://doi.org/10.1109/TIE.2021.3071707

32. Haili Li, Jiantao Yao, Pan Zhou, Xinbo Chen, Yundou Xu, Yongsheng Zhao. High-Force Soft Pneumatic Actuators Based on Novel Casting Method for Robotic Applications. *Sensors and Actuators A: Physical*. 2020;306:111957. https://doi.org/10.1016/j.sna.2020.111957

33. Xiaoqian Chen, Xiang Zhang, Yiyong Huang, Lu Cao, Jinguo Liu. A Review of Soft Manipulator Research, Applications, and Opportunities. *Journal of Field Robotics*. 2022;39(3):281–311. https://doi.org/10.1002/rob.22051

About the Author:

Daniil A. Korotych, Senior Lecturer of the Department of Hydraulics, Hydropneumoautomatics and Thermal Processes, Don State Technical University (1, Gagarin Sq., Rostov-on-Don, 344003, Russian Federation), SPIN-code, ORCID, ResearchGate, ScopusID, ResearcherID, daniilberuk@gmail.com

Conflict of Interest Statement: **the author declares no conflict of interest.**

The author has read and approved the final version of manuscript.

Об авторе:

Даниил Андреевич Коротыч, старший преподаватель кафедры «Гидравлика, гидропневмоавтоматика и тепловые процессы» Донского государственного технического университета (344003, Российская Федерация, г. Ростов-на-Дону, пл. Гагарина, 1), SPIN-код, ORCID, ResearchGate, ScopusID, ResearcherID, daniilberuk@gmail.com

Конфликт интересов: **автор заявляет об отсутствии конфликта интересов.**

Автор прочитал и одобрил окончательный вариант рукописи.

Received / Поступила в редакцию 14.06.2025
Reviewed / Поступила после рецензирования 04.07.2025
Accepted / Принята к публикации 18.07.2025

MACHINE BUILDING AND MACHINE SCIENCE
МАШИНОСТРОЕНИЕ И МАШИНОВЕДЕНИЕ

UDC 621.791
https://doi.org/10.23947/2687-1653-2025-25-3-208-220

Original Empirical Research

Study of Effect of Electrode Arrangement on Layer Geometry and Fusion Zone Morphology under Twin-Arc Surfacing

Iakov P. Skoblikov[1] ✉, **Evgeny I. Efimov**[2], **Victor V. Murzin**[1]
[1] Saint Petersburg State Marine Technical University, Saint Petersburg, Russian Federation
[2] TRINITECH LLC, Saint Petersburg, Russian Federation
✉ iakov98sp@gmail.com

EDN: AAVODZ

Abstract

Introduction. Increasing the productivity of single-wire surfacing through raising the wire feed rate causes defects — undercuts and poor fusion between layers, which reduces the quality of the deposited coating and increases the reject rate. To solve this problem, multiwire surfacing techniques are being developed in a shielded gas environment which increase productivity without compromising quality. The literature shows that the relative position of electrodes in multiwire systems affects significantly the thermal and electrophysical characteristics of the arc, and therefore, the geometry of the reinforcement and the shape of the fusion penetration. However, the available studies are fragmentary: there is insufficient data on the morphology of the fusion zone, and the relationship of its parameters and specific electrode arrangement schemes under twin-arc surfacing in a shielded environment, which leaves a scientific gap. The objective of this research is to evaluate the change in the geometric parameters of the reinforcement of the deposited layer and the morphology of the fusion zone with different relative positions of the electrodes under twin-arc surfacing in a shielded gas environment.

Materials and Methods. The experiment was conducted on a 6-axis Fanuc 120iD robot with an EWM Titan XQ500 power source and an experimental surfacing head consisting of two welding torches. The layers were deposited on steel substrates of grade St3 using the GMAW Pulse method with Sv 08G2S wire with a diameter of 1.2 mm in an Ar/CO_2 environment (98%/2%) under a fixed surfacing mode (WFS = 6.5 m/min for each torch, TS = 4 mm/s, MW = 150°C). The following parameters were adopted as the studied factors: distances between electrodes (z = 15, 18, 21 mm), their angle of inclination (α = 5°, 10°). On the cross-sections of the deposited layers prepared by grinding and etching, the geometric parameters of reinforcement (height h, width S, wetting angle γ) and fusion penetration (depths a, a_1, width b) were measured. Quantitative analysis of the weld geometry was performed using Digimizer software to assess the effect of the relative position of the electrodes on the formation of the layer.

Results. It has been found that the distance between the electrodes (z) affects significantly the reinforcement geometry: a growth of z causes an increase in the layer width (S) and the wetting angle (γ), but a decrease in its height (h). The axial fusion depth (a) demonstrated a nonlinear dependence on z, reaching a maximum (~2.2 mm) at z = 18 mm. The inclination angle (α) had a minor effect (<5%) on the reinforcement parameters, but affected significantly the shape of the main fusion zone (a_1): an increase in α decreased a_1 and made the penetration more gently sloping. At z = 21 mm, the impact of α on the penetration disappeared. The relationships between the relative positions of the electrodes under twin-arc surfacing, the geometric parameters of the reinforcement, and the depth of the fusion zone were specified.

Discussion. The explanation of the established dependences is based on the change in the thermal and electrophysical properties of the electric arc depending on the mutual arrangement of the electrodes. The axial depth of fusion penetration depends not only on the distance between the electrodes, but also on the volume of the weld pool. With an excessive volume of the weld pool for a specific surfacing mode, a damping effect of heat flows from the electric arc to the base metal occurs — the volume of the weld pool absorbs part of the heat, which causes a decrease in the depth of penetration. The change in the arc pressure vector with an increase in the angle between the electrodes explains the decrease in the depth of the main fusion zone.

Conclusion. The regularities of the effect of the mutual arrangement of electrodes on the geometry of the deposited layer and the shape of the fusion zone under twin-arc surfacing in a shielded gas have been experimentally established. It is shown that an increase in the distance between the electrodes results in an increase in the width of the bead, a decrease in its height, and an increase in the wetting angle. It has been noted that the penetration depth depends on the volume of the weld pool. It is determined that the angle of inclination of the electrodes in the studied modes has an insignificant effect — less than 5% — on the geometry of the deposited metal, although hypothetically, it can be enhanced at smaller interelectrode distances. The data obtained extract clear trends and form the basis for further in-depth study of the thermal and electrophysical aspects of the process of twin-arc surfacing in a shielded gas environment.

Keywords: twin-arc welding, GMAW, multiwire welding, mutual arrangement of electrodes, morphology of the deposited layer, fusion zone, electromagnetic interaction of arcs

Acknowledgments. The authors appreciate the management of TRINITECH LLC. They would like to thank Director F.A. Shamrai and Lead Engineer A.I. Kurakin for their interest in the research and for providing the opportunity to carry out work at the company's production facilities.

For Citation. Skoblikov IP, Efimov EI, Murzin VV. Study of Effect of Electrode Arrangement on Layer Geometry and Fusion Zone Morphology under Twin-Arc Surfacing. *Advanced Engineering Research (Rostov-on-Don).* 2025;25(3):208–220. https://doi.org/10.23947/2687-1653-2025-25-3-208-220

Оригинальное эмпирическое исследование

Исследование влияния взаиморасположения электродов на геометрические параметры слоя и морфологию зоны проплавления при наплавке расщепленной дугой

Я.П. Скобликов[1] ✉, Е.И. Ефимов[2], В.В. Мурзин[1]

[1] Санкт-Петербургский государственный морской технический университет, г. Санкт-Петербург, Российская Федерация

[2] ООО «ТРИНИТЕХ», Ленинградская область, Российская Федерация

✉ iakov98sp@gmail.com

Аннотация

Введение. Повышение производительности однопроволочной наплавки за счёт увеличения скорости подачи проволоки приводит к дефектам — подрезам и несплавлениям между слоями, что снижает качество наплавленного покрытия и увеличивает брак. Для решения этой проблемы в среде защитных газов развиваются многопроволочные методы наплавки, позволяющие повысить производительность без ухудшения качества. В литературе показано, что взаиморасположение электродов в многопроволочных системах существенно влияет на теплофизические и электрофизические характеристики дуги, а следовательно — на геометрию усиления и форму проплавления. Однако имеющиеся исследования фрагментарны: недостаточно данных по морфологии зоны проплавления и взаимосвязи её параметров с конкретными схемами расположения электродов при наплавке расщеплённой дугой в защитной среде, что оставляет научный пробел. Цель данной работы — оценить изменение геометрических параметров усиления наплавленного слоя и морфологии зоны проплавления при различных взаиморасположениях электродов при наплавке расщеплённой дугой в среде защитного газа.

Материалы и методы. Эксперимент проводился на 6-осевом роботе Fanuc 120iD с источником питания EWM Titan XQ500 и экспериментальной наплавочной головкой, состоящей из двух сварочных горелок. Слои наплавлялись на стальные подложки марки Ст3 методом GMAW-Pulse проволокой Св-08Г2С диаметром 1.2 мм в среде Ar/CO_2 (98 %/2 %) при зафиксированном режиме наплавки (WFS = 6,5 м/мин на каждую горелку, TS = 4 мм/с, MBT = 150 °C). В качестве исследуемых факторов приняты следующие параметры: расстояния между электродами (z = 15, 18, 21 мм), угол их наклона (α = 5°, 10°). На поперечных сечениях наплавленных слоев, подготовленных шлифовкой и травлением, измерялись геометрические параметры усиления (высота h, ширина S, угол смачивания γ) и проплавления (глубины a, a_1, ширина b). Количественный анализ геометрии шва выполнялся с использованием ПО Digimizer для оценки влияния взаиморасположения электродов на формирование слоя.

Результаты исследования. Установлено, что расстояние между электродами (z) существенно влияет на геометрию усиления: увеличение z приводит к росту ширины слоя (S) и угла смачивания (γ), но снижению его высоты (h). Глубина осевого проплавления (a) демонстрирует нелинейную зависимость от z, достигая максимума (~2,2 мм) при z = 18 мм. Угол наклона (α) оказал незначительное влияние (<5 %) на параметры усиления, но существенно повлиял на форму основной зоны проплавления (a_1): увеличение α уменьшало a_1 и делало проплавление более пологим. При z = 21 мм влияние α на проплавление исчезало. Выявлены зависимости между взаиморасположением электродов при наплавке расщеплённой дугой, геометрическими параметрами усиления и глубиной зоны проплавления.

Обсуждение. Объяснение установленных зависимостей основано на изменении теплофизических и электрофизических свойств электрической дуги в зависимости от взаимного расположения электродов. Осевая глубина проплавления зависит не только от расстояния между электродами, но и от объёма сварочной ванны. При избыточном объёме сварочной ванны для конкретного режима наплавки возникает эффект демпфирования тепловых потоков от электрической дуги к основному металлу — объём сварочной ванны поглощает часть тепла, что приводит к уменьшению глубины проплавления. Изменение вектора давления дуги при увеличении угла между электродами объясняет уменьшение глубины основной зоны проплавления.

Заключение. Экспериментально установлены закономерности влияния взаимного расположения электродов на геометрию наплавленного слоя и форму зоны проплавления при наплавке расщеплённой дугой в защитном газе. Показано, что увеличение расстояния между электродами приводит к росту ширины валика, уменьшению его высоты и увеличению угла смачивания. Отмечено, что глубина проплавления зависит от объёма сварочной ванны. Определено, что угол наклона электродов в исследованных режимах оказывал незначительное влияние — менее 5 % — на геометрию наплавленного металла, хотя гипотетически оно может усиливаться при меньших межэлектродных расстояниях. Полученные данные выявляют чёткие тенденции и формируют основу для дальнейшего углублённого изучения теплофизических и электрофизических аспектов процесса наплавки расщеплённой дугой в среде защитного газа.

Ключевые слова: наплавка расщепленной дугой, GMAW, многопроволочная сварка, взаимное расположение электродов, морфология наплавленного слоя, зона проплавления, электромагнитное взаимодействие дуг

Благодарности. Авторы выражают искреннюю признательность руководителям компании ООО «Тринитех» — директору Ф.А. Шамраю и ведущему инженеру А.И. Куракину за проявленный интерес к исследованию и предоставленную возможность проведения работ на производственных объектах компании.

Для цитирования. Скобликов Я.П., Ефимов Е.И., Мурзин В.В. Исследование влияния взаиморасположения электродов на геометрические параметры слоя и морфологию зоны проплавления при наплавке расщепленной дугой. *Advanced Engineering Research (Rostov-on-Don).* 2025;25(3):208–220. https://doi.org/10.23947/2687-1653-2025-25-3-208-220

Introduction. The development of welding and surfacing technologies plays a key role in the automotive industry, shipbuilding, energy, and other branches of mechanical engineering, where high performance characteristics of parts are required. Gas-shielded arc surfacing and welding remain among the most common techniques for obtaining wear-resistant and corrosion-resistant surface layers. One of the tasks of modern welding production is to increase the productivity of surfacing while maintaining quality. Currently, this task is relevant in additive technologies based on GMAW, where it is often required to increase the deposition rate to reduce production times and costs [1]. This is especially urgent in the manufacture of large-sized parts in shipbuilding, aerospace, and other industries [2]. The use of multiwire deposition also allows for the control of the chemical composition of the deposited metal using filler wires with different chemical compositions [3].

Achieving greater productivity by simply increasing the wire feed speed and/or welding line speed in traditional single-wire gas-shielded welding and surfacing processes results in defects such as undercuts or humping. According to [4], undercuts are caused by high heat input, while humping is explained by the high instantaneous cooling rate of the weldpool, due to the excessive tool speed for the selected surfacing mode.

From papers [5–7] devoted to the study of defect formation in the process of high-speed welding, it follows that the maximum productivity of single-wire welding/surfacing systems in a shielding gas, providing defect-free formation, is in the region of 3–4 kg/h for steel wires. This assessment is comparable to the conclusions of paper [8], devoted to the study of multiwire welding.

The authors of [8] reviewed multiwire welding/surfacing and compared this method to traditional single-wire processes. One of the conclusions is that a significant increase in surfacing productivity is achieved not by increasing the wire feed rate or the diameter of the fed wire in a single-wire system, but by increasing the number of melted wires using a single working tool. In [2], numerous techniques of surfacing in a shielded gas environment using several consumable electrodes are distinguished. However, there is no detailed description of the surfacing system, where two electrodes are connected to one power source. It is briefly mentioned that this surfacing process is unstable, and its implementation requires systems for forced control of the surfacing mode, providing a uniform speed of wire melting. The authors of paper [9] confirm that the double-wire surfacing is not stable when working at high voltages (27–33 V): the electric arc burns alternately on each electrode with a certain frequency. However, when the voltage is reduced to 26 V, a V-shaped stable arc is formed, providing a globular transfer of metal into the weldpool. The globule is formed due to the merging of electrode metal droplets under the action of the electromagnetic field generated by the flow of electric current through the electrodes. It should be noted that the study in [9] was conducted using modified equipment for submerged arc welding and a power source providing a hard/flat volt-ampere characteristic (VAC), typical for submerged arc welding or welding in a shielded gas environment with short circuits. In [10], the authors studied the process of twin-arc welding using a pulsed surfacing mode. This mode provides stable droplet transfer of metal according to the mechanism: one drop per pulse (ODPP). To control the droplet size, the authors have proposed a technique based on the dependence of the droplet diameter on the median value of the pulse current. It is found that this adjustment is required, since the force of their mutual attraction to each other depends on the size of the droplets. When droplets of molten metal collide in the arc gap, the arc combustion is destabilized.

The arrangement of electrodes in the welding/surfacing process plays a key role that determines the form of reinforcement of the deposited metal and the fusion zone, as well as the formation of defects. Among the multiwire surfacing techniques, systems with a longitudinal or transverse arrangement of the working tool relative to the movement vector are distinguished. The process with a longitudinal arrangement of electrodes is called tandem. This arrangement of electrodes is typical for systems that perform welded joints [11]. For surfacing, a transverse arrangement of electrodes relative to the displacement vector of the working tool is typical [11].

In addition to the spatial arrangement of the electrodes, the shape of the reinforcement and the fusion zone are significantly affected by the positioning of the electrodes relative to each other. The electrodes can be spaced apart or brought together at a certain distance or tilted relative to each other [11]. The distance between the electrodes during twin-arc surfacing has a significant effect on the pressure of the electric arc and the heat distribution in it. The authors [11] performed numerical simulation of the thermal fields of an electric twin-arc without a gap and with a gap of 1 mm between the electrodes. In this case, the electrodes were located in parallel. When surfacing with a gap, a decrease in the electric arc pressure of 1.3 times was calculated, and compared to single-wire surfacing — by 4.2 times. According to the experiments conducted in this work, it was determined that when surfacing with a gap, the penetration depth decreased, and the width of the deposited metal increased.

Based on the above, it follows that twin-arc surfacing in a shielded gas is of interest to heavy industry, including those using additive methods of electric arc deposition. This process is capable of providing stable burning of an electric arc when using pulsed surfacing modes, but requires detailed adjustment of current pulses for metal transfer in the ODPP mode. The use of two wires in one welding head allows for a significant reduction in electric arc pressure compared to traditional single-wire welding systems. When the electrodes are moved apart from each other, the electric arc pressure decreases, which changes the shape of the reinforcement and the penetration zone.

Based on the analysis, it has been revealed that there is no comprehensive study of the effect of the relative position of electrodes under multiwire twin-arc surfacing in a shielded gas environment on:

– thermal characteristics of the electric arc;
– pressure distribution in the electric arc;
– geometric parameters of the reinforcement shape and the fusion zone of the base metal;
– micro- and macrostructure.

The research objective is to systematically evaluate the effect of the working tool configuration on the geometric parameters of the reinforcement and the shape of the fusion under twin-arc surfacing in a shielded gas environment. To perform this study, a designed surfacing head was used, consisting of two welding torches fixed on a bracket that allowed them to adjust their relative position to each other. The analysis of the geometric parameters of the reinforcement shape and the fusion zone was performed on macrosections.

The following tasks were set within the framework of the objective:

– validate the selection of factors for experimental verification;
– develop and implement an experimental plan with a number of repetitions that allows calculating the confidential intervals for key indicators; perform measurements of the geometric parameters of the deposited layer of the fusion zone;
– conduct a statistical analysis of the results with an assessment of the significance of factors and their interactions;
– formulate practical recommendations for optimizing the process.

Materials and Methods. A 6-axis Fanuc 120iD robot was used in conjunction with an EWM Titan XQ500 power source to conduct the research. The working tool was an experimental surfacing head consisting of two welding torches mounted on an adjustable bracket. A ruler and a digital level were used to adjust the relative position of the welding torches. Figure 1 shows a photo and an installation diagram.

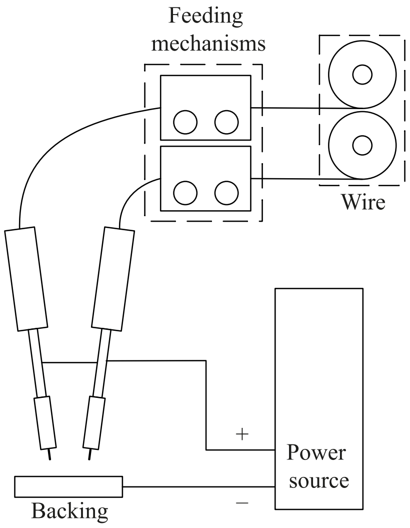

a)

b)

Fig. 1. Laboratory setup: *a* — laboratory setup diagram; *b* — photo of the laboratory setup

The substrates were made of St3 steel sheets with dimensions of 150×70×20 mm. Surfacing was performed by the GMAW-Pulse method using Sv-08G2S welding wire with a diameter of 1.2 mm. The chemical composition of the wire is given in Table 1. A mixture of argon (98%) and carbon dioxide (2%) was used as a shielded gas environment. The temperature of the substrate preheating was controlled using a HIKMICRO B20 thermal imager. To visualize the macrostructure of the deposited layer and the heat-affected zone, samples were etched by an electrolytic method in a concentrated solution of sodium chloride (NaCl). The results were analyzed using Digimizer software.

Table 1

Chemical Composition of Wire Sv-08G2S (wt.%)

C	Si	Mn	P	S	Ni	Cr	Cu
0.05–0.11	0.70–0.95	1.80–1.90	≤ 0.030	≤ 0.025	≤ 0.025	≤ 0.020	≤ 0.025

The following parameters were selected as independent factors to determine the relative position of the torches: the distance between the electrodes (z) and their angle of inclination relative to the vertical (α). The surfacing was performed with the same extension (SO) equal to 20 mm. Figure 2 shows a schematic representation of the described parameters.

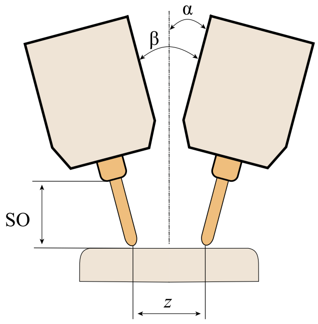

Fig. 2. Parameters under study

The layers were deposited with a wire feed rate (WFS) of 6.5 m/min on each torch and a constant linear speed (TS) of 4 mm/sec. Current (*I*) and voltage (*U*) were recorded during deposition. Substrates with identical overall dimensions were used to maintain a similar thermal pattern. Before depositing the layer, the substrates were cleaned to a metallic shine and heated to a temperature (MBT) of 150°C. Heating was performed with a gas torch. The shielded gas flow rate for each torch was 15 l/min. Table 2 shows the deposition mode values.

Table 2

Surfacing Mode

WFS, m/min	*I*, A	*U*, B	TS, mm/s	MBT, °C	SO, mm	Gas consumption, l/min
6.5	420	25	4	150	20	15

The determination of the limiting values of the factors was carried out on account of the design features of the working tool and the conditions for the formation of the deposited metal. The minimum value α, that could be set for the working tool was 5°, and the maximum was 10°. The minimum value of parameter *Z*, equal to 15 mm, was also determined by the design of the surfacing head. The maximum value of parameter *Z* was taken to be equal to 21 mm, since with a larger distance between the electrodes under the same surfacing mode it was not possible to obtain a continuous layer. To assess the effect of the selected factors, it was decided to conduct two single-factor experiments, where the grouping value was the angle of inclination of the electrodes. Table 3 shows the experimental plan taking into account the boundary conditions.

Table 3

Test Plan

Experiment	*z*, mm	α, °
1	15	5
2	18	5
3	21	5
4	15	10
5	18	10
6	21	10

Sampling was carried out on a section equal to 3/4 of the length of the deposited layer. It was assumed that on this section of the layer the thermal picture during deposition of the layer was identical. Figure 3 shows a photograph of the selection of samples for the study.

Fig. 3. Sampling

After cutting out the samples, grinding and etching of the cross-sections of the deposited layers were performed. Figure 4 shows the macrostructure of the cross-sections of the deposited layers.

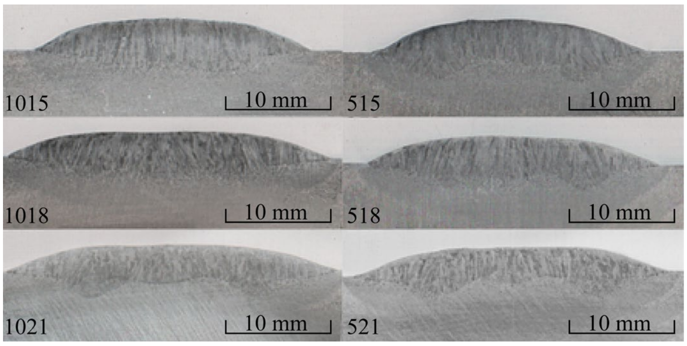

Fig. 4. Photo of the macrostructure of the deposited metal

To quantify the impact of the relative position of the electrodes on the formation of the layer, the Digimizer program outlined and measured the areas of the layer cross-section that characterized the reinforcement and the fusion zone. The following geometric parameters of the bead were selected as a response to the variable factors: layer height (h), layer width (S), bead wetting angle (ɣ).

Analyzing the fusion shape of each deposited layer, several zones with similar geometric characteristics can be identified. The first zone (P_1), characteristic of all deposition modes, is located on the layer axis. The second zone (P_2) occurs on both sides of the axial zone and is called the main zone. Figure 5 shows a schematic representation of the fusion zones under study.

Depending on the relative position of the electrodes, the shape of the fusion changes — it changes its depth (a or a_1) and width (b). Figure 6 shows a schematic representation of the specified parameters.

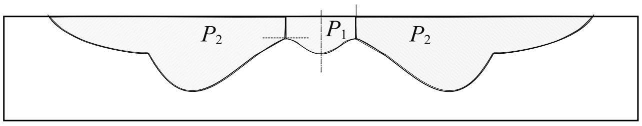

Fig. 5. Fusion zones

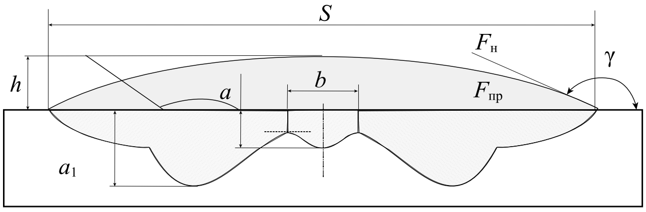

Fig. 6. Layer cross-section shape diagram

Research Results. Figure 7 shows photographs of the macrostructure of the deposited metal with reference points applied to them for measuring the shape of the deposited layer and the fusion zone in the Digimizer program. Figure 8 shows graphs reflecting the geometric parameters of the reinforcement and the fusion zone for each deposited layer. The measurements are performed in the Digimizer program. The graphs are grouped according to the criterion of the angle of inclination of the electrodes relative to the vertical.

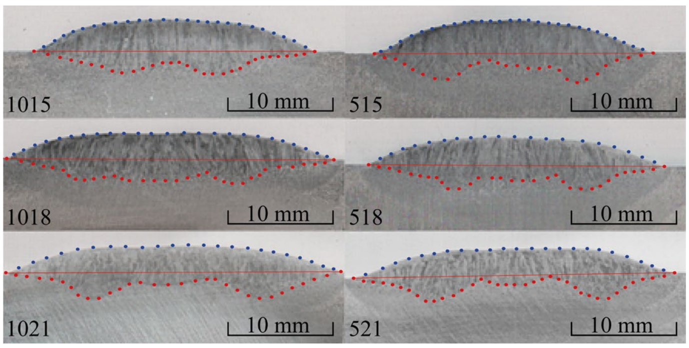

Fig. 7. Determination of boundaries of geometric parameters of reinforcement and fusion zone

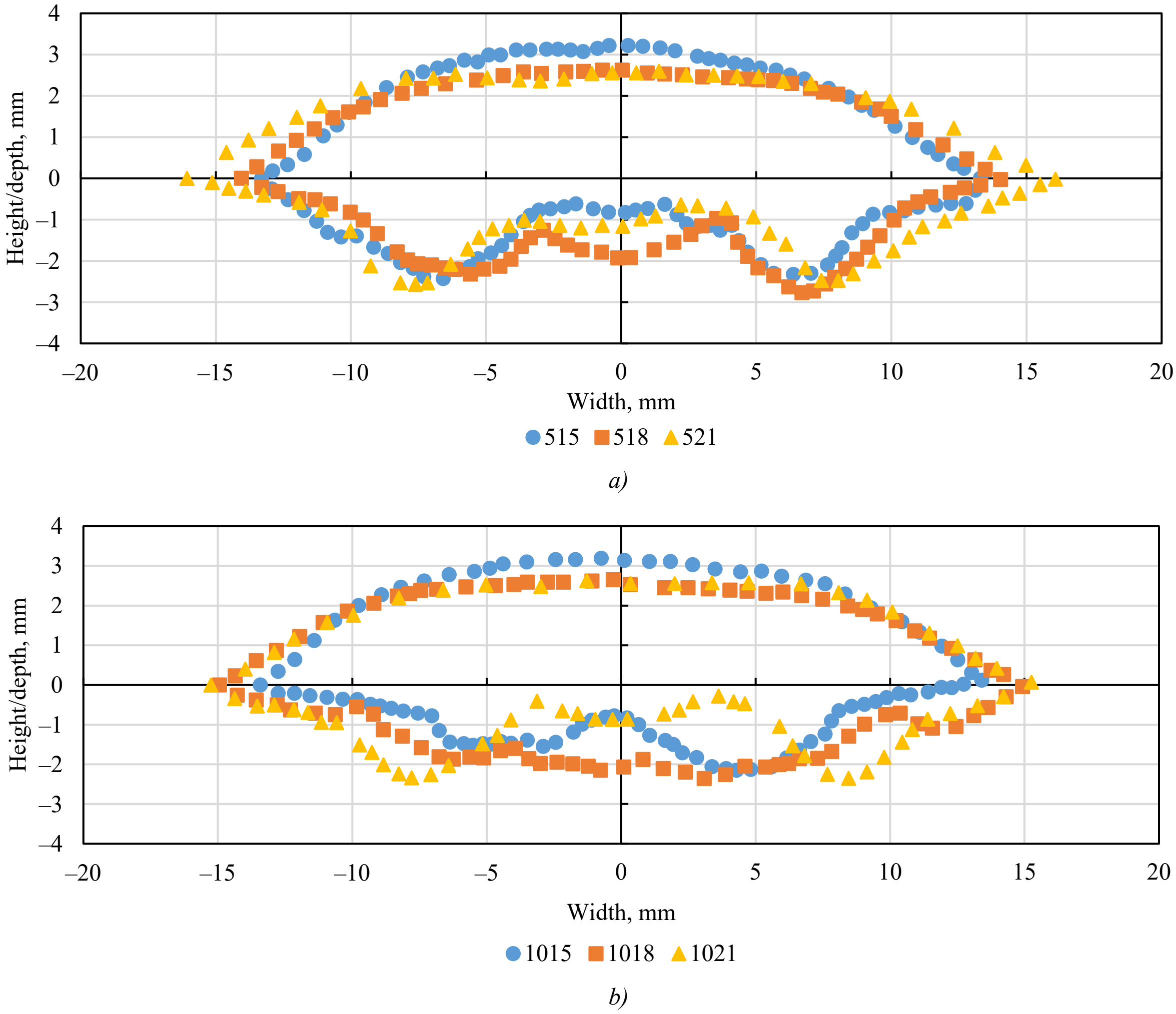

Fig. 8. Geometric parameters of reinforcement and fusion shape:
a — at α = 5° for z = 15, 18, 21 mm; *b* — at α = 10° for *z* = 15, 18, 21 mm

Based on the data obtained, graphs were constructed to assess the magnitude and nature of the responses under study. Figures 9–11 show graphs describing the change in the geometric characteristics of the gain depending on the relative position of the electrodes. Figures 12–13 show graphs illustrating how the width and depth of fusion on the layer axis and the depth of penetration in the main zone change when the relative position of the electrodes changes.

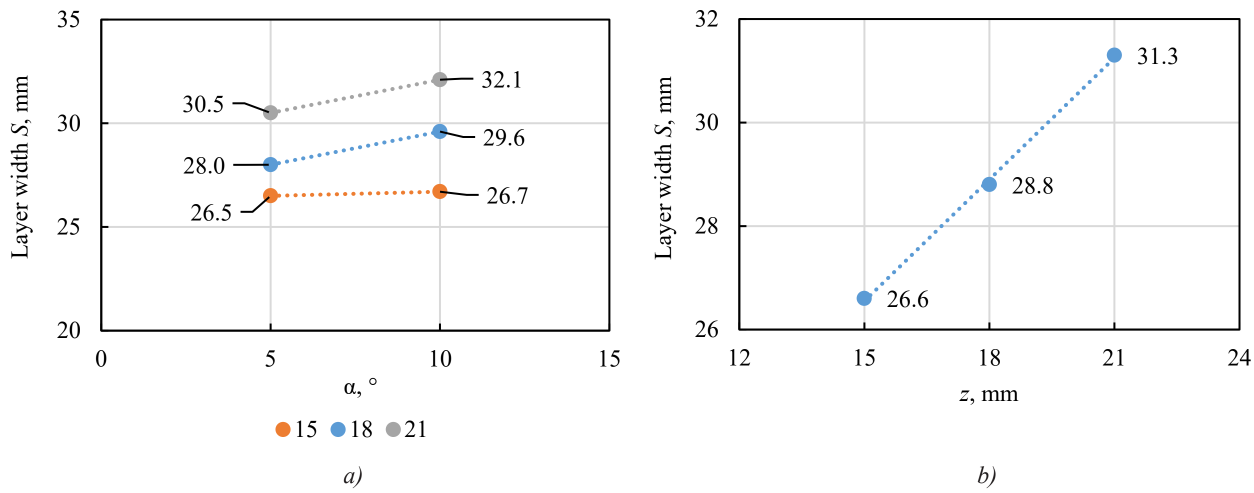

Fig. 9. Change in gain width from relative position of electrodes:
a — dependence of layer width on angle of inclination of electrodes α;
b — dependence of layer width on distance between electrodes *z*

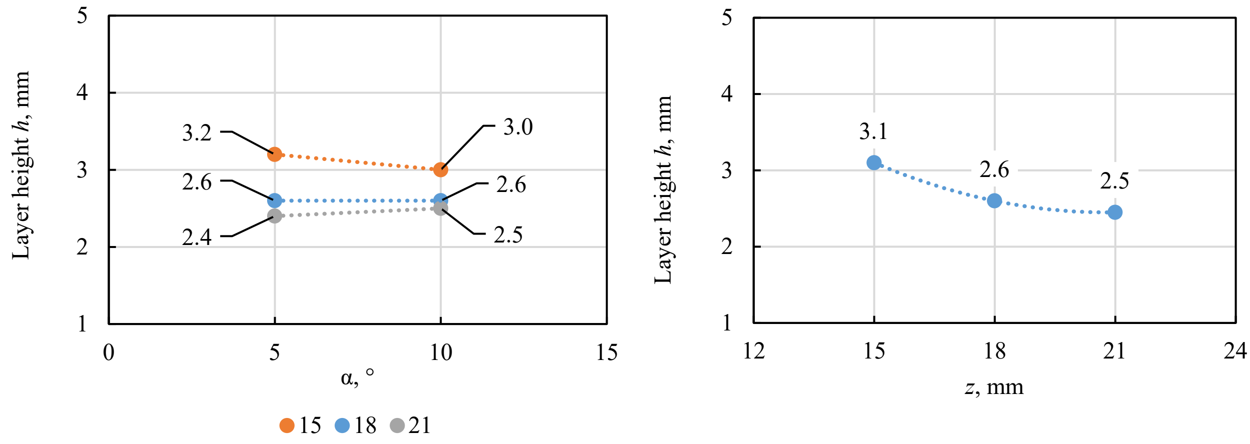

a) *b)*

Fig. 10. Change in height of gain of relative position of electrodes:
a — dependence of layer height on angle of inclination of electrodes α;
b — dependence of layer height on distance between electrodes *z*

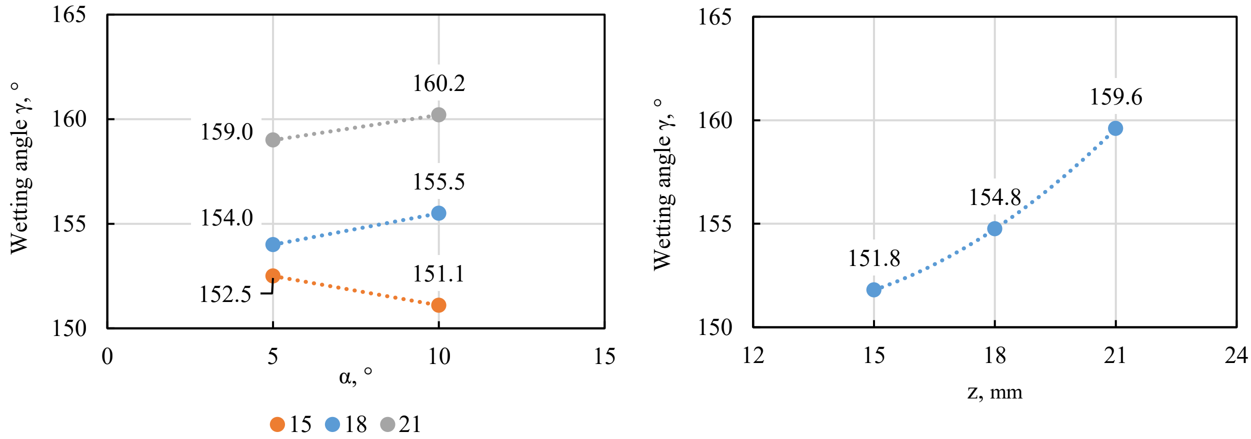

a) *b)*

Fig. 11. Dependence of wetting angle of gain on relative position of electrodes:
a — dependence of wetting angle of gain on angle of inclination of electrodes α;
b — dependence of wetting angle of gain on distance between electrodes *z*

The results of the measurements show that the width, height and wetting angle of the deposited layer depend on the distance between the electrodes. As the distance between the electrodes grows, the width of the layer increases, its height decreases, and the wetting angle becomes larger.

The impact of the angle between the burners on the roller geometry is determined to be insignificant. When changing the angle of inclination between the burners, the studied geometric characteristics of the reinforcement change by an amount not exceeding 5%.

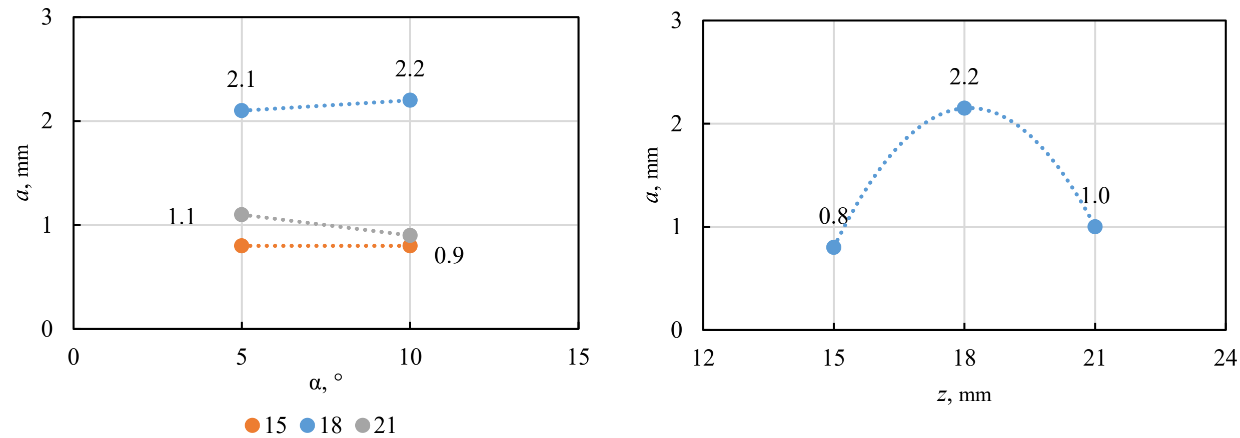

a) *b)*

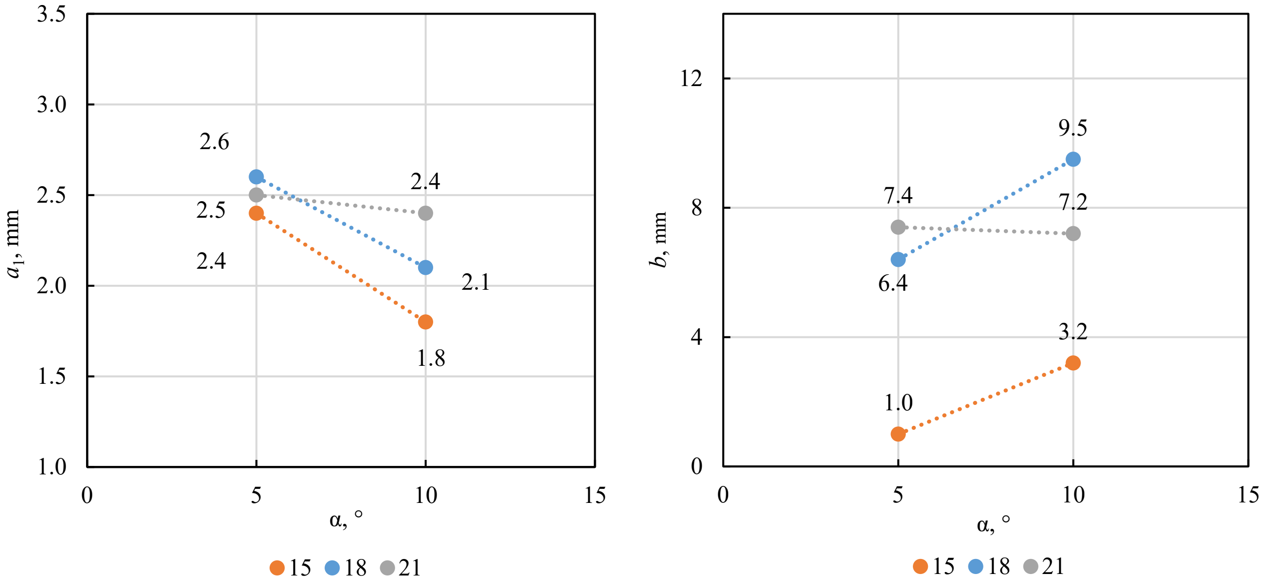

c) *d)*

Fig. 12. Depth and width of fusion in different zones:
a — dependence of axial fusion depth on electrode inclination angle α;
b — dependence of axial fusion depth on distance between electrodes *z*;
c — dependence of main fusion depth on electrode inclination angle α;
d — width of axial fusion depth depending on electrode inclination angle α

It follows from the measurement results that with relatively close electrode position, the change in the axial fusion depth is insignificant. The main effect on the axial depth is exerted by the distance between the electrodes.

The change in the width of the axial fusion zone is determined by the angle of the electrodes: with a growth in the angle between the electrodes, the width of the axial zone increases. The depth of fusion penetration in the main zone also depends on the angle between the electrodes — with an increase in the angle, the depth of axial fusion decreases. However, with a relatively large distance between the electrodes, the effect of the angle on the change in the width and depth of individual fusion zones is absent. The dependence of the cross-sectional area of the melted metal on the relative position of the electrodes has not been established.

Discussion. Dependences have been identified that confirm the effect of the angle and distance between the electrodes on the shape of the fusion and the geometric parameters of the deposited layer.

The change in the geometry of the deposited layer depending on the distance between the electrodes occurs due to the different distribution of the mass of molten metal over the deposited surface. When the heat sources are separated, a weldpool with a different mirror area is formed. As a result, with an increase in the distance between the electrodes, the deposited layers become wider, the layer height – smaller, and the wetting angle increases.

Changing the angle of inclination of the electrodes relative to the vertical plane with a constant distance between the electrodes does not have a significant effect on the geometric parameters of the deposited layer. The lack of significant effect on the shape of the reinforcement is explained by the fact that the angle of inclination determines the vector of the electric arc pressure and the force of interaction of electromagnetic fields, but does not determine the area of the weldpool mirror. These results agree with theoretical expectations.

Based on the analysis of the data on the shape of the fusion, it follows that both factors — the angle of inclination of the electrodes and the distance between them — are significant. This is explained by the fact that these parameters affect the interaction of electromagnetic fields that arise when electric current flows through the electrodes. This interaction, in turn, affects the distribution of heat in the electric arc and its pressure on the weldpool mirror.

When unidirectional electric current flows through conductors, an electromagnetic vacuum is created in the space between them. For this reason, a concentration of charged particles occurs in the interelectrode space. The effect of convergence of electric arcs under surfacing and the rush of plasma flows into the space between the electrodes is observed. This interaction is mentioned in [11–13]. Figure 13 shows an image of the combustion process of electric arcs, taken during the experiment.

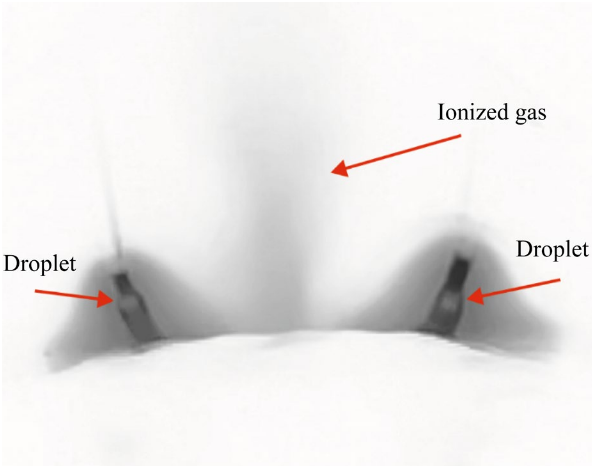

Fig. 13. Image of droplet transfer during surfacing of a layer with parameters:
Z = 18 mm; α = 10°

Due to the plasma cloud between the electrodes, an axial fusion zone is formed. As the distance between the electrodes increases, the intensity of the interaction of the electromagnetic fields decreases, and the fusion penetration depth in the axial zone also decreases. With a distance between the electrodes of 18 mm and 21 mm, the axial fusion depth is 2.2 mm and 1 mm, respectively. However, with a relatively small distance between the electrodes (15 mm), the fusion depth in the axial zone is 0.9 mm. Based on the results obtained in [11], it follows that with a decrease in the distance between the electrodes, the electric arc pressure and the concentration of ionized gas in the area between the electrodes increase. Consequently, the value of the axial fusion depth should increase — which does not correspond to the data obtained.

This discrepancy is probably due to the fact that with a distance between the electrodes equal to 15 mm, a weldpool with a smaller mirror is formed during surfacing than when surfacing with a distance of 18 mm. This fact is confirmed by the smaller layer width obtained during the experiment. A weldpool with a relatively smaller mirror area, but the same volume of molten metal, has a greater thickness. Therefore, it can be concluded that a thicker layer of liquid metal prevents heat transfer from the plasma cloud and molten metal droplets to the base metal. As a result, the axial fusion depth in this experiment does not correspond to the theoretical expectation.

The effect of the angle of inclination of the electrode relative to the vertical plane on the depth of the axial fusion zone has not been determined. Most likely, the absence of this effect is explained by the significant distance between the electrodes. When the electrodes are brought closer together, the intensity of the interaction of electromagnetic fields will increase — and this factor will begin to have weight when assessing the axial fusion depth. To confirm this hypothesis, additional research is required.

In turn, the main depth of fusion penetration changes its values slightly with a change in the angle of inclination of the electrodes due to a change in the interaction of electromagnetic fields and a change in the pressure vector of the electric arc. With an increase in the inclination of the electrodes relative to each other, the vector of the pressure force of the electric arc is not perpendicular to the surface, but tends to the axis of the deposited layer. Taking into account the mutual attraction of the electric arcs, the main fusion zone has a flat, rather than pointed shape — as in surfacing with parallel torches to the vertical plane [13].

Conclusion. Thus, the following can be noted: surfacing using a twin-arc in a shielded gas environment is of interest to industry, in particular for high-performance surfacing and electric arc additive manufacturing technology. According to the literature review, this process has not been fully disclosed in terms of the interaction of electromagnetic fields, the distribution of the thermal field in an electric arc, as well as the morphology of the micro- and macrostructure of the deposited metal depending on the relative position of the electrodes under twin-arc surfacing.

As for the work done, the data obtained are insufficient to build a mathematical model that makes it possible to predetermine the geometric parameters of the deposited layer and the fusion shape, but they are sufficient to form an idea of the trends and patterns in the deposited and molten metal under twin-arc surfacing in a shielded gas environment with different mutual arrangements of the electrodes.

The following dependences are defined:

1. As the distance between the electrodes grows, the width of the deposited layer increases, the height decreases, and the wetting angle increases — this effect is related to the redistribution of the volume of molten metal over the deposited surface.

2. The depth of fusion penetration in the axial zone depends on the volume and area of the weldpool mirror, as well as on the distance between the electrodes. As the distance grows, the depth of axial fusion increases to a critical value, at which maximum heat transfer from the electric arc to the base metal is reached. With a further growth of distance, the axial depth of fusion penetration decreases. As the distance between the electrodes decreases, the area of the weldpool mirror decreases, which leads to the formation of a layer of liquid metal that dampens the heat from the electric arc.

3. During this experiment, the angle of inclination of the electrodes has a minor effect on the geometry of the deposited layer — changes do not exceed 5%. However, it is hypothesized that with a closer arrangement of the electrodes, this effect will be more noticeable.

4. It is noted that with an increase in the angle of inclination of the electrodes, the depth of the main fusion zone decreases and becomes flatter, and with a distance between the electrodes equal to 21 mm, the effect of the angle of inclination on the width and depth of individual fusion zones is practically absent.

This study serves as a starting point for further research of the thermophysical and electrophysical properties of an electric twin-arc in a shielded gas environment depending on the relative position of the electrodes.

References

1. Somashekara MA, Suryakumar S. Studies on Dissimilar Twin-Wire Weld-Deposition for Additive Manufacturing Applications. *Transactions of the Indian Institute of Metals.* 2017;70:2123–2135. https://doi.org/10.1007/S12666-016-1032-3

2. Rui Xiang, Jiankang Huang, Xiaoquan Yu, Huayu Zhao, Ding Fan. A Review of Double-Electrode GMAW: Approaches, Developments and Variants. *Journal of Manufacturing Processes.* 2025;133:1160–1182. https://doi.org/10.1016/j.jmapro.2024.12.017

3. Sudnik W. Physical Mechanisms and Mathematical Models of Bead Defects Formation During Arc Welding. In book: *Arc Welding*. London: InTech; 2011. P. 243–266. https://doi.org/10.5772/30803

4. Zong R, Chen J, Chen MA. Undercutting Formation Mechanism in Gas Metal Arc Welding. *Welding Journal*. 2016;95:174–184.

5. Lin Wang, Ji Chen, Juansong Wu, Jinqiang Gao. Backward Flowing Molten Metal in Weld Pool and Its Influence on Humping Bead in High-Speed GMAW. *Journal of Materials Processing Technology*. 2016;237:342–350. https://doi.org/10.1016/j.jmatprotec.2016.06.028

6. Bajcer B, Hrženjak M, Pompe K, Jež B. Improvement of Energy and Materials Efficiencies by Introducing Multiple-Wire Welding. *Metalurgija*. 2007;46(1):47–52.

7. Siyuan Han, Guoqiang Liu, Xinhua Tang, Lidong Xu, Haichao Cui, Chendong Shao. Effect of Molten Pool Behaviors on Welding Defects in Tandem NG-GMAW Based on CFD Simulation. *International Journal of Heat and Mass Transfer*. 2022;195:123165. https://doi.org/10.1016/j.ijheatmasstransfer.2022.123165

8. Elsukov SK, Sokolov GN, Zorin IV, Fastov SA, Polunin IA. Investigation of the Arc Process of a Split Electrode in a Gas Metal Arc Welding. *Izvestia VSTU.* 2020;237(2):62–66. https://doi.org/10.35211/1990-5297-2020-2-237-62-66

9. Kaiyuan Wu, Jiatong Zhan, Xuanwei Cao, Min Zeng, Nian Ding. Metal Transfer of Aluminum Alloy Double-Wire Pulsed GMAW with a Median Waveform. *Journal of Materials Processing Technology*. 2020;286:116761. https://doi.org/10.1016/j.jmatprotec.2020.116761

10. Guoqiang Liu, Siyuan Han, Xinhua Tang, Haichao Cui. Effects of Torch Configuration on Arc Interaction Behaviors and Weld Defect Formation Mechanism in Tandem Pulsed GMAW. *Journal of Manufacturing Processes*. 2021;62:729–742. https://doi.org/10.1016/j.jmapro.2021.01.007

11. Xiaoli Wang, Yangsen Liu, Qi Zhang, Chengfu Luo, Qingxian Hu. Numerical Analysis Arc Behavior in Single-Power Double-Wire Single-Arc Gas Metal Arc Welding. *Results in Engineering*. 2025;26:105538. https://doi.org/10.1016/j.rineng.2025.105538

12. Ning Xiao, Haoyu Kong, Qingjie Sun, Ninshu Ma. Study of Process, Microstructure, and Properties of Double-Wire Narrow-Gap Gas Metal Arc Welding Low-Alloy Steel. *Materials*. 2024;17(24):6183. https://doi.org/10.3390/ma17246183

13. Kaiyuan Wu, Yifei Wang, Taoyuan Tao, Xiaobin Hong. Effect of Phase Shift on Arc Interference and Weld Bead Formation in Aluminum Alloy Tandem GMAW with a Median Pulsed Waveform. *The International Journal of Advanced Manufacturing Technology.* 2022;120:8013–8030. https://doi.org/10.1007/s00170-022-09200-5

About the Authors:

Iakov P. Skoblikov, Postgraduate student of the Department of Welding of Ship Structures, Saint Petersburg State Marine Technical University (3, Lotsmanskaya, Saint Petersburg, 190121, Russian Federation), SPIN-code, ORCID, ScopusID, ResearchGate, iakov98sp@gmail.com

Evgeny I. Efimov, Head of the Engineering Center of TRINITECH LLC (24B, Central Office, Sverdlovskoye Town, Vsevolozhsk District, Leningrad Region, 188400, Russian Federation), SPIN-code, boodoomber@yandex.ru

Viktor V. Murzin, Cand.Sci. (Eng.), Associate Professor of the Department of Welding of Ship Structures, Saint Petersburg State Marine Technical University (3, Lotsmanskaya, Saint Petersburg, 190121, Russian Federation), SPIN-code, vik-murzin@mail.ru

Claimed Contributorship:
IP Skoblikov: conceptualization, investigation, methodology, visualization.
EI Efimov: investigation, resources, supervision.
VV Murzin: writing – review & editing.

Conflict of Interest Statement: **the authors declare no conflict of interest.**

All authors have read and approved the final manuscript.

Об авторах:
Яков Павлович Скобликов, аспирант кафедры «Сварки судовых конструкций» Санкт-Петербургского государственного морского технического университета (190121, Санкт-Петербург, ул. Лоцманская, д. 3), SPIN-код, ORCID, ScopusID, ResearchGate, iakov98sp@gmail.com

Евгений Игоревич Ефимов, руководитель инжинирингового центра ООО «ТРИНИТЕХ» (88400, Ленинградская обл., Всеволожский р-н, г.п. Свердловское, п. Центральное Отделение, д. 24Б), SPIN-код, boodoomber@yandex.ru

Виктор Васильевич Мурзин, кандидат технических наук, доцент кафедры «Сварки судовых конструкций» Санкт-Петербургского государственного морского технического университета (190121, Санкт-Петербург, ул. Лоцманская, д. 3), SPIN-код, vik-murzin@mail.ru

Заявленный вклад авторов:
Я.П. Скобликов: разработка концепции, проведение исследования, разработка методологии, визуализация.
Е.И. Ефимов: проведение исследования, предоставление ресурсов, научное руководство.
В.В. Мурзин: написание рукописи, внесение замечаний и исправлений.

Конфликт интересов: **авторы заявляют об отсутствии конфликта интересов.**

Все авторы прочитали и одобрили окончательный вариант рукописи.

Received / Поступила в редакцию 23.06.2025
Reviewed / Поступила после рецензирования 21.07.2025
Accepted / Принята к публикации 01.08.2025

INFORMATION TECHNOLOGY, COMPUTER SCIENCE AND MANAGEMENT
ИНФОРМАТИКА, ВЫЧИСЛИТЕЛЬНАЯ ТЕХНИКА И УПРАВЛЕНИЕ

UDC 004.89
https://doi.org/10.23947/2687-1653-2025-25-3-221-232

Original Empirical Research

EDN: HLYDVW

Reconstructing a Full-Body Model from a Limited Set of Upper-Limb Motion Data

Artem D. Obukhov ✉, **Daniil V. Teselkin**
Tambov State Technical University, Tambov, Russian Federation
✉ obuhov.art@gmail.com

Abstract

Introduction. Accurate reconstruction of the human body model is required when visualizing digital avatars in virtual simulators and rehabilitation systems. However, the use of exoskeleton systems can cause overlapping and shielding of sensors, making it difficult for tracking systems to operate. This underlines the urgency of the task of reconstructing a human body model based on a limited set of data on arm movements, both in the field of rehabilitation and in sports training. Existing studies focus on either large-scale IMU networks or full video monitoring, without considering the issue of reconstructing a body model based on arm motion data. The objective of this research is to develop and test machine learning methods aimed at reconstructing body model coordinates using limited data, such as arm position information.

Materials and Methods. To conduct the study, a virtual simulation environment was created in which a virtual avatar performed various movements. These movements were recorded by cameras with a first-person and side view. The positions of the keypoints of the body model relative to the back point were saved as reference data. The regression task considered was to reconstruct the user's arm positions in a full body model in five different variations, including keypoint coordinates extracted from a video and a virtual scene. The task also involved comparing different regression models, including linear models, decision trees, ensembles, and three deep neural networks (DenseNN, CNN-GRU, Transformer). The accuracy was estimated using MAE and the mean Euclidean deviation of body segments. Experimental studies were conducted on five datasets, whose size varied from 25 to 180 thousand frames.

Results. The experiments showed that ensembles (LightGBM) were best-performing in most situations. Among neural network models, the CNN-GRU-based model provided the lowest error. Training models on a sequence of 20 frames did not provide significant improvement. Using the inverse kinematics module on a number of scenarios allowed reducing the error to 3%, but in some cases worsened the final result.

Discussion. The analysis of the results obtained showed low reconstruction accuracy when using computer vision datasets, as well as the lack of superiority of complex models over simpler ensembles and linear models. However, the trained models allowed, with some error, for the reconstruction of the position of the user's legs for a more reliable display of the digital model of his body.

Conclusion. The data obtained showed the complexity of solving the problem of reconstructing a human body model using a limited amount of data, as well as a large error in a number of machine learning models. The comparison of models on different datasets proved low applicability of first-person data that did not contain information on the distance to the arm s. On the other part, using absolute values of arm positions as input information provided for the reconstruction of the body model with significantly less error.

Keywords: reconstruction of the human body model, machine learning, virtual simulators, limited data

Acknowledgements. The authors would like to thank the head of the scientific project, M.N. Krasnyansky, Dr.Sci.(Engineering), Professor, Rector of TSTU for organizing the research process.

Funding Information. The research is done with the financial support from the Ministry of Education and Science of the Russian Federation within the framework of the project "Development of an Immersive Virtual Reality Interaction System for Professional Training Based on an Omnidirectional Platform" (124102100628-3).

For Citation. Obukhov AD, Teselkin DV. Reconstructing a Full-body Model from a Limited Set of Upper-Limb Motion Data. *Advanced Engineering Research (Rostov-on-Don)*. 2025;25(3):221–232. https://doi.org/10.23947/2687-1653-2025-25-3-221-232

Оригинальное эмпирическое исследование

Подход к реконструкции модели тела на основе ограниченного набора данных о двигательной активности рук

А.Д. Обухов ✉, **Д.В. Теселкин**

Тамбовский государственный технический университет, г. Тамбов, Российская Федерация

✉ obuhov.art@gmail.com

Аннотация

Введение. Точная реконструкция модели тела человека крайне важна для визуализации цифровых аватаров в виртуальных тренажерах и реабилитационных системах. Однако использование экзоскелетных систем может привести к перекрытию и экранированию датчиков, что затрудняет работу систем отслеживания. Это подчеркивает актуальность задачи реконструкции модели тела человека на основе ограниченного набора данных о движениях рук, как в сфере реабилитации, так и в спортивной подготовке. Существующие исследования сосредоточены либо на масштабных IMU-сетях, либо на полном видеоконтроле, не рассматривая вопрос реконструкции модели тела на основе данных о движениях рук. Цель данной работы заключается в разработке и тестировании методов машинного обучения, направленных на восстановление координат модели тела с использованием ограниченных данных, например, информации о положении рук.

Материалы и методы. Для проведения исследования была сформирована виртуальная имитационная среда, в которой виртуальный аватар выполнял различные движения. Эти движения фиксировались камерами с видом от первого лица и боковой. В качестве эталонных данных сохранялись положения ключевых точек модели тела относительно точки спины. Рассматривалась задача регрессии, целью которой было восстановление положения рук пользователя в полной модели его тела в пяти различных вариациях, включающих координаты ключевых точек, извлеченные из видео и виртуальной сцены. Задача также подразумевала сравнение различных моделей регрессии, среди которых были линейные модели, деревья решений, ансамбли, а также три глубокие нейронные сети (DenseNN, CNN-GRU, Transformer). Точность оценивалась с использованием MAE и среднего Евклидова отклонения сегментов тела. Проведены экспериментальные исследования на пяти наборах данных, размер которых варьировался от 25 до 180 тысяч кадров.

Результаты исследования. Эксперименты показали, что ансамбли (LightGBM) наиболее эффективны в большинстве ситуаций. Среди нейросетевых моделей наименьшую погрешность обеспечила модель на базе CNN-GRU. Обучение моделей на последовательности из 20 кадров не дало значительного улучшения. Применение модуля инверсной кинематики на ряде сценариев позволяет снизить погрешность до 3 %, но в ряде случаев ухудшает итоговый результат.

Обсуждение. Анализ полученных результатов показал низкую точность реконструкции при использовании наборов данных от компьютерного зрения, а также отсутствие превосходства сложных моделей перед более простыми ансамблями и линейными моделями. Тем не менее, обученные модели позволяют с некоторой погрешностью восстанавливать положение ног пользователя для более достоверного отображения цифровой модели его тела.

Заключение. Полученные данные показывают сложность решения задачи реконструкции модели тела человека при использовании ограниченного объема данных, а также большую погрешность у ряда моделей машинного обучения. Сравнение моделей на различных наборах данных показало низкую применимость данных от первого лица, не содержащих информацию о расстоянии до рук. С другой стороны, использование в качестве входной информации абсолютных значений положения рук позволяет осуществить реконструкцию модели тела со значительно меньшей погрешностью.

Ключевые слова: реконструкция модели тела человека, машинное обучение, виртуальные тренажеры, ограниченные данные

Благодарности. Авторы благодарят руководителя научного проекта М.Н. Краснянского, доктора технических наук, профессора, ректора Тамбовского государственного технического университета за организацию научно-исследовательского процесса.

Финансирование. Работа выполнена при финансовой поддержке Министерства науки и высшего образования РФ в рамках проекта «Разработка иммерсивной системы взаимодействия с виртуальной реальностью для профессиональной подготовки на основе всенаправленной платформы» (124102100628-3).

Для цитирования. Обухов А.Д., Теселкин Д.В. Подход к реконструкции модели тела на основе ограниченного набора данных о двигательной активности рук. *Advanced Engineering Research (Rostov-on-Don).* 2025;25(3):221–232. https://doi.org/10.23947/2687-1653-2025-25-3-221-232

Introduction. Virtual simulators integrated with controlled exoskeletons allow simulating physical activity and rehabilitation exercises in a controlled environment [1]. To achieve the maximum immersion effect, precise tracking of the user's entire body kinematics is required to form a virtual avatar that corresponds to real human movements. However, upper exoskeletons can block sensors that demand direct visual control (e.g., HTC Vive Tracker), as well as create electromagnetic interference and limit the view of external cameras, which requires the use of additional markers [2]. In these cases, traditional tracking systems, such as infrared markers and multiple capture cameras, cannot consistently provide a complete set of position data for all body segments [3]. Thus, researchers are faced with the task of reconstructing a full body model based on limited information, such as arm or hand position data.

One of the possible solutions is to use wearable sensors such as inertial measurement units (IMU). However, a sufficient number of sensors (at least 11, and often up to 18 elements) are required to fully reconstruct the body model [4]. As the number of sensors reduces, the accuracy of the data decreases sharply. At the same time, computer vision technologies are actively developing and are increasingly used in virtual reality systems to track hands and fingers, which makes the task of reconstructing a body model from limited data obtained only from the user's hands particularly topical [5].

The task of reconstructing a full human skeletal model from a limited set of visual data (e.g., arm movements) has a considerable practical and scientific value. Classic marker-based motion capture systems used infrared cameras and joint markers, while computer vision-based algorithms are being developed and successfully implemented for markerless solutions. Modern convolutional neural networks, such as OpenPose, BlazePose, and MediaPipe Pose, are capable of detecting 2D positions of body keypoints without additional labels [6]. These methods effectively detect visible points (arms, shoulders, pelvis, etc.), but without depth information from a single camera, the distance to the body is not restored, which complicates the full 3D reconstruction of the body model. A solution to this problem can be found by means of stereo cameras and triangulation methods [7]. Using such approaches, modern models (e.g., MediaPipe Pose) can track up to 33 keypoints with an error of about 1–2 cm. Under real conditions, that allows obtaining 3D coordinates of major joints (e.g., hands, elbows, knees) through combining data from several cameras and minimizing projection error. However, such tracking systems often prove unsuitable if the cameras only see the hands, and it is necessary to estimate the rest of the skeleton based on the movements of the hands without direct visual control. This is a hot issue in virtual reality systems, where cameras are present only on the headset and record only the user's hands in the working area. In this regard, it is required to consider existing approaches to solving this problem.

The main area of work on this task involves the use of regression-based methods or neural networks that are able to complement the pose relying only on partial data [4]. For example, regression models trained on video pairs with partially masked bodies and arms can reconstruct missing body parts under complex conditions [8, 9]. This indicates that modern models are indeed able to display full body pose from partial visual information about the arms. Other studies use neural network architectures that focus on motion sequences, such as recurrent networks (LSTM/GRU) and specifically Transformer [10, 11]. For example, paper [12] describes AvatarPoser, a Transformer-based model that predicts a full 3D pose of the body (including legs and torso) from the position of the head and arms. This system extracts deep features from incoming motion signals and separates global body movement and local joint orientations. For accurate pose matching, limb optimization is also performed by the inverse kinematics method [12]. Furthermore, the idea of improving the robustness of predictions in the absence of visibility is implemented in the EgoPoser model, which also relies on the Transformer mechanisms to account for intermittent arm motion data, ensuring stable predictions [13]. It is worth noting that training these models requires marking full poses, which leads to the need to use large datasets, such as Human3.6M, CMU MoCap/AMASS, MPI-INF-3DHP and others, where there is synchronized video and a 3D skeleton [14, 15]. However, existing datasets that compare the first-person view with a full body model are insufficient, which makes the task of collecting and comparing such data hot issues. The formation of such a dataset can be organized by recreating human movements in a virtual scene, where you can flexibly adjust the position of virtual cameras for recording video, and obtain accurate coordinates of body points with the required frequency [4].

In this study, the main subject for the implementation of the obtained scientific results is a virtual simulator system based on an upper controlled exoskeleton. Modern models of VR-headsets are focused on positioning by cameras, assuming that the main source of information on arm movement comes from the built-in headset camera used to recognize arms. In addition, to expand the experimental base and identify patterns in human movements, it is assumed that there is an external frame-by-frame capture system that records the user's body position as a whole. The objective of this research is to develop and test machine learning methods for reconstructing body coordinates based on partial arm position data. In conclusion of the study, it is planned to compare both classical regression models and neural network models, including modern architectures based on attention mechanisms, which will allow us to evaluate the advantages of each approach in various experimental scenarios.

Materials and Methods. First, the procedure for collecting and primary processing the data was considered. The data was collected in a virtual environment, where the process of using a VR-headset with a camera was imitated. All data (first-person view, side camera view) were tracked by virtual cameras. Then, the videos were processed by MediaPipe library models, which allowed for hand detection to isolate 21 keypoints of the palm, as well as extracting data on 33 key points of the body model from the side virtual camera. In parallel, the true metric coordinates of all body segments (18 key points of the standard digital avatar model specified in the Unity game engine), including hand position points, were recorded in the virtual space. These real coordinates (reference) formed the target Y set for most scenarios. Using a virtual camera made it possible to bypass the limitations of physical sensors and obtain reference information about the body pose. MediaPipe was selected as the main hand tracking framework due to its modular processing graph system and ready-made ML models (palm detector and full body model). We introduced the abbreviation "CV" for the data obtained during processing by computer vision and MediaPipe models (denoted as cx_i, cy_i, cz_i), and the "reference" was understood as the metric coordinates of body points (denoted as vx_i, vy_i, vz_i), recorded in the virtual scene relative to the user's back.

Next, we considered the data preparation procedure for various regression scenarios. To analyze the machine learning models and their capabilities, 5 datasets (experiments) were formed, differing in which features X were used and which target variables Y were predicted:

1) Set 1 "Arms (first-person view) → Arms (reference)": $X = \{(cx_i, cy_i, cz_i)\} \in \mathbb{R}^{63}$, $i = 1$–21 — coordinates of keypoints of arms in FPV (63 values), $Y = \{(vx_i, vy_i, vz_i)\} \in \mathbb{R}^{18}$, $i = 1$–6 – metric coordinates of the same points of arms (18 values).

2) Set 2 "Arms (first-person view) → Body (reference)": $X = \{(cx_i, cy_i, cz_i)\} \in \mathbb{R}^{63}$, $i = 1$–21 – coordinates of the arms (obtained from FPV, 63 values), $Y = \{(vx_i, vy_i, vz_i)\} \in \mathbb{R}^{54}$, $i = 1$–18 — metric coordinates of all points of the body (54 values). This way, a complete reconstruction of the body is performed on the basis of the arms data.

3) Set 3 "Arms (first person view) → Body (CV)": $X = \{(cx_i, cy_i, cz_i)\} \in \mathbb{R}^{63}$, $i = 1$–21 – coordinates of arms (FPV based on CV, 63 values), $Y = \{(vx_i, vy_i, vz_i)\} \in \mathbb{R}^{99}$, $i = 1$–33 — coordinates of 33 body points from an additional side view video (99 values). It differs from the previous task in that regressions are performed exclusively on CV data.

4) Set 4 "Body (CV) → Body (reference)": $X = \{(cx_i, cy_i, cz_i)\} \in \mathbb{R}^{99}$, $i = 1$–33 — coordinates of body points (side camera view, 99 values), $Y = \{(vx_i, vy_i, vz_i)\} \in \mathbb{R}^{54}$, $i = 1$–18 — metric coordinates of all body points (54 values). The task is to check the accuracy of direct data conversion from CV to metric values of 18 keypoints.

5) Set 5 "Arms (reference) → Body (reference)": $X = \{(vx_i, vy_i, vz_i)\} \in \mathbb{R}^{18}$, $i = 1$–6 — metric coordinates of arm points (18 values), $Y = \{(vx_i, vy_i, vz_i)\} \in \mathbb{R}^{54}$, $i = 1$–18 — metric coordinates of the entire body (54 values). It differs from set 2 in that only reference data are used. Thus, the very fact of reconstructing movement based on a limited set of points is verified.

Next, we consider the models used to solve the five regression problems mentioned above. The architectures of all the models in different problems are similar; the differences for each set are only in the input and output dimensions. In total, two classes of models are considered: classic regression models from the Scikit-Learn library (as well as XGBoost and LightGBM models) and neural network models based on the Keras framework [16, 17].

Classical models include: LinearRegression, ElasticNet (with L1/L2 regularization), ensembles of trees (RandomForestRegressor, HistGradientBoostingRegressor), boosting (XGBRegressor, LightGBMRegressor), and KNN regressor. Since the target variable includes multiple outputs (point coordinates), the models are wrapped in a MultiOutputRegressor, which allows predicting all parameters simultaneously. All tree-type models are configured with 100 trees and a depth of 5, while boosted models have learning_rate = 0.05.

Next, we consider neural network architectures.

A Fully Connected Network (we denote it as DenseNN). The input layer corresponds to the feature dimension X (from now on, it depends on the dataset), followed by 4 fully connected layers: 256, 512, 1024, and 128 neurons with ReLU activation and Dropout sparsification layers (25%). The model ends with an output layer of dimension Y (also depends on the dataset). Batch normalization (BatchNorm) and the Adam optimizer (lr = 1e–3) with the MSE loss function are used.

Convolutional Recurrent Network (CNN-GRU). After the input layer, 1D convolution (128 filters, kernel = 3) and BatchNormalization are applied. This is followed by a GRU layer (128 units) with sequence return. The attention mechanism is implemented: a dense layer with tanh activation above the GRU output produces frame weights, which are then multiplied with the GRU output using softmax and summed. Then there is a fully connected layer of 128 neurons with activation of ReLU and Dropout (30%), after which the output layer comes. Adam optimizer (lr = 1e–3) with MSE loss function.

Transformer. First, several 1D convolutions (kernel = 3, dilation_rate 1, 2 and 4) are applied to create local context. Then, a Squeeze-and-Excite layer is added for adaptive filtering of channels [18]. Furthermore, trainable positional embeddings and 3 encoder blocks of the transformer are introduced, each implementing MultiHeadAttention (4 heads, key in 64/4 size), subsequent summation and normalization, and then — a two-layer dense network (size 256, 64) with Dropout — again summation and normalization. After the encoders, GlobalAveragePooling1D is performed, then — a fully connected layer of 128 neurons with ReLU activation and Dropout (25%), followed by a linear output. Adam optimizer (*lr* = 1e–3) with MSE loss function.

Based on the conducted review and the existing experience in this area, we can propose an approach to solving the regression problems under consideration. A dataset of animation of typical human movements is formed, which is applied to a virtual avatar in a simulation scene. The movements are recorded using several virtual cameras: one of them is located at the avatar's eye level (FPV), and the second watches it from the side (side camera), covering its entire height. Additionally, metric values of 18 points of the body model are recorded. The final data view for each source is shown in Figure 1.

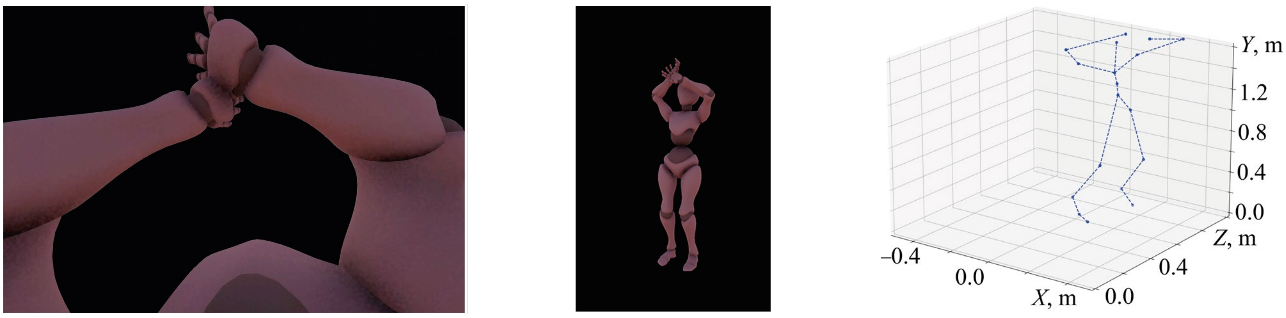

a) *b)* *c)*

Fig. 1. Source data: *a* — frame from first-person camera; *b* — frame from side camera; *c* — skeleton constructed using reference data

Video data is processed by the corresponding models (MediaPipe Pose/Hands), after which the point coordinates are saved in arrays. Then, within the framework of the proposed approach, machine learning models are trained, which, based on the initial data alone (e.g., information about the arms), form a complete 3D configuration of the body. After predicting the pose, the elbow and knee joints can be further adjusted so that the segment lengths and limb positions better match the arm signatures. Also, to assess the contribution of the temporal context to the accuracy of the reconstruction problem, it is proposed to conduct an additional experiment to solve the regression problem for each set not based on the data of one frame, but on a certain sequence of N-frames.

In this paper, there is no focus on correcting the body model after reconstruction according to the inverse kinematics rules. The major objective is to train and compare a set of regressors (linear, tree-type, KNN models) and neural networks (DenseNN, CNN-GRU and Transformer) to determine the most accurate model. The selection is based on the metrics of the mean absolute error (MAE), the total deviation (Euclidean distance) for all points of the model from the reference ones, as well as on assessing the computational complexity (prediction time). This solves the problem of reconstructing a body model based on a limited set of information about arm movements. In addition, other regression options are considered within the experimental section. The calculation is made using the following formulas:

$$MAE = \frac{1}{N}\sum_{i=1}^{N} |y_i - \hat{y}_i|,$$

$$\Delta = \frac{1}{MJ}\sum_{n=1}^{M}\sum_{j=1}^{J} \| y_{n,j} - \hat{y}_{n,j} \|, \quad \| v \| = \sqrt{v_x^2 + v_y^2 + v_z^2},$$

where y_i — true value; $\hat{y}_i$ — model prediction, N — number of compared values, M — number of frames; J — number of joints (keypoints), $y_{n,j}, \hat{y}_i \in \mathbb{R}^3$ — true and predicted 3-D position vector of j-th joint in n-th frame.

Research Results. In accordance with the described methodology, data was collected on 11 types of various complex animations, including body movements, jumps and active movements. Nine types were used for training, and two — for validation (data from them were not used in the training process). The total volume was 239968 records, but at each stage, filtering and selection of records was performed in the event that one of the sources did not return correct values (most often, this involved obtaining arm coordinates using computer vision). Thus, for sets 1–3, 25 and 8 thousand records were selected for training and validation, for sets 4 and 5 — 183 and 56 thousand, respectively. During the learning process, the training sample was further divided in the ratio 75/25. The dimension of the data for each experiment was indicated above when describing the corresponding sets. Figure 2 shows the comparative results of all models for all data sets using the MAE metric. Figure 3 shows the total deviation metric. And Figure 4 shows a comparison of models based on the calculation time of one forecast. Next, we compare the results obtained.

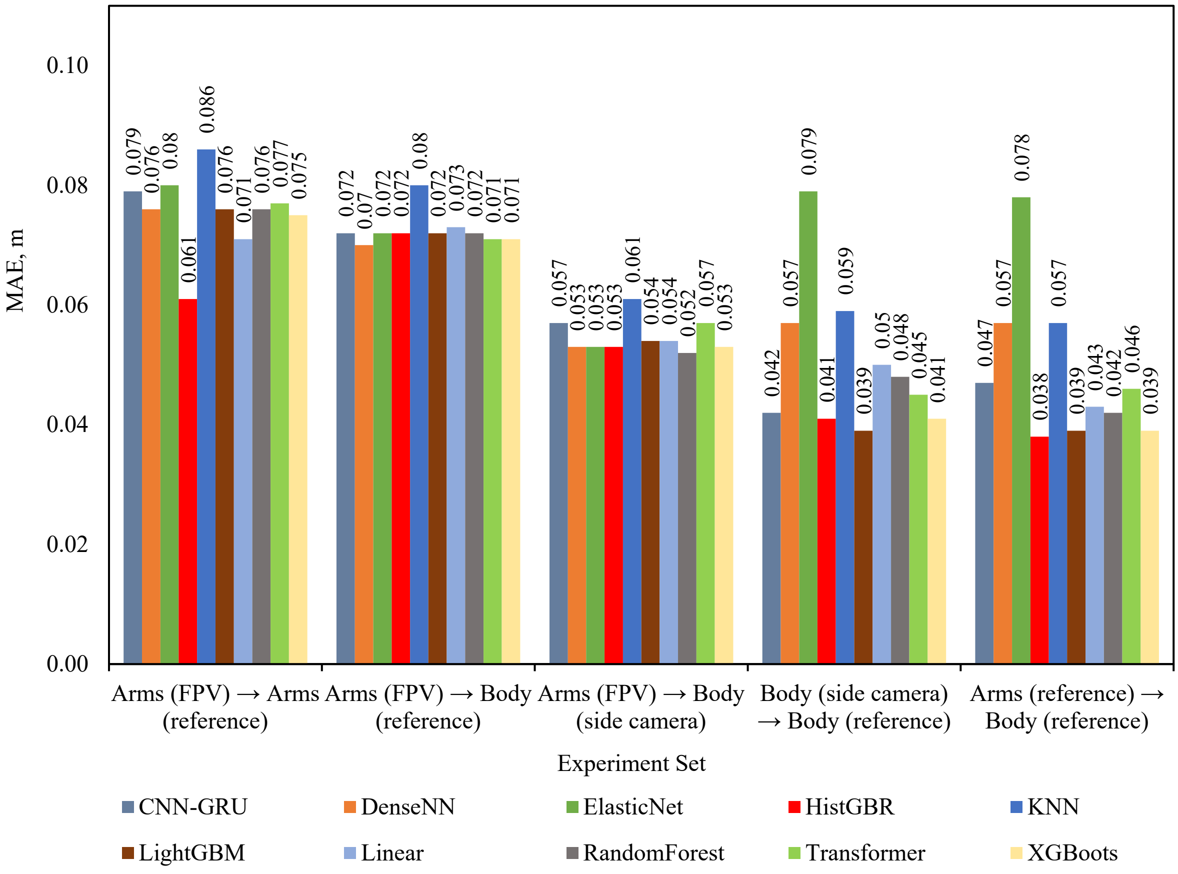

Fig. 2. Comparison of models by MAE metric

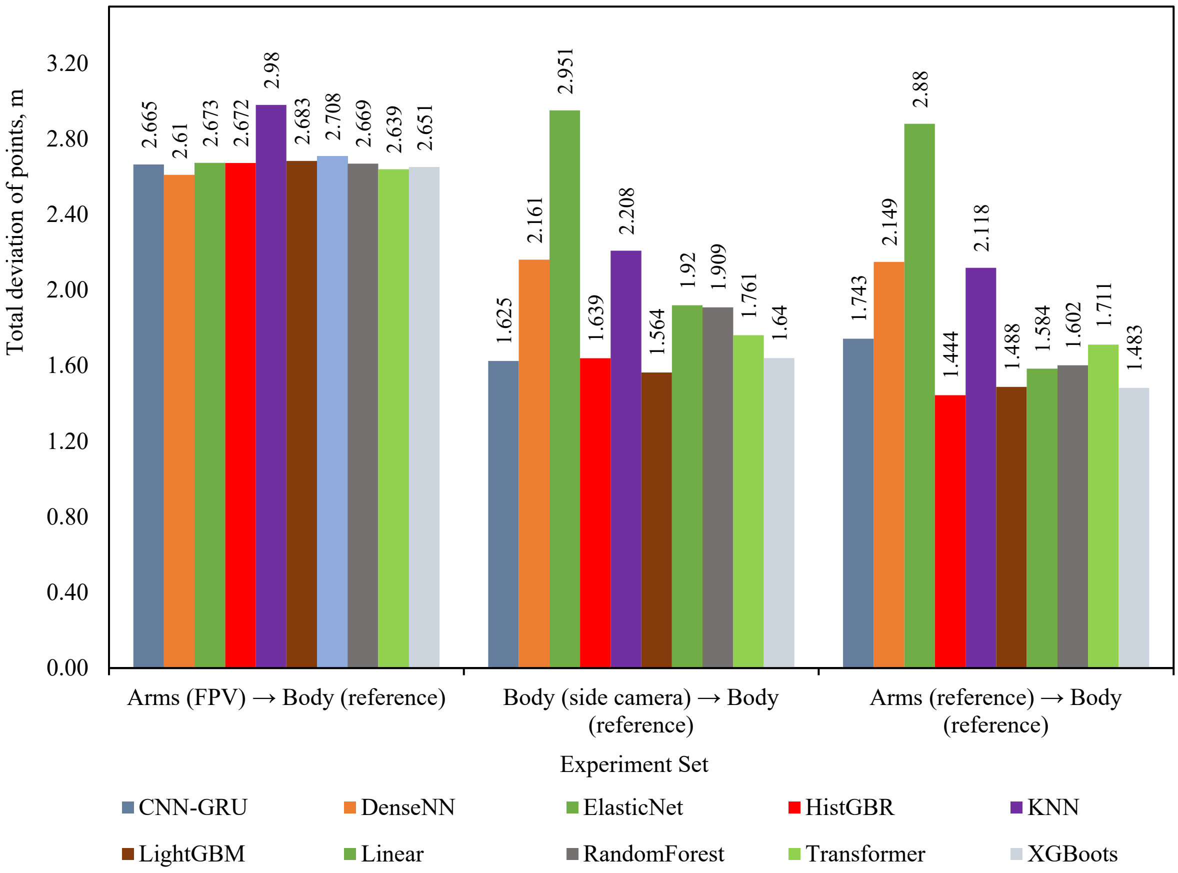

Fig. 3. Comparison of models by total deviation

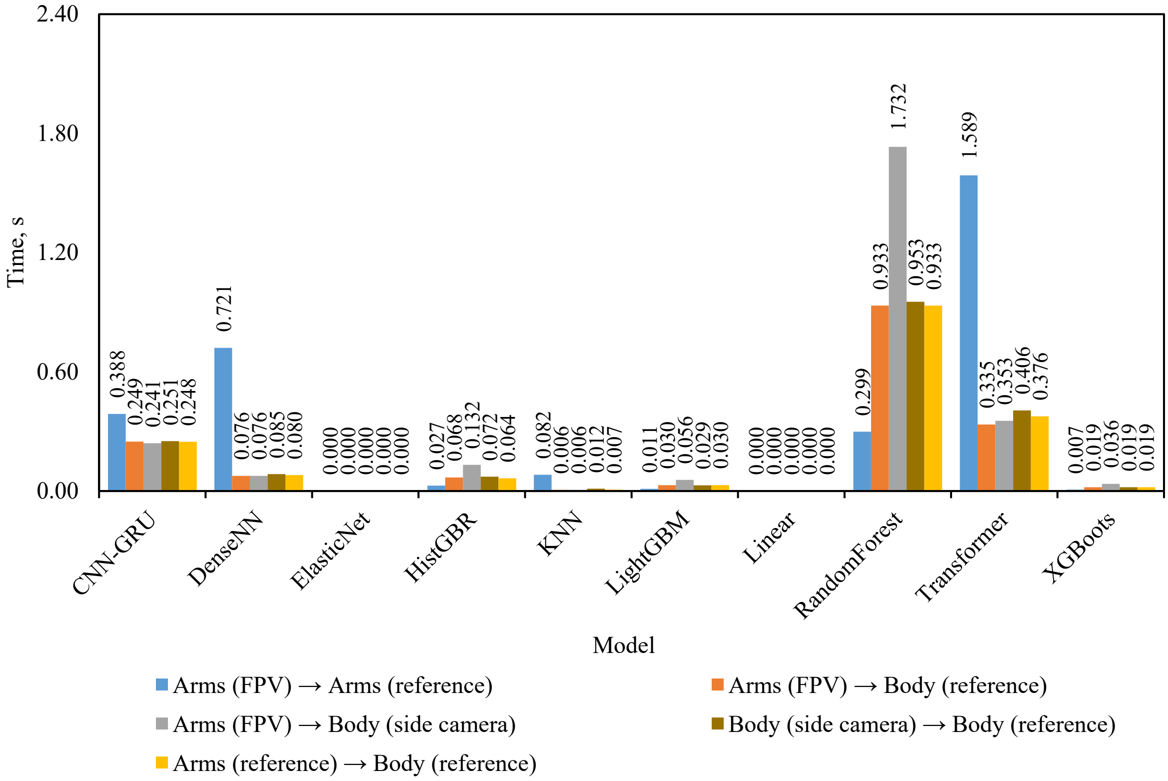

Fig. 4. Comparison of models by performance

The analysis of the data obtained shows the heterogeneity of the behavior of the models when changing the source of input information and on various metrics. In most scenarios, gradient ensembles (HistGBR, LightGBM, XGBoost, and randomForest) demonstrate the lowest MAE error. Neural network models perform worse, especially when complex tasks of reconstructing a body based on arm data (CV) are considered. Nevertheless, if we evaluate all models according to MAE, then it is not possible to single out a clear leader. On the other hand, the total deviation of all points (Fig. 3) clarifies significantly the situation when solving three regression problems. Ensembles are superior, as in the previous case, but CNN-GRU is the best among neural network models. The obtained values of the total deviation, ranging from 1.4 to 3.5 meters, indicate low efficiency of solving the regression problem by all models, especially on the set of "Arms (FPV) → Body (reference)". When evaluating the performance of models by computation time, it can be noted that classical machine learning models (linear and ensembles) have sufficient performance for real-time use. At the same time, CNN-GRU, Transformer and specifically Random Forest, are extremely computation-consuming, which makes them applicable only in offline (not real-time) systems. For DenseNN, long calculations are often observed at the first call of the model.

Given our experience in body reconstruction tasks, it is important to evaluate models not only by the specified metrics, but also visually. For this purpose, we reconstruct body skeletons for sets 2, 4, and 5 using the LightGBM and CNN-GRU models. This comparison (Fig. 5) allows us to evaluate how the most accurate architecture (LightGBM) differs visually from the more complex one (CNN-GRU).

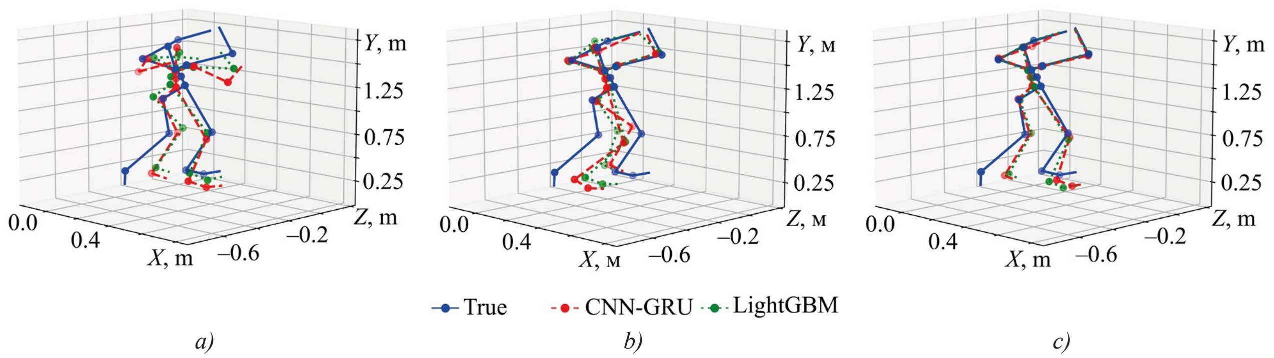

Fig. 5. Visual comparison of CNN-GRU and LightGBM models:
a — on the set "Arms (FPV) → Body (reference)"; *b* — on the set
"Body (CV) → Body (reference)"; *c* — on the set "Arms (reference) → Body (reference)"

Visual comparison shows that there is a noticeable difference between the CV data and the real position, since the first-person camera is not able to accurately determine the real depth and distance to the arms. This results in an approximate position of the upper body (first graph — Fig. 5). When using the full-body CV data, there is also a significant error, although the pose matches to some extent. The third set, based on the arms from the reference (which can be obtained by extracting coordinates from the VR controllers or absolute position sensors), shows that the upper body is reconstructed quite accurately, while the legs are only approximately reconstructed, with a large error. Thus, for all three sets and both models, we can talk only about an approximate reconstruction, which generally corresponds to the results of the total deviation metrics in Figure 3.

Next, an experiment was conducted to train the listed models not on a single frame, but on a sequence of 20 frames. This allowed us to identify some dynamic characteristics and increase the volume of initial information. As a visual comparison showed, since the determining metric was the total deviation, we considered only it (Fig. 6). In general, the use of a frame sequence slightly reduced the total deviation; some models showed even worse results. From a visual point of view (Fig. 7), there was a certain improvement for the LightGBM model, where the reconstruction quality increased significantly, even when reconstructing the body based on arm data (FPV). This also concerned the other two datasets. However, for the neural network model as a whole, no significant improvements were found.

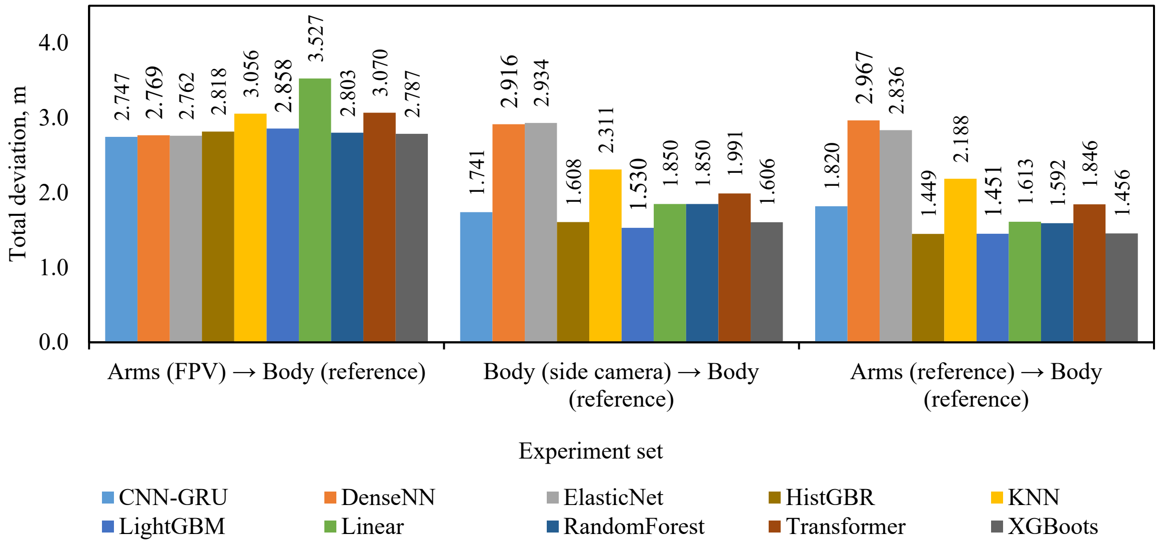

Fig. 6. Comparison of models by total deviation
(trained on a sequence of frames)

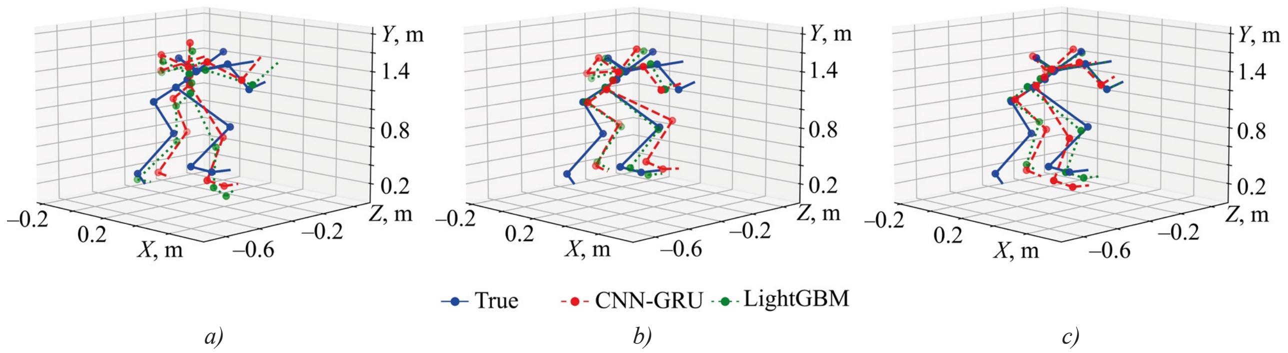

Fig. 7. Visual comparison of CNN-GRU and LightGBM models (trained on a sequence of frames):
a — on set "Arms (FPV) → Body (reference)"; *b* — on set "Body (CV) → Body (reference)";
c — on set "Arms (reference) → Body (reference)".

At the end of the experiment, a test was conducted on the implementation of point correction based on the inverse kinematics (IK) model. For this, after predicting body points using machine learning models, the developed IK module was used, which first corrected the end links (hands and feet) using the FABRIK method [19, 20], taking into account the angular limitations of the elbows and knees. Then, the module redistributed the resulting displacements between the pelvis and the thoracic region, automatically aligning the spinal axis. The results of this module are presented in Figure 8.

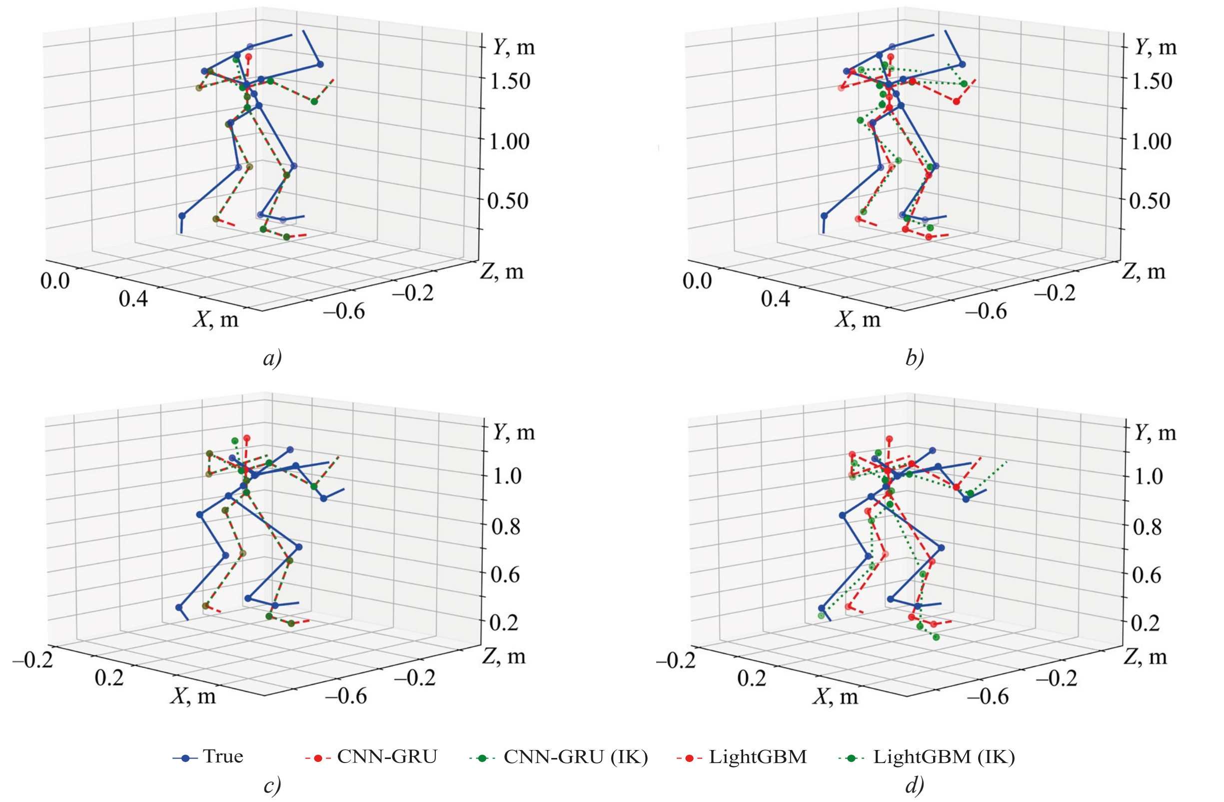

Fig. 8. Visual comparison of models with and without inverse kinematics correction (indicating total deviation before and after correction) on “Arms (FPV) → Body (reference)” dataset: *a* — CNN-GRU (before = 3.511, after = 3.436 m); *b* — LightGBM (before = 3.183, after = 3.112 m); *c* — CNN-GRU on a sequence of frames (before = 2.952, after = 2.991 m); *d* — LightGBM on a sequence of frames (before = 3.261, after = 3.306 m)

The resulting visualizations and numerical evaluations demonstrate that the implementation of the proposed two-pass inverse kinematics generally reduces the total Euclidean deviation of joints from the reference for single frames, but the effect varies depending on the model type and body position. In the first experiment, for the CNN-GRU model, the total deviation decreased from 3.511 to 3.436 meters, and for LightGBM — from 3.183 to 3.112 meters, which corresponded to an improvement of about 2–3%. Graphically, this is manifested in a more natural head alignment and a reduction in the “bends” in the elbows and knees. A different picture is observed in the second experiment, based on 20 frames and a different animation: for CNN-GRU, the error increased from 2.952 to 2.991 meters, and for LightGBM — from 3.261 to 3.306 meters. It is noted that the correction procedure tends to straighten the skeleton, which in this case only worsens the situation. This indicates that geometric constraints applied post factum can improve static anatomical plausibility, but in complex animations, worsen the current pose.

Discussion. The conducted research has revealed several patterns. First, reconstructing a full body model from a limited dataset is possible, especially, when the input and output data are from the same source. This was evidenced by the high-quality reconstruction of the body model based on the arm position. However, significant problems were identified in reconstructing the user's leg position, as there was insufficient information about arm movements to predict complex animation. Third, using arm positions from a first-person video stream obtained through computer vision to reconstruct a full body model resulted in high errors due to the lack of distance data to the arms, having only their position relative to the user's eyes. Pre-processing of data simulated in a virtual environment also showed difficulties in recognizing arms in complex animations, which negatively affected the learning process.

When comparing different machine learning architectures for this task, it is worth noting that simpler linear models show good results in predicting the position of body segments, since there are clear dependences between the input and output data that can be approximated by these models. Complex neural network models also solve a similar problem, showing greater flexibility in working with complex input data, but they are not characterized by high performance, and the process of their training is expensive. In a visual comparison, neural network models did not show high efficiency, demonstrating results comparable or even worse.

The experiment shows that the use of a data source with a very limited information value (information about the position of the arms from the computer vision system is just such a source) causes a significant error in solving the regression problem. Firstly, the tracking object often goes out of sight and is not recognized by the model (this is clearly seen in the reduction in the volume of training data in sets 1 and 2). Secondly, the lack of correct data about the depth, i.e., the distance to the arms, complicates their absolute positioning. In VR systems, this aspect is mitigated by triangulation using data from multiple cameras, but in the simulations conducted, the neural network model for arm recognition did not reflect the correct coordinates along Z axis. A potential solution to the problem and the topic of further research could be obtaining data directly from VR-headsets equipped with integrated cameras. This would expand the training set with natural motion data and provide better quality arm capture in the virtual frame, as the headset's capture system could return metric space coordinates to the digital model, providing a type 5 set (“Arms (reference) → Body (reference)”).

When analyzing the topicality of the study within the subject area, it should be compared to existing works. The main difference is the limitation on the use of arm movement data, since a more accurate approach is considered to be the use of at least 5 body points for further reconstruction [21]. This is proved by our previous studies [4], in which the optimal number of points for reconstruction is indicated as at least 5–7, obtained using a reference tracking system.

It is important to note that many VR applications and games implement a tracking system based only on controllers and a headset, followed by reconstruction of a simplified body position using IK algorithms, which allows the arm movements to be extended to the entire body. As the authors [21] emphasize, in such systems, the same readings from sensors located on the arms can correspond to numerous different full poses. This points to the need for additional tuning of inverse kinematics to avoid artifacts, and trained models should select a plausible option. Therefore, the complexity of the task without additional sources of information about the position of the legs or torso remains high. The conducted study highlights this problem, indicating the need to search for and collect additional sources of information to achieve, at a minimum, the mapping of “Arms (reference) → Body (reference)”, and ideally — to recognize the entire trajectory of movement, which will help to more accurately predict the position of other body parts. A promising direction here may be the use of not only pre-trained neural networks (e.g., MediaPipe), but also the capture of all information about the surrounding world, which will allow for better segmentation of the user's arms, and perhaps, the torso and legs.

Another limitation of the study is the lack of an assessment of the impact of the training sample size on the quality of the models. In this paper, data from 11 different animation types were collected, two additional types were used for validation, but given the volumes and variability of movements, the set should be significantly larger. However, the study aimed at comparing models within a given task, which demonstrated the ambiguity of their efficiency compared to classic linear models and ensembles. This also indicates the need for further improvement of the model architecture.

Finally, the stage of body model correction based on the kinematic model, implemented through the imposition of anatomical constraints and re-evaluation of the pose, gave ambiguous results — in one pose, it reduced the total deviation, and in another, on the contrary, it increased it. On the other hand, it should be taken into account that the IK module should work with already distorted data on the arms and head in the case of set 1. Therefore, the transition to a higher-quality dataset can reduce the error in the kinematics module.

Conclusion. Thus, as a result of the conducted research, an approach to predicting the body model based on a limited set of points was developed, including the stages of data processing, solving regression problems and using the IK module to correct the body model. The corresponding experimental studies were conducted, which showed that LightGBM-type models (among ensembles) and CNN-GRU with an attention mechanism (among neural network models) demonstrated the best results for the selected metrics. The comparison also showed low accuracy of the body model reconstruction when using models (ElasticNet, KNN, DenseNN), which indicated their weak generalization ability. During the visual comparison, contradictions were revealed in the quality of skeleton reconstruction when performing complex animation, since the position of the arms was insufficient to determine the position of the legs and head. In addition, the use of correction based on inverse kinematics is not always justified for complex poses, since the imposition of anatomical constraints and overestimation of the pose can cause additional distortions.

Comparison of the developed models also allows us to draw conclusions about the degree of their applicability: models trained on a first-person data set do not provide reliable reconstruction of the body model, showing a high visual error, which limits their use to only theoretical comparison; while models trained on real arm positions (set 5) show more reliable predictions of body position, which may be in demand in virtual simulators without a sufficient set of sensors. Since the models trained on set 5 work with absolute arm positions, this provides their versatility when selecting a tracking system, because arm position data can be obtained not only using a computer vision system, but also virtual reality controllers or inertial sensors that track arm position.

This study forms several directions for further research within the framework of the body model reconstruction task. The conducted comparative experiments of machine learning models have shown that in order to successfully solve the task, it is required to collect more information about human movements, expand the dataset, and implement more effective learning models with greater generalization ability.

References

1. Tiboni M, Borboni A, Vérité F, Bregoli Ch, Amici C. Sensors and Actuation Technologies in Exoskeletons: A Review. *Sensors*. 2022;22(3):884. https://doi.org/10.3390/s22030884

2. Vélez-Guerrero MA, Callejas-Cuervo M, Mazzoleni S. Artificial Intelligence-Based Wearable Robotic Exoskeletons for Upper Limb Rehabilitation: A Review. *Sensors*. 2021;21(6):2146. https://doi.org/10.3390/s21062146

3. Zihe Zhao, Jiaqi Wang, Shengbo Wang, Rui Wang, Yao Lu, Yan Yuan, et al. Multimodal Sensing in Stroke Motor Rehabilitation. *Advanced Sensor Research*. 2023;2(9):2200055. https://doi.org/10.1002/adsr.202200055

4. Obukhov A, Dedov D, Volkov A, Teselkin D. Modeling of Nonlinear Dynamic Processes of Human Movement in Virtual Reality Based on Digital Shadows. *Computation*. 2023;11(5):85. https://doi.org/10.3390/computation11050085

5. Kuan Cha, Jinying Wang, Yan Li, Longbin Shen, Zhuoming Chen, Jinyi Long. A Novel Upper-Limb Tracking System in a Virtual Environment for Stroke Rehabilitation. *Journal of NeuroEngineering and Rehabilitation*. 2021;18:166. https://doi.org/10.1186/s12984-021-00957-6

6. Jen-Li Chung, Lee-Yeng Ong, Meng-Chew Leow. Comparative Analysis of Skeleton-Based Human Pose Estimation. *Future Internet*. 2022;14(12):380. https://doi.org/10.3390/fi14120380

7. Obukhov AD, Dedov DL, Surkova EO, Korobova IL. 3D Human Motion Capture Method Based on Computer Vision. *Advanced Engineering Research (Rostov-on-Don)*. 2023;23(3):317–328. https://doi.org/10.23947/2687-1653-2023-23-3-317-328

8. Islam MdM, Nooruddin Sh, Karray F, Muhammad G. Human Activity Recognition Using Tools of Convolutional Neural Networks: A State-of-the-Art Review, Data Sets, Challenges, and Future Prospects. *Computers in Biology and Medicine*. 2022;149:106060. https://doi.org/10.1016/j.compbiomed.2022.106060

9. Obukhov A, Dedov D, Volkov A, Rybachok M. Technology for Improving the Accuracy of Predicting the Position and Speed of Human Movement Based on Machine-Learning Models. *Technologies*. 2025;13(3):101. https://doi.org/10.3390/technologies13030101

10. Titarenko DYu, Ryzhkova MN. Possible Neural-Network Use for Error Recognition during Physical Exercising. *Radio Engineering and Telecommunications Systems*. 2024;(3):62–72. https://doi.org/10.24412/2221-2574-2024-3-62-72

11. Hung Le Viet, Han Le Hoang Ngoc, Khoa Tran Dinh Minh, Son Than Van Hong. A Deep Learning Framework for Gym-Gesture Recognition Using the Combination of Transformer and 3D Pose Estimation. *Cybernetics and Physics*. 2024;13(2):161–167. https://doi.org/10.35470/2226-4116-2024-13-2-161-167

12. Jiaxi Jiang, Paul Streli, Huajian Qiu, Andreas Fender, Larissa Laich, Patrick Snape, et al. AvatarPoser: Articulated Full-Body Pose Tracking from Sparse Motion Sensing. In book: Avidan S, Brostow G, Cissé M, Farinella GM, Hassner T (eds). *Computer Vision — ECCV 2022*. Cham: Springer; 2022. P. 443–460. https://doi.org/10.1007/978-3-031-20065-6_26

13. Jiaxi Jiang, Paul Streli, Manuel Meier, Christian Holz. EgoPoser: Robust Real-Time Egocentric Pose Estimation from Sparse and Intermittent Observations Everywhere. In book: Leonardis A, Ricci E, Roth S, Russakovsky O, Sattler T, Varol G (eds). *Computer Vision — ECCV 2024*. Cham: Springer; 2024. P. 277–294. https://doi.org/10.1007/978-3-031-72627-9_16

14. Baradel F, Groueix Th, Weinzaepfel Ph, Brégier R, Kalantidis Y, Roges G. Leveraging MoCap Data for Human Mesh Recovery. In: *Proc. IEEE/CVF Conference on 3D Vision (3DV)*. New York City: IEEE; 2021. P. 586–595. https://doi.org/10.1109/3DV53792.2021.00068

15. Seong Hyun Kim, Sunwon Jeong, Sungbum Park, Ju Yong Chang. Camera Motion Agnostic Method for Estimating 3D Human Poses. *Sensors*. 2022;22(20):7975. https://doi.org/10.3390/s22207975

16. Kumar S, Srivastava M, Prakash V. Advanced Hybrid Prediction Model: Optimizing LightGBM, XGBoost, Lasso Regression and Random Forest with Bayesian Optimization. *Journal of Theoretical and Applied Information Technology*. 2024;102(9):4103–4115. URL: https://jatit.org/volumes/Vol102No9/32Vol102No9.pdf (дата обращения: 01.06.2025).

17. Nidhi Dua, Shiva Nand Singh, Vijay Bhaskar Semwal. Multi-Input CNN-GRU Based Human Activity Recognition Using Wearable Sensors. *Computing*. 2021;103(7):1461–1478. https://doi.org/10.1007/s00607-021-00928-8

18. Vosco N, Shenkler A, Grobman M. Tiled Squeeze-and-Excite: Channel Attention with Local Spatial Context. In: *Proc. IEEE/CVF International Conference on Computer Vision Workshops*. New York City: IEEE; 2021. P. 345–353. https://doi.org/10.1109/ICCVW54120.2021.00043

19. Kolpashchikov DYu, Gerget OM, Danilov VV. FABRIK-Based Comparison of the Inverse Kinematic Algorithms Operation Results for Multi-Section Continuum Robots. *BMSTU Journal of Mechanical Engineering*. 2022;753(12):34–45. https://doi.org/10.18698/0536-1044-2022-12-34-45

20. Lamb M, Lee S, Billing E, Högberg D, Yang J. Forward and Backward Reaching Inverse Kinematics (FABRIK) Solver for DHM: A Pilot Study. In: *Proc. 7th International Digital Human Modeling Symposium*. 2022;7(1):26. https://doi.org/10.17077/dhm.31772

21. Qiang Zeng, Gang Zheng, Qian Liu. DTP: Learning to Estimate Full-Body Pose in Real-Time from Sparse VR Sensor Measurements. *Virtual Reality*. 2024;28(2):116. https://doi.org/10.1007/s10055-024-01011-1

About the Authors:

Artem D. Obukhov, Dr.Sci. (Eng.), Associate Professor of the Department of Automated Decision Support Systems, Tambov State Technical University (112, Michurinskaya Str., Tambov, 392000, Russian Federation), SPIN-code, ORCID, ResearchGate, ScopusID, ResearcherID, obuhov.art@gmail.com

Daniil V. Teselkin, Assistant Professor of the Department of Automated Decision Support Systems, Tambov State Technical University (112, Michurinskaya Str., Tambov, 392000, Russian Federation), SPIN-code, ORCID, ResearchGate, ScopusID, dteselk@mail.ru

Claimed Contributorship:

AD Obukhov: conceptualization, funding acquisition, investigation, methodology, project administration, resources, supervision, writing – original draft preparation, writing – review & editing.

DV Teselkin: data curation, formal analysis, software, validation, visualization, writing – original draft preparation.

Conflict of Interest Statement: **the authors declare no conflict of interest.**

All authors have read and approved the final version of manuscript.

Об авторах:

Артём Дмитриевич Обухов, доктор технических наук, доцент кафедры «Системы автоматизированной поддержки принятия решений» Тамбовского государственного технического университета (392000, Российская Федерация, г. Тамбов, ул. Мичуринская, 112), SPIN-код, ORCID, ResearchGate, ScopusID, ResearcherID, obuhov.art@gmail.com

Даниил Вячеславович Теселкин, ассистент кафедры «Системы автоматизированной поддержки принятия решений» Тамбовского государственного технического университета (392000, Российская Федерация, г. Тамбов, ул. Мичуринская, 112), SPIN-код, ORCID, ResearchGate, ScopusID, dteselk@mail.ru

Заявленный вклад авторов:

А.Д. Обухов: разработка концепции, получение финансирования, проведение исследования, разработка методологии, научное руководство, написание черновика рукописи, написание рукописи, предоставление ресурсов, административное руководство исследовательским проектом.

Д.Л. Теселкин: курирование данных, формальный анализ, разработка программного обеспечения, валидация результатов, визуализация, написание черновика рукописи.

Конфликт интересов: **авторы заявляют об отсутствии конфликта интересов.**

Все авторы прочитали и одобрили окончательный вариант рукописи.

Received / Поступила в редакцию 24.06.2025
Reviewed /Поступила после рецензирования 20.07.2025
Accepted / Принята к публикации 31.07.2025

INFORMATION TECHNOLOGY, COMPUTER SCIENCE AND MANAGEMENT
ИНФОРМАТИКА, ВЫЧИСЛИТЕЛЬНАЯ ТЕХНИКА И УПРАВЛЕНИЕ

UDC 51-74
https://doi.org/10.23947/2687-1653-2025-25-3-233-241

Original Empirical Research

Mathematical Modeling of Charge Power Assessment with Exclusion of Loess Subsidence by Deep Hydraulic Blasts

Elena O. Tarasenko
North-Caucasus Federal University, Stavropol, Russian Federation
✉ galail@mail.ru

EDN: OVUJUV

Abstract

Introduction. Subsidence loess soils, widespread in Russia, China and Central Asia, are a challenge in modern construction due to their tendency to subsidence and low strength under external loads. Insufficient attention to their mechanical-and-physical properties can cause deformation of structures, which creates a safety hazard and financial losses. Scientific research in this area is fragmentary and does not provide sufficient understanding of compaction methods and their impact on the durability of structures. Moreover, there are no developed optimized mathematical models to predict the efficiency of engineering and technology processes of compaction. Thus, the objective of this study is to develop a mathematical model that determines the explosive charge capacity for compaction of loess. This model is aimed at eliminating the experimental stage, which improves the quality of compaction and contributes to saving financial resources in construction.

Materials and Methods. Mathematical modeling was carried out by including the solution to the inverse applied problem of assessing the power of an explosive charge when eliminating loess subsidence. Initial-boundary value problems with a semiempirical partial differential equation describing the compaction of loess with and without the ejection of soil onto the construction site's surface were considered by analyzing specific models and mathematical approaches. Based on the solution to these problems using the analytical method, a mathematical model for assessing the power of an explosive charge was developed. The power was determined numerically using two methods: calculations in a program developed in the Python language, and modeling a computational experiment with an assessment of the error of the result. In this case, the effect of the mechanical-and-physical properties of soils, their isotropy and anisotropy were taken into account.

Results. A mathematical model of the explosive charge power during compaction of subsiding loess using deep hydraulic blasts was constructed. The density of dry soil before and after compaction, the vertical diffusion coefficient, dispersion coordinate changes of gas in the compacted soil, and the depth of the explosive charge were taken into account. With an average density of dry compacted soil, the absolute error of the calculated values of the charge power was 3.28 g for compaction of loess without ejection, and 21.13 g for the situation with soil ejection onto the surface. The adequacy of the proposed mathematical solution to the experimental data of a full-scale construction site was shown.

Discussion. The proposed model allows for the assessment of the explosive charge power for isotropic and anisotropic geological systems. The resulting analytical representations demonstrate the degree and nature of the influence of mechanical-and-physical properties of soils on the magnitude of the charge power. Numerical comparison with both experimental data on natural soil compaction and recommendations for compaction of subsidence soils of high power by the hydraulic blasting method has shown that the proposed mathematical model is consistent with empirical data.

Conclusion. The main result of the study is a mathematical model of the explosive charge power when eliminating loess subsidence using deep hydraulic blasts. Analytical representations of the charge power are constructed taking into account the mechanical-and-physical properties of soils. A numerical estimate of the power consistent with the values of empirical data is obtained. The practical significance of the study involves the possibility of using the mathematical model as a calculation method and implementing it in research and design organizations. Further study will be aimed at constructing solutions using mathematical modeling and other inverse problems within the framework of the engineering and technology process of soil compaction.

Keywords: charge power, subsidence, loess, deep hydraulic blast, charge depth, compaction with ejection, compaction without ejection, isotropy, anisotropy, computational experiment

Acknowledgements. The author would like to thank Boris Fedorovich Galay, Dr.Sci. (Geology and Mineralogy), Professor, for his consultation and assistance in writing the article. The author also appreciates the editors and reviewers for their attentive attitude to the article and comments that improve its quality.

For Citation. Tarasenko EO. Mathematical Modeling of Charge Power Assessment with Exclusion of Loess Subsidence by Deep Hydraulic Blasts. *Advanced Engineering Research (Rostov-on-Don)*. 2025;25(3):233–241. https://doi.org/10.23947/2687-1653-2025-25-3-233-241

Оригинальное эмпирическое исследование

Математическое моделирование оценки мощности заряда при исключении просадочности лёссов глубинными гидровзрывами

Е.О. Тарасенко
Северо-Кавказский федеральный университет, г. Ставрополь, Российская Федерация
✉ galail@mail.ru

Аннотация

Введение. Просадочные лёссовые грунты, широко распространённые в России, Китае и Средней Азии, представляют собой значимую проблему в современном строительстве из-за своей склонности к просадке и низкой прочности при внешних нагрузках. Недостаточное внимание к их физико-механическим свойствам может привести к деформации сооружений, что создаёт угрозу безопасности и финансовые потери. Научные исследования в этой области являются фрагментарными и не дают достаточного понимания методов уплотнения и их влияния на долговечность конструкций. Кроме того, не существует разработанных оптимизированных математических моделей, позволяющих предсказать эффективность инженерно-технологических процессов уплотнения. Таким образом, целью данного исследования является разработка математической модели, определяющей мощность заряда взрывчатого вещества для уплотнения лёссов. Данная модель направлена на исключение экспериментального этапа, что улучшает качество уплотнения и способствует экономии финансовых ресурсов в строительстве.

Материалы и методы. Математическое моделирование проводили путём включения решения обратной прикладной задачи оценки мощности заряда взрывчатого вещества при устранении просадочности лёссов. Начально-граничные задачи с полуэмпирическим дифференциальным уравнением в частных производных, описывающим уплотнение лёсса с выбросом и без выброса грунта на поверхность строительной площадки, рассматривались путём анализа конкретных моделей и математических подходов. На основе решения этих задач с использованием аналитического метода была создана математическая модель оценки мощности заряда взрывчатого вещества. Мощность определяли численно двумя методами: расчётами в программе, разработанной на языке Python, и путём моделирования вычислительного эксперимента с оценкой погрешности результата. При этом учитывали влияние физико-механических свойств грунтов, их изотропность и анизотропность.

Результаты исследования. Построена математическая модель мощности заряда взрывчатого вещества при уплотнении просадочных лёссов с использованием глубинных гидровзрывов. Учтены плотность сухого грунта до и после уплотнения, коэффициент вертикальной диффузии, дисперсионные координатные изменения газа в уплотняемом грунте, а также глубина заложения заряда взрывчатого вещества. При средней плотности сухого уплотнённого грунта абсолютная погрешность расчётных значений мощности заряда составила 3,28 г для уплотнения лёссов без выброса и 21,13 г — для ситуации с выбросом грунта на поверхность. Показана адекватность предлагаемого математического решения экспериментальным данным натурного строительного объекта.

Обсуждение. Предложенная модель позволяет проводить оценку мощности заряда взрывчатого вещества для изотропных и анизотропных геологических систем. Полученные аналитические представления демонстрируют степень и характер влияния физико-механических свойств грунтов на величину мощности заряда. Численное сравнение как с экспериментальными данными натурного уплотнения грунтов, так и с рекомендациями по уплотнению просадочных грунтов большой мощности гидровзрывным методом показало, что предложенная математическая модель согласуется с эмпирическими данными.

Заключение. Основным результатом исследования является математическая модель мощности заряда взрывчатого вещества при устранении просадочности лёссов глубинными гидровзрывами. Построены аналитические представления мощности заряда с учётом физико-механических свойств грунтов. Получена численная оценка мощности, согласующаяся со значениями эмпирических данных. Практическая значимость исследования состоит в возможности применения математической модели в качестве расчётной методики и внедрения в исследовательские и проектные организации. Дальнейшие исследования будут направлены на построение решений средствами математического моделирования и других обратных задач в рамках инженерно-технологического процесса уплотнения грунтов.

Ключевые слова: мощность заряда, просадочность, лёссы, глубинный гидровзрыв, глубина заложения заряда, уплотнение с выбросом, уплотнение без выброса, изотропность, анизотропность, вычислительный эксперимент

Благодарности. Автор выражает признательность и благодарит Бориса Фёдоровича Галая, доктора геолого-минералогических наук, профессора за консультирование и оказанную помощь при написании статьи. Также автор благодарен редакции и рецензентам за внимательное отношение к статье и замечания, которые позволили повысить её качество.

Для цитирования. Тарасенко Е.О. Математическое моделирование оценки мощности заряда при исключении просадочности лёссов глубинными гидровзрывами. *Advanced Engineering Research (Rostov-on-Don).* 2025;25(3):233–241. https://doi.org/10.23947/2687-1653-2025-25-3-233-241

Introduction. Research into the surface of the earth's crust has shown the distribution of structurally unstable subsidence loess soils throughout the world. They predominate in Russia [1], China [2] and Central Asia [3]. Loess covers about 17% of Russia's territory. Loess soils are most often found in the North Caucasus, southern Russia, Crimea and other areas.

On a planetary scale, loess is a rock of the Quaternary period. It is characterized by yellow, yellow-brown or yellow-fawn colors [4]. Loess has low density and high macroporosity, which allows water to penetrate deeply into the soil structure. This causes rapid soaking [5] and subsidence [6]. Calculated subsidence from its own weight reaches values of 2.5 m [7].

It is not possible to construct safe and durable buildings and structures on subsidence soils. Designing and constructing objects on loess, as well as insufficient research of their physical and mechanical properties, lead to deformations of buildings and structures, reducing their safe service life. As a result, financial costs grow, and the security threat rapidly increases.

The elimination of subsidence is carried out by various methods, whose selection depends on the conditions of their implementation. This paper examines the method of compaction of loess by deep hydraulic blasts, showing economic efficiency at low production costs [8].

The engineering and technology process of compaction is performed on the basis of a comprehensive detailed study of the mechanical-and-physical properties of subsidence loess soils, which are widely presented in modern literature. Studies have been conducted on the permeability of subsidence soils [9], the deformation characteristics of loess [10] with different moisture content, compaction energy [11], creep [12] and mechanical stability of clays [13]. Strength and deformation properties of clayey soils from the point of view of physical-chemical theory are analyzed under the action of external loads, compressive load, counterpressure [14]. However, a mathematical description of the mechanical-and-physical properties of subsidence clays and loams, as well as their changes as a result of compaction by deep blasts, is not carried out in the noted works. Research is performed on the basis of field and compression tests of loess soils.

Mathematization of individual properties of explosive compaction soils, namely their strength characteristics, is given in the reports on engineering and geological surveys [15]. Adaptation of strength indicators to values for numerical calculations is implemented. Studies on the indicators of specific adhesion and the angle of internal friction of soils compacted by deep blasts using the regression analysis method are performed in [16]. Modeling of the vertical diffusion coefficient of gas in loess soils compacted by blasts is implemented [17]. Regression models of individual physical parameters of soils, such as porosity, permeability, water saturation [18], and filtration depending on pressure [19], are constructed. These studies allow us to evaluate the mechanical-and-physical properties of loess soils after their compaction by deep blasts, but do not describe the specifics of the implementation of the engineering and technology process of loess compaction.

Mathematical modeling of compaction of loess soils by deep hydraulic blasts requires solving individual inverse applied problems — assessing the power of the explosive charge, the depth of its placement, dispersion coordinate changes of gas atoms formed during the blast, in soils, and others. One of these problems sets the objective of this research — mathematical modeling of the power of the explosive charge taking into account the mechanical-and-physical properties of compacted geological systems, their anisotropy and isotropy.

The development of the model will not only improve the quality of compaction, but also reduce the financial costs of implementing the engineering and technology process. Compaction of loess using the proposed model eliminates the stage of trial preliminary blasts at the construction site, which is performed to determine the optimal power of the explosive charge and obtain the required mechanical properties of non-subsiding soils.

The research objective is implemented through mathematical modeling tools (analytically and numerically). Analytical representations will be constructed to estimate the explosive charge power based on the solution to initial boundary value problems with a semi-empirical diffusion equation. The mechanical-and-physical properties of compacted soils will be taken into account. Numerical modeling tools will be used to obtain an estimate of the charge power. Conducting a computational experiment will allow us to establish the adequacy of the proposed solution to the inverse problem to the experimental data.

Materials and Methods. The inverse problem of estimating the power of an explosive charge arises within the framework of mathematical modeling of compaction of subsidence soils by deep blasts. To eliminate the subsidence of loess, the process of their compaction is described by the model based on a given differential semi-empirical diffusion equation. It also takes into account the initial and boundary conditions. The mathematical formulation of the density model of compacted soils has the form [17]:

$$\frac{\partial q}{\partial t}+\sum_{i=x,y,z}\frac{\partial\left(u_i q\right)}{\partial i}+\alpha q=\sum_{i=x,y,z}\left(\frac{\partial}{\partial i}\sum_{j=x,y,z}K_{ij}\frac{\partial q}{\partial j}\right)+Q, \tag{1}$$

$$q\left(t_0,x,y,z\right)=Q\cdot\delta\left(x-x^0\right)\cdot\delta\left(y-y^0\right)\cdot\delta\left(z-z^0\right), \tag{2}$$

$$K_{zz}\left.\frac{\partial q}{\partial z}\right|_{z=z^0}=0,\ t>t_0, \tag{3}$$

$$\left.q\left(t,x,y,z\right)\right|_{z=z^0},\ t>t_0, \tag{4}$$

where $q(t, x, y, z)$ — density of compacted soil during a deep blast at time t; u — parameter of horizontal gas propagation; K_{xx}, K_{yy}, K_{zz} — diffusion coefficients; α — parameter of interaction of gas produced by blast and loess subsidence soil; Q — power of explosive charge (i.e., amount of gas ejected by the charge at time t_0 at point (x_0, y_0, z_0)); δ — Dirac delta function.

Initial boundary value problem (1)–(3) corresponds to the process of loess compaction by deep blasts with soil ejection onto the surface. Problem (1), (2), (4) is the compaction of loess without ejection onto the surface. The analytical solutions to problems (1)–(3) and (1), (2), (4) can be represented, respectively, in the form [17]:

$$q_1\left(t,x,y,z\right)=\frac{Q}{\left(4\pi t\right)^{3/2}\sigma_x\sigma_y\sigma_z}\times exp\left\{-\frac{\left(x-u_x\cdot t\right)^2}{4\sigma_x^2\cdot t}-\frac{y^2}{4\sigma_y^2\cdot t}\right\}\times\left[exp\left\{-\frac{\left(z-H\right)^2}{4\sigma_z^2\cdot t}\right\}+exp\left\{-\frac{\left(z+H\right)^2}{4\sigma_z^2\cdot t}\right\}\right], \tag{5}$$

$$q_2\left(t,x,y,z\right)=\frac{Q}{\left(4\pi t\right)^{3/2}\sigma_x\sigma_y\sigma_z}\times exp\left\{-\frac{\left(x-u_x\cdot t\right)^2}{4\sigma_x^2\cdot t}-\frac{y^2}{4\sigma_y^2\cdot t}\right\}\times\left[exp\left\{-\frac{\left(z-H\right)^2}{4\sigma_z^2\cdot t}\right\}-exp\left\{-\frac{\left(z+H\right)^2}{4\sigma_z^2\cdot t}\right\}\right]. \tag{6}$$

In solutions (5) and (6): (0, 0, H) — coordinates of the location of the concentrated explosive charge with power $Q = const > 0$, acting at the moment of time t_0; H — depth of the explosive charge; σ_x^2, σ_y^2, σ_z^2 — dispersion changes in the coordinates of gas atoms in the soil.

Statement of the inverse problem of estimating the power of an explosive charge: let the average values of the soil density and the explosive charges compacted by the method of deep blast be established, corresponding to relations (5) and (6) for cases of soil compaction with and without ejection onto the surface. The value of the depth of the explosive charge H is known. The value of the dispersion coordinate changes of gas atoms in the soil σ is determined. It is required to estimate the power of the explosive charge Q.

Research Results. We implement solutions to inverse applied problems on the assessment of charge power during compaction of subsiding loess by deep hydraulic blasts based on analytical and numerical methods of mathematical modeling.

According to (5) and (6), two cases are possible: compaction with ejection onto the surface and without ejection. In the first case, based on (5), we obtain the equation:

$$q_1\left(t,x,y,z\right)-\frac{Q}{\left(4\pi t\right)^{3/2}\sigma_x\sigma_y\sigma_z}\times exp\left\{-\frac{\left(x-u_x\cdot t\right)^2}{4\sigma_x^2\cdot t}-\frac{y^2}{4\sigma_y^2\cdot t}\right\}\times\left[exp\left\{-\frac{\left(z-H\right)^2}{4\sigma_z^2\cdot t}\right\}+exp\left\{-\frac{\left(z+H\right)^2}{4\sigma_z^2\cdot t}\right\}\right]=0. \tag{7}$$

In the second case, based on (6), we arrive at the equation:

$$q_2(t,x,y,z)-\frac{Q}{(4\pi t)^{3/2}\,\sigma_x\sigma_y\sigma_z}\times exp\left\{-\frac{(x-u_x\cdot t)^2}{4\sigma_x^2\cdot t}-\frac{y^2}{4\sigma_y^2\cdot t}\right\}\times\left[exp\left\{-\frac{(z-H)^2}{4\sigma_z^2\cdot t}\right\}-exp\left\{-\frac{(z+H)^2}{4\sigma_z^2\cdot t}\right\}\right]=0. \quad (8)$$

For geological systems, the characteristic mechanical-and-physical properties are anisotropy and isotropy. If the geological system under study is anisotropic, then the filtration properties of the soil depend on the direction of groundwater movement. When implementing soil compaction by blasts with surface ejection, the desired root Q of equation (7) takes the analytical representation:

$$Q=\frac{(4\pi t)^{3/2}\cdot q_1(t,x,y,z)}{exp\left\{-\frac{(x-u_x\cdot t)^2}{4\sigma_x^2\cdot t}-\frac{y^2}{4\sigma_y^2\cdot t}\right\}}\times\frac{\sigma_x\cdot\sigma_y\cdot\sigma_z}{\left[exp\left\{-\frac{(z-H)^2}{4\sigma_z^2\cdot t}\right\}+exp\left\{-\frac{(z+H)^2}{4\sigma_z^2\cdot t}\right\}\right]}. \quad (9)$$

If the system under study is isotropic, then the filtration properties of the soil do not depend on the direction of groundwater movement. Let us assume that the dispersion coordinate changes are equal in all directions $\sigma_z = \sigma_y = \sigma_x$, then, under compacting soils with ejection onto the surface, the desired root Q of equation (7) takes the analytical representation:

$$Q=\frac{(4\pi t)^{3/2}\cdot q_1(t,x,y,z)}{exp\left\{-\frac{(x-u_x\cdot t)^2}{4\sigma_z^2\cdot t}-\frac{y^2}{4\sigma_z^2\cdot t}\right\}}\times\frac{\sigma_z^3}{\left[exp\left\{-\frac{(z-H)^2}{4\sigma_z^2\cdot t}\right\}+exp\left\{-\frac{(z+H)^2}{4\sigma_z^2\cdot t}\right\}\right]}. \quad (10)$$

Now let us consider the case of soil compaction by deep blasts without ejection onto the surface. If the geological system under consideration is anisotropic, then the desired root Q of equation (8) takes the analytical form:

$$Q=\frac{(4\pi t)^{3/2}\cdot q_2(t,x,y,z)}{exp\left\{-\frac{(x-u_x\cdot t)^2}{4\sigma_x^2\cdot t}-\frac{y^2}{4\sigma_y^2\cdot t}\right\}}\times\frac{\sigma_x\cdot\sigma_y\cdot\sigma_z}{\left[exp\left\{-\frac{(z-H)^2}{4\sigma_z^2\cdot t}\right\}-exp\left\{-\frac{(z+H)^2}{4\sigma_z^2\cdot t}\right\}\right]}. \quad (11)$$

If the system under consideration is isotropic, then $\sigma_z = \sigma_y = \sigma_x$ and we can write the required root Q of equation (8) in the form:

$$Q=\frac{(4\pi t)^{3/2}\cdot q_2(t,x,y,z)}{exp\left\{-\frac{(x-u_x\cdot t)^2}{4\sigma_z^2\cdot t}-\frac{y^2}{4\sigma_z^2\cdot t}\right\}}\times\frac{\sigma_z^3}{\left[exp\left\{-\frac{(z-H)^2}{4\sigma_z^2\cdot t}\right\}-exp\left\{-\frac{(z+H)^2}{4\sigma_z^2\cdot t}\right\}\right]}. \quad (12)$$

Constructed relations (9)–(12) define analytically the power of the explosive charge depending on the mechanical-and-physical properties of the compacted soils and the depth of the charge. To estimate the power values, we use numerical modeling tools.

Computational experiment. We conduct a computational experiment to solve inverse problems arising in the mathematical modeling of loess compaction by deep blasts to provide numeric evaluation of the explosive charge power. The calculations are based on data from a full-scale construction site.

At the construction site "Construction of a Commodity and Raw Material Warehouse", "Stavrolen" LPG LLC (Budyonnovsk), compaction of subsidence soils [8] with a thickness of 28 m was performed using deep blasts. The total subsidence of the soil under its own weight was from 43 to 78 cm. Groundwater was recorded at a depth of 29–31 m [20]. The average density of dry soil before compaction was 1.43 g/cm³.

At the construction site, drainage blast holes with a diameter of 20 cm were drilled on a cm grid to perform compaction. Charges of water-resistant ammonite weighing 10,000 g were placed in them at a depth of H = 600 cm. A month after compaction, control holes were drilled with the selection of monoliths. The density of dry soil took values in the range from 1.60 g/cm³ to 1.75 g/cm³. The average density of dry compacted soil was 1.66 g/cm³ [8]. Loess refers to soils with a columnar structure and is orthotropic vertically [20]. Taking into account the physical parameters of the soil, we calculate the coefficient of vertical diffusion of gas in soil Kz, according to [17]. Using Kz, we determine the dispersion coordinate changes of gas atoms in the soil, which are equal to $\sigma_z = 0.726$. The parameter of horizontal gas propagation is zero $u_x = 0$. The calculation of the values of the explosive charge power is made according to formula (12). Loess compaction is implemented without ejecting soil onto the surface.

Table 1 presents the result of the assessment of the explosive charge power for known values of compacted soil density, dispersion coordinate changes of gas atoms in the soil, and the depth of the charge. The calculations were conducted using the author's program, developed in the high-level programming language Python, designed to calculate the explosive charge power.

Table 1

Estimated Explosive Charge at Different Values of Compacted Soil Density without Ejection onto the Surface

Soil density, g/cm³	Estimated explosive charge, g
1.60	9797.53
1.61	9809.56
1.62	9815,83
1.63	9836.05
1.64	9876.28
1.65	9936.51
1.66	9996.72
1.67	10046.74
1.68	10094.16
1.69	10114.28
1.70	10137.53
1.71	10159.82
1.72	10186.04
1.73	10208.27
1.74	10228.49
1.75	10243.71

Let us analyze the results presented in Table 1. To exclude the property of subsidence and reach the density of dry compacted soil ≥1.60 g/cm³, the power of the explosive charge can take values in the range from 9797.53 to 10243.71 g. According to experimental data, the power of the explosive charge is 10000 g [8]. The absolute error of calculations for soil density values from 1.60 g/cm³ to 1.75 g/cm³ does not exceed 0.244. With an average soil density q = 1.66 g/cm³, the absolute error is 3.28 g.

We consider the compaction of loess with the ejection of soil onto the surface. We calculate the values of the explosive charge power using formula (10) at $\sigma_z = 0.726$ and the density of dry soil from 1.60 g/cm³ to 1.75 g/cm³. The results obtained are presented in Table 2.

Table 2

Estimated Power of Explosive Charge at Different Values of Compacted Soil Density with Ejection onto the Surface

Soil density, g/cm³	Calculated Explosive Charge, g
1.60	9852.18
1.61	9881.62
1.62	9952.77
1.63	10021.13
1.64	10053.84
1.65	10094.28
1.66	10123.92
1.67	10157.54
1.68	10187.62
1,69	10204.75
1.70	10221.83
1.71	10242.25
1.72	10256.89
1.73	10279.34
1.74	10293.79
1.75	10301.24

The analysis of the explosive charge power values presented in Table 2 shows that the calculated charge power can take values from 9852.18 g to 10301.24 g. The absolute calculation error does not exceed 0.301. With the average soil density q = 1.66 g/cm^3, the absolute error is 123.92 g. The minimum absolute error is 0.02113 at q = 1.63 g/cm^3.

Figures 1, 2 show a graphical interpretation of the calculated values of the explosive charge power at different indicators of the density of dry compacted soil and experimental data on the charge power. The charge power values are marked in accordance with the recommendations for compaction of subsidence soils of high power by the hydraulic blasting method[1] (solid line). When the explosive charge is placed at the specified depth, its power is equal to 9960 g. Figure 1 shows the case of loess compaction by deep blast without ejection onto the surface, Figure 2 — with ejection onto the surface.

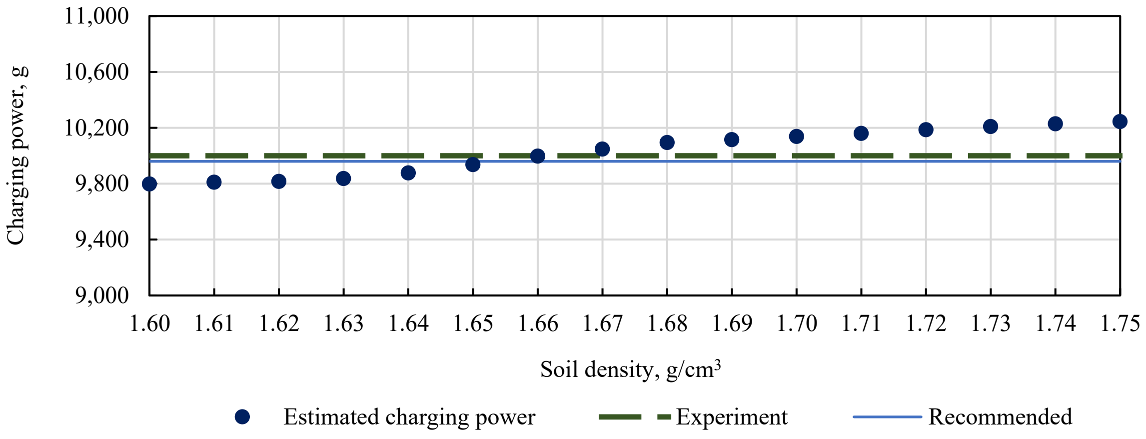

Fig. 1. Estimated and experimental power of explosive charge at different values of soil density without ejection onto the surface

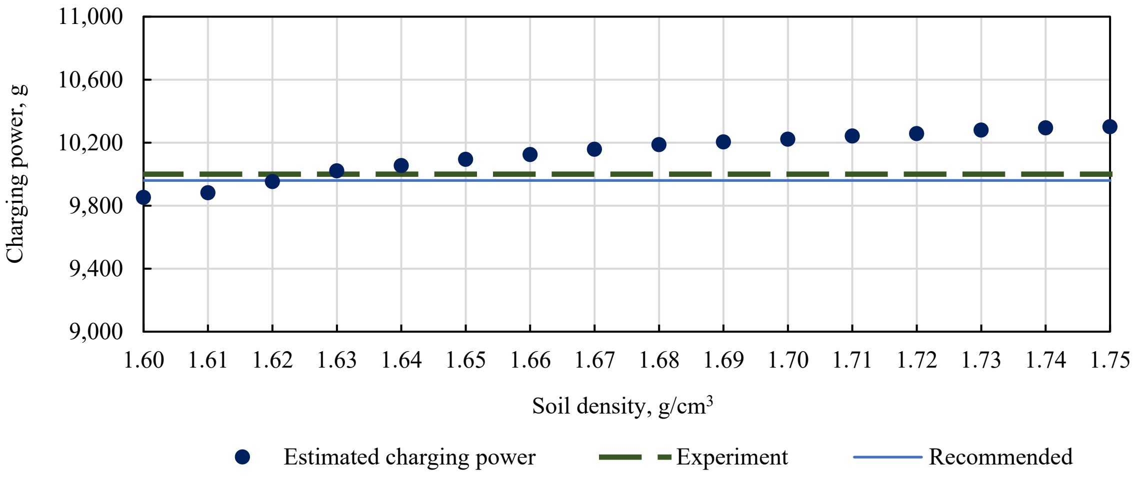

Fig. 2. Estimated and experimental power of explosive charge at different values of soil density with ejection onto the surface

Upon completion of the engineering and technology process of compaction of loess using deep blasts, in accordance with [8], after the discharge of water from the pit, the upper buffer layers of the construction site are further compacted using surface methods.

Discussion. The constructed mathematical model of the explosive charge power is described analytically (9)–(12). The model is intended for performing numerical calculations and assessing the charge power values. The formulas show the nature and degree of dependence of the charge power and the mechanical-and-physical properties of soils, their isotropy and anisotropy. A growth of the charge power entails an increase in soil density, a decrease in subsidence and porosity.

The ideas obtained allowed us to conduct a theoretical experiment on the numerical evaluation of the values of the explosive charge power. The calculated values have an absolute computational error in the intervals: (3.28; 243.71) g — compaction without soil ejection onto the surface, and (21.13; 301.24) g — compaction with soil ejection onto the surface of the construction site.

[1] Recommendations for compaction of high-power subsidence soils using hydraulic blasting. Moscow: Stroiizdat; 1984. 56 p. (In Russ.) URL: https://meganorm.ru/Data2/1/4293782/4293782665.pdf (accessed: 01.06.2025).

The disadvantage of the proposed approach is that the density of the compacted loess, the value of the dispersion coordinate changes of gas atoms in the soil are determined on the basis of field and laboratory tests. The depth of the explosive charge is also specified in advance. Thus, when assessing the power of the charge, stamp and compression data will be contained. The proposed model takes into account the isotropy and anisotropy of soils. The results obtained in this study are adequate to the experimental data and confirm the possibility of their practical application in planning the engineering and technology process of compaction of subsidence soils by deep hydraulic blasts.

Conclusion. The main research result is a mathematical model for assessing the power of an explosive charge. Analytical expressions for the power of the charge are obtained. The mechanical-and-physical properties of soils, their isotropy and anisotropy are taken into account. Numerical values of power are found using a program developed in Python. The results obtained are in good agreement with the values of a natural experiment and the recommended values based on empirical data.

The practical significance of the study involves the possibility of using the mathematical model as a calculation method in research and design organizations engaged in theoretical investigation and practical implementation of compaction of subsidence loess soils. Further research will be aimed at constructing solutions through mathematical modeling and other inverse problems within the framework of the engineering and technology process of soil compaction.

References

1. Trofimov VT (ed), Balykova SD, Andreeva TV, Ershova AV, Shaevich YaE. *Reference Engineering-Geological Sections of Loess Rocks of Northern Eurasia*. Monograph. Moscow: KDU; 2008. 608 p. (In Russ.)

2. Xiaoyu Zhu, Jessica Gray, Ying Gu, Tong He. Genesis of Loess Particles on the Chinese Loess Plateau. *Geochemistry, Geophysics, Geosystems*. 2022;23(7):e2022GC010428. https://doi.org/10.1029/2022GC010428

3. Torgoev IA, Aleshin YuG. Seismogenic Liquefaction Landslides in Loess-Like Loams. In: *Proc. Annual Session of the RAS Scientific Council on the Problems of Geoecology, Engineering Geology and Hydrogeology. "Sergeev Readings. Fundamental and Applied Issues of Modern Soil Science"*. Moscow: GeoInfo; 2022. P. 224–229. (In Russ.)

4. Korolev VA, Grigorieva IYu. The Ecological-Geological Systems of Loess Soil Massifs. *Engineering Geology World*. 2022;XVII(2):42–64. (In Russ.) https://doi.org/10.25296/1993-5056-2022-17-2-42-64

5. Jianhua Ma, Runqiang Zeng, Xingmin Meng, Zonglin Zhang, Shufen Zhao, Ziran Wei. Field Research on Preferential Infiltration in Rainfall-Induced Loess Landslides. *Engineering Geology*. 2025;354:108184. https://doi.org/10.1016/j.enggeo.2025.108184

6. Jinduo Yang, Xi-An Li, Lincui Li, Zhang Jing, Weiping Wang. Formation Mechanism of Metastable Internal Support Microstructure in Malan Loess and Its Implications for Collapsibility. *Engineering Geology*. 2025;346:107892. https://doi.org/10.1016/j.enggeo.2024.107892

7. Shijie Zhai, Guangyin Du, Zhongxun Zhuang, Changhui Gao, Chuanle Wang. Effect of Resonance Compaction Method on the Bearing Capacity Considering Geotechnical Spatial Variability Characteristics. *Engineering Geology*. 2023;324:107256. https://doi.org/10.1016/j.enggeo.2023.107256

8. Galay BF. *Compaction of Subsidence Soils by Deep Explosions*. Stavropol: Servisshkola, 2015. 240 p. (In Russ.)

9. Zekun Li, Penghui Ma, Jianqi Zhuang, Qingyi Mu, Jiaxu Kong, Luqing Zhao, et al. Permeability Characteristics, Structural Failure Characteristics, and Triggering Process of Loess Landslides in Two Typical Strata Structures. *Engineering Geology*. 2024;341:107728. https://doi.org/10.1016/j.enggeo.2024.107728

10. Prokopov AYu, Sychev IV, Ryazantseva A. Determining the Stabilised Subfoudation Soil Deformation Modulus according to the Plate Load Tests and Geotechnical Monitoring Data. *Modern Trends in Construction, Urban and Territorial Planning*. 2023;2(3):17–30. https://doi.org/10.23947/2949-1835-2023-2-3-17-30

11. Jing Yang, Xirong Niu, Qigao Guo, Zhiheng Wen, Hailong Cao. Strength and Deformation Characteristics of Compacted Loess with Different Moisture Content and Compaction Energy. *Results in Engineering*. 2023;20:101637. https://doi.org/10.1016/j.rineng.2023.101637

12. Xiaowei Liu, Xudong Zhang, Xiaogang Fu, Tianxiang Yang, Zisong Su. Experimental Study on Creep Characteristics of Saturated Q_2 Loess. *Frontiers in Earth Science*. 2022;10:815275. https://doi.org/10.3389/feart.2022.815275

13. Osipov VI, Sokolov VN, Karpenko FS. Physicochemical Mechanics of Disperse Porous Materials as a New Approach to Assessing Mechanical Stability of Clay Soils. *Geology*. *Engineering Geology. Hydrogeology. Geocryology*. 2024;4:50–63. https://doi.org/10.31857/S0869780924040059

14. Karpenko FS. Clayey Soils Properties on the Physicochemical Theory of Strength Positions. *Soil Science*. 2023;2:3–12. (In Russ.) https://doi.org/10.53278/2306-9139-2023-2-21-3-12

15. Petrakov AA, Prokopov AYu, Petrakova NA, Panasjuk MD. Interpretation of Strength Properties of Soil for Numerical Analyses. *Izvestiya TulGU. Sciences of Earth*. 2021;1:225–236.

16. Tarasenko EO. Mathematical Modeling of the Strength Properties of Lesses by the Method of Correlation-Regression Analysis. *International Journal for Computational Civil and Structural Engineering*. 2024;20(1):171–181. https://doi.org/10.22337/2587-9618-2024-20-1-171-181

17. Tarasenko EO. Estimation of the Vertical Diffusion Coefficient of Gas in Compacted Soils by Means of Mathematical Modeling. *Proceedings of ISP RAS*. 2024;36(5):181–190. https://doi.org/10.15514/ISPRAS-2024-36(5)-13

18. Kozhevnikova PV, Kuntsev VE, Dorogobed AN, Motryuk EN. Mathematical Modeling of the Distribution of the Reliability of Petrophysical Parameters in the Construction of a Geological Model. *Modern High Technologies*. 2021;2:31–37. https://doi.org/10.17513/snt.38490

19. Jingping Wang, Haichun Ma, Jiazhong Qian, Peichao Feng, Xiaohui Tan, Lei Ma. Experimental and Theoretical Study on the Seepage Mechanism Characteristics Coupling with Confining Pressure. *Engineering Geology*. 2021;291:106224. https://doi.org/10.1016/j.enggeo.2021.106224

20. Galay OB. *Budennovsk: Geology and City*. Monograph. Stavropol: Stavropolservisshkola, 2022. 318 p. (In Russ.)

About the Author:

Elena O. Tarasenko, Cand.Sci. (Phys.-Math.), Associate Professor of the Department of Computational Mathematics and Cybernetics, North-Caucasus Federal University (1, Pushkin Str., Stavropol, 355017, Russian Federation), SPIN-code, ORCID, ResearcherID, ScopusID, ResearchGate, galail@mail.ru

Conflict of Interest Statement: **the author declares no conflict of interest.**

The author has read and approved the final version of manuscript.

Об авторе:

Елена Олеговна Тарасенко, кандидат физико-математических наук, доцент, доцент кафедры «Вычислительная математика и кибернетика» Северо-Кавказского федерального университета (355000, Российская Федерация, г. Ставрополь, ул. Пушкина, 1), SPIN-код, ORCID, ResearcherID, ScopusID, ResearchGate, galail@mail.ru

Конфликт интересов: **автор заявляет об отсутствии конфликта интересов.**

Автор прочитал и одобрил окончательный вариант рукописи.

Received / Поступила в редакцию 11.06.2025
Reviewed / Поступила после рецензирования 01.07.2025
Accepted / Принята к публикации 15.07.2025

INFORMATION TECHNOLOGY, COMPUTER SCIENCE AND MANAGEMENT
ИНФОРМАТИКА, ВЫЧИСЛИТЕЛЬНАЯ ТЕХНИКА И УПРАВЛЕНИЕ

Check for updates

UDC 681.5 *Original Empirical Research*

https://doi.org/10.23947/2687-1653-2025-25-3-242-255

Obtaining a Set of Vibration Signals from Rolling Bearings with Varying Degrees of Local Defect Development in the Outer Race

Zoya A. Kolosova ✉, **Olga P. Kolosova**, **Dmitry A. Shnayder**

South Ural State University, Chelyabinsk, Russian Federation

✉ kolosovaza@susu.ru

EDN: CRISFJ

Abstract

Introduction. The creation of reliable test sets of vibration signals remains a critical challenge in vibrodiagnostics, as the lack of data on early-stage bearing defects hinders the development and validation of diagnostic algorithms. Experimental acquisition of such signals is limited by the absence of appropriate test specimens and the long duration required for defect progression. Existing numerical simulation approaches demand high computational resources and complex setup, reducing their practical applicability. A significant gap in current research is the absence of a simple, reproducible, and validated methodology for generating signals that reflect the progressive development of defects. The objective of this study is to create a simplified methodology for generating a test set of bearing vibration signals that can be used to develop and verify new vibrodiagnostic techniques. The methodology is based on a combination of experimental and simulated signals.

Materials and Methods. Experimental data were obtained from a laboratory rig simulating a rotor unit with a rolling bearing (type 180603). To simulate early-stage defects (single and double chipping pits), dynamic finite element modelling was performed using ANSYS Mechanical (version 16.2) based on plane elements Plane162 using the LS-DYNA package. The resulting impulse sequences were superimposed onto the measured signal from a healthy bearing to generate combined signals. All signals (3 experimental, 2 combined) were analyzed using Fourier transform, bandpass filtering (5.4 kHz), and calculation of statistical parameters: root mean square (RMS), crest factor, and kurtosis. Analysis was conducted in Mathcad (version 15.0).

Results. As a result of the study, a method for generating a test set of vibration signals from a rolling bearing was developed, covering the serviceable state and the sequential development of a local defect of the outer ring. The results showed a correlation between the amplitude of vibration signals and the stages of defects — an increase in amplitudes was observed in the high-frequency region, which confirmed the interaction of rolling elements and defective surfaces. Additional statistical analysis revealed an increase in diagnostic parameters (RMS value, crest factor, and kurtosis) as the damage developed. It was found that the simulated signals reproduced the characteristic signs of a defect and fitted correctly into the general trend of parameter changes.

Discussion. The data obtained demonstrate that the proposed technique makes it possible to simplify the generation of reference signals without the need for long-term accumulation of experimental data or damage to equipment. The physical validity of the simulated pulses and the consistency of growth dynamics of diagnostic parameters with real data confirm the possibility of using this method for standardized testing of vibrodiagnostic techniques.

Conclusion. The developed methodology provides an efficient and reproducible approach to generating test signal sets for vibrodiagnostics. It can be used to accelerate algorithm verification, reduce experimental costs, and improve diagnostic reliability. Future research will focus on simplifying impulse generation through analytical modelling and extending the methodology to other bearing types and defect forms.

Keywords: vibrodiagnostics, rolling bearing, FEM, vibration signal modeling

Acknowledgements. The authors would like to thank A.P. Beketov, Research Fellow of Russian Federal Nuclear Center – Zababakhin All-Russia Research Institute of Technical Physics, for constructing a finite element model of the intact bearing.

For Citation. Kolosova ZA, Kolosova OP, Shnayder DA. Obtaining a Set of Vibrational Signals from Rolling Bearings with Varying Degrees of Local Defect Development in the Outer Race. *Advanced Engineering Research (Rostov-on-Don).* 2025;25(3):242–255. https://doi.org/10.23947/2687-1653-2025-25-3-242-255

Оригинальное эмпирическое исследование

Получение набора вибрационных сигналов подшипника качения с разной степенью развития локального дефекта наружного кольца

З.А. Колосова ✉, **О.П. Колосова**, **Д.А. Шнайдер**
Южно-Уральский государственный университет, г. Челябинск, Российская Федерация
✉ kolosovaza@susu.ru

Аннотация

Введение. Создание достоверных тестовых наборов вибрационных сигналов остаётся актуальной задачей вибродиагностики, поскольку отсутствие данных по ранним стадиям дефектов подшипников затрудняет разработку и верификацию алгоритмов диагностики. Экспериментальное получение таких сигналов ограничено отсутствием соответствующих образцов и длительностью процесса накопления повреждений. Существующие подходы на основе численного моделирования требуют высоких вычислительных ресурсов и сложной настройки, что снижает их практическую применимость. Пробелом в исследованиях является отсутствие простой, воспроизводимой и валидированной методики генерации сигналов, отражающих последовательное развитие дефекта. Целью данного исследования является создание упрощённой методики формирования тестового набора сигналов вибрации подшипника, который может использоваться для разработки и верификации новых методов вибродиагностики. Методика основана на комбинировании экспериментальных и смоделированных сигналов.

Материалы и методы. В исследовании использовались экспериментальные данные, полученные с лабораторной установки, моделирующей роторный узел с подшипником качения (тип 180603). Для имитации ранних стадий дефекта (единичная и двойная ямка выкрашивания) применялось динамическое моделирование методом конечных элементов в среде ANSYS Mechanical (версия 16.2) на основе плоских элементов Plane162 с применением пакета LS-DYNA. Полученные последовательности импульсов накладывались на измеренный сигнал исправного подшипника для формирования комбинированных сигналов. Все сигналы (3 экспериментальных, 2 комбинированных) подвергались анализу с использованием преобразования Фурье, полосовой фильтрации (октавная полоса частот 5,4 кГц) и расчёта статистических параметров: СКЗ, пик-фактора и коэффициента эксцесса. Анализ проводился в среде Mathcad (версия 15.0).

Результаты исследования. В результате исследования разработана методика формирования тестового набора вибрационных сигналов подшипника качения, охватывающая исправное состояние и последовательное развитие локального дефекта наружного кольца. Результаты показали корреляцию между амплитудой вибрационных сигналов и стадиями дефектов — наблюдался рост амплитуд в высокочастотной области, что подтверждает взаимодействие тел качения с дефектными поверхностями. Дополнительный статистический анализ выявил увеличение диагностических параметров (среднего квадратического значения, пик-фактора и коэффициента эксцесса) по мере развития повреждения. Установлено, что смоделированные сигналы воспроизводят характерные признаки дефекта и корректно вписываются в общую тенденцию изменения параметров.

Обсуждение. Полученные данные демонстрируют, что предложенная методика позволяет упрощенно формировать эталонные сигналы без необходимости длительного накопления экспериментальных данных или повреждения оборудования. Физическая обоснованность смоделированных импульсов и согласованность динамики роста диагностических параметров с реальными данными подтверждают возможность использования данной методики для стандартизированного тестирования методов вибродиагностики.

Заключение. Разработанная методика обеспечивает эффективное и воспроизводимое формирование тестовых наборов сигналов для вибродиагностики. Она может быть использована для ускоренной верификации алгоритмов, снижения затрат на эксперименты и повышения надёжности диагностики. В дальнейшем планируется упрощение генерации импульсов на основе аналитического моделирования и расширение методики на другие типы подшипников и дефектов.

Ключевые слова: вибродиагностика, подшипник качения, МКЭ, моделирование сигналов вибрации

Благодарности. Авторы благодарят научного сотрудника ФГУП «РФЯЦ-ВНИИТФ имени академика Е.И. Забабахина» Александра Павловича Бекетова за построение конечно-элементной модели исправного подшипника.

Для цитирования. Колосова З.А., Колосова О.П., Шнайдер Д.А. Получение набора вибрационных сигналов подшипника качения с разной степенью развития локального дефекта наружного кольца. *Advanced Engineering Research (Rostov-on-Don).* 2025;25(3):242–255. https://doi.org/10.23947/2687-1653-2025-25-3-242-255

Introduction. In modern industry, there is a tendency for the size, complexity and productivity of machinery to increase, which results in growing capital expenditure on its acquisition, repair and maintenance. Equipment shutdowns cause significant losses due to short-received production.

A considerable part of rotating industrial equipment contains rolling bearings. In most cases, their technical condition is the decisive factor in ensuring trouble-free operation — i.e., the failure of a rolling bearing causes the failure of the entire product. Experts in vibrodiagnostics are faced with the need to analyze and interpret vibration signals to assess the condition of rolling bearings. The presence of a set of signals reflecting various stages of fault growth is critical for the development and testing of new diagnostic techniques. This allows not only for improvement of accuracy and reliability of diagnostic algorithms, but also for their adaptation to real operating conditions of the equipment. However, obtaining such a set of signals under real conditions is a difficult task [1]. Traditional methods include either waiting for the natural occurrence of a fault, which can take a significant amount of time, or intentional damage to the bearing, which is not always advisable and can cause additional costs. In this regard, there is a need to develop alternative approaches to obtaining vibration signals with varying degrees of fault development.

One such technique is mathematical modeling and simulation of bearing vibration signals [2]. Researchers have developed various models, including systems with three [3] and two degrees of freedom [4]. These models take into account factors, such as radial clearance, number of balls, and localized faults on the inner race, outer race, or balls. Advanced stochastic models have been proposed that take into account random sliding of roller elements and periodically changing transfer functions [5]. Simulations by MATLAB have been used to generate vibration time signals and frequency spectra [4].

However, modeling bearing vibration signals remains a non-trivial task related to a number of technical and methodological difficulties. First, real bearing systems have a high degree of complexity [6]. An accurate representation of all factors affecting bearing vibrations in a single model is practically impossible. Models often simplify complex interactions between components, which can result in potential inaccuracies in predictions. Second, bearings exhibit nonlinear dynamic behavior, specifically in the presence of faults [7]. This nonlinearity is difficult to capture in mathematical models, especially when dealing with composite faults, such as simultaneous faults on the inner and outer races. Third, there is a problem of parameter uncertainty [8]. Numerous models depend on parameters that are difficult to measure or accurately estimate, such as contact stiffness and damping coefficients. This further complicates the modeling process and can cause inaccuracies in the results [9]. More complex models require significant computational resources, making real-time analysis challenging for industrial applications. Some models may ignore important factors, such as temperature effects, lubrication conditions, or manufacturing variations, leading to discrepancies between predicted and actual behavior [9]. Due to the lack of calibration bearings, experimental validation capabilities are limited, challenging the completeness and reliability of verification of the developed mathematical models [10].

This research objective is to develop a simplified methodology for generating a test set of bearing vibration signals reflecting various types and stages of faults, and to check its applicability for testing and verifying vibration diagnostics algorithms. The proposed approach is aimed at overcoming the limitations of existing modeling methods related to high computational complexity and insufficient adequacy of reproducing real operating conditions of the system.

For this purpose, a method was developed that combines experimental recording of the initial signal from equipment in good condition and finite element modeling of the system's behavior in the presence of faults. Based on the modeling, a sequence of pulses was obtained that simulated the effect of bearing damage. These pulses were added to the initial signal, creating a set of combined signals corresponding to different stages of fault development.

This approach provides the formation of a standardized and easily reproducible dataset that can be used for testing and comparative evaluation of various vibration diagnostics methods. The proposed method of simulating faulty signals is a promising direction for the development of vibration diagnostics and can be useful for various industries where the reliability and durability of equipment are important.

Materials and Methods. The development of a method for obtaining a set of signals from a bearing with different stages of fault development includes the following stages: obtaining a correct signal experimentally, creating a model of the bearing being studied, simulating the fault on the model, obtaining a sequence of fault pulses, and mixing this sequence with a real correct signal.

Obtaining a correct signal from a laboratory setup is advisable because it is difficult to take into account numerous factors affecting the real signal during modeling, such as noise from the equipment itself, noise from the measuring device, the existing imbalance of the equipment shafts, etc.

To compare the real and simulated signals, signals from bearings with faults were also obtained on the laboratory setup. To obtain the pulse sequence, finite element modeling (FEM) was used, which is one of the most efficient and widely used approaches to the numerical analysis of mechanical systems and structures [10]. The pulse sequences obtained using FEM were added to the real correct signal to form signals with a fault.

1. Obtaining a correct signal experimentally

The object of the study was a single-row radial ball bearing with a seal type 180603 as per GOST 8882–75[1]. The geometric characteristics of this bearing are given in Table 1.

Table 1

Geometric Characteristics of Rolling Bearings

Characteristic, dimensions	Designation, formula	Value
Overall dimensions		
External diameter, mm	D	47
Internal diameter, mm	d	17
Width, mm	B	19
Dimensions of rolling elements		
Diameter, mm	d_b	9.5
Quantity	z	6
Contact angle, rad	β	0
Angular pitch of rolling elements, rad	$g = 2\pi/z$	$\pi/3$
Diameter of the circle passing through centers of rolling elements, mm	$D_0 = (D+d)/2$	32
Initial radial clearance, µm	g	8–15
Dimensions of rolling tracks		
Minimum thickness along the gutter, mm	$h = [(D–d)/2–d_b]/2$	2.750
Diameter of the outer track, mm	$d_o = D–2\times h$	41.500
Diameter of the inner track, mm	$d_i = d+2\times h$	22.500
Radius of cross section, mm	$r = 0{,}515\times d_b$	4.893

[1] GOST 8882–75. *Single Row Radial Sealed Ball Bearings. Technical Conditions*. Electronic Fund of Legal and Regulatory Documents. URL: https://base.garant.ru/5926172/ (accessed: 09.06.2025).

The bearing diagram is shown in Figure 1.

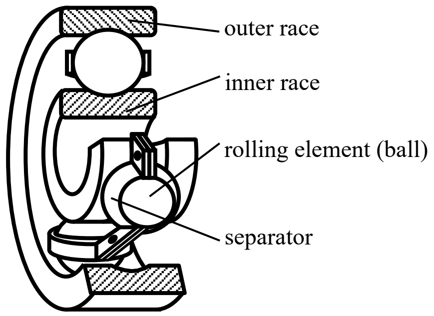

Fig. 1. Rolling bearing diagram

Bearings of this type are installed in the supports of a laboratory setup, which simulates the simplest rotary machine and basically represents a rotor on two supports. As in any real machine, the setup diagram contains manufacturing faults, such as static and dynamic imbalance, skew and tilt of the axes, which brings the operating conditions of the bearing setup closer to real ones.

Structurally, the laboratory setup, whose diagram is shown in Figure 2, consists of a base platform on which two supports and an asynchronous electric motor of the 4A80A type with a power of 1.1 kW and a nominal rotation frequency of 1000 rpm are mounted. A shaft with a flywheel rotates in the supports on rolling bearings. The shaft is connected to the motor through a coupling.

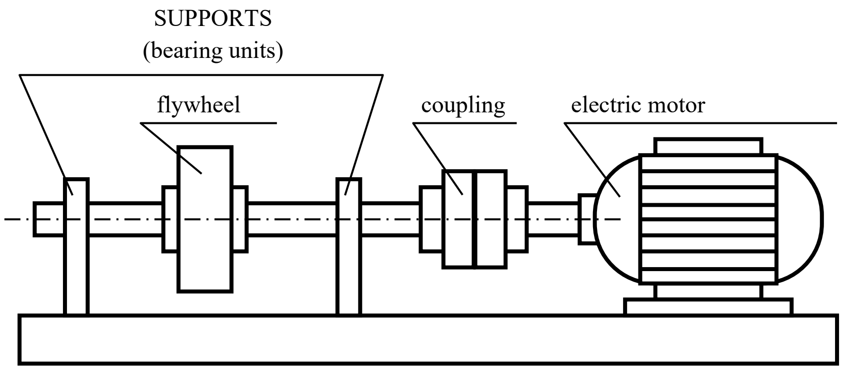

Fig. 2. Laboratory setup diagram

Due to the presence of friction in the bearings, the rotation frequency of the laboratory setup rotor is slightly different from the nominal rotation frequency of the engine and is 995 rpm, or 16.58 Hz, or 104.2 rad/s. A new, correct bearing is placed in the right support of the setup (closest to the engine and less accessible). The bearing under study is located in the left support, farthest from the engine, in the radial vertical direction.

For the experimental study of rolling bearing vibrations, the measuring system shown in Figure 3 was used. The measuring system included a piezoelectric accelerometer, a signal amplifier, an oscilloscope, an analog-digital converter (ADC), and a computer. In addition, to calibrate the measuring system, a signal generator was connected instead of the accelerometer and amplifier.

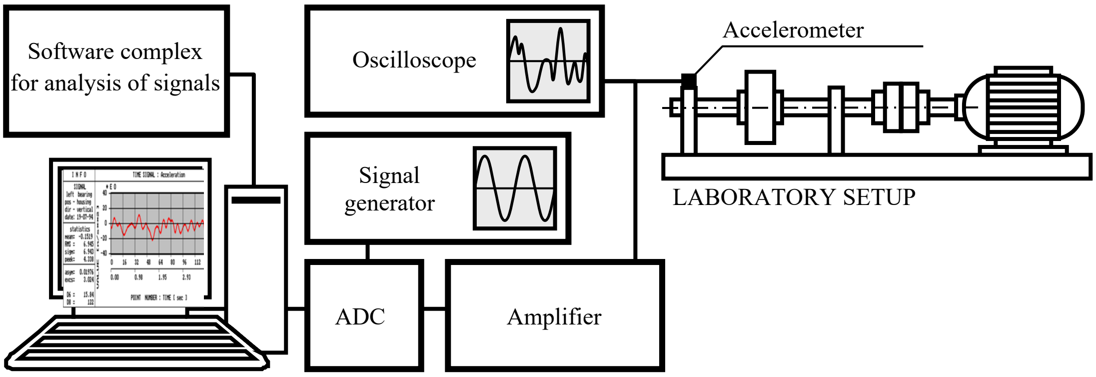

Fig. 3. Measuring system

Three bearings of type 180603 as per GOST 8882–75[2] were installed sequentially in the left support of the laboratory setup:

– healthy rolling bearing;

– faulty bearing with a developed fault (intensive chipping of the rolling tracks);

– bearing in a critical condition with a crack in the outer race.

Vibration acceleration signals were recorded from each of the listed bearings with a sampling frequency of 16 kHz and a duration of 0.12 seconds.

2. Construction of a bearing model using the finite element method

The model of a healthy rolling bearing placed in the support of the laboratory setup is shown in Figure 4. The model is constructed using Plane162 elements. The elastic support of the laboratory setup is rigidly fixed to the base. A bearing is inserted into the support — the support and the outer race of the bearing have common nodes along the contact line. The shaft and the inner race of the bearing are connected in a similar way. The outer and inner races of the bearing are elastic. The shaft and separator are rigid. The rolling elements are modeled as follows: the central part of the ball is rigid; the periphery is elastic.

All elastic elements of the model use a material with the following properties: E = 210 GPa; μ = 0.33; ρ = 7850 kg/m³. Rayleigh damping is introduced into the material.

Loads on the model:

– shaft, as a rigid body, is given a law of motion — the angle of rotation around z axis with time $\varphi(t)=\omega t$;

– radial load $q_1 = q_0$, is applied to the shaft, directed vertically downwards (the static load of the bearing is simulated);

– radial load $q_2 = q_{0/2}$, whose direction rotates together with the shaft around z axis is applied to the shaft (the imbalance is simulated).

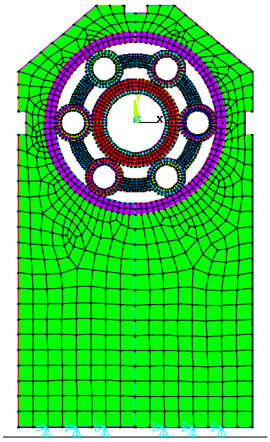

Fig. 4. Bearing model based on Plane162 elements

To ease the task in a computational sense, the following simplifications of the model were introduced.

1. Hollow balls were inserted, which led to a decrease in the number of nodes in the model. In this case, the density of the rigid part of the ball was recalculated so that the mass of the ball remained unchanged.

2. The finite element mesh was compacted near the contact surfaces. The dimensions of the elements in these areas were minimal.

3. The structural elements of the system, whose rigidity can be neglected (shaft, separator), were made of the material “Rigid”.

The calculation feature of the model under consideration is that for subsequent processing of the calculated vibration acceleration signal (in particular, for applying the fast Fourier transform to it), it is required that the signal recording step in time be constant.

3. Simulation of a local fault of the outer race of a bearing

The objective of the experiment-calculated study is to obtain vibration signals of a bearing for different degrees of development of a local fault of the outer race of a rolling bearing. The problem is solved through superimposing a sequence of short-term, rapidly decaying “single pulses” caused by the rolling element hitting a fault (pit) on the measured signal of a healthy bearing. The sequence of pulses is obtained using the FEM model.

[2] GOST 8882–75. *Single Row Radial Sealed Ball Bearings. Technical Conditions*. Electronic Fund of Legal and Regulatory Documents. URL: https://base.garant.ru/5926172/ (accessed: 09.06.2026).

The depth of the chipping pit is considered equal to the depth of the dangerous point in the contact zone of the rolling element and the track when the endurance condition is violated — reaching equality of the amplitude value of the maximum equivalent stress in the contact of the rolling element and the track to the endurance limit of the material — steel ШХ15:

$$max\,\sigma_{экв} = 2\sigma_0. \tag{1}$$

The fatigue limit of steel ШХ15 GOST 801–79[3] during heat treatment of the type "quenching at 840°C in oil and tempering at 300°C", used for ball bearings, is σ_{-1} = 650 MPa. However, the fatigue limit σ_{-1} for a symmetrical stress cycle is not suitable for contact strength calculations, since the contact stress cycle is zero (pulsating). The fatigue limit in a zero-to-tension cycle σ_0 is determined using a schematized diagram of limiting amplitudes, linking the average cycle stress σ_m and its amplitude stress $\sigma_a = \sigma_{-1} - \psi\sigma_m$, where coefficient ψ = 0.2–0.3 for alloy steels. From which:

$$\sigma_0 = \frac{\sigma_{-1}}{(1+\psi)} = 520\ \text{МПа}. \tag{2}$$

To determine the maximum equivalent stress, we consider the stress state at a point located at depth z below the center of the elliptical contact area. We introduce the coordinate system *Cxyz: C* — center of the elliptical contact area, *z* axis is perpendicular to the contact area, x axis is directed along the major semi-axis of the contact area, *y* axis is directed along the minor semi-axis of the contact area. The semi-axes of the contact area are: major — *a*, minor — *b*. For ease of writing formulas, we denote: $a/b = \beta$, $z/a = \zeta$.

In areas parallel to the coordinate planes, the shear stresses are equal to 0, the normal stresses are the main ones and are determined by the following formulas:

$$\sigma_z = -p_0 \frac{1}{\sqrt{1+\zeta^2}\cdot\sqrt{1+\left(\frac{\zeta}{\beta}\right)^2}}, \tag{3}$$

$$\sigma_x = -p_0\cdot\frac{\beta}{1-\beta^2}\cdot\left\{1-\sqrt{\frac{\beta^2+\zeta^2}{1+\zeta^2}}+2\zeta\cdot(L-K)-2\mu\cdot\left[1-\frac{1}{\beta^2}\cdot\sqrt{\frac{\beta^2+\zeta^2}{1+\zeta^2}}+\zeta\cdot\left(\frac{1}{\beta^2}L-K\right)\right]\right\}, \tag{4}$$

$$\sigma_y = -p_0\cdot\frac{\beta}{1-\beta^2}\cdot\left\{-1+\frac{1+\zeta^2\cdot\left(\frac{2}{\beta^2}-1\right)}{\sqrt{1+\zeta^2}+\sqrt{\beta^2+\zeta^2}}-2\zeta\cdot\left(\frac{1}{\beta^2}L-K\right)+2\mu\cdot\left[1-\sqrt{\frac{\beta^2+\zeta^2}{1+\zeta^2}}+\zeta\cdot(L-K)\right]\right\}, \tag{5}$$

where $K(e)$, $L(e)$ — complete elliptic integrals depending on eccentricity *e* of the elliptical contact area of the rolling element and the bearing race.

The eccentricity of the contact area *e*, the greatest intensity of pressure between the contacting bodies p_0, the minor semi-axis of the elliptical contact area are found from the Hertz problem of contact between spherical rolling elements and a toroidal bearing race.

The equivalent tensile stress is determined from (3), (4) and (5) using the Huber-Mises strength hypothesis:

$$\sigma_{экв} = \frac{1}{\sqrt{2}}\cdot\sqrt{(\sigma_x-\sigma_y)^2+(\sigma_x-\sigma_z)^2+(\sigma_y-\sigma_z)^2}. \tag{6}$$

According to the calculation results using formulas (1), (2) and (6) for the bearing under consideration, the depth of the chipping pit on the inner raceway was 0.56 mm, on the outer raceway — 0.60 mm. Assuming the shape of the chipping pit is hemispherical, its transverse size (diameter) is considered equal to twice the depth.

In the flat model of a healthy rolling bearing, we introduce a fault in the form of a V-shaped notch on the outer raceway (Fig. 5). We round off the width and depth of the fault and take them equal to 0.5 mm.

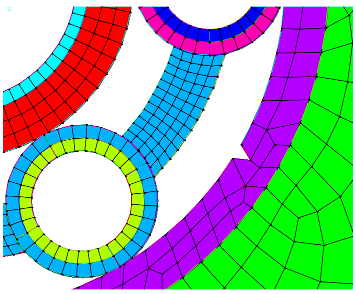

Fig. 5. Bearing outer race fault model

[3] GOST 801–79. *Bearing Steel.*

Such a change in the model of a healthy bearing can describe a single chipping pit. Moreover, it is practically impossible to obtain an experimental vibration signal for a single chipping pit due to the long duration and labor intensity of the experiment. A local fault of double width corresponding to a "double" chipping pit — two closely located pits that merged into one — was also considered. Using these models in the LS DYNA program, vibration acceleration signals were calculated in the vertical direction of the upper support point lying on the symmetry axis.

The calculation was carried out for the following parameters:

– dimensions of finite elements in contact zones $a_{эл} \approx 0.8$ mm;

– damping value in the material $b = 0.25$;

– radial load parameter $q_0 = 2160$ kN/m;

– process implementation time $T = 1.2$ s;

– signal recording time step $\Delta t = 1$ µs.

4. Processing a set of signals

As a result of the measurement and simulation techniques described above, a set of vibration signals was generated, including three signals measured on a laboratory setup and two signals obtained by mixing the simulated fault pulses with the real signal of a healthy bearing. The combined signals are intended to fill gaps in the sample and compensate for the lack of experimental data on bearings with an early-stage fault.

Fast Fourier transform was used to analyze the time and frequency characteristics of vibration signals, which allowed us to obtain amplitude spectra in the frequency domain. Spectrum analysis was performed in a wide frequency range (0–8 kHz).

To isolate pulses caused by local faults, the signals were filtered in an octave frequency band of 5.4 kHz. The resulting narrowband signals were used to identify fault pulses and calculate their maximum amplitudes.

The average value of the maximum pulse amplitudes was calculated as the arithmetic mean for all selected pulses in a narrowband signal. This parameter was used to quantify the severity of the fault.

The following statistical parameters were calculated for quantitative evaluation and comparison of signals: root mean square (RMS) of vibration acceleration, peak factor, and excess coefficient. The selection of these parameters was validated by their efficiency in identifying local bearing faults [11, 12].

RMS was calculated using the following formula [13]:

$$\text{СКЗ} = \sqrt{\frac{1}{N}\sum_{i=1}^{N} x_i^2}, \tag{7}$$

where x_i — i-th vibration acceleration value, N — number of signal samples.

The peak factor was defined as the ratio of the maximum value of the signal to the RMS value [14]:

$$Pf = \frac{max(x)}{\text{СКЗ}}, \tag{8}$$

where x — vibration acceleration values.

The excess coefficient was calculated using the formula for a large sample ($N > 100$) [15, 16]:

$$E = \frac{1}{N}\sum_{i=1}^{N}\left(\frac{x_i - \overline{x}}{s}\right)^4, \tag{9}$$

where $\overline{x}$ denotes the arithmetic mean value of vibration acceleration, s — standard deviation.

The calculated parameters were used to construct a correspondence table for the degree of development of the bearing outer race fault, which made it possible to assess the likelihood of the simulated signals and their suitability for testing vibration diagnostics methods.

Research Results

1. Measured signals

Three signals were obtained, corresponding to different states of the bearing: healthy condition, developed fault (multiple pits), emergency condition (race crack). Figure 6 shows the shapes of vibration signals in the time domain (1 — healthy rolling bearing; 2 — faulty bearing with developed chipping of the rolling raceways; 3 — bearing under the emergency condition with a crack in the outer race).

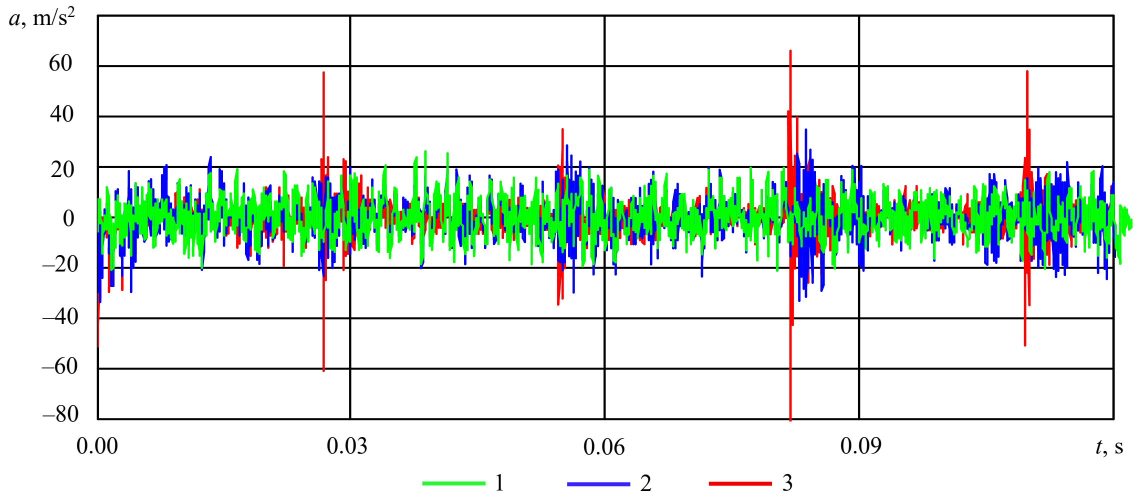

Fig. 6. Measured vibration acceleration signals

Figure 7 shows the amplitude spectra of signals in the frequency domain (1 — healthy rolling bearing; 2 — faulty bearing with developed chipping of the rolling raceways; 3 — bearing under the emergency condition with a crack in the outer race). As the fault develops, an increase in amplitudes is observed in the high-frequency region (about 5.4 kHz), and sequences of short-term pulses appear in the signals.

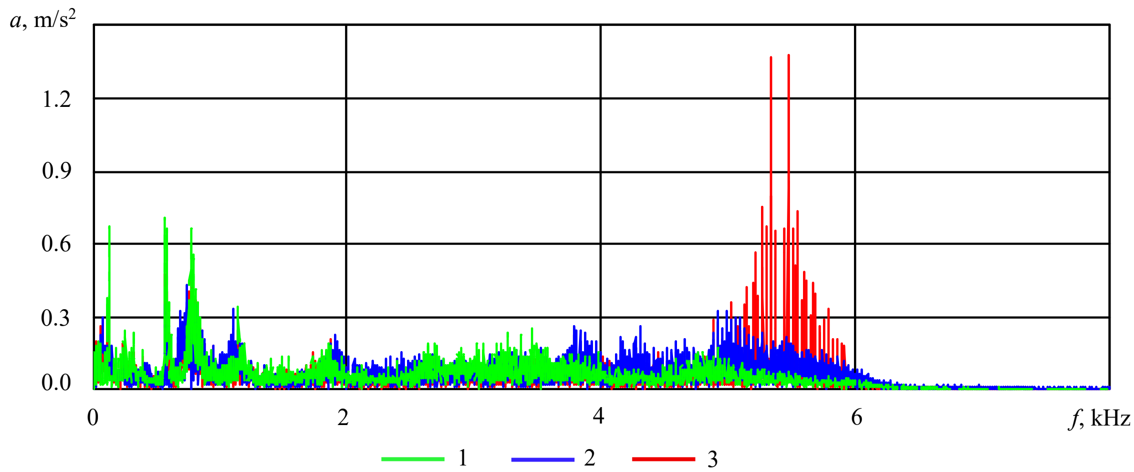

Fig. 7. Amplitude spectra of measured vibration signals

After filtering in the octave band of 5.4 kHz, the fault pulses were isolated. Narrowband signals are shown in Figures 8 and 9.

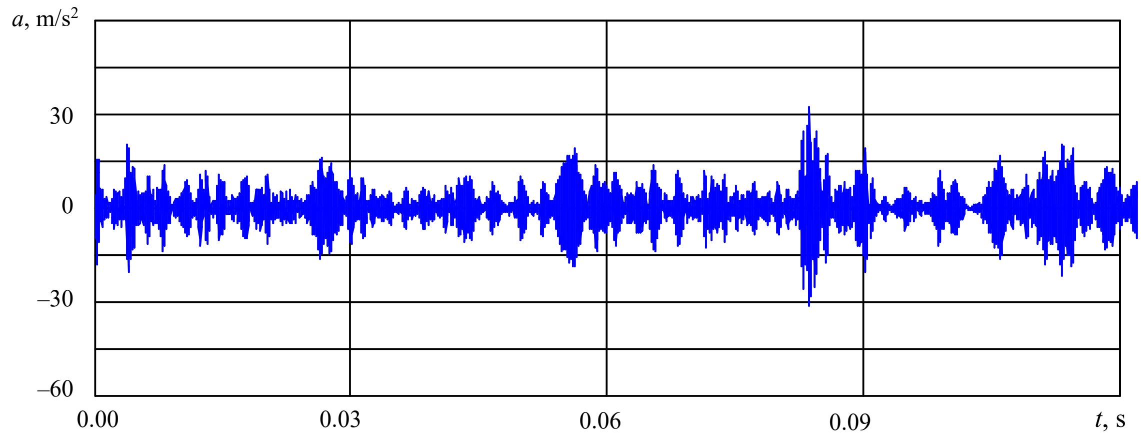

Fig. 8. Narrowband vibration signal of a rolling bearing with developed chipping of the rolling raceways

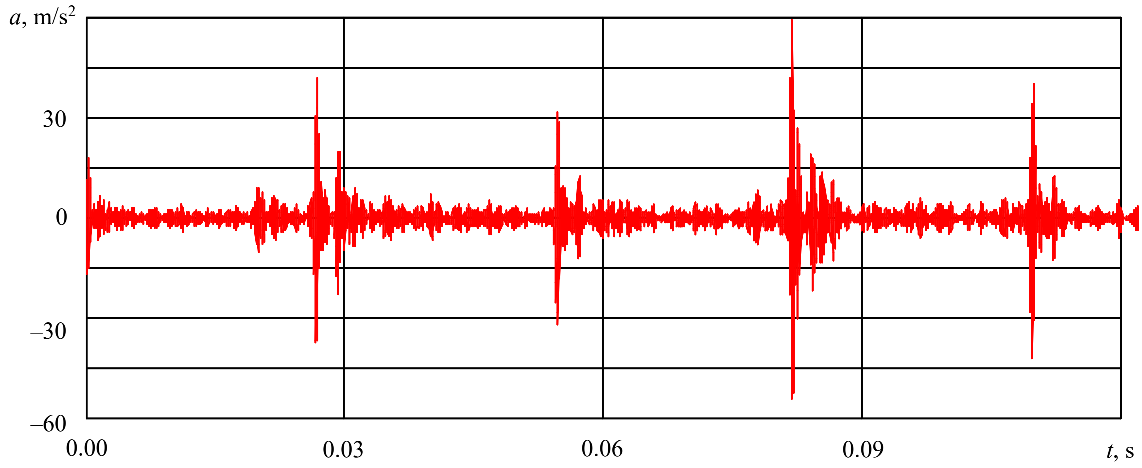

Fig. 9. Narrowband vibration signal of a rolling bearing with a crack in the outer race

The average value of the maximum pulse amplitudes was: 24.3 m/s^2 — for a large multiple pit (a sequence of the strongest pulses in a bearing signal with chipping); 39.8 m/s^2 — for a race crack.

2. Combined signals

The pulses obtained through dynamic simulation of the FEM model are shown in Figure 10. The correct signal from the setup, with which the pulses obtained were mixed, is shown in Figure 11.

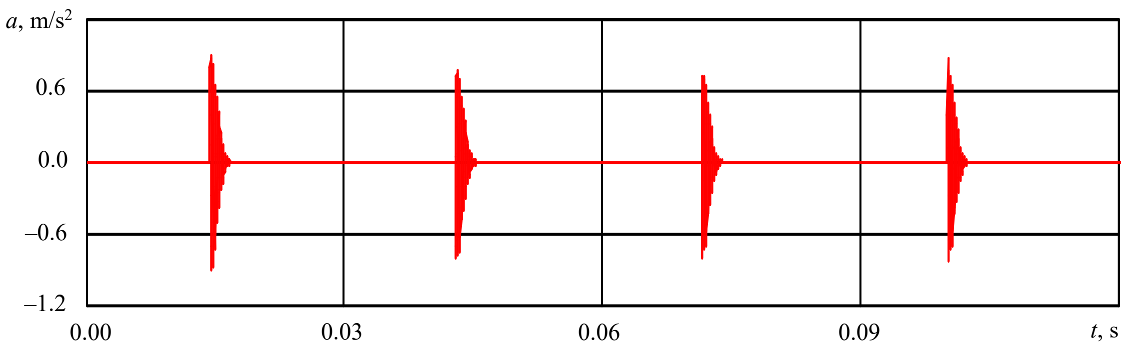

Fig. 10. Sequence of received pulses

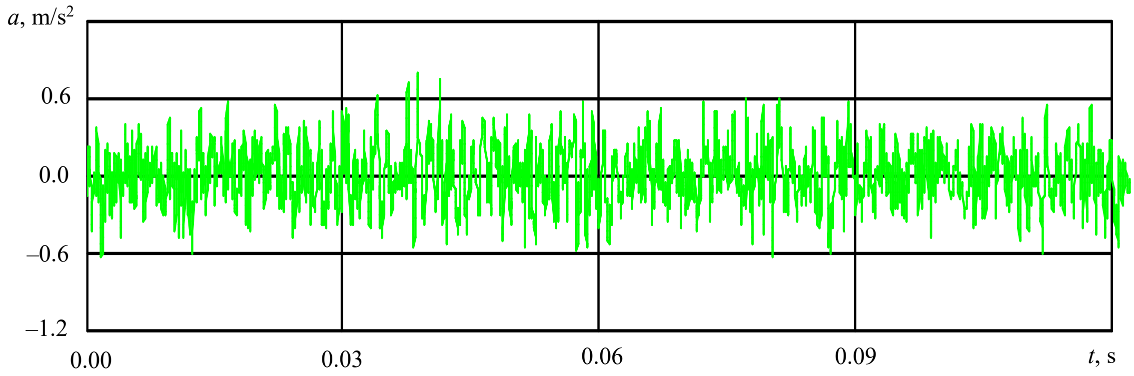

Fig. 11. Measured vibration signal of healthy bearing

Two combined signals were generated, corresponding to the early stages of the fault: with a single and double chipping pit. Figure 12 shows the time representations of the signals obtained (1 (green line) — vibration signal of a healthy bearing; 2 (blue line) — combined vibration signal of a faulty bearing with a single chipping pit; 3 (red line) — combined vibration signal of a faulty bearing with a double chipping pit.

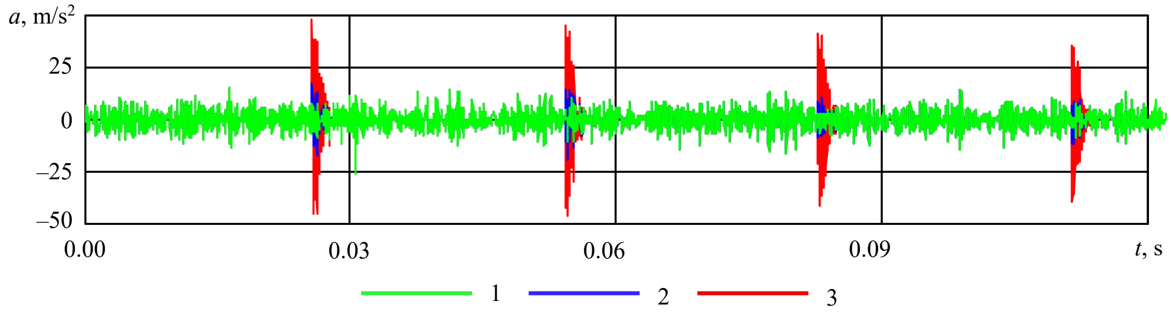

Fig. 12. Combined vibration signals of a rolling bearing for different degrees of fault development

The signal with a single pit visually differs little from the healthy one due to the relative smallness of the pulses. After filtering in the 5.4 kHz band, the fault pulses were isolated. Figure 13 shows a narrowband signal for a single pit.

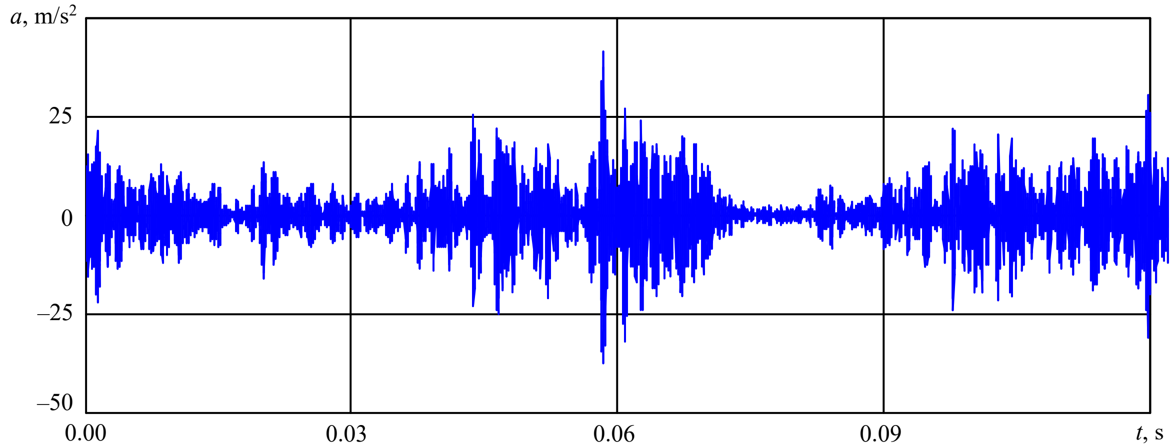

Fig. 13. Narrowband signal of bearing with single chipping pit

The average value of the maximum pulse amplitudes was:

– 9.6 m/s^2 — for a single pit;

– 14.7 m/s^2 — for a double pit.

3. Comparison of statistical parameters of measured and calculated signals

For all signals, the following statistical parameters were calculated:

– average value of the maximum amplitude of fault pulses A;

– RMS, calculated using formula (7);

– peak factor Pf, calculated using formula (8);

– excess coefficient E, calculated using formula (9).

The results are presented in Table 2.

Table 2

Statistical Analysis Results of Calculated Vibration Signals for Healthy and Faulty Rolling Bearings

Signal	Technical condition	A, m/s^2	RMS	Pf	E
Measured	Healthy condition, no faults	0	6.81	3.04	3.03
Combined	Faulty, early stage of development — single pit	10	6.86	3.86	3.10
Combined	Faulty, developed fault — double pit	15	6.93	4.49	3.27
Measured	Faulty, developed fault — multiple pit	25	7.15	5.64	4.30
Measured	Emergency, race crack	40	7.67	6.96	8.09

Figure 14 shows the change in the normalized values of statistical parameters depending on the degree of fault development.

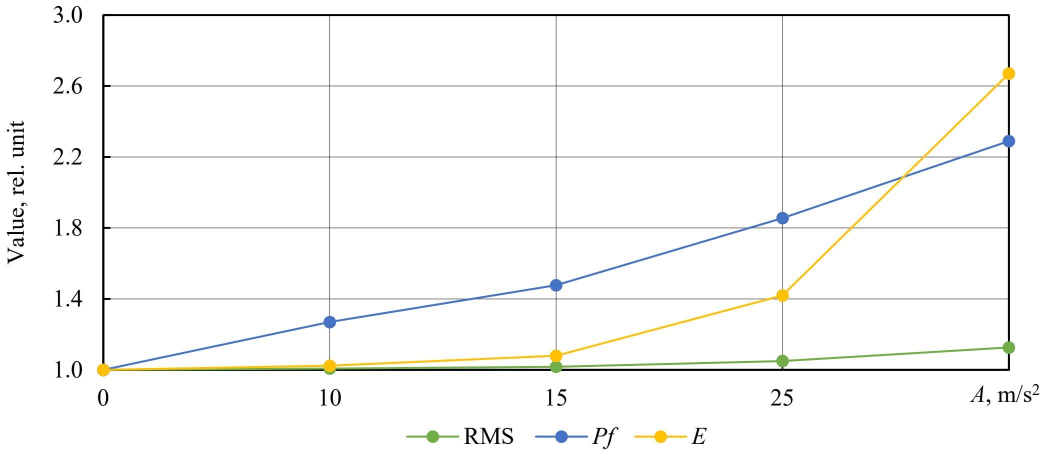

Fig. 14. Growth of statistical parameters depending on the fault development

Discussion. The main objective of this study was to develop a methodology for generating a set of bearing vibration signals at various stages of development of a local fault of the outer race. The proposed approach, combining experimental data and numerical modeling, made it possible to fill in the gaps in the experimental base, especially at the early stages of the fault, whose acquisition under laboratory conditions was difficult due to the lack of appropriate samples.

The analysis of the signals obtained has shown that as the fault develops, characteristic changes are observed in both the time and frequency domains. Sequences of short-term pulses appear in the signals, while in the spectra, there is an increase in amplitudes in the vicinity of the bearing unit's natural frequency — ~5.4 kHz. These changes are due to the impact nature of the interaction of the rolling elements and the faulty surface. When a fault enters the contact zone, an impact occurs that excites the unit's own vibrations. The amplitude of these vibrations is modulated by the flicker frequency of the fault, which manifests itself in the form of decaying pulses in the narrowband signal.

Statistical analysis revealed a steady increase in key diagnostic parameters — RMS, peak factor and excess coefficient — as the damage degree increased, which is consistent with the expected behavior of the vibration signal during the development of a local fault. However, a key aspect of the analysis was to check the likelihood of the simulated signals included in the set to compensate for the lack of experimental data at the early stages of the fault.

The analysis has shown that the parameter values for combined signals logically fit into the general trend observed in the measured signals. Thus, for a signal with a single pit (early stage), the RMS was 6.86 m/s^2, the peak factor was 3.86, and the excess was 3.10; for a signal with a double pit, it was 6.93 m/s^2, 4.49, and 3.27, respectively. These values are between the healthy state and the developed fault, indicating a consistent and physically based change in the signal with an increase in the degree of damage.

Thus, the simulated signals not only fill the gaps in the set, but also retain the correct dynamics of changes in diagnostic parameters, which confirms their validity and suitability for use as reference signals in the development and testing of vibration diagnostics methods. However, the analysis of the trend characteristic has shown that the growth of the parameters does not correspond to the threshold values specified in GOST R ISO 20816–1–2021[4] standard (an increase of 2.5 times for a faulty state and 10 times for an emergency). This suggests that unified thresholds may not be accurate enough for specific types of equipment, and that individual calibration of diagnostic models is required on the basis of experimental or simulated data. The proposed methodology allows such calibration to be performed without the need for long-term collection of fault statistics or intentional damage to equipment.

An important advantage of the approach is the ability to simulate the development of a fault for a specific bearing and operating conditions. However, the method has limitations. In particular, creating a finite element model requires significant time and skill resources. To reduce labor intensity, the key characteristics of the pulses generated by the fault are analyzed:

– carrier frequency of the pulse is equal to the natural frequency of the bearing unit — 5.4 kHz;
– largest pulse amplitudes — random with an average value 1 m/s^2;
– pulse repetition frequency coincides with the frequency of the fault (flickering of the rolling elements on the outer race);
– initial phase — random;
– pulse shape — exponentially decaying.

[4] GOST R ISO 20816–1–2021. *Mechanical Vibration. Measurement and Evaluation of Machine Vibration*. Electronic Fund of Legal and Regulatory Documents. URL: https://docs.cntd.ru/document/1200182677 (accessed: 20.05.2025).

The amplitude distribution and attenuation pattern correspond to those observed in real signals with a crack in the race. This indicates that the pulse generated by the fault can be described analytically, which makes it possible to replace resource-intensive FEM modeling with simulating predetermined pulse shapes and thereby significantly simplify and speed up the signal generation procedure.

Thus, the proposed technique not only solves the problem of forming a complete set of signals for vibration diagnostics, but also opens up the prospect of creating individualized diagnostic models adapted to specific equipment. In the future, it is planned to develop a simplified algorithm for generating pulses based on the obtained characteristics, which will make the method more accessible for practical application.

Conclusion. During the research, a method for generating a test set of vibration signals from rolling bearings was developed, combining experimental data and numerical modeling. The proposed approach provides reproducing various stages of the development of a local fault in the outer race, including early ones for which there are no experimental samples, without the need for long-term data accumulation or equipment damage.

The analysis has shown that the simulated signals fit correctly into the general trend of changes in diagnostic parameters (RMS, peak factor, excess), which confirms their validity and suitability for testing vibration diagnostics methods. The resulting set of signals can serve as a standardized basis for comparative evaluation of diagnostic algorithms.

The practical significance of the work involves reducing the costs of experimental research, accelerating the verification of diagnostic models, and increasing the reliability of assessing the technical condition of equipment.

In the future, it is planned to simplify the generation of pulses based on the identified mathematical characteristics, expand the methodology to other types of bearings and faults, as well as integrate it with data analysis techniques to create solutions in the field of predictive maintenance.

References

1. Nguyen Duc Thuan, Hoang Si Hong. HUST Bearing: A Practical Dataset for Ball Bearing Fault Diagnosis. *arXiv*. 2023. https://doi.org/10.48550/arXiv.2302.12533

2. Jing Liu, Yimin Shao. A New Dynamic Model for Vibration Analysis of a Ball Bearing due to a Localized Surface Defect Considering Edge Topographies. *Nonlinear Dynamics*. 2015;79:1329–1351. https://doi.org/10.1007/s11071-014-1745-y

3. Halmos F, Wartzack S, Bartz M. Investigation of Failure Mechanisms in Oil-Lubricated Rolling Bearings under Small Oscillating Movements: Experimental Results, Analysis and Comparison with Theoretical Models. *Lubricants*. 2024;12(8):271. https://doi.org/10.3390/lubricants12080271

4. Jain PH, Bhosle SP. Mathematical Modeling, Simulation and Analysis of Non-Linear Vibrations of a Ball Bearing due to Radial Clearance and Number of Balls. *Materials Today: Proceedings*. 2023;72(3):927–936. https://doi.org/10.1016/j.matpr.2022.09.093

5. Menck O. The Finite Segment Method–A Numerical Rolling Contact Fatigue Life Model for Bearings Subjected to Stochastic Operating Conditions. *ASME Journal of Tribology*. 2023;145(3):031201. https://doi.org/10.1115/1.4055916

6. Wrzochal M, Adamczak S. The Problems of Mathematical Modelling of Rolling Bearing Vibrations. *Bulletin of the Polish Academy of Sciences: Technical Sciences*. 2020;68(6):1363–1372. https://doi.org/10.24425/bpasts.2020.135398

7. Lihai Chen, Ao Tan, Lixiu Yang, Xiaoxu Pang, Ming Qiu. Defect Size Evaluation of Cylindrical Roller Bearings with Compound Faults on the Inner and Outer Races. *Mathematical Problems in Engineering*. 2022;2022(2):1–12. https://doi.org/10.1155/2022/6070822

8. Malanchuk Y, Moshynskyi V, Korniienko V, Malanchuk Z. Modeling the Process of Hydromechanical Amber Extraction. *E3S Web of Conferences*. 2018;60:00005. https://doi.org/10.1051/e3sconf/20186000005

9. Ali Safian, Hongsheng Zhang, Xihui Liang, Nan Wu. Dynamic Simulation of a Cylindrical Roller Bearing with a Local Defect by Combining Finite Element and Lumped Parameter Models. *Measurement Science and Technology*. 2021;32(12):125111. https://doi.org/10.1088/1361-6501/ac2317

10. Tianhe Wang, Lei Chen, Hong Lu, Shaojun Wang, Zhangjie Li, Wei Zhang, et al. Finite Element Dynamic Model and Vibration Signal Simulation of Rolling Bearing with Local Faults. In: *Proc. 18th International Manufacturing Science and Engineering Conference*. New York NY: ASME. 2023;2:105504. https://doi.org/10.1115/MSEC2023-105504

11. Gururaj Upadhyaya, Kumar HS. A Comparative Study of Statistical Features Used in Rolling Element Bearing Health Diagnosis Using Six Sigma Approach. In: *Proc. 2nd Indian International Conference on Industrial Engineering and Operations Management.* Southfield, MI: IEOM Society International; 2022. https://doi.org/10.46254/IN02.20220244

12. Jain PH, Bhosle SP. Study of Effects of Radial Load on Vibration of Bearing Using Time-Domain Statistical Parameters. *IOP Conference Series: Materials Science and Engineering*. 2021;1070:012130. https://doi.org/10.1088/1757-899X/1070/1/012130

13. Trufanov NN, Churikov DV, Kravchenko OV. Application of Spectral Analysis Methods for Data Pre-processing of Anomaly Detection Problem of Vibration Diagnostics in Non-destructive Testing. *Journal of Physics: Conference Series*. 2021;2127:012028. https://doi.org/10.1088/1742-6596/2127/1/012028

14. Garad A, Sutar KB, Shinde VJ, Pawar AC. Analysis of Vibration Signals of Rolling Element Bearing with Localized Defects. *International Journal of Current Engineering and Technology*. 2017;7:37–42.

15. Tetter V, Tetter A, Denisova I. Researching the Possibility of Determining the Technical Condition of Rolling Bearings by the Kurtosis Factor. In: *Proc. International Russian Automation Conference (RusAutoCon)*. New York City: IEEE; 2023. P. 149–153. https://doi.org/10.1109/RusAutoCon58002.2023.10272799

16. Puzyr V, Mykhalkiv S. Classification of the Technical Condition of Rolling Bearing by the Scalar Indicators and Support Vector Machines. *Progresivna tehnìka, tehnologìâ ta ìnženerna osvìta*. 2023.

About the Authors:

Zoya A. Kolosova, Postgraduate student of the Automation and Control Department, South Ural State University (76, Lenin Ave., Chelyabinsk, 454080, Russian Federation), ORCID, SPIN-code, ScopusID, ResearchGate, kolosovaza@susu.ru

Olga P. Kolosova, Cand.Sci. (Eng.), Professor of the Technical Mechanics Department, South Ural State University (76, Lenin Ave., Chelyabinsk, 454080, Russian Federation), ORCID, kolosovaop@susu.ru

Dmitry A. Shnayder, Dr.Sci. (Eng.), Professor of the Automation and Control Department, South Ural State University (76, Lenin Ave., Chelyabinsk, 454080, Russian Federation), ORCID, SPIN-code, ScopusID, ResearcherID, ResearchGate, shnaiderda@susu.ru

Claimed Contributorship:

ZA Kolosova: formal analysis, writing – original draft preparation.
OP Kolosova: methodology, visualization.
DA Shnayder: conceptualization, writing – review & editing.

Conflict of Interest Statement: **the authors declare no conflict of interest.**

All authors have read and approved the final manuscript.

Об авторах:

Зоя Александровна Колосова, аспирант кафедры «Автоматика и управление» Южно-Уральского государственного университета (454080, Российская Федерация, г. Челябинск, пр. Ленина, д. 76), SPIN-код, ORCID, ScopusID, ResearchGate, kolosovaza@susu.ru

Ольга Петровна Колосова, кандидат технических наук, профессор кафедры «Техническая механика» Южно-Уральского государственного университета (454080, Российская Федерация, г. Челябинск, пр. Ленина, д. 76), ORCID, kolosovaop@susu.ru

Дмитрий Александрович Шнайдер, доктор технических наук, профессор кафедры «Автоматика и управление» Южно-Уральского государственного университета (454080, Российская Федерация, Челябинская область, г. Челябинск, пр. Ленина, д. 76), SPIN-код, ORCID, ScopusID, ResearcherID, ResearchGate, shnaiderda@susu.ru

Заявленный вклад авторов:

З.А. Колосова: формальный анализ, написание черновика рукописи.
О.П. Колосова: разработка методологии, визуализация.
Д.А. Шнайдер: разработка концепции, внесение замечаний и исправлений в текст рукописи.

Конфликт интересов: **авторы заявляют об отсутствии конфликта интересов.**

Все авторы прочитали и одобрили окончательный вариант рукописи.

Received / Поступила в редакцию 16.06.2025
Reviewed / Поступила после рецензирования 02.07.2025
Accepted / Принята к публикации 21.07.2025

INFORMATION TECHNOLOGY, COMPUTER SCIENCE AND MANAGEMENT
ИНФОРМАТИКА, ВЫЧИСЛИТЕЛЬНАЯ ТЕХНИКА И УПРАВЛЕНИЕ

UDC 004.94; 303.732
https://doi.org/10.23947/2687-1653-2025-25-3-256-268

Original Theoretical Research

EDN: PWKCXM

Improving Business Process Model and Notation Diagrams with the Node-Function-Object Approach

Alexander G. Zhikharev, Elena V. Malkush, Sergey I. Matorin ✉
Belgorod State National Research University, Belgorod, Russian Federation
✉ matorin@bsuedu.ru

Abstract

Introduction. The BPMN standard system (notation) is widely used in business process modeling. However, it is not expressive enough to represent technical and production mechanisms. BPMN poorly describes parallel flows with strict resource constraints, insufficiently supports modeling of physical parameters and technological conditions. These and other shortcomings worsen the analysis of performance and reliability, reduce the applicability of models for optimization and verification. The objective of the presented work is to create a method that uses an alternative notation and thus limits the impact of the listed shortcomings of BPMN in modeling production processes.

Materials and Methods. The basis of the new solution was a comparison of BPMN and the notation for the system "node – function – object" (NFO). The elements of the diagrams were the intersections of some connections (nodes). They contained functional elements (functions, processes), which in some cases also had the characteristics of a substance (objects). A comparative analysis of the normative systems of BPMN and NFO showed the possibility of mutual transformation of diagrams. The processes were visualized using the CASE (Computer Aided Software Engineering) tool NFO-toolkit and the Stormbpmn program according to the BPMN rules. The NFO diagram was described in the XPDL[1] language.

Results. Six sequential operations have been developed for converting a NFO diagram into BPMN, and four — for the reverse transformation. The scheme of component production is shown in the context and decomposition, from the requirement for the development of the workflow to the issuance of products. Decompositions of the NFO elements "Injection Molding Machine", "Master" and "Development Department" are presented, each of which corresponds to a decomposition of the same-name track of the BPMN notation pool. It has been proven that converting a BPMN diagram to a NFO improves the description of the process as a whole and to any degree of detail. The NFO approach does not refer to the graphical notation system of BPMN, which increases labor costs and the risk of simulation errors. The XPDL language describes processes, connectors, splitters, relationships, external entities, and other elements of NFO diagrams.

Discussion. The main advantages of NFO notation over the BPMN approach are: easier procedure for creating models and their better visualization. A simple graphic set of NFO reduces simulation time and increases its accuracy. The NFO approach is focused on taking into account information and material connections. This means that it is possible to conduct functional cost CASE analysis, which is impossible using the BPMN method. The XPDL language is suitable for describing elements of NFO diagrams, and the solution can be Russified.

Conclusion. Content redundancy and other shortcomings of the BPMN notation are eliminated through using a more universal and convenient notation — NFO. The research results will contribute to the development of the theory and practice of graph-analytic modeling of production processes, and simplify the procedure for their development and automation.

Keywords: graph-analytic modeling of production processes, process automation model, BPMN notation, NFO notation, "node — function — object" system, CASE tool NFO-toolkit, XPDL language

[1] XPDL Support and Resources. URL: https://wfmc.org/xpdl/ (accessed: 08.06.2025).

Acknowledgements. The authors would like to thank their colleagues of the department for their assistance in selecting materials on BPMN. In addition, they appreciate the Editorial team of the Journal and the reviewer for their competent expertise and valuable recommendations for improving the article.

For citation. Zhikharev AG, Malkush EV, Matorin SI. Improving Business Process Model and Notation Diagrams with the Node-Function-Object Approach. *Advanced Engineering Research (Rostov-on-Don).* 2025;25(3):256–268. https://doi.org/10.23947/2687-1653-2025-25-3-256-268

Оригинальное теоретическое исследование

Усовершенствование диаграмм Business Process Model and Notation с помощью подхода «узел – функция – объект»

А.Г. Жихарев, **Е.В. Малкуш**, **С.И. Маторин** ✉
Белгородский государственный национальный исследовательский университет, Белгород, Российская Федерация
✉ matorin@bsuedu.ru

Аннотация
Введение. При моделировании бизнес-процессов широко используется нормативная система (нотация) BPMN. Однако она недостаточно выразительна для представления технических и производственных механизмов. BPMN плохо описывает параллельные потоки с жесткими ресурсными ограничениями, слабо поддерживает моделирование физических параметров и технологических условий. Эти и другие недочеты ухудшают анализ производительности и надежности, снижают применимость моделей для оптимизации и верификации. Цель представленной работы — создать метод, который задействует альтернативную нотацию и таким образом ограничит влияние перечисленных недостатков BPMN при моделировании производственных процессов.
Материалы и методы. Базой нового решения было сопоставление BPMN и нотации для системы «узел — функция — объект» (УФО). Элементы диаграмм — это перекрестки некоторых связей (узлы). В них расположены функциональные элементы (функции, процессы), имеющие в некоторых случаях и характеристики субстанции (объекты). Сравнительный анализ нормативных систем BPMN и УФО показал возможность взаимного преобразования диаграмм. Процессы визуализировали с помощью CASE-инструмента (от англ. computer aided software engineering) NFO-toolkit (от англ. набор инструментов УФО) и программы Stormbpmn по правилам BPMN. УФО-диаграмму описали на языке XPDL[2].
Результаты исследования. Разработаны шесть последовательных операций для преобразования УФО-диаграммы в BPMN и четыре — для обратной трансформации. В контексте и декомпозиции показана схема выпуска комплектующих — от требования на разработку технологического процесса до выдачи изделий. Представлены декомпозиции УФО-элементов «Термопластавтомат», «Мастер» и «Отдел разработки», каждому из которых соответствует декомпозиция одноименной дорожки пула BPMN-нотации. Доказано, что преобразование диаграммы BPMN в УФО улучшает описание процесса в целом и с любой степенью подробности. УФО-подход не обращается к графической системе обозначений BPMN, из-за которой возрастают трудозатраты и риски ошибок моделирования. На языке XPDL описаны процессы, соединители, разветвители, связи, внешняя сущность и другие элементы УФО-диаграмм.
Обсуждение. Основные преимущества УФО-нотации перед BPMN-подходом: более легкая процедура создания моделей и лучшая их наглядность. Простой графический набор УФО сокращает время моделирования и повышает его точность. УФО-подход ориентирован на учет информационных и материальных связей. Значит, можно проводить функционально-стоимостной CASE-анализ, что невыполнимо методом BPMN. Язык XPDL подходит для описания элементов УФО-диаграмм, причем решение можно русифицировать.
Заключение. Содержательная избыточность и другие недостатки нотации BPMN исключаются при использовании более универсальной и удобной нотации — УФО. Итоги исследования будут способствовать развитию теории и практики графоаналитического моделирования производственных процессов, позволят упростить процедуру их разработки и автоматизации.

Ключевые слова: графоаналитическое моделирование производственных процессов, модель автоматизации процесса, нотация BPMN, нотация УФО, система «узел — функция — объект», CASE-инструмент NFO-toolkit, язык XPDL

Благодарности. Авторы выражают признательность коллегам по кафедре за помощь в подборе материалов по BPMN. Благодарим редакционную команду журнала и рецензента за компетентную экспертизу и ценные рекомендации по улучшению статьи.

[2] XPDL Support and Resources. URL: https://wfmc.org/xpdl/ (дата обращения: 08.06.2025).

Для цитирования. Жихарев А.Г., Малкуш Е.В., Маторин С.И. Усовершенствование диаграмм business process model and notation с помощью подхода «узел — функция — объект». *Advanced Engineering Research* (*Rostov-on-Don*). 2025;25(3):256–268. https://doi.org/10.23947/2687-1653-2025-25-3-256-268

Introduction. Information systems and technologies provide automation of processing and production, which is essential for the modern economy [1]. Thus, in 2024, the analytical portal IaaSSaaSPaaS reported that BPM (Business Process Management) systems are used in Russia by about 12,000 organizations, and hundreds of IT companies are engaged in the implementation[3].

An integral part of the procedure for creating such solutions is the formulation of requirements for them. This is an important element of design [2], which is based on modeling and analysis of automated processes [3]. The analysis is performed using both mathematical tools and graphical notations (IDEF, DFD, EPC, BPMN families, etc. [4]). Each of the listed groups has its own characteristics [5], which are assessed differently by researchers and users [6].

One of the most popular notations is BPMN specification (Business Process Model and Notation)[4]. According to the statistical report of the company “Business Logic”, BPMN is widely used to describe business processes and occupies more than half of the market — 54% [7]. This particular notation is recommended to be used, e.g., in [8]. At the same time, BPMN has significant disadvantages[5], and they have been repeatedly discussed in the literature. Some of them are listed below:

– complex semantics and modeling methods [8];

– hard-to-read linear diagrams when using multiple tracks [9];

– inability to specify the cost of performing actions in monetary terms [8];

– connecting elements do not reflect material and information flows [10];

– difficult-to-model big hierarchical systems, which include large organizations [11].

Business process modeling experts admit that such shortcomings often cause errors when constructing diagrams in BPMN notation. Diagrams can be incomprehensible. This complicates the interaction between developers and can cause the design deadlines to be missed[6, 7]. There have even been proposals to abandon BPMN. The author of one such work[8] claims that the notation in question has no particular advantages. He compares BPMN to a cargo cult, i.e., mechanical copying of actions without understanding the essence of the processes. It is noted that the system was proposed not by business practitioners, but by software developers.

BPMN has integrated tools for translating diagrams into business process execution languages (e.g., XPDEL) [12], and the literature contains recommendations for converting other notations into BPMN. Thus, in [13], IDEF0 is considered from this point of view.

Therefore, the shortcomings of BPMN are known and widely discussed, but there are no constructive suggestions for overcoming them in the public domain. The presented study is intended to fill this gap. The objective of this work is to create alternative, more universal notations that will reduce the impact of the above-mentioned shortcomings of BPMN in modeling production and processing. First of all, it is necessary to solve problems related to the difficulties of modeling and reading diagrams.

Materials and Methods. The authors [14] investigated graph-analytic notations as normative systems. In this sense, the notation of the system-object approach “node – function – object” (NFO approach) turned out to be more universal in comparison with other graphic notations. In this case, universality is provided by the representation of any system in the form of an element “node – function – object” [10], for which the following statements are true.

Node — a structural element of a supersystem. It represents a crossroad of connections (flows of transmitted elements) of a system with other systems in this supersystem.

Function — a functional element. It performs a certain role to support the supersystem through balancing a given node (transforming input flows into output flows).

[3] BPM Systems Market 2024: Analytical Review. URL: https://iaassaaspaas.ru/rating/bpm-sistemy (accessed: 12.06.2025).
[4] Top-8 Methods of Business Process Analysis for 2025. (In Russ.) URL: https://listohod.ru/blog/top-8-metodov-analiza-biznes-processov (accessed: 12.06.2025).
[5] BPMN Notation: Pros, Cons, and Scope. (In Russ.) URL: https://www.directum.ru/blog-post/notacija_bpmn__pljusy_minusy_i_oblast_primenenija (accessed: 12.06.2025).
[6] Typical Mistakes in Modeling Business Processes in BPMN Notation. (In Russ.) URL: https://www.artofba.com/post/common_mistakes_bpmn_diagrams_part1_ru (accessed: 12.06.2025).
[7] Top 25 Errors in BPMN. (In Russ.) URL: https://bpmn2.ru/blog/top-25-oshibok-bpmn (accessed: 12.06.2025).
[8] Why You Should Abandon BPMN. (In Russ.) URL: https://habr.com/ru/articles/681262 / (accessed: 12.06.2025).

Object — a substantial element. This function is implemented in the form of a certain material formation that has design, operational and other characteristics.

The content classification of connections as flows of elements assumes two levels. In material connections, there are substantial (S) and energy (E). In information connections, there are data (D) and control (C) connections.

The analysis of existing graphic notations shows that their alphabet and, accordingly, diagrams, are intersections of connections in which functional elements are located, which in some cases have the characteristics of a substance. Thus, all alphabetic elements of all graphic notations are nodes with functions and often with object characteristics. This allows us to consider the notation of the NFO approach, i.e., NFO notation as universal [14].

The following are the correspondences between BPMN and NFO notations. They are found during comparative analysis and will be the basis for solving the problems of diagram transformations and their evaluation.

1. BPMN Activity corresponds to NFO element that has both a node and a function defined, and is assigned the name "Subprocess". The decomposition diagram of such an element contains NFO elements named "Tasks". BPMN Pool or Track as a context of subprocesses corresponds to NFO element that has a node, a function, and an object defined.

2. BPMN Gateway corresponds to NFO element, which has both a node and one of the logical functions defined: "AND", "OR", "Exclusive OR", "Complex", etc.

3. BPMN Sequence Flow corresponds to the relationship of NFO notation named "Control Transfer".

4. BPMN Message Flow corresponds to the relationship of NFO notation named "Message".

5. BPMN Event corresponds to the relationship of NFO notation with the name of the corresponding event.

For visualization, we use the CASE tool (Computer Aided Software Engineering) NFO-toolkit and the Stormbpmn program in accordance with the BPMN rules.

Thus, according to the stated research objective, we use the listed materials and methods to assess the potential of transforming NFO diagrams into BPMN diagrams and vice versa. Let us consider the possibility of full replacement of BPMN diagrams with NFO diagrams. We find out, firstly, to what extent the NFO approach is able to eliminate the shortcomings of BPMN diagrams. Secondly, we study the task of describing NFO diagrams in the XPDL language[9].

Research Results. To implement the tasks and goals of the work, we simulate a production situation: we show a diagram of the interaction of departments associated with the component release.

Converting NFO diagram to BPMN. Converting diagrams in system-structural notations (particularly, in DFD and IDEF0) to NFO diagrams does not require the development of a specific procedure. NFO diagram in which NFO elements are functional nodes (without defining objects) is equivalent to DFD diagram. NFO diagram in which NFO elements are defined to the object level and there is no relationship "Mechanism" is equivalent to IDEF0 diagram. Thus, for the situation under consideration, instead of developing recommendations for converting various notations into BPMN, a method for converting NFO diagrams into BPMN is needed. This transformation is provided through performing six operations, which are described below. The correspondence of BPMN elements and NFO is given in the Materials and Methods section. The logical operation sign "→" (implication) means replacing the object to the left of the sign with the object to the right of it.

1. *Context NFO diagram is converted to BPMN pool.*

1.1. Context NFO element as a process or object → open BPMN diagram pool.

1.2. External entities of the context NFO diagram → closed BPMN diagram pools.

1.3. Functional (external) relationships of the context NFO element as a process or object that are not related to external entities (or it is not practical to show these entities) → start or end events in the open BPMN pool.

2. *Processes on decomposition of the context object of NFO diagram are transformed into BPMN subprocesses or into pool tracks.*

2.1. Processes on decomposition of context NFO element as a process or object → BPMN subprocesses, if the open pool has one track.

2.2. Processes on decomposition of context NFO element as a process or object → tracks of the open BPMN pool, if the open pool has several tracks.

3. *NFO diagram relationships are converted into BPMN diagram relationships.*

3.1. Information relationships (flows) according to NFO diagram data → BPMN message flows or data objects.

3.2. Information relationships (flows) according to NFO diagram control → BPMN operation flows.

3.3. Material relationships (flows) of NFO diagram → BPMN operation flows with corresponding names.

[9] XPDL Support and Resources. URL: https://wfmc.org/xpdl/ (accessed: 08.06.2025).

4. ***Multiple input and output relationships of NFO elements as processes are connected to BPMN subprocesses via gateways.***

4.1. If NFO element has several input arrows, they are connected through a gateway whose logical function is determined by the value of the input connections.

4.2. If NFO element has several output arrows, they exit through a gateway whose logical function is determined by the value of the output connections.

5. ***If NFO elements corresponding to the subprocesses are decomposed, then the processes in these decompositions → BPMN tasks.***

6. ***Markers corresponding to the names of the relationships are installed on the relationships, if this makes sense.***

Figures 1–3 show an example of converting NFO diagram into BPMN diagram using the procedure presented above. The NFO diagrams (Fig. 1 and 2) were created using the CASE tool NFO-toolkit, and the BPMN diagram (Fig. 3) was created using the Stormbpmn program in accordance with the BPMN rules.

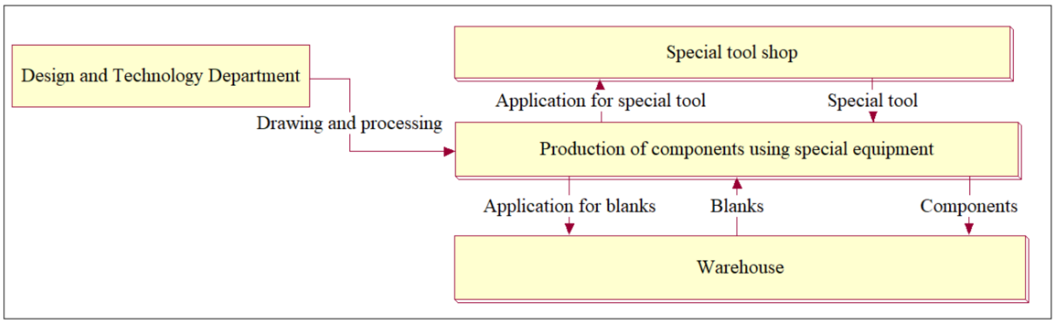

Fig. 1. Context NFO diagram

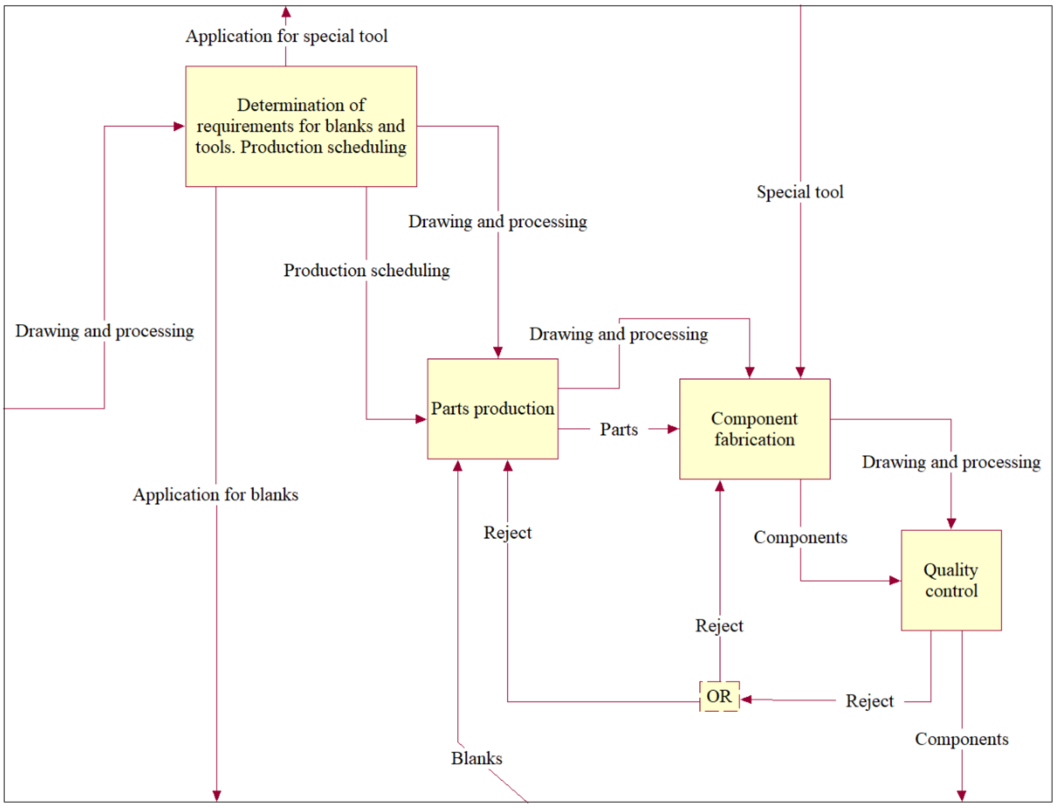

Fig. 2. Decomposition of context NFO diagram

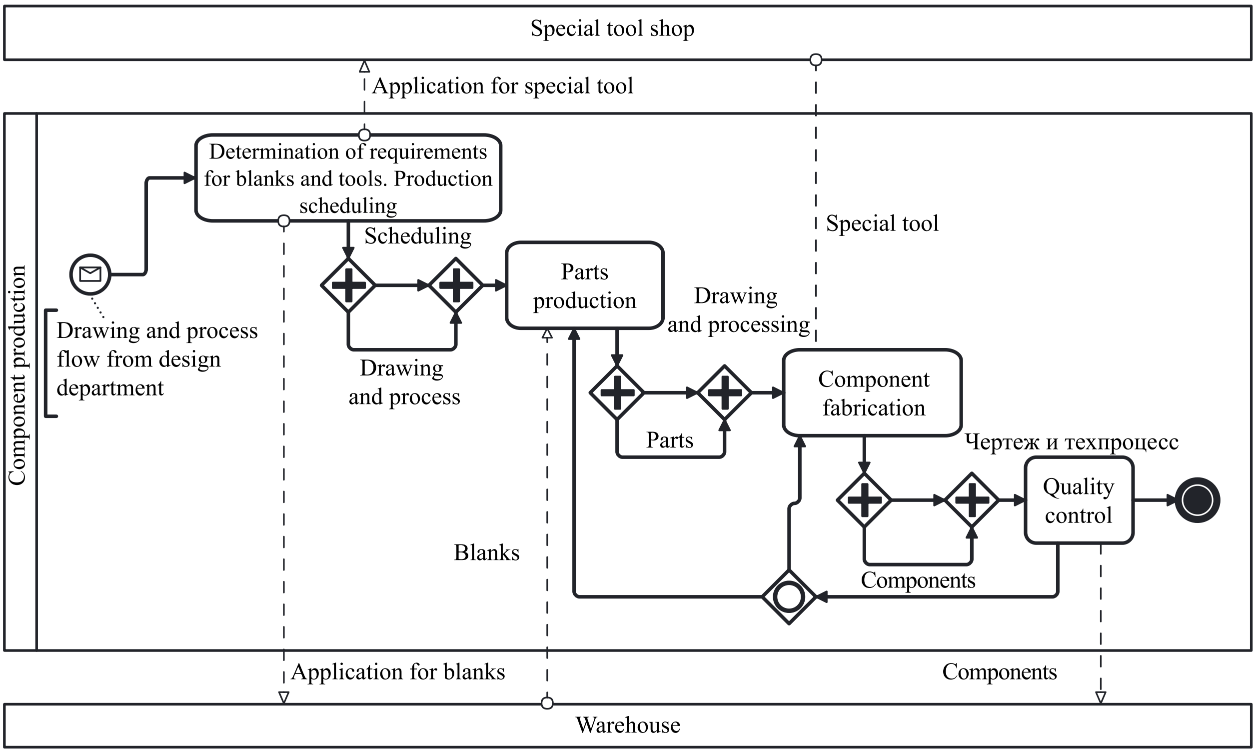

Fig. 3. BPMN diagram corresponding to NFO diagrams

Figure 3 shows clearly the problem of visibility and comprehensibility of the BPMN diagram. The reason is the requirement of the IDEF3 standard integrated into BPMN for the presence of only one input and one output. The fact is that each organizational-business and engineering-manufacturing process involves not only the transformation of the input product into an output one, but also document flow. Thus, any process must have at least two inputs and two outputs: product (material or informational) and documentary (informational). This is not taken into account by the programmers who created BPMN. In addition, Figure 3 allows us to state that event marker icons essentially do not add anything to the diagram content, since all connections are labeled. At the same time, graphic elements are more difficult to use. You need to remember both their meaning and the placement rules.

Converting BPMN diagram to NFO. The following four operations provide converting BPMN diagram to NFO. The correspondence between BPMN and NFO elements is presented in the Materials and Methods section. The logical operation sign "→" (implication) means replacing the object to the left of the sign with the object to the right of it.

1. ***BPMN pool with relationships is converted into context NFO diagram.***

1.1. Pool → context NFO element defined to the object level.

1.2. Pool start event and end event(s) → functional relationships of the context NFO element corresponding to the NFO approach relationship classification.

1.3. If, in addition to the pool, there are tracks associated with it, then the pool relationships with tracks → functional relationships of the context NFO element corresponding to the classification.

1.4. Tracks external to the pool → NFO elements (defined to the object level) as external entities in relation to the context NFO element.

1.5. If there are BPMN elements on the external tracks, then these tracks → NFO elements with subsequent decomposition.

2. ***BPMN pool tracks are transformed into a decomposition diagram of context NFO element corresponding to BPMN pool.***

2.1. Pool track → decomposition elements of context NFO element corresponding to BPMN pool.

2.2. Each BPMN track → NFO element defined to the object level.

2.3. Start event(s) and end event(s) of a track, as well as relationships to other tracks (if any) → functional relationships of NFO element corresponding to a track from the NFO approach relationship classification.

3. ***Subprocesses on BPMN track are transformed into NFO element decomposition diagram corresponding to the BPMN track.***

3.1. Subprocesses on BPMN track → elements of decomposition of NFO element corresponding to BPMN track.

3.2. Each BPMN subprocess → NFO element defined to the function level.

3.3. Subprocess relationships → relationships from the NFO approach relationship classification taking into account BPMN event triggers.

3.4. BPMN track gateways → NFO elements with certain logical functions.

3.5. Gateway relationships → relationships from the NFO approach relationship classification taking into account BPMN event triggers.

4. ***The tasks of BPMN subprocess are transformed into a decomposition diagram of the NFO element corresponding to the BPMN subprocess.***

4.1. BPMN subprocess tasks → decomposition elements of the NFO element corresponding to the BPMN subprocess.

4.2. Each BPMN task → NFO element defined to the function level.

4.3. Task relationships → relationships from the NFO approach relationship classification taking into account BPMN event triggers.

4.4. BPMN subprocess gateways → NFO elements with defined logical functions.

Figures 4–9 show an example of converting BPMN diagram into NFO using the above procedure. Here, the BPMN diagram (Fig. 4) was also created using the Stormbpmn program in accordance with the BPMN rules. To build the NFO diagram (Fig. 5–9), the CASE tool NFO-toolkit was used.

The scheme of production of plastic components from the requirement for development of the process to the issuance of products is shown. In this case, the following are taken into account:

– development, analysis and fine-tuning of the process for manufacturing a part on an injection molding machine;
– parameters for setting up the injection molding machine;
– obtaining plastic;
– loading the machine;
– heating the plastic to a specified temperature;
– forming and releasing products.

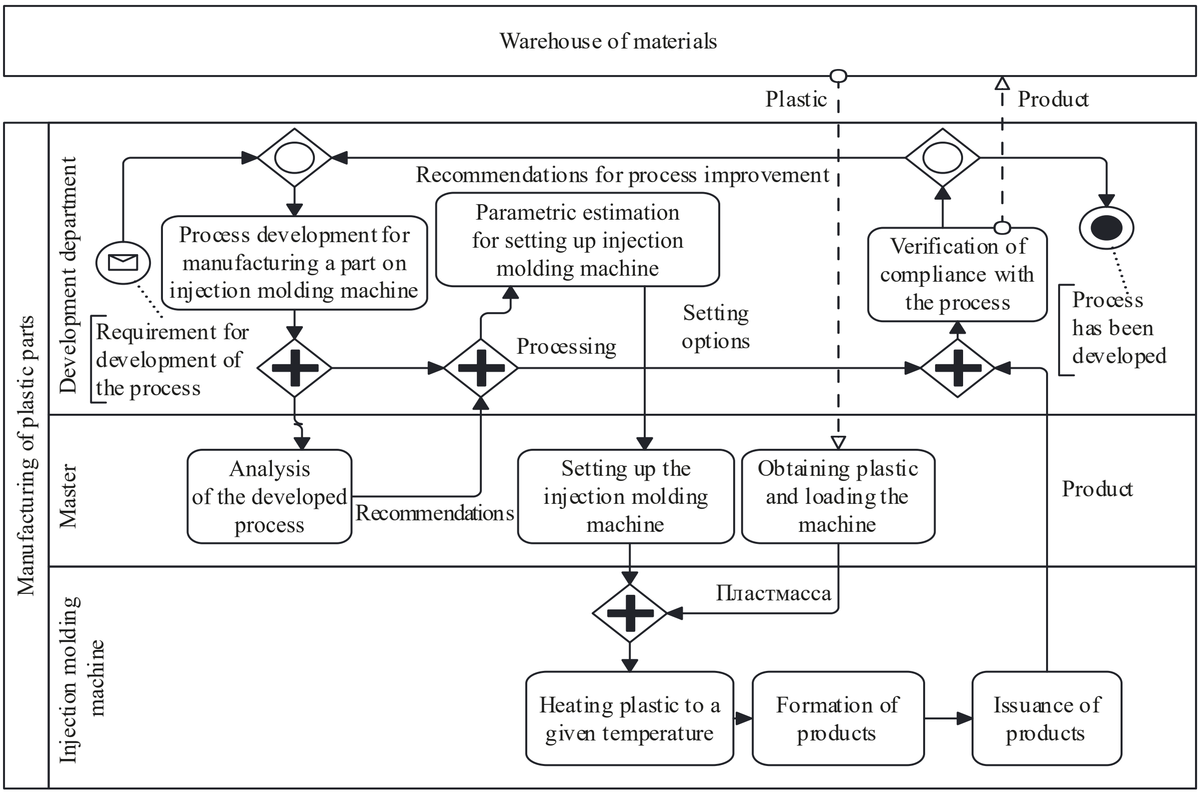

Fig. 4. BPMN diagram

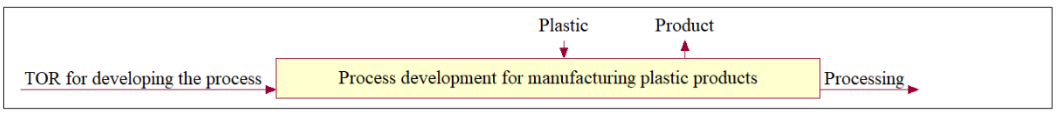

Fig. 5. Context NFO diagram with functional relationships of BPMN diagram

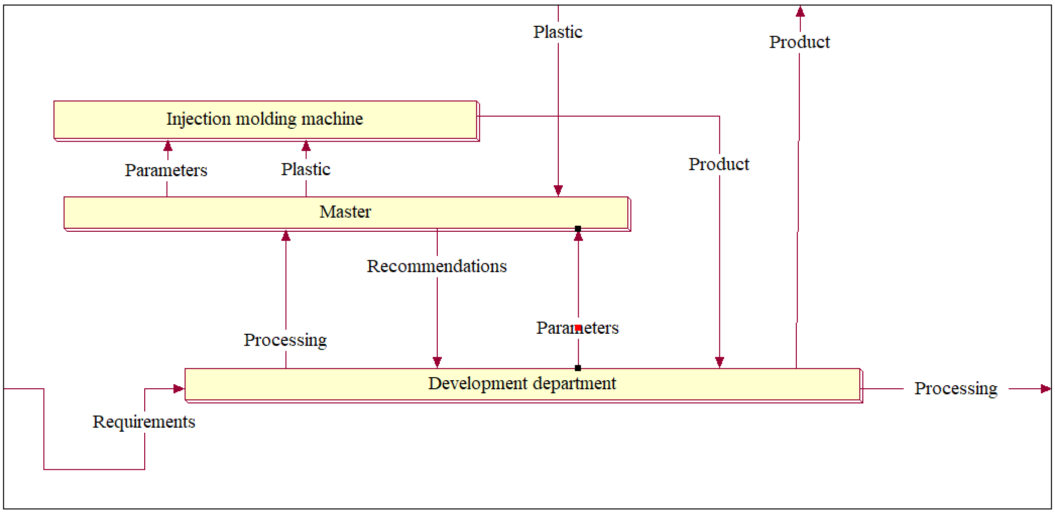

Fig. 6. Decomposition of context NFO diagram corresponding to the tracks of BPMN diagram pool

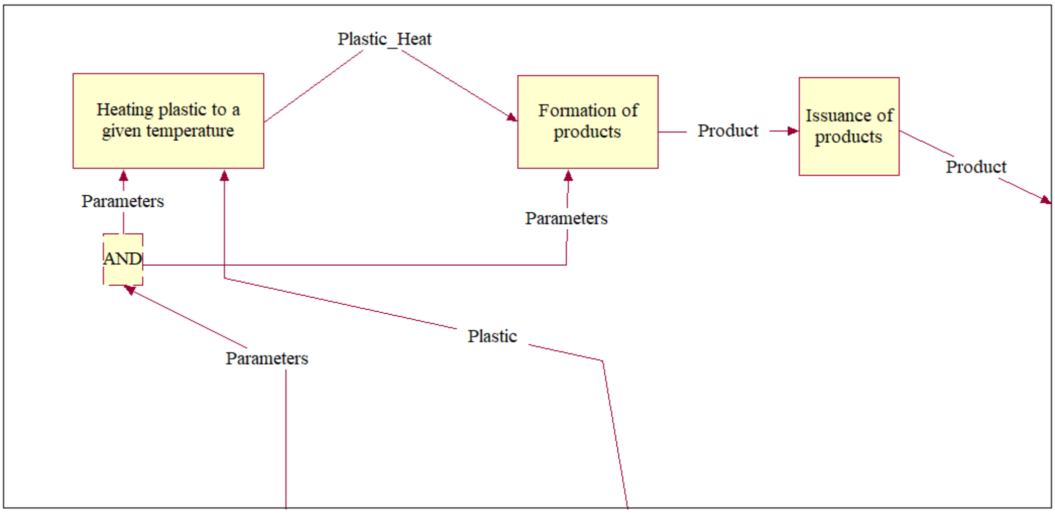

Fig. 7. Decomposition of NFO element “Injection Molding Machine”, corresponding to decomposition of the track of the pool “Injection Molding Machine” of BPMN diagram

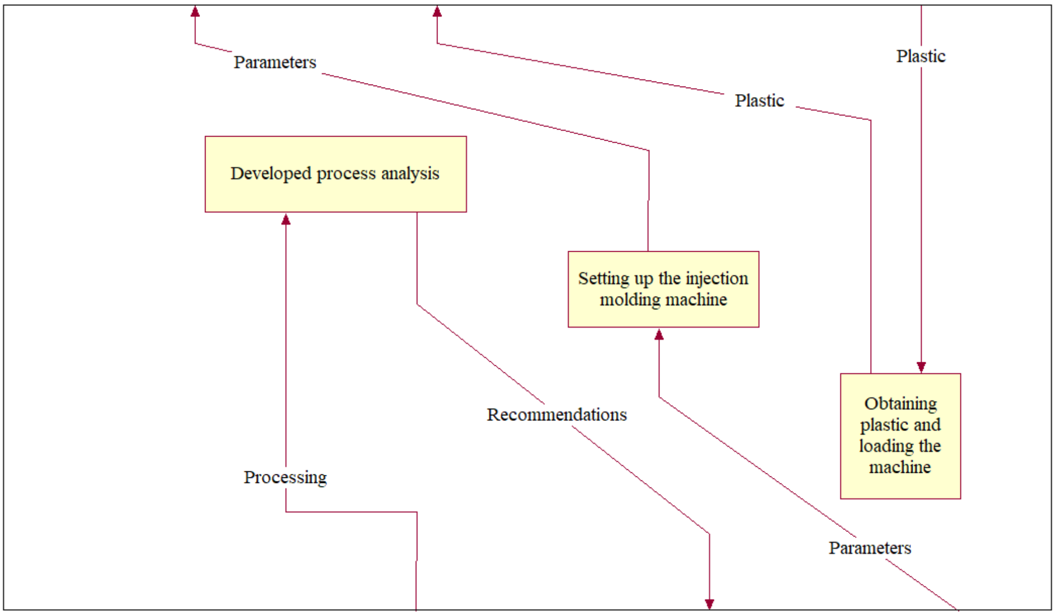

Fig. 8. Decomposition of NFO element “Master”, corresponding to the decomposition of the pool track “Master” of BPMN diagram

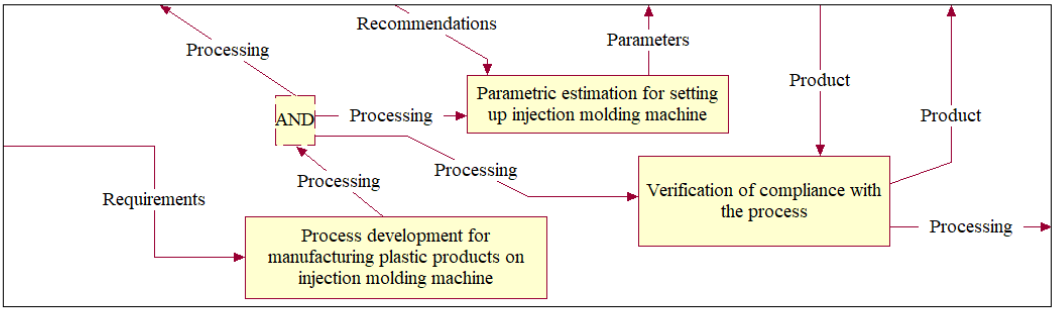

Fig. 9. Decomposition of NFO element "Development Department", corresponding to decomposition of pool track "Development Department" of BPMN diagram

Analysis of Figures 4–9 allows us to state that the transformation of BPMN diagram into a diagram in NFO notation makes the description of the process more understandable, since it provides seeing it not only as a whole (in context), but also to any degree of detail. In this case, fewer icons are used, and this is a more convenient option, since it does not require remembering the meaning of graphic elements and the rules for their placement.

Description of NFO diagrams in XPDL language. In the Introduction section, the advantage of BPMN over other notations is noted: the means of translating BPMN diagrams into business process execution languages (e.g., XPDEL[10]) allow for the automation of organizational-business and engineering-manufacturing processes. However, this feature is easily transferred to the NFO notation. The main elements of the method for describing NFO diagrams in the XPDL language are presented in Table 1 by analogy with paper [15].

Table 1

Description of NFO Diagrams in XPDL Language

NFO diagram element	XPDL Construction
Process (context)	<Activity id=«Имя»> <BlockActivity /> … </Activity>
Process (on decomposition)	<Activity id=«Имя»> <Implementation> <SubFlow /> … </Implementation> </Activity>
Connector "AND"	<Activity> <Route/> <TransitionRestriction> <Join Type=«AND»/> </TransitionRestriction> </Activities>
Splitter "AND"	<Activity> <Route/> <TransitionRestriction> <Split Type=«AND»/> </TransitionRestriction> </Activities>
Connector "OR"	<Activity> <Route/> <TransitionRestriction> <Join Type=«OR»/> </TransitionRestriction> </Activities>
Splitter "OR"	<Activity> <Route/> <TransitionRestriction> <Split Type=«AND»/>

[10] XPDL Support and Resources. URL: https://wfmc.org/xpdl/ (дата обращения: 08.06.2025).

	</TransitionRestriction> </Activities>
Connector “Exclusive OR”	<Activity> <Route/> <TransitionRestriction> <Join Type=«XOR»/> </TransitionRestriction> </Activities>
Splitter “Exclusive OR”	<Activity> <Route/> <TransitionRestriction> <Split Type=«XOR»/> </TransitionRestriction> </Activities>
Functional relationship without a source (input) or without a consumer (output))	<Transition/> id=«Имя» />
Supportive connection between subprocesses	<Transition id=«L» from=«Имя!» to=«Имя?» />
External entities	<Activity> <Route type=«in» /> </Activity> или <Activity> <Route type=«out» /> </Activity>
Process executor	<Participant type=«______»/> 1. Role 2. OrganisationUnit 3. Human 4. System 5. Resource 6. RecourceSet
Interaction of two processes using two relashionships	<Activities> <Activity id=«Имя!»> <Implementation> <SubFlow /> <TransitionRamification> <Split Type=«AND» /> <Transition id=«M» from=«Имя!» to=«Имя?» /> <Transition id=«I» from=«Имя!» to=«Имя?» /> </TransitionRamification> </Implementation> </Activity> <Activity id=«Имя?»> <Implementation> <SubFlow /> <TransitionMerger > < Join Type =«AND» /> <Transition id=«M» from=«Имя!» to=«Имя?» /> <Transition id=«I» from=«Имя!» to=«Имя?» /> </TransitionMerger> </Implementation> </Activity> </Activities>

The table shows that when converting BPMN diagrams to NFO, it is possible to translate them into the process execution language.

Discussion. Thus, in BPM systems, not only BPMN notation can be used to build process models for the purpose of their automation, but also NFO notation, which provides a simpler procedure for creating models and their greater visibility.

The adequacy and practical value of this approach can be judged by the following data compiled by the authors:

– BPMN diagram;

– context NFO diagram with functional relationships of the BPMN diagram;

– decomposition of the context NFO diagram corresponding to the tracks of the BPMN diagram pool;

– decomposition of the NFO element "Injection molding machine" corresponding to the decomposition of the track of the "Injection molding machine" pool of the BPMN diagram;

– decomposition of the NFO element "Master" corresponding to the decomposition of the track.

The illustrative material proves the advantages of NFO notation. The transformation from BPMN diagram to NFO has revealed two advantages of this approach. First: the description in NFO notation opens up the possibility of analyzing the process as a whole (i.e., in context) and with any level of refinement (decomposition). Second: NFO notation uses fewer specific icons. This is a more convenient option, because:

– time required to remember the meaning of graphic elements and the rules for their placement is cut;

– risk of incorrect use of graphic elements in diagrams is reduced.

All this is clearly visible in Figures 4–9. In addition, to show the acquisition and dispatch of material resources to an external entity within BPMN, it is required to use a dotted arrow intended to indicate a message flow, not a material flow. This creates problems both at the stage of constructing the model by the analyst and at the stage of reading it by the designer or manager. Diagrams in NFO notation do not have this drawback.

Next. The NFO diagram shows better from which resources the desired result is obtained. This is explained by the fact that the NFO approach is initially focused on accounting for both material and information flows (connections). Hence another advantage. It is possible to conduct a functional cost analysis using a CASE tool that provides construction of NFO diagram. This is impossible for a diagram in BPMN notation, since this principle does not have a standard interpretation of connections as flow elements.

Discussing the data in Table 1, it is appropriate to note the prospects for Russification of the material. Here, the XPDL language constructs are naturally presented in English. However, it is planned to automate the execution of the models created by the authors of the article. And in the new solutions, the process names will be in Russian. As we can see, in this case, the attribute "Name" is written in Cyrillic.

Conclusion. Research of the normative systems of notation of the system-object approach "node – function – object" (NFO) and BPMN show that NFO notation is more universal and provides eliminating a number of shortcomings of BPMN diagrams through reproducing them by NFO notation. The results of the presented work will contribute to the development of the theory and practice of graph-analytic modeling of processes.

As a result of the conducted research, procedures for mutual transformation of BPMN and NFO diagrams were created. In addition, a description of the elements of the NFO approach notation in the XPDL business process execution language is shown, which equalizes the applied capabilities of the NFO notation with BPMN. In the future, XPDL structures will be Russified. It is assumed that the models created by the authors of this article will be executed by software methods, and the process names will be in Russian.

In general, the application of the results obtained will simplify the procedure for constructing graphical models of processes and their automation.

References / Список литературы

1. Panteleev AS, Shmatin AK. Problems of Digitalization and Robotization in Modern Russian Realities. *Avtomatizirovannoe Proektirovanie v Mashinostroenii*. 2022;(13):155–158. (In Russ.) https://doi.org/10.26160/2309-8864-2022-13-155-158

2. Bochkaryov PYu, Korolev RD, Bokova LG. Comprehensive Assessment of the Manufacturability of Products. *Advanced Engineering Research (Rostov-on-Don)*. 2023;23(2):155–168. https://doi.org/10.23947/2687-1653-2023-23-2-155-168

3. Korotkii AA, Yakovleva DA, Maslennikov AA, Golovko IV. Modeling of Information Support to Optimize Logistics Tasks in Transport Sector Using a Programmable Container Transformer Simulator. *Advanced Engineering Research (Rostov-on-Don)*. 2020;20(3):311–316. https://doi.org/10.23947/2687-1653-2020-20-3-311-316

4. Alenikov AS, Mamonova IV, Kololeeva KI. Variant Approaches to the Choice of Notation When Modeling Business Processes in the Enterprise. *Bulletin of the Academy of Knowledge*. 2020;39(4):33–41.

5. Aksenova OP, Aksenov KA, Antonova AS, Smoliy EF. The Analysis of Graphic Notations for Simulation Modeling of Enterprise Business Processes. *Scientific Review. Technical Science.* 2014;(1):45–54. URL: https://science-engineering.ru/ru/article/view?id=17 (accessed: 17.06.2025).

6. Udaltsova NL. Modern Methods of Business Process Analysis and Modeling. *Leadership and Management*. 2021;8(2):185–200. https://doi.org/10.18334/lim.8.2.112126

7. Vakorin MP, Konstantinov DS, Mylnikova AP. Assessment of the Applicability of Business Process Description Notation for Modeling the Information Security Risk Management Process in an Organization. *Young Scientist.* 2022;445(50):6–8. (In Russ.) URL: https://moluch.ru/archive/445/97853/ (accessed: 15.06.2025).

8. Repin V. *Modeling Business Processes in BPMN Notation in Business Studio 5*: *Field Guide*. Moscow: Izdatel'skie resheniya; 2020. 106 p. (In Russ.)

9. Potryasaev SA. Integrated Modeling of Complex Processes Based on BPMN Notation. *Journal of Instrument Engineering*. 2016;59(11):913–920. https://doi.org/10.17586/0021-3454-2016-59-11-913-920

10. Zhikharev AG, Zimovets OA, Tuboltsev MF, Kondratenko AA. *Systems Theory and Systems Analysis.* SI. Matorin (ed). Moscow: Direktmedia Pablishing; 2021. 456 p. (In Russ). URL: https://biblioclub.ru/index.php?page=book&id=574641 (accessed: 05.06.2025).

11. Belaychuk AA, Bratchenko SA. Essential and Redundant Gateways in BPMN 2.0. *Business Strategies.* 2017;(4):3–7. https://doi.org/10.17747/2311-7184-2017-4-03-07

12. Ivanov S, Kalenkova A. Comparing Process Models in the BPMN 2.0 XML Format. *Proceedings of ISP RAS*. 2015;27(3):255–266. https://doi.org/10.15514/ISPRAS-2015-27(3)-17

13. Matveev AS, Rudenko AYu, Prochukhan VV. Development of Recommendations for Transition from IDEF0 Notation of Business Processes Modeling to BPMN Notation. *Business. Education. Law. Bulletin of Volgograd Business Institute*. 2016;36(3):176–182. URL: https://vestnik.volbi.ru/upload/numbers/336/article-336-1688.pdf (accessed: 17.06.2025).

14. Zimovets OA, Malkush EV, Matorin SI, Korsunov NI. Comparison of DFD, IDEF0, IDEF3, EPC and BPMN Notations with UFO-analysis Notation. *Economics. Information Technologies.* 2024;51(4):936–945. https://doi.org/10.52575/2687-0932-2024-51-4-936-945

15. Klimenko AV, Zhulin AB, Plaksin SM, Golovshchinsky KI, Sivasheva NM, Suvorova IK, et al. *Development of Methodological Recommendations for the Description and Optimization of Processes in Executive Authorities in the Context of Preparation for the Implementation of the EAR*: *Research Report*. Moscow: Higher School of Economics; 2010. 193 p. (In Russ). URL: https://textarchive.ru/c-1946975.html (accessed: 08.06.2025).

About the Authors:

Alexander G. Zhikharev, Dr.Sci. (Eng.), Associate Professor, Director of the Institute of Engineering and Digital Technologies, Belgorod State National Research University (85, Pobedy Str., Belgorod, 308015, Russian Federation), SPIN-code, ORCID, ScopusID, zhikharev@bsuedu.ru

Elena V. Malkush, Postgraduate student of the Department of Information and Robotic Systems, Belgorod State National Research University (85, Pobedy Str., Belgorod, 308015, Russian Federation), SPIN-code, malkush@bsuedu.ru

Sergey I. Matorin, Dr.Sci. (Eng.), Professor of the Department of Information and Robotic Systems, Belgorod State National Research University (85, Pobedy St, Belgorod, 308015, Russian Federation), SPIN-code, ORCID, ScopusID, ResearcherID, matorin@bsuedu.ru

Claimed Contributorship:

AG Zhikharev: project administration, conceptualization, investigation, writing – review & editing.
EV Malkush: investigation, visualization, methodology.
SI Matorin: methodology, investigation, writing – original draft preparation.

Conflict of Interest Statement: **the authors declare no conflict of interest.**

All authors have read and approved the final manuscript.

Об авторах:

Александр Геннадиевич Жихарев, доктор технических наук, доцент, директор Института инженерных и цифровых технологий Белгородского государственного национального исследовательского университета (308015, Российская Федерация, г. Белгород, ул. Победы, 85), SPIN-код, ORCID, ScopusID, zhikharev@bsuedu.ru

Елена Викторовна Малкуш, аспирант кафедры «Информационных и робототехнических систем» Белгородского государственного национального исследовательского университета (308015, Российская Федерация, г. Белгород, ул. Победы, 85), SPIN-код, malkush@bsuedu.ru

Сергей Игоревич Маторин, доктор технических наук, профессор кафедры «Информационных и робототехнических систем» Белгородского государственного национального исследовательского университета (308015, Российская Федерация, г. Белгород, ул. Победы, 85), SPIN-код, ORCID, ScopusID, ResearcherID, matorin@bsuedu.ru

Заявленный вклад авторов:

А.Г. Жихарев: административное руководство исследовательским проектом, разработка концепции, проведение исследования, написание рукописи, внесение замечаний и исправлений.

Е.В. Малкуш: проведение исследования, визуализация, разработка методологии.

С.И. Маторин: разработка методологии, проведение исследования, написание черновика рукописи.

***Конфликт интересов*: авторы заявляют об отсутствии конфликта интересов.**

Все авторы прочитали и одобрили окончательный вариант рукописи.

Received / Поступила в редакцию 23.06.2025
Reviewed / Поступила после рецензирования 24.07.2025
Accepted / Принята к публикации 11.08.2025